

Direct Photon Shine: Direct Photon and  $\pi^0$  Production in  
 $\sqrt{s_{NN}} = 200$  GeV *Au+Au* Collisions

Justin Frantz

Submitted in partial fulfillment of the  
requirements for the degree  
of Doctor of Philosophy  
in the Graduate School of Arts and Sciences

COLUMBIA UNIVERSITY  
2005

© 2005

Justin Frantz

All Rights Reserved

# ABSTRACT

Direct Photon Shine: Direct Photon and  $\pi^0$  Production in  $\sqrt{s_{NN}} = 200$  GeV  $Au+Au$  Collisions

Justin E. Frantz

With substantial additional statistics due to the inclusion of a new Run2 trigger data sample, the PHENIX Collaboration has measured the first positive direct photon ( $\gamma_{direct}$ ) signal in  $Au + Au$  collisions at  $\sqrt{s_{NN}} = 200$  GeV and midrapidity ( $|y| \leq 0.35$ ). The measurement is made in 10 centrality bins covering 0-92% of the full geometric cross section. Additionally, the new data has extended the previous PHENIX  $\pi^0$  measurement [69] by 4 GeV/c in its  $p_T$  range, matching the  $\gamma_{direct}$  measurement with a  $p_T$  range of 1-14 GeV/c which make them the highest  $p_T$  measurements yet in RHIC  $Au + Au$ . The  $\gamma_{direct}$  yields are compared amongst themselves, with references, and with the  $\pi^0$ . The suppression in meson hard scattering previously discovered at RHIC [69] is found to be absent in the direct photons. Specifically, using the NLO perturbative QCD prediction of  $\gamma_{direct}$  as a reference, the nuclear modification factor  $R_{AA}$  is found to be consistent with one and  $p_T$ -independent for  $p_T > 6$  GeV/c.

Thus, like the  $d + Au$  results, these direct photon measurements represent possibly the best available confirmation of the conclusion that the aforementioned suppression effect is not due to differences in initial state hard-scattering, but rather, is due to a final state medium which quenches hard quarks and gluons, but not hard direct photons. This conclusion is consistent with final state modifications predicted as indicators of Quark Gluon Plasma (QGP) formation [171]. In addition, the possible model-generated mechanisms for this suppression are constrained further (though only slightly) by our updated  $\pi^0$   $R_{AA}$  results due to the higher  $p_T$  values reached. The suppression continues to be independent of  $p_T$ , signaling strong

energy dependence.

The direct photon invariant yields in ( $p_T < 6$  GeV/ $c$ ) region are compared to predictions of thermal production and new mechanisms of photon enhancement [89],[178]. Large uncertainties do not allow any definite conclusions about observations or constraints of such enhancements.

# Contents

<b>1</b>	<b>Introduction</b>	<b>1</b>
<b>2</b>	<b>Particles, The Strong Force, and, QCD</b>	<b>6</b>
2.1	Particle Physics: Quantum Mechanics, Forces, and Fields . . . . .	7
2.2	QCD: The Strong Force . . . . .	9
2.2.1	Quarks, Gluons, and Color Confinement . . . . .	9
2.2.2	QCD, QED, and Standard Model Basics . . . . .	13
2.3	Perturbation Theory and Perturbative QCD (pQCD) . . . . .	17
2.3.1	Feynman diagrams and Renormalization . . . . .	17
2.3.2	The Running Coupling Constant $\alpha_S$ . . . . .	21
2.3.3	Factorization, PDF's and Fragmentation . . . . .	23
<b>3</b>	<b>The Phase Transition, QGP, and HI Physics</b>	<b>30</b>
3.1	Non-Perturbative and Lattice QCD . . . . .	30
3.2	Enter Relativistic Heavy Ions . . . . .	37
3.3	The Space-Time Geometry of a RHI Collision . . . . .	38
3.3.1	Basics And Static Structure . . . . .	38
3.3.2	Spacial Evolution . . . . .	39
3.3.3	Time Evolution and Thermal Equilibrium . . . . .	41
3.4	4-Momentum Space Evolution: The Energy Density $\epsilon$ . . . . .	43
3.5	QGP Signatures . . . . .	44

<b>4</b>	<b>QGP Signatures in <math>\gamma_{direct}</math> and Hard <math>\pi^0</math> Physics</b>	<b>46</b>
4.1	Hard Scattering and High- $p_T$ Suppression . . . . .	47
4.2	Quantifying Medium Effects . . . . .	48
4.3	Scaling And <i>The</i> $R_{AB}$ . . . . .	49
4.3.1	AB Scaling . . . . .	49
4.3.2	Centrality . . . . .	51
4.3.3	The Glauber Model and Thickness Functions . . . . .	53
4.3.4	Binary and Participant Scaling . . . . .	55
4.3.5	Experimental $R_{AB}$ : $T_{AB}$ or $N_{coll}$ ? . . . . .	59
4.4	The Baseline: Review of Hard Scattering in Particle Physics . . . . .	60
4.4.1	The Basics: $p_T$ $x_T$ Scaling, <i>Etc.</i> . . . . .	61
4.4.2	Nuclear Effects . . . . .	67
4.4.3	The $k_T$ Smearing Debate . . . . .	70
4.5	The Mechanism of High $p_T$ Suppression in the QGP . . . . .	74
4.5.1	Gluon Radiation . . . . .	74
4.5.2	Is it Really a QGP Signature? . . . . .	77
4.6	Review of Hard Scattering in $A + A$ . . . . .	78
4.6.1	pre-RHIC: SPS . . . . .	78
4.6.2	RHIC . . . . .	79
4.7	Mechanisms for Direct Photon Enhancement and Measurements in $A + A$ . . . . .	83
4.7.1	Experimental Results . . . . .	83
4.7.2	Thermal Radiation . . . . .	84
4.7.3	Jet-Plasma $\gamma_{direct}$ Production . . . . .	90
<b>5</b>	<b>Experiment</b>	<b>93</b>
5.1	RHIC: Trains of Trains . . . . .	93
5.1.1	“Runs” and “runs” . . . . .	95
5.1.2	RCF and PHONCS . . . . .	97
5.2	PHENIX . . . . .	97

5.3	Central Magnet and Interaction Region . . . . .	98
5.4	Introduction to Particle Energy Loss in Matter . . . . .	101
5.5	BBC/ZDC Detectors and Triggering . . . . .	102
5.6	Charge Particle Tracking . . . . .	105
5.7	EMCal Overview . . . . .	107
5.8	Introduction to Showering . . . . .	108
5.8.1	PbSc and PbGl . . . . .	109
5.8.2	Organization And History . . . . .	112
5.8.3	Nominal Resolution . . . . .	112
5.8.4	Clustering . . . . .	113
5.8.5	Shower Merging . . . . .	115
5.8.6	Photon Corrected Energy $E_{core}$ . . . . .	116
5.9	Data Acquisition and Triggering . . . . .	117
<b>6</b>	<b>Analysis</b>	<b>124</b>
6.1	Glauber Model Calculations . . . . .	126
6.2	EMCal Calibration . . . . .	130
6.2.1	Direct Methods: The Ideal “General Theory” of Calibrations .	130
6.2.2	Averaging Methods of PHENIX . . . . .	131
6.2.3	Test Beams, MIP calibrations, Energy Sharing . . . . .	132
6.2.4	$\pi^0$ Corrections . . . . .	136
6.2.5	PbGl and the Slope Method . . . . .	137
6.2.6	Calibration Quality, Final Resolution . . . . .	139
6.2.7	A Problem . . . . .	142
6.2.8	Timing Calibrations . . . . .	143
6.2.9	Systematic Uncertainties . . . . .	147
6.3	Raw Data Extraction . . . . .	148
6.3.1	Offline Reconstruction and Software . . . . .	148
6.3.2	Data QA . . . . .	150
6.3.3	Dead and Hot Towers . . . . .	152

6.3.4	Cluster/Single Photon Extraction: Cuts . . . . .	156
6.3.5	$\pi^0$ Yield Extraction . . . . .	160
6.4	Level2 High $p_T$ Tile Trigger . . . . .	170
6.4.1	Event Counting . . . . .	170
6.4.2	Trigger Efficiencies . . . . .	170
6.4.3	Photon Efficiencies . . . . .	172
6.4.4	Photon Matching . . . . .	175
6.4.5	PbG1 Efficiencies . . . . .	175
6.4.6	$\pi^0$ Efficiencies: The Software Cut . . . . .	176
6.4.7	$\pi^0$ Matching . . . . .	180
6.4.8	Systematic Errors . . . . .	180
6.5	Introduction to Corrections . . . . .	186
6.5.1	Invariant Yields and Cross Sections . . . . .	186
6.5.2	Formulae . . . . .	187
6.5.3	Bin Shift Correction . . . . .	189
6.5.4	Power Law Fitting . . . . .	191
6.6	Acceptance and Efficiency Calculations . . . . .	195
6.6.1	Geometric Acceptance $a$ . . . . .	195
6.6.2	Efficiency Calculation $\epsilon$ . . . . .	197
6.6.3	Simulation and Embedding . . . . .	198
6.6.4	Smearing . . . . .	201
6.6.5	Final Efficiencies . . . . .	202
6.6.6	Systematic Uncertainties: Simulation/PID . . . . .	202
6.6.7	Systematic Uncertainties: Embedding . . . . .	211
6.6.8	Systematic Uncertainties: Calibration . . . . .	211
6.6.9	Systematic Uncertainties: Smearing . . . . .	213
6.6.10	Calibration and Smearing Correlations . . . . .	214
6.6.11	Other Sources of Uncertainty and Error Summary . . . . .	216
6.7	$\gamma$ Conversions and Hadron Contamination . . . . .	218

6.7.1	Photon Conversions . . . . .	218
6.7.2	Charged Contamination . . . . .	220
6.7.3	Jet and Other Correlations Present in $X_{ch}$ . . . . .	221
6.7.4	Systematic Errors: $X_{ch}$ . . . . .	223
6.7.5	Neutral Hadron Contamination . . . . .	223
6.7.6	Systematic Uncertainty: $X_{n/\bar{n}}$ . . . . .	225
6.8	Background Decay Photon Calculation . . . . .	227
6.9	Summary of Systematic Errors . . . . .	231
<b>7</b>	<b>Results</b>	<b>235</b>
7.1	$\pi^0$ Spectra . . . . .	235
7.2	$\pi^0$ $R_{AA}$ Values . . . . .	236
7.2.1	$\pi^0$ $R_{AA}$ vs. Centrality ( $N_{part}$ ) . . . . .	239
7.3	$\gamma_{all}$ Spectra . . . . .	240
7.4	Establishment of the Direct Photon Signal: $R_{\gamma_{direct}}$ . . . . .	241
7.5	Direct Photon Spectra . . . . .	243
7.6	Direct Photon $R_{CP}$ . . . . .	243
<b>8</b>	<b>Discussion of Results</b>	<b>245</b>
8.1	The Setting . . . . .	246
8.2	$N_{collision}$ Scaling and High $p_T$ Suppression . . . . .	249
8.2.1	Spectral Shapes . . . . .	250
8.2.2	Systematic Error Cancellations in Spectral Ratios . . . . .	252
8.2.3	The Ratio $R_{CP}$ . . . . .	254
8.2.4	Absolute Value of $R_{CP}$ . . . . .	258
8.2.5	$T_{AA}$ Scaling . . . . .	260
8.2.6	Other Evidence . . . . .	266
8.3	Direct Photon $R_{AA}$ and NLO pQCD Performance at RHIC . . . . .	268
8.3.1	Modifications or Enhancements of Direct $\gamma$ ? . . . . .	273
8.3.2	Suppression of Bremsstrahlung/Fragmentation Photons? . . . . .	284

8.4	High( <i>er?</i> ) $p_T$ $\pi^0$ Suppression . . . . .	287
8.5	Au+Au: An Ideal $\gamma_{direct}$ Laboratory? . . . . .	290
8.6	Summary and Restatement of Conclusions . . . . .	290
<b>A</b>	<b>Run Info</b>	<b>313</b>
<b>B</b>	<b><math>\pi^0</math> Invariant Yields</b>	<b>315</b>
<b>C</b>	<b>Direct Photon Invariant Yields</b>	<b>325</b>
<b>D</b>	<b><math>\pi^0</math> <math>R_{AA}</math> Values</b>	<b>333</b>

# List of Figures

2.1	All known elementary particles/fields . . . . .	14
2.2	Gluon Compton Scattering . . . . .	19
3.1	Phase Transition . . . . .	34
3.2	Stefan-Boltzmann Limit . . . . .	36
3.3	Phase Diagram . . . . .	37
3.4	Geometry of a HI Collision . . . . .	40
4.1	Geometry of a HI Collision - Part II . . . . .	52
4.2	$\pi^0$ Production vs. $\sqrt{s}$ and $p_T, x_T$ . . . . .	62
4.3	Direct $\gamma$ Production vs. $\sqrt{s}$ and $x_T$ . . . . .	65
4.4	Disagreements between various $\gamma_{direct}$ data sets at $\sqrt{s}19.4$ GeV. . . . .	65
4.5	Cronin and other Nuclear Effects . . . . .	69
4.6	Disagreements between world's inclusive pion data and NLO QCD. figure taken from [33]. Note that the initial data from PHENIX Run2 is included. . . . .	72
4.7	Disagreements between world's inclusive $\gamma_{direct}$ data and NLO QCD figure taken from [33]. . . . .	73
4.8	Lowest order diagram in the GLV opacity expansion. . . . .	76
4.9	Hard Scattering Results at the SPS . . . . .	78
4.10	High $p_T$ inclusive spectra results from RHIC . . . . .	80

4.11 Particle Pair $\phi$ Angular Correlations measured at RHIC. In <i>a)</i> the Jet Structure is obvious due to the correlations at small angle (near side) and at $180^\circ$ (away side). Both STAR and PHENIX observe this Jet signal [135],[21] . In <i>b)</i> it shown that the away side correlation is reduced at high $p_T$ (disappearance) but enhanced at low $p_T$ (reappearance). As in <i>a)</i> this behavior is also shown to depend on orientation with respect to the reaction plane, explaining the high $p_T$ portion of 4.10 . . . . .	82
4.12 The two direct photon results in HI physics previous to this result, the upper limits set by WA80 [44] and the first measurements by WA98 [143] . . . . .	84
4.13 Photon self-energy diagrams in finite temperature QCD. . . . .	86
4.14 Prediction of Jet-Plasma or “Jet Passage” Photon Radiation from the QGP in [89] . . . . .	91
5.1 The RHIC Complex . . . . .	95
5.2 PHENIX vs. STAR . . . . .	99
5.3 PHENIX Magnetic Field . . . . .	100
5.4 PHENIX side view showing the location of the BBC and ZDC detectors.	103
5.5 PHENIX Centrality Determination . . . . .	104
5.6 EMCal: PbSc/PbGl . . . . .	110
5.7 PbSc Module . . . . .	111
5.8 PbGl Tower . . . . .	112
5.9 High Momentum $\pi^0$ Inefficiency Due to Cluster Merging . . . . .	116
5.10 Typical distribution of the spread of energy in a cluster amongst surrounding towers, when the photon impacts a tower center. figure from [141]. . . . .	117
5.11 Crazy DAQ . . . . .	118
6.1 “Banana Plot” of Glauber Simulated BBC/ZDC Response . . . . .	128

6.2	Test Beam Response of the PbSc EMCal to various particle beams. . .	133
6.3	Improvement of calibration with an iterative “Kalman” method . . .	134
6.4	Typical Energy Distribution from which MIP-average correction is extracted. . . . .	135
6.5	Demonstration of the Slope Correction for the energy calibration. . .	138
6.6	Improvement of relative calibration for PbGl towers from Slope Cor- rection. . . . .	139
6.7	Overall reduction in $\pi^0$ mass resolution due to calibration improve- ments between Run1 and Run2 for PbSc . . . . .	140
6.8	Resolution of Final Calibration . . . . .	141
6.9	Cluster $z - y$ position for clusters with energy $> 4$ GeV for a single PbSc sector. . . . .	143
6.10	Identification of the problem with the Afterburner Correction. . . . .	144
6.11	TOF distribution for PbSc Clusters . . . . .	146
6.12	Parametrization of TOF Energy Dependence . . . . .	146
6.13	TOF distribution mean ( $t_0$ of section 6.2) for three sectors . . . . .	151
6.14	Number of hits vs EMCal tower index with 4 different $p_T$ cuts for run 30009. . . . .	154
6.15	Gaussian fit to the distribution of number of hits with the cut $p_T >$ 1.0 GeV for run 30009. . . . .	154
6.16	Energy spectrum <i>a)</i> before the hot tower removal; <i>b)</i> after the hot tower removal. Notice how the erroneous high energy tail of the distribution is gone. . . . .	156
6.17	$\chi^2$ vs $P_{photon}$ . . . . .	160
6.18	An example of foreground and background in the cluster pair invari- ant mass distributions. Details are explained in the text. The green line is explained in 6.3.5.4. . . . .	162
6.19	The mixed background from triggered events is virtually indistin- guishable from the mixed background from minimum bias events. . .	166

6.20	Example of Peak Extraction Yield Ratios. . . . .	168
6.21	Peak Extraction Errors . . . . .	169
6.22	Number of triggered events per centrality bin for trigger 2. The trigger fires preferentially on peripheral events, in fact, the triggered events in the three most central bins are due to malfunctioning and poor centrality resolution by the trigger. Above bin 4, the # of events per bin decreases as expected due to the decrease in multiplicity per event: the greater the multiplicity, the higher probability the event will contain a high $p_T$ trigger photon. . . . .	171
6.23	Trigger Cluster Efficiency compared to min bias as a function of transverse momentum for pbsc. . . . .	173
6.24	In the top plot the cluster spectrum is shown as a function of $p_T$ for: minbias (black), minbias where the lvl2 centrality bin matches the offline centrality bin (red), trigger 2 where the same condition holds (blue), and trigger2, same condition but with the random benefit removed (tan). The bottom plot shows the cluster efficiency in cases where the level2 centrality matched the offline centrality determination, from the above plot, tan over red. . . . .	174
6.25	Event normalized yields with no corrections for the trigger 1 match well those for MinBias (no lvl2 trigger) above 5GeV. In blue is the corrected triggered photon spectra and in black is the minimum bias. To the right is the ratio corrected trigger to minbias. . . . .	175
6.26	If a software cut above the 100% plateau is used such that the photon efficiency turns on as a perfect theta function, then then the $\gamma$ 's from $\pi^0$ and hence the $\pi^0$ 's themselves that survive (light blue) and get cut (red) by the software cut are symmetric around $E_{\pi^0}/2$ because of simple energy conservation in the decay. This allows the efficiency of the cut to be derived analytically as a function of $E_{trig}$ and $E_{\pi^0}/2$ by simply taking ratios of the colored regions. . . . .	177

6.27	Monte Carlo results with and without taking into account the detector acceptance. . . . .	178
6.28	Trigger efficiency for $\pi^0$ for trigger 1. The trigger data is only added where the efficiency is greater than 0.35, namely 5 GeV to keep systematics low. . . . .	179
6.29	Trigger efficiency for $\pi^0$ for trigger 2. . . . .	179
6.30	As in Figure 6.25, the triggered data sample is corrected with the derived efficiency and compared to the minimum bias sample in the overlap region for 0-100% centrality. The two spectra compare well. .	180
6.31	Trigger 1 efficiencies with (blue) and without (red) random benefit. To remove random benefit, the trigger primitive tiles that fired the trigger were associated with clusters. . . . .	182
6.32	The Trigger 1 efficiency turn-on for photons is different for different amounts of the random benefit discussed in this section. Since this random benefit is simply a reflection of event multiplicity it is dependent only on centrality. . . . .	182
6.33	For Trigger 1, the maximally different efficiency curves of $\pi^0$ efficiency curves are made into a ratio as explained in the text. Since the ratio is to good approximation equal to 1, it can be assumed the errors and systematic uncertainties discussed in the text are negligible above 5 GeV/c. . . . .	183
6.34	Explained in text. . . . .	185
6.35	Convergence of Bin Shift Correction . . . . .	191
6.36	Both in the published PHENIX 200 GeV data ([15]) and continuing to higher $p_T$ with the new data, we see that the modified power law consistently underestimates the data points at the high end. . . . .	193
6.37	Transition function used in the standard fitting function. . . . .	194
6.38	Example of Peak Extraction Yield Ratios. . . . .	196

6.39	Ratio of efficiencies for different centrality bins. Since multiplicity is already a small effect between adjacent centrality bins, we can safely neglect removing hits from an event before embedding a particle. . . .	201
6.40	Final efficiency calculation for $\pi^0$ vs. $p_T$ and centrality. The noticeable drop in the efficiency at high $p_T$ is due to the inability of the clustering algorithm to separate the two decay photon clusters into two distinct clusters already demonstrated in Figure 5.9. The efficiency shown is for the shower shape PID (PID2) cut, since this was the only PID cut used in the final results. . . . .	203
6.41	Final efficiency calculation for single photons vs. $p_T$ and centrality. The efficiency shown is for the shower shape PID (PID2) cut, since this was the only PID cut used in the final results. . . . .	204
6.42	Survival probability of $\pi^0$ with tight asymmetry cut compared between simulation and real data. . . . .	207
6.43	Comparison of $\chi^2$ distributions between real data and test beam/simulation. figure from [141]. . . . .	209
6.44	Fastmc study of position resolution effects. Relatively large modifications in the position resolution shifted $\pi^0$ widths can correspond to very tiny differences in the overall efficiency. This must be taken into account for determining the matching between simulation and real data $\pi^0$ resolution. . . . .	210
6.45	Ratios of fully corrected spectra for different PID selection for cross-check of $\gamma$ efficiency errors. The dark black circles correspond to PID0. . . . .	210
6.46	Ratio of simulated and real $\pi^0$ survival probabilities for all centralities.	212
6.47	The energy scale in fast MC is modified by 1.5%, the full uncertainty of the real energy scale, in order to determine the uncertainty in the yields due to the calibration. . . . .	213
6.48	Cross check of the energy scale: electron $E/p$ . . . . .	214

6.49	Derivation of energy 8% smearing uncertainty in the efficiency calculation. . . . .	215
6.50	Study of error correlations between calibration scale and simulation tuning. . . . .	217
6.51	Conversion photons lost due the charged particle veto tagging. . . . .	219
6.52	Extraction of the portion of clusters coming from charged tracks. The correlation in the hit distance between charged tracks and EMCal hits is measured in order to determine the fraction of clusters coming from charge tracks. This is used to generate the correction $X_{ch}$ . Details are discussed in the text. . . . .	221
6.53	Charged contamination measured as a function of transverse momentum for central events. . . . .	221
6.54	Angular widths and yields of jet correlation as a function of leading particle momentum taken from [63] for d+Au events measured by PHENIX. . . . .	222
6.55	Efficiency for detecting neutrons and antineutrons in the PbSc (W0) and PbGl (E1) EMCal. . . . .	225
6.56	Fraction of neutron/antineutron contamination in the extracted raw photon sample for PbGl, PbSc. This fraction is the correction $X_{n/\bar{n}}$ applied to the final data. . . . .	226
6.57	Results of the decay photon background simulation for minimum bias events. . . . .	228
6.58	PHENIX Preliminary Measurements of $\eta$ to $\pi^0$ ratios, in p+p, d+Au, and Au+Au. The PHENIX results are consistently in the 0.45 range, which agrees with the current world data set for high $p_T$ meson production at all high energies. [70] . . . . .	229

6.59	Studies of errors in the $\gamma/\pi^0$ ratio due to the systematics of the $\pi^0$ fit. In the figure is shown the propagated error in the $\gamma_{sim}$ alone which can be quite large. The $\pi^0$ fit is shifted according to the different error bands, so when the simulated photon spectra is divided by $\pi^0$ the error is reduced to $\sim < 4\%$ . This is another reason it is preferable to use the double ratio $R_{\gamma_{direct}}$ . . . . .	230
6.60	Ratio of fully corrected $\pi^0$ and inclusive single photon spectra measured in the PbGl calorimeter to those of the PbSc calorimeter for minimum bias events. . . . .	234
7.1	200 GeV $Au + Au$ $\pi^0$ Production with Level2 Trigger Sample Included.	236
7.2	$\pi^0 R_{AA}$ in 200 GeV $Au + Au$ collisions for the four most central bins. The grey box at $R_{AA} = 1$ represents the systematic error band for the thickness scaling, ( <i>i.e.</i> from Table 6.1) not included in the data points themselves. . . . .	237
7.3	$\pi^0 R_{AA}$ in 200 GeV $Au + Au$ collisions for the remaining centrality bins, including Minimum Bias. The grey box at $R_{AA} = 1$ represents the systematic error band for the thickness scaling, ( <i>i.e.</i> from Table 6.1) not included in the data points themselves. . . . .	238
7.4	Integrated $\pi^0 R_{AA}$ vs. $N_{participant}$ . . . . .	239
7.5	Inclusive $\gamma_{all}$ Spectra . . . . .	240
7.6	Direct photon double ratio $R_{\gamma_{direct}}$ vs. $p_T$ . . . . .	242
7.7	Invariant yields of direct photons for various centrality selections. . .	244
8.1	$d + Au$ $\pi^0$ Result . . . . .	248
8.2	Original $\pi^0$ results as presented in [69] . . . . .	250
8.3	Spectral shape comparisons. . . . .	252
8.4	Shape comparisons of ratio of spectra for the most central bins. . . .	253
8.5	$R_{CP}$ for $\pi^0$ and $\gamma_{direct}$ using the 50-60% centrality bin . . . . .	256

8.6	Integrated $R_{CP}$ vs. $N_{participants}$ for $\pi^0$ (light points) and $\gamma_{direct}$ (dark points) using the 50-60% centrality bin. . . . .	257
8.7	$R_{MBC}$ vs. transverse momentum . . . . .	259
8.8	Scaling vs. $T_{AA}$ . . . . .	261
8.9	Measurement of Cronin $\alpha$ for $\gamma_{direct}$ . . . . .	265
8.10	Demonstration of Approximate Binary Scaling in $Au + Au$ PHENIX Open Charm. . . . .	267
8.11	Preliminary $p + p$ result for $\gamma_{direct}$ . . . . .	269
8.12	Agreement of pQCD with PHENIX $\pi^0$ data. . . . .	271
8.13	Possible sizes of " $k_T$ smearing" deviations from pQCD for 200 GeV $\pi$ and $\gamma$ . . . . .	272
8.14	$\gamma_{direct}$ $R_{AA}$ values, using the $\mu_{scale} = 1.0p_T$ NLO prediction for $\gamma_{direct}$ [16] as the " $p + p$ " reference. The grey box at $R_{AA} = 1$ represents the systematic error band for the thickness scaling, ( <i>i.e.</i> from Table 6.1) not included in the data points themselves. For the $\gamma$ (light circles) the systematic difference from using the $\mu_{scale} = 0.5, 2.0 p_T$ NLO predictions are included as the triangular points. . . . .	274
8.15	Close-up of $\gamma_{direct}$ $R_{AA}$ showing the full extent of the upper limits for the two most central bins. . . . .	275
8.16	Three predictions of HI Thermal Radiation . . . . .	277
8.17	Comparison of PHENIX (this thesis) data, and prediction of hard photon enhancement from [89]. The NLO pQCD prediction [16] is also shown for comparison, and disagrees with the LO calculation used in [89]. . . . .	280
8.18	Again the prediction in [89] is compared to our data, but this time for other centrality bins. A similar level of matching is observed. The theoretical prediction should only work well in the most central events if a QGP is present. Therefore the excellent agreement between the prediction and the data in the central bin is probably an accident. . .	282

8.19	Fractions of direct (red) and Bremsstrahlung/fragmentation (photons) photons from the same NLO pQCD prediction [16]. . . . .	283
8.20	Prediction of medium-induced enhancement of Bremsstrahlung/fragmentation photons in the form of $R_{AA}$ from [178]. . . . .	285
8.21	Comparison of new data points for $R_{AA}$ (from this thesis) with that of the previously published PHENIX result [69]. . . . .	288
8.22	Comparison plot of $R_{AA}$ predictions from suppression models [104] and [105] against the same PHENIX result [69]. . . . .	288
8.23	$\gamma/\pi^0$ Ratio in our data. Significant enhancement is seen in this ratio. Hence the title of this thesis. . . . .	291
8.24	$\gamma$ to $\pi^0$ ratios at various energies. Such a large value of this ratio at this value of $x_T$ would normally only be seen at higher $\sqrt{s}$ . Figure taken from [36]. . . . .	292

# List of Tables

5.1	Overview of level 1 triggers . . . . .	120
5.2	Overview of level 2 trigger algorithms. . . . .	122
6.1	Table of Glauber Model Predictions with systematic errors. . . . .	129
6.2	Number of hot towers in the PbSc reject list. . . . .	155
6.3	Cut Names . . . . .	158
6.4	Material budget in front of the PbSc Calorimeter . . . . .	218
6.5	Summary of the dominant sources of systematic errors on the $\pi^0$ and inclusive $\gamma$ yields extracted independently with the PbG1 and PbSc electromagnetic calorimeters. The error estimates are quoted at two $p_T$ values in central events for the PbG1 and PbSc. For the combined $\pi^0$ and inclusive $\gamma$ spectra and $\gamma/\pi^0$ ratios, the approximate statistical and systematic errors are quoted for the most peripheral and most central reactions. . . . .	232
6.6	Summary of sources of systematic uncertainty for the corrections applied to the final $\pi^0$ spectra in percent of yield. . . . .	233
6.7	Summary of sources of systematic uncertainty for the corrections applied to the final inclusive ( $\gamma_{all}$ ) spectra in percent of yield. . . . .	233
B.1	$\pi^0$ invariant yield vs. $p_T$ for centrality fraction 0-10%. For points with no errors given, data value represents 90% confidence level upper limit. . . . .	315

B.2	$\pi^0$ invariant yield vs. $p_T$ for centrality fraction 10-20%. For points with no errors given, data value represents 90% confidence level upper limit. . . . .	316
B.3	$\pi^0$ invariant yield vs. $p_T$ for centrality fraction 20-30%. For points with no errors given, data value represents 90% confidence level upper limit. . . . .	317
B.4	$\pi^0$ invariant yield vs. $p_T$ for centrality fraction 30-40%. For points with no errors given, data value represents 90% confidence level upper limit. . . . .	318
B.5	$\pi^0$ invariant yield vs. $p_T$ for centrality fraction 40-50%. For points with no errors given, data value represents 90% confidence level upper limit. . . . .	319
B.6	$\pi^0$ invariant yield vs. $p_T$ for centrality fraction 50-60%. For points with no errors given, data value represents 90% confidence level upper limit. . . . .	320
B.7	$\pi^0$ invariant yield vs. $p_T$ for centrality fraction 60-70%. For points with no errors given, data value represents 90% confidence level upper limit. . . . .	321
B.8	$\pi^0$ invariant yield vs. $p_T$ for centrality fraction 70-80%. For points with no errors given, data value represents 90% confidence level upper limit. . . . .	322
B.9	$\pi^0$ invariant yield vs. $p_T$ for centrality fraction 80-92%. For points with no errors given, data value represents 90% confidence level upper limit. . . . .	323
B.10	$\pi^0$ invariant yield vs. $p_T$ for centrality fraction 0-100%. For points with no errors given, data value represents 90% confidence level upper limit. . . . .	324

C.1	Direct photon invariant yield vs. $p_T$ for centrality fraction 0-10%. For points with no errors given, data value represents 90% confidence level upper limit. . . . .	325
C.2	Direct photon invariant yield vs. $p_T$ for centrality fraction 10-20%. For points with no errors given, data value represents 90% confidence level upper limit. . . . .	326
C.3	Direct photon invariant yield vs. $p_T$ for centrality fraction 20-30%. For points with no errors given, data value represents 90% confidence level upper limit. . . . .	327
C.4	Direct photon invariant yield vs. $p_T$ for centrality fraction 30-40%. For points with no errors given, data value represents 90% confidence level upper limit. . . . .	328
C.5	Direct photon invariant yield vs. $p_T$ for centrality fraction 40-50%. For points with no errors given, data value represents 90% confidence level upper limit. . . . .	329
C.6	Direct photon invariant yield vs. $p_T$ for centrality fraction 50-60%. For points with no errors given, data value represents 90% confidence level upper limit. . . . .	330
C.7	Direct photon invariant yield vs. $p_T$ for centrality fraction 60-70%. For points with no errors given, data value represents 90% confidence level upper limit. . . . .	331
C.8	Direct photon invariant yield vs. $p_T$ for centrality fraction 70-80%. For points with no errors given, data value represents 90% confidence level upper limit. . . . .	331
C.9	Direct photon invariant yield vs. $p_T$ for centrality fraction 80-92%. For points with no errors given, data value represents 90% confidence level upper limit. . . . .	332

C.10	Direct photon invariant yield vs. $p_T$ for centrality fraction 0-100%. For points with no errors given, data value represents 90% confidence level upper limit. . . . .	332
D.1	Nuclear modification factor $R_{AA}$ vs. $p_T$ for centrality fraction 0-10%. Additional (overall) systematic uncertainty from thickness scaling fac- tor listed in table 6.1 and not included here. . . . .	333
D.2	Nuclear modification factor $R_{AA}$ vs. $p_T$ for centrality fraction 10-20%. Additional (overall) systematic uncertainty from thickness scaling fac- tor listed in table 6.1 and not included here. . . . .	334
D.3	Nuclear modification factor $R_{AA}$ vs. $p_T$ for centrality fraction 20-30%. Additional (overall) systematic uncertainty from thickness scaling fac- tor listed in table 6.1 and not included here. . . . .	335
D.4	Nuclear modification factor $R_{AA}$ vs. $p_T$ for centrality fraction 30-40%. Additional (overall) systematic uncertainty from thickness scaling fac- tor listed in table 6.1 and not included here. . . . .	336
D.5	Nuclear modification factor $R_{AA}$ vs. $p_T$ for centrality fraction 40-50%. Additional (overall) systematic uncertainty from thickness scaling fac- tor listed in table 6.1 and not included here. . . . .	337
D.6	Nuclear modification factor $R_{AA}$ vs. $p_T$ for centrality fraction 50-60%. Additional (overall) systematic uncertainty from thickness scaling fac- tor listed in table 6.1 and not included here. . . . .	338
D.7	Nuclear modification factor $R_{AA}$ vs. $p_T$ for centrality fraction 60-70%. Additional (overall) systematic uncertainty from thickness scaling fac- tor listed in table 6.1 and not included here. . . . .	339
D.8	Nuclear modification factor $R_{AA}$ vs. $p_T$ for centrality fraction 70-80%. Additional (overall) systematic uncertainty from thickness scaling fac- tor listed in table 6.1 and not included here. . . . .	340

D.9 Nuclear modification factor $R_{AA}$ vs. $p_T$ for centrality fraction 80-92%. Additional (overall) systematic uncertainty from thickness scaling factor listed in table 6.1 and not included here. . . . .	341
D.10 Nuclear modification factor $R_{AA}$ vs. $p_T$ for centrality fraction 0-100%. Additional (overall) systematic uncertainty from thickness scaling factor listed in table 6.1 and not included here. . . . .	342

## Acknowledgements

Of course I must start where everyone should, by thanking my parents, especially my mom who inspired me to want to be a scientist. I'm certain it was their two sharp minds directed at each other in discussion or (I suppose a son should not reveal how often) *sometimes* in argument that helped me to develop my analytical thinking. For all my "distinguished" education, they are still a formidable and in fact, mostly superior match when it comes to debating one subject or the other. Some people describe me as having two sides to my personality--this certainly started as a reflection of the duo of my father the builder, business man, football player, and Steelers fan and my mother, the chemist, biologist, and high school science teacher. I also cannot fail to honor my mother's constructive criticism of my points of view--in high school I could not persuade her to accept the fundamental geometric definition of space being made up of infinitely small points. Her adamant denial of the ability for something to be infinitely divisible does not seem so crazy now as it did then; such a proposal now forms the basis of the renowned, cutting-edge string theory.

Next, my new wife Jen (a.k.a. "Cutie") deserves all my thanks and praise since, among other things, she nearly had to share her special day (our wedding) with my Ph.D. defense which originally was scheduled the same week. She faced this as well as other neglect during the period of the last year with superhuman (or at least super-Cutie) patience, and not only tolerated my thesis distraction, but also sustained me emotionally, physically--literally cooking for me so many of those thesis writing days--and even financially as I was booted from my cheaper Columbia apartment housing to our new expensive Chelsea neighborhood--her patience with my many (now more expensive) parking tickets was also not insignificant. I do appreciate how lucky I am to have her in my life, and this thesis writing experience has been no exception.

There are three people I feel the most indebted to regarding the specific work presented in this thesis. I will list them somewhat chronologically. Especially in my

early days with the group, the person who really showed me the ropes and taught me the most about both PHENIX and many other aspects of heavy ion physics was Mickey Chiu—there is no doubt that it would’ve taken me longer to graduate had I not had his help. He is a great guy, a very unassuming and beautiful person. At my time here at Columbia, I had the extreme fortune of being able to have *two* advisors, both of whom are considered outstanding leaders in our field. Jamie Nagle, who should absolutely be considered a co-advisor to me on this analysis, first enticed me into the Heavy Ion group on a Saturday afternoon tour of Brookhaven. He looked after me early on, forcing me to keep my eye on the physics instead of just my work in the counting house. In this analysis, I’ve always been able to turn to him for support and direction which I did quite regularly. Besides being a physicist of the rarest quality, he has the highest character, integrity, and a genuine desire to treat people in the best possible manner. Finally it was Brian Cole, my first boss in the group, who was gracious enough to also adopt me as his thesis advisee and carry me through the end of this journey. For the unwavering support and advice in the analysis and especially in my thesis writing—the countless rounds of editing, rephrasing, and re-editing, I thank him especially. His friendship and his brilliance were invaluable to the completion of this work and to me personally.

There were several others who advised and helped me on the specific details of this analysis. Foremost here is Christian Klein-Boesing who was my “double” in PHENIX for this analysis, performing a duplicate (but superior since he also incorporated the PbGl calorimeter) analysis which helped uncover many problems in my analysis. I am deeply indebted to him, as well as Terry Awes, Saskia Madio-duszewski, Gabor David, Klaus Reygers and Takao Sakaguchi. Terry, Saskia, and Gabor, played the role of foster advisor to me for many basic questions about photon measurements and calorimetry. David d’Enterria together with Klaus, helped me with much support and help with several specific things—it was their work especially Klaus’s previous analysis, upon which I based this analysis. I would also like to thank everyone in PHENIX, the PHENIX hard/photon physics working group, the

EMCal working group, and the DAQ working group, especially Mike Tannenbaum, Edward Kistenev, and John Haggerty. Finally in this group I acknowledge Paul Stankus, who first got me interested in direct photons.

Bill Zajc was instrumental to my career in grad school at Columbia in so many ways. By taking a chance on this football player, he opened more doors than one at Columbia for me and generously supported me in my research both financially and so often intellectually with his wisdom, patience, and ingenuity. Thanks Bill. I cannot also forget to thank everyone at Nevis, especially Ann Therrien and Elaine Schmidt for always taking care of me, and similarly, Lalla Grimes in the department office who truly acted to me as a mom away from home, as she does for so many grad students.

I cannot forget all my colleagues who supported me in this work in slightly less direct, but no less important ways. Of this group are my fellow “workers” at Columbia—besides Mickey, foremost are Chun Zhang whose unselfish attitude and good-hearted-ness made every interaction with him enjoyable and Sean Kelly, without whose humor I could not have survived the early days in the counting house, and who I perhaps could relate to the most of my fellow physicists while simultaneously looking up to him. Sotiria Batsouli, Dave Winter, and Jiangyong Jia, gave me much “post-doctoral” support but even more friendship. I thank the rest of the Columbia students, Christine Aidala, Jiamin Jin, and Michael Bjornal as well as my Stony Brook partners, (again) Jiangyong Jia, Felix Matathias, and Sergey Butsyk for general support not limited to but including in Sergey’s case, authentic Russian vodka shots and canned fishes. I thank all my DAQ buddies, most especially Steve Adler and Martin Purschke for friendship and humor, Martin also for never being too busy to help with many computing issues. I end my more specific thank you’s by thanking my first advisors at Columbia, Janet Conrad and Mike Shaevitz, who supported me in my first particle physics endeavor of neutrinos as well as in trying something new as I switched to the PHENIX group.

We physicists would like to believe there are no politics in physics. This is not

quite true. It is true that *physics* is never political and that ultimately the truth is all that matters in the field. However *physicists*, being human, are by nature political, and because of this, the speed at which the truth is realized is indeed often affected by political wrangling and personal “wars” between one physicist or the other. Of course, no one can deny the almost invariably positive effect of a spirited argument. Indeed, a “thick skin” should be considered a necessity since a “thin skin” is usually much more harmful than the evoking criticism. But when the relationships of the arguers become so injured that basic respect is no longer afforded, to my experience, it always makes the understanding of the truth occur much more slowly than necessary. Even as a young physicist I have observed this to be true several times, and in multiple experimental collaborations, not just PHENIX. Other negative “personality issues” such as selfishness usually have similar negative effects as to the speed with which the truth is understood. Historical examples of stagnating politics in physics abound, perhaps the most poignant being the story of Boltzmann, in which the lack of respect given by his colleagues to his theory of statistical mechanics, today a mainstay of modern physics, drove him to commit suicide. A different time and situation maybe; nonetheless, the effects of politics in physics still creep into our work today.

The reason I have written the previous paragraph is to point out that the way people treat other people in the field of physics (as probably in virtually every other human endeavor) does matter, at least in the short term. My relationships with all my fellow physicists certainly matter to me. And for this reason I would like to make my final thank you to all the people in my life that have shaped my personality and taught me how to treat others with respect and how to be mindful of their desires. This includes most importantly my sisters Heidi and Gretchen, the rest of my family, my best friends Brad, Bobby, Vassili, and Elbert, the DLIA connection, and my many coaches, teammates, and friends growing up, in high school, and college. Thank you all.

To God, the infinite, living source and personality of all truth, wisdom, love, and many other wonderful things. To Valentin and Lyudmila. To Macky Henckel, a man of science, of the world, and yet always of the mountain he remains true. To the victims of September 11, which occurred during the time the data for this dissertation was collected.

# Chapter 1

## Introduction

---

This dissertation is about recent work done in a speciality of physics that is ambiguously named. For now, it is known as Relativistic Heavy Ion (RHI) Physics, High-Energy Heavy Ion Physics, *Ultra*-relativistic Heavy Ion Physics, and more generally High-Energy Nuclear Physics. The last name places it properly in its context. It should definitely be considered a branch of the broader field of nuclear physics. But the names “Ultra” and “High-Energy” are only temporary, since physics experiments are constantly performed with higher and higher energies, making today’s “high” tomorrow’s “medium”, and so on. In this regard, “relativistic” is properly absolute, expressing that the energy is at least large enough that our ions will travel at nearly the speed of light; however, being that only physicists would know this, the term is less than desirable. The name “Heavy” is also not 100% accurate since the field also includes the study of “Light” Ions. The research the dissertation represents was done at the Relativistic Heavy Ion *Collider* (RHIC) facility located within Brookhaven National Lab (BNL), using the multi-component detector that makes up the PHENIX experiment. The stated goal of RHIC and its several experiments is to experimentally produce and measure an extremely rare and special state of matter known as the Quark-Gluon Plasma (QGP) using its extremely energetic nuclear collisions.

The atomic nucleus was discovered by Rutherford in 1912. By pointing a known

type of positively charged radiation called alpha ( $\alpha$ ) particles at a gold foil, he and his group noticed that a very small fraction of the  $\alpha$ 's were deflected almost completely backwards, leading him to conclude that there must be very small, very heavy positively charged particles in the foil. This led him to propose that these heavy particles were actually the center around which the negatively-charged electrons orbited to make up the proposed neutral atom, the fundamental building block of normal matter. Not only did this discovery provide the first nearly full and accurate description of the whole atom, a quite burning question on its own at the time, but it also opened up a new question of just how such an atomic structure could remain stable. Eventually, this new question would become one of the driving forces behind the development of Quantum Mechanics and hence the modern theories of today. It turns out that alpha particles are themselves Helium nuclei: that is,  $He^{++}$  ions. Therefore these experiments were the first experimental heavy (considering the gold) and light (considering the  $He$ ) ion collisions and nuclear physics was born.

Nearly 100 years later, we have made many strides in understanding nuclear structure and the force that ultimately keeps the nucleus held together. We have even been able to predict and control the outcome of nuclear fission reactions to our benefit as an energy source. However we still cannot fully explain many very fundamental aspects of the phenomena we observe in higher energy nuclear collisions and, more generally, other *hadronic* collisions governed primarily by the Strong force. We hope that this is mostly due to the fact that the theory we've constructed to describe the force, called Quantum Chromodynamics (QCD) in its current form is very difficult to calculate in some regimes of low energy. There, a very accurate approximation called perturbation theory, which otherwise has been very successful in predicting and describing QCD in the high energy limit, breaks down. Therefore we have turned to a reliance on the difficult *lattice* calculations of QCD. These calculations, which are notoriously time-consuming, are supplemented by more expedient phenomenological models and approximations which are largely driven by experimental data. Therefore, it has become important to gather data from a wide

variety of conditions in order to test and guide the development of these models and formulations. Herein lies the point of our incompletely-named experimental field: to study the behavior of QCD under the extreme conditions of matter created in many-bodied large and small nucleus-nucleus collisions.

We expect that such matter provides an extremely promising laboratory in which to test models of *non-perturbative* QCD expressly because lattice QCD predicts that within them, the QGP could be formed. All nuclear matter is explained as containing (indeed built up from) members of two groups called Quarks and Gluons. These are the fundamental particle types making up the basis of QCD and within the nucleons or other hadrons the theory describes them as being *confined* together such that essentially they can never be isolated in a stable state. However, at sufficiently high temperature and density, the theory describes a melting of normal confined hadronic matter into a “soup”-like plasma, the QGP, where bulk quantities of quarks and gluons are free to thermodynamically participate alone. Since the aspects of QCD models which are hardest to calculate and hence least well understood specifically involve the transition between quark and gluon degrees of freedom to those of hadrons and nuclei, the capability to study the formation of the QGP will provide exactly the right types of new information about these processes. If indeed RHI collisions can provide this capability, and we find that they can be described robustly in some QCD-based set of calculations especially of the QGP, we will most certainly have improved the understanding of non-perturbative QCD, and quite possibly even usher in the advance of a combined description including the models, basic perturbative QCD (pQCD) and lattice QCD, which can accurately predict virtually all phenomena associated with the Strong force.

But answering these questions about QCD and creating the QGP may have even more profound consequences than simply allowing us to confirm one theory and understand the matter it describes, which is another reason that we as scientists are excited about using the heavy ion laboratory. I think it is proper to say that whereas Rutherford’s work represented the end of a human quest that began millennia ago,

seeking to answer the question posed by the ancient Greeks of what constituted the fundamental structure of *matter*, humanity has now embarked upon and is in the beginning stages of a new quest to understand the fundamental structure of *space itself*<sup>1</sup>. Over the past half of the century much evidence has accumulated that the vacuum has its own structure. As it turns out, the QCD phase transition associated with the formation of the QGP, according to certain predictions, may also coincide with a transition of the very vacuum state itself such that the mass of Strong matter particles it hosts would be altered. In the case that this also turns out to be the case, just as Rutherford's result transcended its immediate importance in stimulating the development of quantum theory, the study of the QGP could also contribute to what is perhaps the next major milestone of human physical understanding of the most fundamental scientific kind.

Of course before we can even hope to achieve such lofty goals, we must first establish the basic experimental evidence for QGP formation. In closing this introduction then, let us note two more specific and practical things about Rutherford's work which we shall also attempt to emulate in this dissertation to address this more immediate but no less important goal. First, faced with a bulk sample of a dense, seemingly amorphous substance he was able to glean information about its smallest elemental structure by using a *penetrating* probe, the  $\alpha$  particle. In fact, what we have under-emphasized about Rutherford's discovery is its more commonly acknowledged *null* effect: it was the penetration of most the  $\alpha$ 's, without any scattering whatsoever which allowed him to deduce that the atom possesses only a small nucleus. Similarly (right down to an important null effect!) this dissertation addresses our goal by using a probe, the photon, which because of its nature is expected to be able to penetrate matter created in RHIC collisions, matter which we know for sure will be extremely hot, dense, and Strongly interacting whether or not it is in the QGP state. Second, Rutherford exploited the fact that his  $\alpha$  probes were charged and therefore subject to electromagnetism, a theory that in

---

<sup>1</sup>let us hope that *this* journey does not take as long!

most aspects, has been considered well-understood for now over a century or two. Such well-understood probes are essential if one is ever to have a hope of measuring anything new.

In fact, as we shall relate in this thesis, by detecting, measuring, and studying photons that are released in RHIC collisions, we have already been able to observe new phenomena (*e.g.* an anomalously large direct photon to  $\pi^0$  ratio) that confirms some specific calculations made with QCD and is consistent with the claim that we have indeed created the QGP. This is just one such observation with one such probe in a conglomeration of results that have just been discovered at RHIC by several different separate experiments, which paint an exciting picture and signify that we are beginning to realize our goals of exploring the fundamentally interesting conditions necessary for QGP formation, and quite possibly have indeed discovered it.

## Chapter 2

# Particles, The Strong Force, and, QCD

It is a fundamental concept that there is such a thing as electric charge which causes objects to be attracted and repelled by one another, in proportion to the amount and “sign” the charge. Soon after Rutherford discovered the nucleus, it was found that nuclei of different elements were made up of different numbers of a smaller type of particle with a positive charge called a proton. A single proton can make up the nucleus of the element hydrogen. Later it was discovered that along with the protons, there were neutral particles which in all respects were very much like protons, (*e.g.* in mass) but without charge called neutrons. However, the presence of the neutrons could not account for something unexplainable within the framework of electromagnetism at the time: a collection of like positive charges, especially so closely packed in such a dense space as a nucleus, should sharply repel each other. Therefore it was postulated that there must be another force, which was called the *Strong* force since it was obviously overpowering the electric force.

Not much more progress was made to understand the strong force until the theory of quantum mechanics was completed some 30-40 years later. This is not surprising since quantum effects cause important modifications to the behavior of small particles like atoms, compared to the interactions of macroscopic objects we are intuitively familiar with. Before proceeding further with the discussion then, it is necessary to introduce some important concepts about Quantum Mechanics and

as it turns out therefore, forces in general.

## 2.1 Particle Physics: Quantum Mechanics, Forces, and Fields

The first proposal in the history of physics which provided a universal explanation of the dynamics of objects, was the concept of the *force* by Isaac Newton in the 1600's, quantified in the equation  $F = ma$ . The interpretation of this proposal is that forces themselves are fundamental, and forces cause objects to move. Once an object is put into motion, it carries a certain amount of *momentum*, a quantity which is always *conserved*: never destroyed, only transferred in form. This first description of physics by humanity is not surprising since forces are the part of any physical description that we can actually feel. Newton quickly realized however that an alternative way to explain the forces he was calculating was through another concept called *energy*. The conservation of differences in this quantity mathematically leads to the force equation and hence all the rest of the force theory. Paradoxically, because only *differences* of energy are necessary to consider, and therefore the absolute values assigned to the total energy of a system are irrelevant, at first energy could be interpreted as and was considered by many to be nothing more than a mathematical construct or trick that facilitated computation. Nonetheless, gradually energy was accepted to be as fundamental as the forces themselves despite this arbitrariness. This process, the introduction of a seemingly purely mathematical concept that facilitates computation leading to its later adoption as a fundamental physical quantity, is one that is repeated over and over again in the history of Physics. Indeed as classical mechanics was completed, and perfected, the process was repeated with the introduction of the Lagrangian and Hamiltonian, mathematical objects from which a quantity called *Action* could be calculated, a quantity which also could be specified with a certain arbitrariness but whose minimization in a system has as its consequence energy conservation itself.

Beginning during this last period of development of classical mechanics, around

the end of the 1700's, electromagnetism was discovered, one might say by a combination of scientists, one of whom was Benjamin Franklin who is credited with discovering electricity, that is, raw electric charge. The next century saw the development of a single theory which described these forces and their relationship with charge perfectly, within the experimental phenomena of the day. The key point of this theory was the concept of *fields*, which as before with energy, at first seemed only to be a restatement of forces or potential energy—in fact, they were defined to be these very quantities up to a constant factor of (1/charge). However, like before, eventually it was accepted that the fields must really be considered fundamental. This was proven when it was realized that the fields existed even without the presence of charge, the most dramatic example of which is light itself.

As if providing the basis of all life on Earth in the manifestation of light wasn't already important enough, the concept of the field assumed an even more important role in physics starting in the early 20th century. The success of the electromagnetic (EM) theory of Maxwell's equations allowed scientists such as Rutherford to explore more deeply the other major component of any physical theory besides the forces: the matter which is accelerated by those forces. As elementary charges, particles, and the structure of the atom were revealed by the ability to look at smaller and smaller objects, it became apparent that particles tinier than a certain size could not be described completely without some reference to wave properties—the famous concept of wave-particle duality. So, following the example of light described as mathematical wave expressions of the EM field, Heisenberg, DeBroglie, Bohr, et. al. described molecules and subatomic particles in the theory of Quantum Mechanics by a complex (in the mathematical sense, i.e. having an imaginary part) probability field which could be represented by mathematical expressions of waves. Besides providing a description for wave-particle duality, most importantly, the field representations existed only in discrete states, and could therefore describe the equally puzzling experimentally observed discreteness or quantization of certain observables like free energy in the thermal blackbody crisis, line spectra, and many

other phenomena.

This new aspect of the field, its quantum nature, was then turned back onto the classical EM field. To describe the photo-electric effect, one also needed to ascribe a quantum nature to the EM field itself: the concept of the photon (also denoted as the  $\gamma$ ). To correctly account for this, and for *relativistic* (very high energy) considerations in the matter probability fields, Quantum Field Theory (QFT) was developed. Quantum Field Theory achieves field quantization by assigning *operators* to a space of vectors which represent states, in the same way quantization is made in the simpler Quantum Mechanics theory. The fields themselves are made up of a discrete number of states each associated with a particular momentum and in this way the electromagnetic field and fields of a particular particles (*e.g.* the “electron field”) are treated on identical footing. Instances of a particular type of particle, like photons or electrons, correspond to the occupation of states in the field, *e.g.* EM or electron respectively. Differences between the mathematical descriptions of different types of fields depend only on the classification of the field’s intrinsic angular momentum (*spin*) as either integer (called a *boson* field) or half-integer (a *fermion* field), as well as the number of linearly independent components of the field, which is to say its rotational transformation properties. Quantum field theory also predicts the existence of anti-particles for each particle, having the same mass but otherwise opposite quantum numbers (*e.g.* opposite charge), a prediction that is now a well established fact.

## 2.2 QCD: The Strong Force

### 2.2.1 Quarks, Gluons, and Color Confinement

Quantum Chromodynamics is the quantum field theory that describes both the strong force and the carriers of the strong charge, also called “color” charge giving the theory its name. But QCD doesn’t just describe the strong force as the force that binds nucleons in a nucleus—in fact, in current QCD theoretical work, this aspect of the strong force is considered a complicated manifestation of something more

fundamental: the binding of even more elementary particles called quarks (denoted as  $q$ ) inside the *nucleon* itself and in many other particles. The quanta which make up the strong field analogous to the photons are called *gluons* and denoted by  $g$  and it is these fields that “glue” together the quarks.

That nucleons and other hadrons were actually made up of sub-particles was first proposed in response to a phenomena that started in the 1950’s as the first real modern particle accelerator, the Cosmotron at BNL, was turned on. A whole “zoo” [98] of new subatomic particles were discovered. The discoveries continued into the 60’s, and even continues today with the latest discovery of something called pentaquarks [137]. It can be noted that these particles had masses (i.e. energies) which exhibited a striking similarity to the enumeration of energy states of atoms [97]. Atoms can be considered particles in their own right but are made up of a sub-atomic structure, specifically fermions. As already existed for the atomic elements then, Gell-Mann proposed a “periodic table” of sorts for many of the new particles [94], which he then explained as determined by the group theory multiplications of fermion spaces. A physical manifestation of the substructure was then seen at SLAC when the first high energy e-p scattering experiments were performed. [87] The “structure” (expressed in *structure functions* of energy and momentum) and angular distributions of this scattering implied that protons were not point particles themselves but had heavy sub components, very similar to the way Rutherford’s original experiments strongly suggested that the atom must have had their smaller denser nuclear components.

Gell-Mann essentially proposed a simple explanation for the spins of fermionic protons and neutrons as well as the spins of the other discovered particles, called *hadrons*. This was simply that the sub-structure components, quarks, were also themselves fermions. Paradoxically, it’s now been shown that much of the proton’s spin in fact cannot be explained this simply [5]. Nonetheless, it has been confirmed in  $e - p$  and  $\nu - p$  scattering that the quarks do in fact have spin 1/2. The Pauli Exclusion Principle requires that no more than a single fermion can exist in the

same distinguishable state, and since it was presumed (and later further verified) that more than one of the quarks making up certain hadrons must also have the same mass and electric charge (*e.g.* the  $\Delta^{++}$  must be made of at minimum three identically charged quarks under Gell-Mann's proposals), it was presumed that these quarks must have an additional quantum number that distinguished these states. It seemed natural to define this as the *real* strong charge, which was called *color* since it had three primary types corresponding to the three primary colors. Note that before color was proposed, there had been put forth other candidates for the origins of the strong charge, most notably an "internally" conserved quantity called isospin which was proposed early on by Heisenberg. Isospin however related the strong charge to the electric charge by construction, and in this way implied that the strong and electric *forces* could be unified in a similar way to how the weak force has since been successfully unified with electromagnetism in the electroweak theory of Glashow, Salam and Weinberg. Color and its description in QCD implies no relation between the strong and the electromagnetic *fields* themselves. The only unification comes in the quark carriers of both electric charge and color, a device which is input into the theory and is not attempted to be understood.

It is considered an empirical fact from experiment that no quantum system observable as distinct from all others, *i.e.* no observable *free* particle contains a net color charge. This phenomena is called color *confinement*. That is, the carriers of strong charge (quarks and gluons) are always confined in systems with net color charge of zero. This was part of Gell-Mann's original proposals. Often, simple reasons are given to explain confinement as if it were an intuitively obvious logical result of a single basic idea. These types of explanations are generally unsatisfying, often oversimplify what is a quite remarkable interplay of nature, and quite often are just not 100% correct. For example confinement is sometimes explained as an intuitively obvious requirement of any theory describing the strong force, put in by construction since we see no everyday examples of objects that appear to have some "other" type of charge like color. In so much as it is ultimately the strong force

that binds nucleons, which admittedly do turn out to be colorless states, one might naively point to this strong “magnetism” as a counterexample, so this would seem to be a wholly unsatisfying “explanation”. Certainly it is relevant, that even from the standpoint of nuclear structure that the theory that describes the strong force should be *short-ranged*. Conceptually related to this idea is another curious property of QCD called *Asymptotic Freedom*. Asymptotic freedom is the property of quarks and gluons having weaker and weaker interactions as the distance scales get smaller and smaller—in a way the converse of confinement—the two ideas are conceptually related, since it implies that at larger distances, the force becomes stronger.

If asymptotic freedom signals a sufficient condition for confinement to exist, then perhaps the true complexity of the situation in QCD is most clearly revealed in the fact that asymptotic freedom would not be present in the exact same QCD theory, if there were only more types (called *flavors*) of quarks. That gluons have color charge and are *self-coupling* is a necessary condition for asymptotic freedom, but is not *sufficient* to establish it. For example, *Weak Force*, a real force experienced by all particles but gluons has mediators analogous to the gluons which are charged, yet this force does not cause confinement.<sup>1</sup> The gluon self-coupling is no-doubt an important feature for asymptotic freedom to be present, but there are simple examples of field theories, *e.g.* the simple  $\phi^4$  field theory, which have self-coupling fields but that do not exhibit asymptotic freedom. In QCD, the self-coupling is a direct consequence of a purely geometric symmetry of the QCD Lagrangian. It is symmetric under a group of *non-Abelian* (having non-commuting generators) transformations. Non-Abelian theories generally do exhibit asymptotic freedom. Another example of this besides QCD, is the scalar Yang-Mills theory, a theory which incidentally, has only two charges.

Keeping these points in mind color confinement then properly just expresses the curious property of the strong force that it increases in strength as the distance

---

<sup>1</sup>the reader who knows something about particle physics may object here, since the Weak force’s weakness is really due to the mediating boson’s having large masses; however, even if those masses were zero, the SU(2) electroweak field theory, even though it is non-Abelian like QCD, would still not exhibit asymptotic freedom—there are too many lepton and other field “flavors” if you will.

between color charges increase which is contrary to all the other forces that we are aware of. The mechanism for this property is generally understood as follows: Because the gluons also carry color charge, they are attracted to each other so that between two colored quarks, the gluon field tends to form a flux tube connecting them. When the quarks begin to separate, this flux tube gets stretched. Much like when the magnetic flux builds up in a solenoid, the system violently resists changes to the stored flux, in this case such that it becomes energetically favorable to simply create a quark-antiquark ( $q\bar{q}$ ) pair which immediately bond to the quarks that were being separated. In this way a single quark is never free.

### 2.2.2 QCD, QED, and Standard Model Basics

*The Standard Model* of Particle Physics classifies all the known fundamental particles/fields according to Figure 2.1. GellMann’s classification scheme for partons which still stands today makes up nearly “half” of those and was based on there being different *flavors* of quarks. Each flavor has a different mass, hence different combinations produce the different observed hadrons with their masses, and existing in particle and anti-particle species. The enumeration of all the fundamental types of quark particles then includes a sum over all colors, flavors and corresponding anti-particles. Originally GellMann proposed the three flavors, up (u), down (d), and strange (s), with electric charges  $\frac{2}{3}e$ ,  $-\frac{1}{3}e$ , and  $-\frac{1}{3}e$  respectively<sup>2</sup> These make up both *baryons*, heavier particles with three quarks or anti-quarks, such as the proton ( $uud$ ), anti-neutron ( $\bar{u}\bar{d}\bar{d}$ ), or the  $\Lambda$  ( $uds$ ), and mesons, lighter particles made up of a  $q\bar{q}$  pair, such as the pion ( $u\bar{d}$ ) and the  $\rho$  ( $u\bar{s}$ ). Since then three other flavors with substantially larger masses have been discovered: charm (c), bottom (b), and top (t) with charges  $\frac{2}{3}e$ , and  $-\frac{1}{3}e$ , and  $\frac{2}{3}e$ , by observing baryons and mesons containing them, such as the  $J/\Psi$  ( $c\bar{c}$ ) or  $B$  ( $u\bar{b}$ ). Yet even heavier flavors could be accommodated by the current field theories up to a certain limit, but experimental results rule

---

<sup>2</sup>Other than the quarks, no free particle has ever been observed to have a charge that is *not* an integer multiple of the fundamental charge quantum  $e = 1.06 \times 10^{-19}$  C. Curiously then, it is only because of *color* charge confinement that (quark) fractional *electric* charges are never observed freely. Within the Standard Model as it currently stands however, this is just a coincidence.

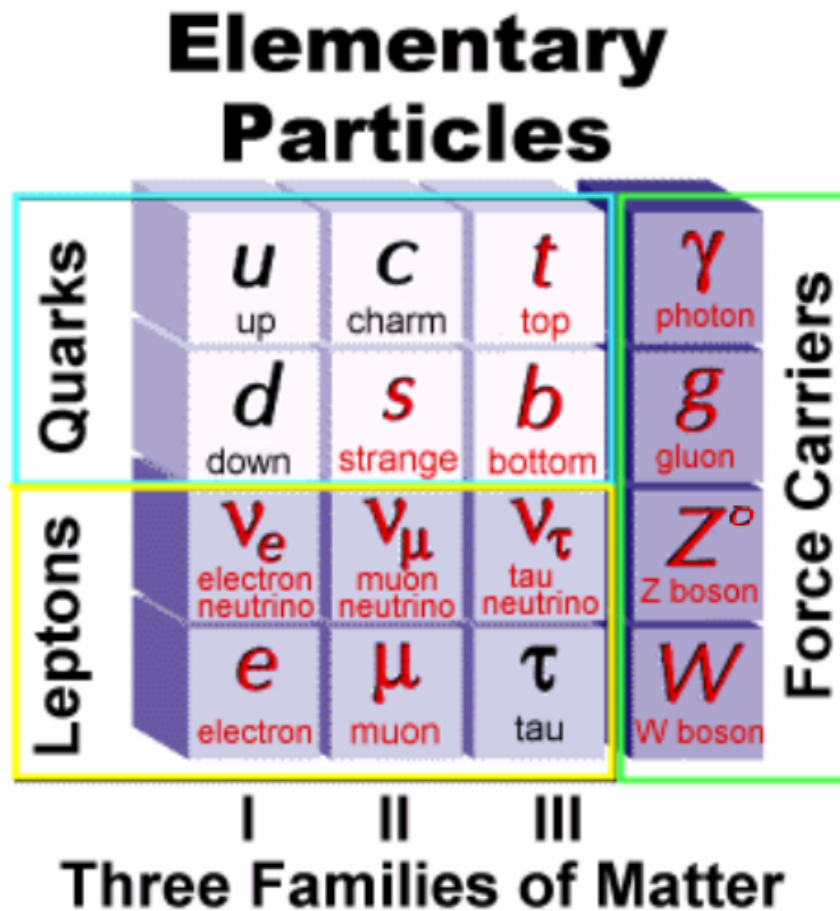


Figure 2.1: The three boxes represent three categories of particles: those that interact via the strong force, those that don't, and those that represent (or mediate) the forces themselves. The  $Z^0$ , and the  $W$  represent the Weak Force, a force experienced by all particles which primarily causes many of them to decay by various means. Those that don't interact via the strong force are called the Leptons. Other than the quarks and the gluon, all the other particles are observable as free particles.

out the possibility of more flavors lighter than the  $Z^0$  by excluding indirect effects *e.g.* a broadening of the  $Z^0$ 's decay width [75]. Searches for more quark generations continue [100] but even at the highest energies achieved thus far ( $\sqrt{s} = 1.8$  TeV), no evidence has been found of their existence, which puts a minimal limit on their mass around 200 GeV.

There are said to be different QFT's for different forces: for example Quantum

Electrodynamics describes electromagnetism, Quantum Flavordynamics describes the weak force, QCD the strong force. Incidentally these three theories together are what officially make up The Standard Model. Characterizing it as one model is the proper point of view. Since many particles participate in interactions with multiple force fields simultaneously, *e.g.* the quarks which carry both electromagnetic and strong charge, there is often intersection between the various “different” (sub) field theories. Such is especially the case in this thesis where we are discussing direct photon production which is dominated by a process that is exactly both QED and QCD at the same time: a purely electromagnetic field is produced from one that is purely chromodynamic through an interaction of a quark field that is both electromagnetic and chromodynamic. For this reason, I will start by introducing a Lagrangian that includes both QED and QCD terms for a single quark flavor  $f$ :

$$\mathcal{L} = -\frac{1}{4}F_{\mu\nu}F^{\mu\nu} - \frac{1}{4}\bar{F}_{\mu\nu}^a\bar{F}_a^{\mu\nu} + m_f\bar{\Psi}\Psi + \bar{\Psi}(\partial_\mu - g_s t^a \bar{A}_\mu^a - g_e A_\mu)\gamma^\mu\Psi \quad (2.1)$$

This is the “direct photon” Lagrangian, if you will. The  $g$ ’s are charge constants—in most cases  $g_e = e$  the basic unit or quantum of electromagnetic charge. The repeated Greek indices indicate normal lorentz contractions while the contracted small  $a$  index indicates a sum over all 8 gluon fields, with the  $t$  being a basis of linearly independent SU(3) matrices. Gluons each carry two color quantum numbers (therefore state vectors), but only 8 combinations of these two states will have the desired non-Abelian nature.  $\psi$  is the Dirac spinor quark field ( $\Psi$  is the color three-vector of these). The vector  $A$  fields are the gauge force fields,  $A_\mu$  representing the photon and  $A_\mu^a$  representing the gluon. Note that this is the Lagrangian for a single quark flavor  $f$ : the full Lagrangian including all flavors should be a sum over the last two terms for each of the six flavors. The first two terms involving the field tensors  $F$  and  $\bar{F}$  (whose components in the case  $F$  are combinations of the normal electromagnetic  $\vec{E}$  and  $\vec{B}$  field components) represent the EM and gluon field self energy. They are defined by the equations:

$$F_{\mu\nu} = \partial_\mu A_\nu - \partial_\nu A_\mu \quad (2.2)$$

$$\bar{F}_{\mu\nu}^a = \partial_\mu A_\nu^a - \partial_\nu A_\mu^a - f^{abc} A^b A^c \quad (2.3)$$

In the case of EM field,  $A_\mu$  is a four vector made up of the normal EM scalar and vector potential fields,  $A_0 = \phi$  (the voltage, for which  $\nabla\phi = \vec{E}$ ) and  $(A_1, A_2, A_3) = \vec{A}$ , the magnetic vector potential (for which  $\nabla \times \vec{A} = \vec{B}$ ). The third term in 2.3 that breaks the “symmetry” between the photon and the gluon tensor is quadratic in the field and is directly due to the non-commutation of the generators of the gauge symmetry. Herein lies the source of asymptotic freedom and gluon self-coupling in QCD and further makes the solutions of the field equations (relations that are implied by the symmetry of the Lagrangian) nonlinear.

The third term in the Lagrangian 2.1 represents the self energy (equivalent to its mass) of the quark field. Therefore, the first three terms define the *free-field* Lagrangian  $\mathcal{L}_0$  and while the last term represents the *interaction* Lagrangian  $\mathcal{L}_I$ , since coupling between different fields is manifest.

It must be remembered that, as this is quantum field theory, 2.1 is an operator equation: every field is itself an operator. This is the fundamental prescription of quantum dynamics. The prescription says that the Lagrangian operator (or the closely related operator, the Hamiltonian) determines the quantum state vectors that fields operate on.  $\mathcal{L}_0$  then determines the quantum state vectors of the free Lagrangian. For these states we have exact solutions, that is to say, representations, which we construct in Fourier momentum space.  $\mathcal{L}_I$  determines how combinations of these state vectors will evolve when the fields interact. Unfortunately we are not aware of any exact solutions for the full  $\mathcal{L}$ . It is not commonly discussed how hard anyone has looked, but we can probably assume that this avenue has been exhausted despite there being considerable freedom in the mathematical representation of the  $\mathcal{L}$ . We note that there do exist field theories that have exact solutions.

With no exact solutions we have two options: numerical solutions and approximation schemes. Fortunately for the latter, 3/4 of a century’s worth of work on a

general, well-tested approximation scheme for quantum dynamics can be applied. This scheme is called *Perturbation Theory* and it applies to just this case: when exact solutions are known in the “free” case, the “interaction” solutions are expanded in a power series of the free solutions in some parameter. The approximated theory of QCD using perturbation theory is aptly named perturbative QCD (pQCD). The dimensionless parameter that the power series is expanded upon in general perturbative quantum field theory is called  $\alpha_X = g_X^2/4\pi$ . where  $g_X$  is either  $g$  term in the Lagrangian: for pQCD, it is  $\alpha_S$ . pQCD can be used to predict many processes and has been fairly successful in describing much experimental data as I will discuss. However, due to asymptotic freedom/confinement, it is impossible to define  $\alpha_s$  such that it is  $< 1$  for all energy scales. Therefore the power series approximation on which pQCD is based upon *diverges* (becomes infinite and hence undefined) and therefore renders the theory unusable in these situations. These energy regimes are called *non-perturbative*. To calculate non-perturbative dynamics numerical calculations are the only option left. The most promising numerical method known (and with a large community of committed practitioners) exploits the ability to average solutions of Green’s function differential equations (in this case the fields) by simulating space-time with a square lattice of a discrete number of points. This is called Lattice QCD, or more generally Lattice Gauge Theory.

## 2.3 Perturbation Theory and Perturbative QCD (pQCD)

### 2.3.1 Feynman diagrams and Renormalization

In perturbative Quantum Field Theory (pQFT) using the Feynman functional integral formalism, the operator which causes a transition from one state to another can be represented as

$$U(i, f) = \int \mathcal{D}\bar{\Psi}\mathcal{D}\Psi\mathcal{D}A \exp -i \int d^4x \mathcal{L}[\Psi, \bar{\Psi}] \quad (2.4)$$

The perturbative expansion is immediately obvious in this form, since as usual the exponential can be thought of as short hand for the normal Taylor series expansion of the *function*  $e^{-Y} = 1 - Y + \frac{1}{2}Y^2 \dots$ . Since the scattering of two particles is really at its heart an example of a transition between quantum states of the system, the *matrix elements* of  $U$  (or elements of the more commonly notated “matrix”  $\mathcal{M} = \mathbb{I} - U$  up to some factors) are the relative probabilities of various allowed scattering processes and defines which processes are allowed and can ultimately be used to calculate scattering cross sections.

Using several different but equivalent motivations, one can derive a systematic way of calculating matrix elements of this operator to finite orders in the “coupling constant” ( $g_x^2$ ) expansion parameter by visualizing integrals as diagrams called Feynman diagrams. Let us take a concrete example which is important to the results of this thesis: gluon Compton scattering, defined as the process  $q + g \rightarrow \gamma + q$ . The interaction term in the Lagrangian contains two terms: 1) a  $\bar{\Psi}g_s\bar{A}_\mu\gamma^\mu\Psi$  term and 2) a  $\bar{\Psi}g_eA_\mu\gamma^\mu\Psi$  term which are multiplied together in the quadratic term of  $e^{-\int \mathcal{L}_I}$  expansion. First of all then, terms 1) and 2) mathematically have different (“dummy”) space-time integration variables, which indicates a “propagation” between two space time points. Now consider if we then specify an initial (final) quantum state for the fields in term 1 (2) to operate on that contain a single free gluon of momentum carrying momentum  $k$  and a single free quark carrying momentum  $p$  (or a photon with momentum  $k'$  and a quark with momentum  $p'$ , respectively): then pQFT says we can calculate the transition probability between these two states by a matrix element represented by the Feynman diagram in Figure 2.2:

The Feynman *Rules* tells us how to mathematically construct the matrix element by associating specific factors with each aspect of this diagram and multiplying all these factors together. The bold points represent *vertices*, simply the two different space-time points. Since we work in Fourier momentum space, the propagation is represented by a mathematical object known as a (in this case, quark) *propagator* with momentum  $iQ$ . Its form and the form of the other factors can be seen in the

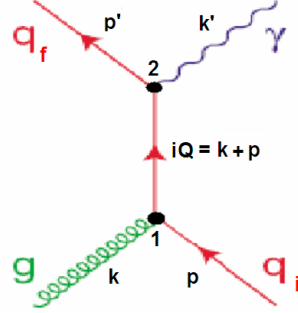


Figure 2.2: Gluon Compton Scattering Feynman Diagram representing the process  $qg \rightarrow q\gamma$

full expression for  $\mathcal{M}$ :

$$i\mathcal{M} = \underbrace{(u(p)\vec{c})}_{q_i} \underbrace{(\epsilon_g(k)a^{*a})}_g \underbrace{\left(i\frac{g_S}{2}t^a\gamma^\mu\right)}_{\text{vert.1}} \underbrace{\left(i\frac{\not{Q} - m}{Q^2 + m}\right)}_{\text{propagator}} \underbrace{(\bar{u}(p')\vec{c}^\dagger)}_{q_f} \underbrace{(\epsilon_\gamma^*(k'))}_\gamma \underbrace{(ig_e\gamma^\nu)}_{\text{vert.2}} \quad (2.5)$$

where  $u(p)$  are the free-field solutions to Dirac Spinor ( $\psi$ ) portion of  $\mathcal{L}$ ,  $\not{Q}$  means  $Q^\nu\gamma_\nu$ ,  $\vec{c}$  is a unit 3-vector representing the quark color,  $a^\alpha$  is a unit 8-vector representing the gluon color state corresponding to  $t^a$  in  $\mathcal{L}$ ,  $m$  is the mass of the quark flavor, and the  $\epsilon$ 's represent the polarization states of the photon and gluon.

At this point we must note that there was an ambiguity in our preparation of the initial and final quantum states. We could have chosen the opposite fermion fields to operate on—this would have amounted to a similar diagram as in Figure 2.2, but with the vertices connecting each particle in the *initial* state with the corresponding particle in the final state (instead of initial-initial, final-final as in 2.2. The Feynman rules tell us that the total matrix element is then a sum of these two diagrams. However everything is the same for this diagram except for the propagator term, so that our total matrix element is the following with now  $Q' = k - p$  ( and with some terms rearranged):

$$\mathcal{M} = \frac{-ig_S g_e}{2} \epsilon_g(k) \epsilon_\gamma^*(k') \bar{u}(p') \gamma^\mu \left[ \frac{\not{Q}' - m}{Q'^2 - m^2} + \frac{\not{Q} + m}{Q^2 - m^2} \right] \gamma^\nu u(p) (\vec{c}^\dagger a^{*a} t^a \vec{c}) \quad (2.6)$$

To use this  $\mathcal{M}$  we use Fermi's Golden rule for scattering which tells us how to use the transition probability (the modulus squared of  $\mathcal{M}$ ) in the scattering calculation [98]. In the Center of Mass (CM) frame with non-identical final state particles this is

$$\frac{d\sigma}{dt} = \frac{\mathcal{M}\mathcal{M}^*}{64\pi s |\mathbf{p}_i|^2} \quad (2.7)$$

where  $p_{i(f)}$  is either initial (final) state particle's momentum and we've introduced the *Mandelstam* variables,  $s = (p + k)^2 \simeq 2p \cdot k$  (the square of the center of mass energy),  $t = (p' - p)^2 \simeq 2p \cdot p' = |p_f||p_i|(1 - \cos\theta_{CM})$ . The third and final Mandelstam variable is  $u = (k' - p)^2 \simeq 2p \cdot k'$  and we shall make use of it in a moment. The Mandelstam variables are useful quantities for formulas in particle physics since they are *Lorentz invariant*<sup>3</sup> and simplify many complicated expressions. For example the quantity  $s + t + u$  is a constant simply equal to the sum of squared masses of all particles in the initial and final states, in our case  $2m^2$ .

Notice that in this equation, taking the modulus squared of (2.6) will result in a cross section that is proportional to  $\alpha_s\alpha$ . This means it is a lower order process to the total cross section in either  $\alpha$  or  $\alpha_s$  separately than purely EM or strong-strong processes of order  $\alpha^2$  or  $\alpha_s^2$  respectively.

The full expression then will involve “squaring” (2.6), which is already quite complicated. The first thing to note is that apart from the last term in parentheses in (2.6),  $C = (\vec{c}^\dagger a^* t^a \vec{c})$ , the matrix element is exactly the same for electrodynamic Compton scattering ( $e\gamma \rightarrow e\gamma$ ) where the gluon is replaced by a simpler photon. This matrix element has been worked out in many textbooks such as [145], using several common simplification techniques such as averaging (summing) over initial (final) polarization and spin states with “trace theorems”. Taking directly from [145], eq. (5.87) and dropping all terms proportional to  $m^2$  since we are generally working in the ultra relativistic limit, we have the following relation:

---

<sup>3</sup>meaning having the same value in all frames of reference with constant velocity

$$|\mathcal{M}_{\text{QED Compton}}|^2 = 16\pi e \left( \frac{u}{s} + \frac{s}{u} \right) \quad (2.8)$$

To use this result for the QCD gluon process we only have to account for the fractional charges of the quarks, as 2.8 was derived for electron Compton scattering, and our color factor  $C$ . The final cross section is then

$$\frac{d\sigma}{dt} = -\frac{f_q^2}{3} \left( \frac{u}{s} + \frac{s}{u} \right) \quad (2.9)$$

It is this gluon Compton scattering process which dominates the full direct photon cross section in  $p + p$  scattering for  $x_T$  values corresponding to the relevant  $p_T$  region results of this dissertation [140]. There is only one other simple diagram that contributes at the order  $\alpha\alpha_S$ : quark anti-quark annihilation ( $q + \bar{q} \rightarrow \gamma + g$ ). But since the projectiles we collide are matter-matter (p+p and Au+Au) (as opposed to e.g.  $p + \bar{p}$  collisions) this contribution only comes from rare  $q\bar{q}$  pair fluctuations of the gluon fields inside the nucleons, discussed in the next section.

### 2.3.2 The Running Coupling Constant $\alpha_S$

We have not discussed what the value of the pQCD expansion parameter  $\alpha_S$  is at this point, so we don't have any conception of at what level the higher order terms contribute. As it turns out in perturbative field theory the situation is actually the other way around: it is actually the higher order terms in the expansion that determine the expansion parameter! This is because the integrals in the higher order terms, sometimes called radiative corrections, diverge. They can diverge in two directions: infrared (at very low momentum) and ultraviolet (as the momentum transfer goes to infinity.) Since empirically we don't observe infinite cross sections, it is essential that the theory be able to render the divergences physically insignificant. For the UV divergences, it is possible to simply factor out the infinity and absorb it into the coupling constant or the mass constants in  $\mathcal{L}$ , effectively re-scaling them. This is called *renormalization* of those constants. The procedure introduces an explicit dependence for the renormalized constants on an arbitrary parameter  $\mu^2$

but nothing further is done with the infinity—it is a philosophical assumption of the theory that since these infinities are undetectable in real life they are somehow cancelled away in the renormalized quantities. It is implicit then the constants can't be predicted *a priori*—they must then be measured at a “reference” value of  $\alpha_S$  taken at one specific value of  $\mu^2 = \mu_0^2$ . Then pQCD can predict  $\alpha_S$  at any other value of  $\mu^2$ . If one is calculating quantities to *leading order* (LO) in  $\alpha_S$  (as we did above for the Compton cross section) and but includes the *leading logarithm* effects of all the higher order terms, then the following relation holds ([140]):

$$\alpha_S(\mu^2) = \frac{\alpha_S(\mu_0^2)}{1 + (21\alpha_S(\mu_0^2)/12\pi) \ln(\mu^2/\mu_0^2)} = \frac{12\pi}{21 \ln(\mu^2/\Lambda_{QCD}^2)} \quad (2.10)$$

where we have absorbed  $\alpha_S(\mu_0^2)$  into a new “fundamental constant of QCD”,  $\Lambda_{QCD}$ . A real constant, that is, one that never gets renormalized. Its value, obtained by a global fit to many data sets, is currently between 100 and 200  $MeV^2$ . However, adding higher orders to pQCD calculations changes its meaning and value. Recently it seems more common to quote the the value of  $\alpha_S$  evaluated at the mass of the  $Z_0$ ,  $\alpha_S(M_Z) = 0.118$ .

$\mu$  is known as the renormalization *scale*. What is the parameter  $\mu$  anyway and why do we care about it? One answer to the second half of that question is that we *don't* care about it at all since it has absolutely no physical significance. Now operationally, we *do* have to choose a value for  $\mu^2$ , so rather we should say that we only care so much that this value does not affect predictions of measurable quantities. In fact, 2.10's derivation is simply a result of the enforcement of this statement, namely for a real quantity  $K$ ,  $\mu \frac{dK}{d\mu}$  should be 0 [59]. However this is not the whole story. Dimensionally, this quantity has the dimensions of mass squared. In actual fact it can be shown in that  $\mu$  arises as an addition to the mass term of propagators in the radiative correction diagrams, which is to say, the  $Q^2$  of those propagators. Therefore  $\mu^2$  is interpreted as a choice  $Q^2$  at which the renormalization is defined. About as often as not in the literature, equation 2.10 is written with  $Q^2$  in place of  $\mu^2$ . With this interpretation 2.10 is viewed as exhibiting several cornerstone concepts

of perturbative QCD. First, it and relations like it in all perturbative QFT's (even QED) define the *running coupling constant*, a coupling (and corresponding charge) which actually depends on the energy of the propagating probe. Second, for pQCD, 2.10 is a mathematical statement of asymptotic freedom/confinement. To say then that the predicted values of measurable quantities do not depend on  $\mu^2$  is not quite right: for one thing since in general we do not work to infinite orders  $n$  in the parameter  $\alpha^n$  (e.g. 2.10 is only the *first* order,  $n = 1$  derivation) in reality, the predicted quantities do depend on  $\mu^2$  interpreted as exactly as  $Q^2$ . This is nicely demonstrated in [156]. For another thing, for the theory to be meaningful at all,  $\mu^2 \equiv Q^2$  must be at a value such that  $0 < \alpha_S < 1$ .

Infrared divergences in pQCD are caused by final state *bremstrahlung* radiation diagrams which can be visualized as additional photon or gluon field external lines being emitted by the external lines of the lowest order diagrams. These are generally handled through cancellations between different terms and can sometimes can simply be “ignored” considering that radiation with vanishing energy is unobservable. Any infrared divergences not able to be dealt with, similar to the UV re-scaling, can be absorbed into the parton distribution and fragmentation functions described the next section—but the best way to get around infrared divergences is to construct experimentally accessible quantities from the more basic cross sections/matrix elements that are “infrared safe”.

Before leaving the subject of divergences I will mention that there are many such ways of *regularizing* them in perturbative QFT's. These are usually referred to as the renormalization *scheme*. Equation 2.10 is derived using one particular scheme known as the “minimal subtraction” (MS) scheme and often  $\Lambda_{QCD}$  is written as  $\Lambda_{MS}$ . Note that 2.10 also assumes that there are exactly 6 flavors of quarks.

### 2.3.3 Factorization, PDF's and Fragmentation

All of the above was derived for quarks and gluons as if they were leptons, photons, or other non-confined fundamental fields. But in reality because of confinement, the

above Feynman diagrammatic processes never occur quite so cleanly. Confinement generally leads to two complications that must be accounted for before we can apply our pQCD cross sections of the previous section to real world scattering involving hadrons. Both of these issues are handled in practice by the *factorization ansatz*, parton distribution functions, (PDF's) and fragmentation functions.

First is the consideration that a hadron always represents a superposition of parton wave functions. This was already alluded to in our discussions of total wave function symmetry/antisymmetry in the parton model where we laid out a structure for each hadron based on the combination of several *valence* quark states. For example the neutron contains three valence quarks, *udd*, two down quarks and an up quark. These quarks along with the gluons that bind them are in bound states which are a Fourier-like superposition over *all* momentum states ( $|p| \in [0, \infty]$ ) the different definite momentum “free” wave states. Furthermore as we hinted to in our discussion of gluon fluctuations, just after 2.9, the valence quark content description of hadron structure is only approximate—in fact, one must include in the total hadronic wave function contributions from a virtual “sea” of *all* quark and anti-quark flavors (appropriately called *sea-quarks*). Combining these wave functions in the cross section calculation, it would seem to be necessary to include an infinite sum/superposition of quark states of varying momenta, a situation that would make the situation very messy.

To make matters worse, the second thing we must account for are the non-perturbative confinement processes themselves that the incoming and outgoing quarks and gluons suffer the on their way “in” and “out” of the larger scattering processes. These non-perturbative confinement processes occur exactly near the  $Q^2 \approx \mu_R^2$  regime where perturbation theory breaks down, as related to our discussions of 2.10, and are physically manifested in the structure of the observed hadrons going in and out of collisions. They will cause the wave function superpositions and the way each component enters the cross section calculation to be altered in uncalculable ways. This again doesn't seem to bode well for the possibility of being able to

make real world calculations. To top it all off, there also are all the higher order (divergent!) terms in the calculations that we are ignoring in our usual finite order calculations!

Fortunately we are saved by the fact that we are only considering **hard** scattering. It turns out that if we only consider very high  $Q^2$  processes, only those parts of the total hadronic wave functions with high momentum (and therefore high momentum fractions  $x$  of the parent hadron) will be relevant: we can essentially pick out only a single well-defined high momentum component of the total wave function superposition. This is the same as saying we can treat the single high momentum parton as a free particle. Furthermore, at such high momenta, the non-perturbative corrections in the cross section calculation will be relatively small. What this amounts to is that experimentally, we can “lump” all of these ambiguities into a single function (one for each hadron participant) of both  $Q^2$  and  $x$ . These functions are called Parton Distribution Functions and Fragmentation Functions and form the basis of factorization.

PDF's are the domain of the *Parton Model*, most sensitively developed as a result of studying *Deep Inelastic Scattering* (DIS) where weakly interacting leptons probe deeply inside hadrons before scattering with partons. These are simply probability distribution functions of (what turns out to be) a fraction  $x$  of the hadron's momentum carried by a parton. They are usually denoted by a function  $G_{a/A}(x)$  describing the probability of finding a parton  $\mathbf{a}$  in hadron  $\mathbf{A}$ . Hence in scattering they define the state of the *incoming* parton thereby describing the structure of incoming hadrons. PDFs are measured through the before-mentioned scattering structure functions, which are simple functions of the PDFs.

Fragmentation functions (FF) are very analogous to PDF's, but they concern the *outgoing* partons and their subsequent confinement into outgoing hadrons. They are also probability distribution functions for the probability of obtaining a hadron with a momentum fraction, usually written  $z$ , of the outgoing partons. However this process of fragmentation is not quite as clean as this sounds. In experiment

what is seen is actually that a single outgoing parton usually creates more than one particle (often many more) all of which are “ejected” near each other. These sprays of particles, roughly a conical pattern of outgoing rays are called *jets*. The study of *jets* then comprises a large part of QCD experimentation. FF’s are most often they are denoted  $D_{B,b}(z)$ , describing the probability of there appearing a hadron (formally this can be any type of particle)  $B$  carrying fraction  $z$  of the original parton  $b$ ’s momentum. They are generally are falling functions of  $z$ . FF’s are very cleanly measured in lepton-lepton scattering, such as  $e^+ + e^-$  scattering, in which there is no cloudiness involving the incoming PDF.

Both FF and PDFs are analogous to renormalized constants of the QCD Lagrangian in the following sense. They represent something we can’t calculate or predict with perturbative calculations. So we measure them. Once measured, as with the renormalized coupling constant, we can use the measured values to universally to predict the results of other processes. And just like the renormalized coupling constant, (in fact *as a result* of the finitely-order approximation of the renormalized coupling constant) they too depend on momentum scales, again logarithmically. This time most often in the literature the scale is explicitly recognized as identically  $Q^2$ , the momentum (squared) transferred from the input scattering probe or, that is, the momentum of the scattering propagator. In the case of the PDF, this scale is called the *factorization scale*; in the case of the FF, the *fragmentation scale*. In both cases the scale represents the approximate boundary in  $Q^2$  below which non-perturbative effects and the other aspects of the real situation we’ve ignored are expected to start contributing.

Often in experiments where a lepton is one of initial scatterer’s, (DIS,  $e+p$ , etc),  $Q^2$  is directly measurable. When this is not the case or whenever an *inclusive* prediction (a prediction that includes many different processes averaged over many different  $Q^2$ ’s) is made, a choice for these scales must be made during the calculation. Most often the factorization, fragmentation, and renormalization scales are chosen to be the same. While this would seem to be desirable from our arguments thus far,

since it is only a logarithmic dependence, the three scales don't necessarily need to be chosen to be the same, and due to how they are used in some cases it may be desirable and correct not to.

Also, similar to the case of the coupling constant (as explicitly demonstrated in the running coupling equation 2.10), once measured at a single scale for a range of  $x$  values, both the PDF's and the FF can be analytically evolved to other scales. Due to the perturbative-approximation origin of this scale dependence, the evolution is governed by coupled sets of pQCD "integro-differential" equations [59]. For PDF's this set of equations are generally referred to as the Altarelli/Parisi equations and the process is known as DGLAP evolution. The first step in this process is to parameterize the measured PDF's. For this there are many different competing forms, most of which involve powers of  $x$ ,  $1 - x$  and other smooth functions of  $x$ . The accuracy of these evolution equations is quite impressive, often shown on a single plot are the predictions matching the measured structure function data over many orders of magnitude in both  $x$  and  $Q^2$ . This success lends credence to pQCD theory in general and especially factorization.

The factorization ansatz or theorem then is simply the statement that whole picture of this section works together with the last, that all the pieces can be put together in one big integral and yield meaningful results that correctly predict experimental scattering data. Mathematically, this means that in such an integral the PDF's, FF's, perturbative cross sections calculated for the partons actually factorize, that is, are simply multiplied together. Often people introduce the factorization theorem like any mathematical theorem by defining it as the actual big integral itself. However, as the formula is different for different processes, in this language there are an infinite set of factorization theorems. Let us simply give the formula for the inclusive differential cross-section of some particle  $C$  (studied in  $p+p$  collisions):

$$\begin{aligned}
\frac{d\sigma_{pp \rightarrow C+X}}{d^3p_C} = & \int dx_{q_i} dx_g dz_q G_{q_i/p}(x_{q_i}, M_\gamma^2) G_{g/p}(x_g, \mu_F^2 a) D_{C/c}(z_C, \mu_F a^2) \times \\
& \frac{\hat{s}}{z_C^2 \pi} \frac{d\sigma_{qg \rightarrow qc}}{d\hat{t}} \delta(\hat{s} + \hat{t} + \hat{u})
\end{aligned} \tag{2.11}$$

We've suppressed the  $f$  on  $q_f$ , but it hardly matters since we've integrated out the momentum of this final state quark (the  $X$ ). One example of the application of this formula would be to calculate the inclusive productions of  $\pi^0$  in  $p+p$  reactions: then  $C = \pi^0$  and  $D_{\pi^0/c}$  is the probability that a  $\pi^0$  will appear with the energy fraction  $z_C$  of original parton  $c$ 's momentum. Therefore within the  $z$  integral, all possible  $c$  quark momenta are "sampled", since we are calculating for a fixed  $\pi^0$  momentum  $p_C$ . Note that if we are calculating inclusive photon production ( $C = \gamma$ ), then in leading order calculations,  $D_{C/c}(z_C) \equiv \delta(z_C - 1)$  and the all the  $z_C$  dependent terms disappear. However at next to leading order (NLO), we must include the possibility of photon final state radiation (bremsstrahlung) from other processes, such as  $qg \rightarrow qg\gamma$ . As usual though, it is easiest to just absorb *all* such higher order effects into an effective photon fragmentation function  $D_{\gamma/c}$ . It turns out that due to the way singularities in the higher order terms cancel, these fragmentation photons can contribute to the inclusive spectrum of photons at a comparable level, which we will come back to in our concluding section.

Because of the revolutionary concept of confinement, the success of factorization is an important confirmation that some of the basic ideas of pQCD are working correctly. As we shall see, equation 2.11 and other factorization theorems like it do correctly describe high-momentum hadronic cross-sections very accurately, and with increasing accuracy as the momentum scale increases, just as expected. And in fact this is an important statement, perhaps *the most* important, as regards the use of factorization in HI physics: it means that such scattering processes, since they are well understood at the hadronic level, can be used to study more complex high-momentum heavy ion collisions.

One final remark about PDF's. While fragmentation functions describe a short-lived process, the “dressing” of bare quarks and gluons into hadrons, PDF's on the other hand provide a statistical window into the steady-state structure of hadrons. Therefore they are of paramount interest because they are partly projections of the specifics of how the partons interact in the long term, something our current perturbation theories cannot give us any real information about. Proton structure has been cited as one of the most important open questions in physics [1]. Often people say that PDF's cannot be calculated. In actual fact they can be and are, through non-perturbative methods such as Lattice QCD [159]. It's just that thus far they have not been able to do very well when confronted with data. However as lattice calculations progress and new non-perturbative techniques are developed (such as the recent Color Glass approximations), we should expect to eventually be able to exhibit our understanding with calculated PDF's that actually work. In the next chapter we will explore some aspects of Lattice QCD focusing mostly however on more general aspects of QCD matter relevant to QGP formation and therefore to the field of Relativistic Heavy Ions.

## Chapter 3

# The Phase Transition, QGP, and HI Physics

---

### 3.1 Non-Perturbative and Lattice QCD

Non-perturbative lattice calculations have occurred almost from the beginning of QCD [174] and in fact were integral to popular acceptance of QCD as the right theory to describe partons and hadrons. For example, it was “on the lattice” that the process of confinement described in the last section was first demonstrated [145] in a self-consistent manner, since the perturbative theory simply breaks down conceptually in this regime. Many theoretical groups have worked and continue to work on lattice formulations, *e.g.* [65], [122], [112]. Lattice calculations require an enormous amount of computing. Many dedicated teraflop computers have been built to perform lattice calculations, and in terms of lattice size (defined below), the calculations still must remain fairly small, and thus are still emerging from a level where they calculate basic quantities such as coupling strengths, correlation functions, and thermodynamic properties to being able to quantify more complex phenomena. Nonetheless, the calculations performed so far can be tested and studied experimentally in certain physical situations. Herein lies one of the major purposes of our field of Relativistic Heavy Ions: hoping that these physical situations can be realized, we

are testing and studying aspects of lattice QCD theory and other non-perturbative models of the same phenomena. The most important of these non-perturbative predictions for our purposes, related to confinement itself, is the prediction of a phase transition in bulk QCD matter from a state where quarks and gluons are confined in hadrons (as in the normal hadronic matter we experience everyday) to a “deconfined” state where they are not. Generally the deconfined state of matter is called a *Quark-Gluon Plasma* (QGP), a name first used by E. Shuryak. [152]. The detailed physical description of this *deconfinement* is still being explored and debated—*e.g.* will the QGP be a weakly interacting plasma, or a strongly interacting one. In this section, however we will describe some of its more definitely known basics as described by Lattice QCD.

But first I will note that there are several “effective” models of some of the same non-perturbative physics that is described by Lattice QCD. These include earlier “effective” theories of hadronic matter [109], [41], [139] which are very abstract, but can provide a phenomenological description of observed experimental data. Some of these theories can be interpreted as implicitly showing a phase transition to deconfinement and one may even credit these theories with providing the impetus to describe the phenomena as a thermodynamical phase transition. As an example, take [119] the *MIT bag model* of hadronic structure. In this model, the confining force is modeled as a “bag” (like an infinite quantum well) and what holds the partons together is an inward “bag pressure”. By balancing the kinetic energy and other interaction terms of the Hamiltonian, one is led to a simple yet relatively successful phenomenological description of many observed hadronic properties and also confinement. Specifically, the breakdown of confinement is described as an overwhelming of the bag pressure by an increase in the energy density at some critical temperature  $T_C$ . This then is the temperature at which the bag model predicts the QGP phase transition and in its simplest form the Bag Model predicts a value of  $T_C = 200$  MeV [176] (we always work in units with a modified Boltzmann constant where temperature has the units of energy: eV meaning electron Volts the

standard particle physics unit of energy). As we shall see below, this value is not far from the range predicted by Lattice QCD.

The Feynman formulation of Quantum Mechanics provides a practical basis for Lattice QCD. The functional integral in 2.4 is defined as a *path integral*, that is, the integral of the action  $e^{\int \mathcal{L}}$  over all possible paths in Minkowski space-time. In Lattice QCD, the first step is of course to make a model of a small region of that space-time as a discrete lattice of space-time points. In order to simplify the calculations, Minkowski space is usually *Wick rotated* into 4-D Euclidean space through the transformation  $t \rightarrow i\tau$ : for thermodynamic lattice calculations, this is the most natural anyway, as we shall see. A single lattice spacing for all four dimensions is denoted  $a$ , with  $N_\sigma$  discrete points in the 3 spacial directions and  $N_\tau$  points in the temporal direction. Once we define all the fields (and their many components) at each point of this model, “paths” in space time can literally be summed and multiplied.

Before we get more specific, in the minimal historical introduction of the field of physics given at the beginning of this dissertation we made an omission we now need to fill in: the development of statistical mechanics by Boltzmann. In a nutshell, this theory describes thermodynamics (the dynamics of the properties like temperature of bulk collective matter such as gases) as a result of the statistical distribution of all possible macroscopic states of a system, and the macroscopic state of thermodynamic equilibrium (*e.g.* the way we normal encounter bulk matter) as the state which has the maximal statistical probability. All of the statistical properties of a system of many particles in equilibrium can be mathematically expressed, literally summed up, in a quantity called the *grand partition function* denoted  $Z$  defined as

$$Z = \sum_{i \leq N_{\text{states}}} e^{\frac{-E}{k_B T} + \mu N_{\text{particles}}}$$

This function then contains all thermodynamic information and from it all thermodynamic quantities can be extracted through differentiation, together with the identification of entropy  $s = k_B \ln Z$ . The generalization of  $Z$  in field theory is

$$Z = \int \mathcal{D}\bar{\Psi}\mathcal{D}\Psi\mathcal{D}A \exp - \int d^4x \mathcal{L}[\Psi, \bar{\Psi}, A] + \mu_B N_{\text{particles}} \quad (3.1)$$

Note the similarity of 3.1 to 2.4. This similarity of form is actually designed by construction and is true only with the transformation from just above to Euclidean 4-space now with the  $\tau$  being interpreted as the inverse temperature,  $T^{-1}$  and with the special conditions that the fields have periodic boundary conditions at the spacial boundaries. However posing the problem this way, equivalent to calculations of hard scattering quantities, is not just a convenience: it is necessary because the scale of  $a$  must be “calibrated” through the calculation of physical quantities (masses, cross-sections, etc...) which are known from the experimental high-energy scattering results. These calculations make use of the Wick rotated version of 2.4. This calibration is necessary for the following reason. One is only interested in the continuum limit for lattice calculations, that is, the limit  $a \rightarrow 0$ . However it is not  $a$  that is adjusted in lattice calculations, since this would mean changing  $N_\sigma/N_\tau$ . Instead it is easier and less computationally intensive to simply change the value of the bare coupling  $g_S$ . Then one can extrapolate to the  $a \rightarrow 0$  limit.

This calibration process is one of the complications of doing lattice calculations, but there are many ways in which lattice calculations are simplified. For example, relative to analytic calculations, the finite, discrete lattice naturally regularizes the divergent integrals that occur in perturbation theory. Also, since it is indeed only the  $a \rightarrow 0$  limit which matters, considerable extra freedom in specifying the action is allowed, as long as all non-physical terms vanish in the  $a \rightarrow 0$  limit. This freedom is exploited by constructing special *improved* or *perfect* actions which minimize or remove completely *discretization* errors that arise naturally in lattice calculations due to the finite lattice spacing.

The basis of one such technique is that on the lattice, the gauge (gluon) action is formulated with the *link variable*  $U$  (which after all is not completely unrelated to our  $U_\mu$  operator from 2.4 hence the notational similarity?) instead of the “raw” field  $\bar{A}_\mu$ .  $U_\mu$  is defined as the integral of  $\bar{A}_\mu$  (where  $\bar{A}_\mu = A_\mu^a t^a$  as above):

$$U_\mu(n) = P \exp ig_S \int nn_k dx_\mu \bar{A}_\mu$$

where  $n_k$  is an adjacent lattice site to  $n$ . Not surprisingly, the gauge field action can then be formulated as sums, products, and traces of these link variables. At least one other important quantity can be easily formulated in terms of link variables: the *Polyakov loop operator* or *Wilson line operator* [176] defined as [150]

$$L(\mathbf{x}) \equiv \frac{1}{N_c} \text{Tr} \prod_{l=1}^{N_\tau} U_{n,0} \quad n^\mu = (l, \mathbf{n}), \mathbf{x} \equiv a\mathbf{n}$$

This quantity can be thought of as a building block of arbitrary functions of  $\bar{A}_\mu$  [145]. The important thing about this quantity for our purposes is that it integrates the pure gauge field even in the vacuum, and therefore its expectation value,  $\langle L(\mathbf{x}) \rangle$  can somehow be thought of as an indicator of the gluonic field in all situations, even when sources (quarks) are not present. A similar indicator for the fermionic quark fields themselves is the *chiral condensate*  $\langle \bar{\psi}\psi \rangle$ .

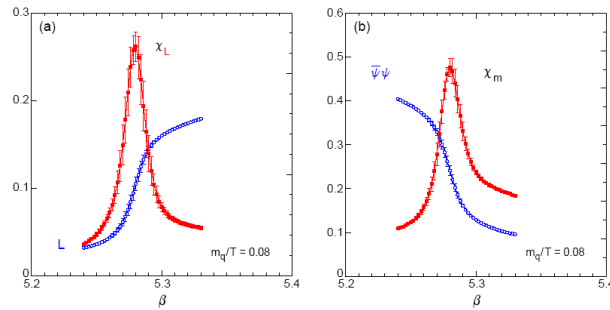


Figure 3.1: Discontinuities in the values of the Polyakov Loop (a) and Chiral Condensate (b) expectation values. These discontinuities indicate the presence of a phase transition. The  $\chi$  quantities are susceptibilities related to the two parameters. The parameter  $\beta$  is called the bare coupling and is proportional to  $1/T$ , (see text) so the temperature increases from *right to left* ( $\leftarrow$ ). Plot taken from [150], originally from [123].

The reason I've introduced these last two quantities is because they both have been calculated on the lattice as a function of temperature with the interesting results shown in Figure 3.1. Since the self-energy of the fields are related to these two

quantities, discontinuities in their values as a function of the temperature  $T$ , signify a phase transition. In the figure, the x-axis has units of  $\beta$ , the bare coupling,  $\propto 1/T$ . Lattice predictions for the critical temperature (at  $\mu = 0$ ) are around  $T_C \simeq 170$  MeV. The discontinuity in 3.1 (b) is often called the “restoration of Chiral Symmetry”. This is because the vanishing of this term from our Lagrangian (2.1) allows the remaining 4-D spinor  $\psi$  terms to be rewritten symmetrically in terms of two 2-D “Chiral” spinor states; therefore, this chiral symmetry of the Lagrangian is grossly manifest. Due to results like these, it is believed that the lattice does demonstrate a phase transition.

What does the lattice say about interesting matter on the other side of the phase transition from the normal hadronic matter? This addresses what is really meant by the concept of deconfinement. As the word name QGP implies, one would imagine that it is the quark and gluon degrees of freedom that individually become relevant in the deconfined phase. Is this what the lattice tells us? The answer can be seen in the quantity  $p/T^4$  calculated on the lattice where  $p$  is the pressure. If one assumes a classical non-interacting ideal gas of quarks and gluons, one would expect to approach the Stefan-Boltzmann pressure limit  $p_{SB}/T^4$  as  $T \rightarrow \infty$ . The quantity  $p_{SB}$  depends on the number of degrees of freedom. As 3.2 shows even with calculations with limited numbers of quark flavors, the lattice values appear to be near (within  $\sim 20\%$  of) the Stefan-Boltzmann limit. The 20% deviations are expected to be due calculational limitations. For this reason, it is believed that the phase transition is in fact to a deconfined system (plasma) of quarks and gluons.

Obviously this is an indirect argument. All figure (3.2) shows is that there are likely more relevant degrees of freedom than just hadrons. In fact there have been many particle-like states proposed which are not exactly hadrons, yet not exactly quarks and gluons either, such as “diquarks” [115] or “baryon junctions” [163]. In its loosest definition, lately the “QGP” moniker seems to effectively been extended to also include other non-hadron states like these [151],[8], [102]: currently any thermalized QCD matter which is not made up of fully formed hadrons could

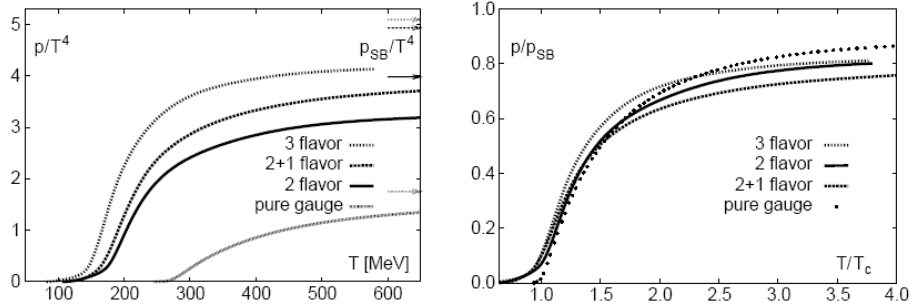


Figure 3.2: Since the quantity  $p/T^4$  calculated on the lattice approaches the Stefan-Boltzmann limit for an ideal gas of Quarks and Gluons, the lattice does indeed exhibit a QGP. Taken from [150] originally from [84].

perhaps be considered a QGP. The lattice calculations so far are just now capable of demonstrating the existence of such bound “non-hadronic” QCD matter states [124].

Finally I show one last important result from lattice QCD. The phase diagram of QCD matter as computed on the lattice in Figure 3.3. The upper left hand portion of the graph corresponds to normal hadronic and nuclear matter, and as such was expected even before lattice calculations were made. Even the extrapolation into the QGP transition region was guessed and plots such of these but in schematic form are often encountered. However it was an important confirmation that such a phase diagram was actually realized on the lattice. Note that from the plot, the QGP phase exists for values of high temperature and *low* baryon density. Low baryon density itself implies that no “normal” nuclear matter which will be “in bulk” either all nucleonic or anti-nucleonic, or correspondingly that the matter contains equal numbers of quarks and anti-quarks which we know is not the case for baryons with their valence content. That the net baryon density is approximately 0 has been verified at RHIC which is one of the first signs that we could have sufficient conditions for QGP formation [48].

Of course the thermodynamic state is determined by three thermodynamic variables, not just two. Therefore a high energy density density is also necessary for the formation of a QGP. From lattice estimates, the requisite energy density is known

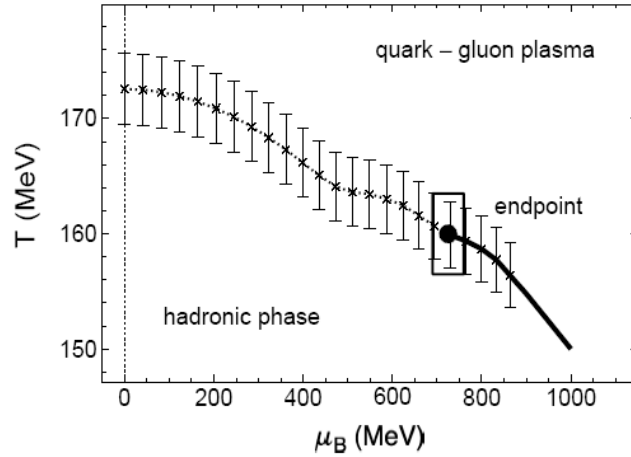


Figure 3.3: Phase Diagram of QCD matter actually calculated on the lattice. Note that the baryon density  $\mu_B$  is just a rescaling of the quark density,  $\mu_B = 3\mu_q$ . Taken from [150] originally from [84]

to be about  $1 \text{ GeV}/\text{fm}^3$  [125]

## 3.2 Enter Relativistic Heavy Ions

Perturbative QCD has been explored for many years and continues to be studied, tested, and improved. So far, despite the complications noted, its performance in predicting the outcome of reactions involving hadrons has been quite impressive, though not always perfect as we shall see. The imperfections nearly always have to do with aspects of the calculations that depend on non-perturbative quantities. Therefore, it is desirable to experimentally study the properties of QCD in the non-perturbative regimes. The possible existence of a QGP phase at extreme values of temperature and densities was recognized in the late 70's and early 80's [54], [152], soon after pQCD calculations were maturing and QCD was in fact accepted by most particle physicists as the correct theory. Around the same time, a natural extension of experimental nuclear physics, using particle accelerators to make high energy beams of heavy ions was also made possible. Since the complex nuclear objects intrinsically carried large particle numbers, it was hoped that at a high enough energy collisions of such relativistic heavy ions could squeeze enough energy and

parton number into a small volume at a temperature above the requisite  $T_C$ , such that in such collisions, the QGP could be created experimentally. Thus was born our field, which was then a fusion of particle and nuclear physics, a combination of applied particle physics and a strange sort of condensed matter physics.

The first RHI experiments were performed at the Lawrence Berkeley Lab (LBL) Bevalac with a per nucleon center of mass (denoted  $\sqrt{s_{NN}}$ ) energy of about 1 GeV. Similar energies were explored at the Brookhaven AGS and the CERN ISR though with much heavier nuclei. Data indicated that no QGP was formed, though collective hydrodynamic behavior was observed. Then, at the CERN Super Proton Synchrotron (SPS) at  $\sqrt{s_{NN}} \sim 14\text{-}17$  GeV, several observations were found to be abnormal compared to normal particle physics observations, though these results could not establish unambiguously that the QGP was created.<sup>1</sup> All of these experiments were fixed target experiments, where a single beam of particles was accelerated into a stationary target. RHIC is the first *collider* (meaning it has two beams pointed at each other) of Heavy Ions allowing the next order of magnitude in energy ( $\sqrt{s_{NN}} = 200$  GeV) to be reached, as well as the first facility built for and dedicated to the study of RHI physics, with the specific goal of creating the QGP in the laboratory.

## 3.3 The Space-Time Geometry of a RHI Collision

### 3.3.1 Basics And Static Structure

What is the shape of a nucleon or a nucleus? From basic scattering considerations and experimental results, the “shapes” of both nucleons and stable nuclei are perfectly spherically symmetric to a within fairly precise limits [147]. Of course, as with atoms and all quantum particles described by wave functions, their actual 3-D shape extends through all space. However we can think of them as being mostly localized around some radial distance from an origin defining the location. This kind of radial wave function for a *nucleon* can be described very well by a simple gaussian, and so describes a “sphere” that has a radius of  $\sim 1 - 2\sigma$ . Described this

---

<sup>1</sup>although this is and likely will remain forever a hotly debated subject

way, the “size” (diameter) of the nucleon is approximately 1 fm. For nuclei, the spherical shape is even better defined by a larger region of constant high density, described mathematically by a *Woods-Saxon* distribution:

$$\rho(r) = \rho_0 \frac{1 + \omega r^2}{1 + \exp((r - R_A)/s)} \quad (3.2)$$

which is sort of like the same gaussian of the nucleon but with its center peak “stretched out” to a length  $R_A$  and with  $s$  now describing the falling gaussian “skin”. The  $\omega r^2$  term usually omitted, “allows for central irregularities” [164]. The radius  $R_A$  of a nucleus goes roughly as  $1.2A^{1/3}$  fm. Therefore for our *Au* nuclei we have a diameter of  $\sim 14$  fm. For completeness, we note that as “grossly” composite objects, nuclei, like atoms, can exist in excited (“orbital structure”) states which are not spherical—see *e.g.* [148]. However these states are generally unstable and therefore very rare for stable elements in a macroscopic sample of matter, such as a particle beam or target. However this may not be the case for *e.g.* radioactive Uranium.

### 3.3.2 Spacial Evolution

We can use these basic length and time <sup>2</sup> descriptions to construct the *space-time geometry* or space geometry together with *what happens when*, for an average RHIC *Au + Au* relativistic heavy ion collision. Here we follow the description of Bjorken [54] in his seminal paper of the RHI field.

First the two nuclei are heading towards each other at so near the speed of light, they have an extremely high Lorentz  $\gamma_L$  factor of  $E/m = 100$ . Special Relativity means that their length along the collision axis is highly Lorentz contracted by a factor of 100 such that they are appropriately described as two “pancakes” as shown in the figure. This of course describes the situation in the CM frame. The Lorentz contraction of the nuclei in this frame is an extremely important concept, since it essentially reduces the space geometry to the 2 transverse dimensions only. These two pancakes essentially pass right through each other, not without interactions

---

<sup>2</sup>We always work in units of time such that the speed of light is 1, therefore we can express time in units of length.

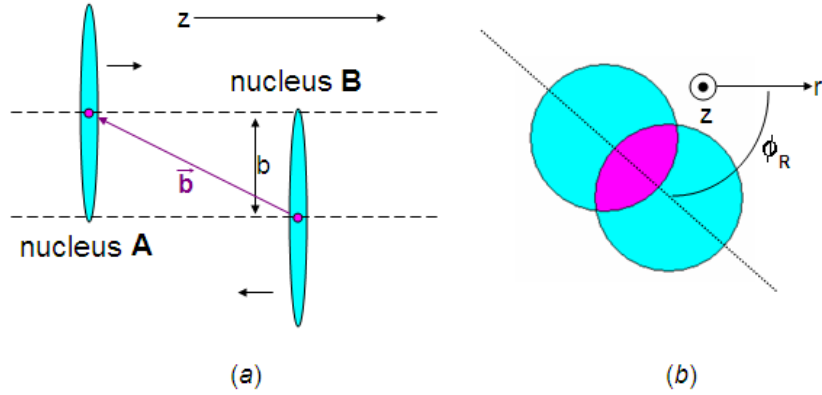


Figure 3.4: In (a), the reaction plane is in the page. Usually only the two components of the impact parameter vector  $\vec{b}$  transverse to the  $z$ -axis are considered (indeed in the literature,  $\vec{b}$  denotes only this 2-vector) and in fact most often, only the 2-vector magnitude  $b$  matters. The mauve region in (b) represents the overlap region. If  $b = 0$ , this overlap region is spherical. We call such events perfectly “central”.

however. In fact if we assume that much of the nucleon-nucleon interactions occur in a similar manner to how they otherwise would in a  $p + p$  collision, we can assume that for any transverse region in which the two pancakes overlap, *every* nucleon present will be struck. This is an assumption well justified by experiment [176].

This overlapping region is defined by the minimum transverse length between the two pancake centers called the impact parameter  $b$ . In general, the shape of the overlap region is described as an almond, and its anisotropy can result in a detectable anisotropy in the products of the collision. This is called *elliptic flow* and is one of the prerequisite signatures discussed above. We call the plane containing the collision axis and the perpendicular line to the “shortways” direction of the almond the “reaction plane” with a specific angle  $\phi_R$  with respect to the spherical polar coordinates defined with the polar axis as the collision axis. We will always work in such coordinates when discussing the immediate vicinity of the nuclei.

Following our assumption of nucleon-nucleon collision phenomena still applying to our case, we should expect that on average about half of each nucleon’s energy

is simply dumped in the region in between the two pancakes around the collision points [176]. This does not describe the real situation for cases where hard scattering occurs between two nucleons, but these processes are relatively rare. So eventually this energy dissipates in the form of many more lower energy and lower mass particles ( $\sim 90\%$  pions) streaming away. This happens on timescales much slower (*e.g.* these particles have  $\gamma_L \approx 1 - 2$  on average) than the speed at which the two collided nuclei fly away from the collision. The general approximate behavior of this deposited energy is that it expands over time in the direction of the outgoing nuclei. In Bjorken's description the expansion rate of a small volume of this energy also changes only in this direction, with a simple proportionality between the rate and the distance from the nuclear crossing point origin,  $v_{\text{expansion}} = z/t$ .

### 3.3.3 Time Evolution and Thermal Equilibrium

In reality there are a multitude of time scales that are relevant and potentially important to consider about a RHI collision. For example there is the initial time at which the two pancakes are overlapped. We could call this the true proper time  $\tau_0$ . Even though the first low-energy interactions start a hair before this, let us choose to ignore these. Immediately after  $\tau_0$ <sup>3</sup>, we are not sure what state the deposited energy is in. It may form quarks, gluons, baryon junctions, hadrons, or maybe even some other kind of “objects” we don't even know about yet. Assuming however that it forms some set of states before it forms hadrons (otherwise even the loosest definition of “QGP” will not apply<sup>4</sup>) then we must assign some finite amount of formation time  $\tau_F$  for whatever are those relevant states to “form”. It is at this point that we say that we actually have some sort of “matter”. However, this matter may not yet be in thermal equilibrium, so we can assign a separate time, the thermalization time  $\tau_{\text{Therm.}}$ , to the point at which this occurs. We can be fairly certain, just due to the sheer particle number and given the known cross sections that thermal equilibrium

---

<sup>3</sup>here we start diverging a little from Bjorken's description, being slightly more precise than his approximate description. Much of this description is discussed in [8]

<sup>4</sup>see the discussions of the Stefan Boltzmann limit in section 3.1.

must occur at least in the hadronic phase, the question is whether it occurs earlier. As we mentioned above, we also have good experimental evidence already that the hadronic phase is being thermalized for sure in RHIC  $Au + Au$  collisions. Let us bring up the two final important time scales in our  $Au + Au$  collisions and, in doing so, briefly describe this evidence.

There are three time scales important to consider about hadronization. These are the times of 1) the already discussed chemical freezeout we shall call  $\tau_{C.F.}$  and 2) *kinetic* freezeout we shall call  $\tau_{K.F.}$ . The third is simply the time it takes to form hadrons in a general collision, which therefore applies to our greater nuclear collision, but also to the many hadron-hadron collisions which occur in the thermalized *hot hadron gas* as it is called. This process may seem conceptually similar to the process of fragmentation from section 2.3.3, but here we are talking about the non-perturbative soft particle production which is assumed to be a bit shorter ( $\hbar/mass^5$ ) at least on order of  $\tau_{CF}$ .

The evidence that thermal equilibrium is being reached at least in the hadronic phase concerns  $\tau_{CF}$ . The evidence we speak of is the success of *statistical models* of hadron production [49], [106]. In this model, the grand canonical partition function 3.1 which assumes thermal equilibrium can be used to predict the abundances (the  $N$  in 3.1) of particles with a single chemical potential  $\mu$  and temperature  $T$  since each particle mass corresponds to a different energy state. By fixing  $\mu$  and  $T$  with the measurement of a single ratio of particles, all other particle ratios can be predicted. The success of these predictions has been quite phenomenal in heavy ion collisions starting even at SPS energies. This is interpreted as a sign that the particles are colliding quantum mechanically, appearing and disappearing at each collision point, and that there are large enough numbers of these collisions occurring

---

<sup>5</sup>This assumes that the picture of fragmentation which describes the appearance of a hadron as a quantum fluctuation or tunneling of a parton has things correct. [104], [28] Has this time scale ever been verified experimentally? A quick look through the literature would seem to indicate not, which is not surprising...this question is intimately linked to that of QGP formation, and as thus, one might say that RHI experiments provide the most promising laboratory for studying this question as well.

to communicate the statistical equilibrium throughout the majority of the volume. The chemical freezeout point is then the point at which the volume disperses enough (due to the Bjorken “hydrodynamic”  $v_{\text{expansion}}$  or just normal thermal expansion) that the collisions are no longer energetic enough to produce new particles. However, collisions still occur, so a thermal equilibrium still exists, now governed by a *plain* partition function without a  $\mu N$  term in the exponential. Eventually however, the expansion becomes so large that the collisions occur very infrequently so that equilibrium no longer can even be communicated properly. This is the point of kinetic freezeout,  $\tau_{\text{KF}}$ .

One the very points of our RHI studies is to try to infer the values of these timescales. For example, the success of the statistical model already gives us the confidence to make a fairly accurate estimate for  $\tau_{\text{CF}}$ . Taking into account the measured  $p_T$  of all particles, including that with the particles’ masses measures of the average particle energy  $m_T = \sqrt{p_T^2 + m^2}$ , ( $\approx 57 \text{ MeV}$  for RHIC experimentally) then we can get an uncertainty relation prediction of  $\tau_{\text{CF}} \simeq 0.35 \text{ fm}$ .

### 3.4 4-Momentum Space Evolution: The Energy Density $\epsilon$

The foremost importance of all these time scales lies in the question of at what point in the collision is the energy density  $\epsilon$  high enough such that a QGP phase could exist according to the theoretical predictions. Because of the many different possibly relevant time scales above, this involves answering the ultimate questions of what it means to “form a QGP” or to be “in the QGP phase”, topics which are currently a hotly debated subject in the field. Fortunately, however the energy density appears to be well within the QGP phase transition regime at nearly all reasonable timescales in the problem [8]. This is because if we take the longest time limit that could possibly contain a QGP,  $t \leq \tau_{\text{CF}}$ , assuming that the Bjorken expansion is approximately correct, then from the observed rapidity/multiplicity distribution of the final state hadrons one obtains an estimate for  $\epsilon$  which is well

above the previously stated  $1\text{GeV}/fm^3$  estimate from the end of section 3.1. This estimate comes from Bjorken's formula:

$$\epsilon = \frac{1}{\tau A} \frac{\langle m_T \rangle dN_{\text{hadrons}}}{dy} \quad (3.3)$$

where  $\langle m_T \rangle$  like above is observed to be  $\approx 0.5$  GeV. In  $Au + Au$  collisions, we observe about 300 charge hadrons per unit of rapidity on average. Assuming another 1/3 of the hadrons are neutral, which we will see is also confirmed by measuring the neutral pions which represent large majority of the neutrals, we get an estimate for  $\epsilon_{\text{CF}}$  of  $5\text{GeV}/fm^3$  already high enough. However this is just the average. For the highest multiplicity events, the ‘‘central’’ events corresponding to small impact parameters as mentioned in the caption for figure (3.4,  $dN/dy \sim 1000$ , so here, our estimate becomes  $\sim 15\text{GeV}/fm^3$  an order of magnitude higher than theoretically necessary. Remember also that this is quite solidly a lower limit [8].

### 3.5 QGP Signatures

How can we tell if we indeed have created the QGP? For this, a number of QGP *signatures* based on phenomenological arguments, common ‘‘bulk matter’’ expectations, and lattice calculations have been proposed. The most basic of these signatures establish that bulk matter in thermodynamic equilibrium has been created, and thus establish the necessary (but not sufficient) observations if one is to claim that the QGP was created. These signatures include expected quantities of simple particle number (degrees of freedom) and transverse energy [54], the observation of hydrodynamic flow within the constraints of models which we are confident apply to a QGP (*e.g.* [128]), or observation of a ‘‘chemical’’ equilibrium consistent with a hadronic ‘‘freeze out’’ into normal matter [49]. For the most part, these have already been established to high degree of confidence [8] (also, see section 3.3.3 below).

Other signatures are based on observations of *anomalous* behavior in the reactions, such that the state of matter created is somehow fundamentally different from normal hadronic matter, and therefore must be considered *new*, such as the QGP

would be. These are mostly modifications in particle production from scattering, such as suppression of  $J/\Psi$  production due to color disassociation in deconfined matter [93], enhancement of thermal radiation (which we shall discuss in detail in the next chapter) due to extra (partonic) degrees of freedom, and suppression of high  $p_T$  hadrons due to interactions with the plasma. These different signatures can be realized through different particle probes. As I've already alluded to, this thesis involves at least two of these types signatures through photon probes. First by reconstructing photons into  $\pi^0$  mesons, high  $p_T$  meson suppression has been observed at the highest transverse momentum yet. Second, using the  $\pi^0$  measurement as a basis for estimating non-interesting meson decay photons, direct photons have been observed and measured. Direct photons have themselves the potential to contribute to the observation of two of the signatures listed, including the high- $p_T$  suppression (by acting as a control) and the signature of enhanced thermal radiation. In addition, a newly proposed third signature could possibly be realized by studying direct photon production in RHIC collisions[89].

## Chapter 4

# QGP Signatures in $\gamma_{direct}$ and Hard $\pi^0$ Physics

The main focus of this thesis is a measurement of direct photon production, but it also includes an extension of the PHENIX  $\pi^0$  measurement to a substantially increased  $p_T$  range. Furthermore, the most significant portion of the  $\gamma_{direct}$  data is at high  $p_T$  where it's most important use is as a reference to verify binary scaling<sup>1</sup> or lack thereof. In this region observing the photon and pion behavior together will make for an interesting new way to study high  $p_T$  suppression. Indeed, because decay photons from  $\pi^0$  clutter things as a large background for the direct  $\gamma$  measurement,  $\pi^0$  and direct  $\gamma$  measurements are always intertwined. With the high pion multiplicity at RHIC, this is even more true. Therefore, in this section I will introduce the basics of experimental descriptions and observables in RHI high- $p_T$  scattering common to measurements of both particle types. Because one must first understand how one's tools work before one can reliably use those tools to make things, I will also introduce relevant information related to the either of the two measurements in standard particle physics, both separately and again in relation to each other.

---

<sup>1</sup>“binary scaling” is a shortened term for “binary-collision” scaling that, as discussed in section 4.3, is in common use in the HI field and which we shall also employ generously. The reader is asked to remember that it has a precise and well-defined meaning. Nuclear thickness scaling,  $T_{AB}$ -scaling or  $N_{collision}$  scaling are also synonyms

## 4.1 Hard Scattering and High- $p_T$ Suppression

The signature of suppression of high transverse momentum particle production exploits the success we have had with the predictive power of pQCD by working in the hard scattering regime where pQCD applies. This means that we should be able to frame nuclear and medium effects in the same pQCD language and therefore make reliable calculations of them.

Simple quantum considerations imply that because of the high  $Q^2$  involved, the actual Feynman diagram level processes occur over a very short timescale. On the other hand, the energy scales of particles participating in non-perturbative ( $\mathcal{O}(\Lambda_{QCD} \approx 10^2 \text{MeV})$ ) and thermal ( $\mathcal{O}(T \approx 10^2 \text{MeV})$ ) processes imply that these occur over comparatively much longer time scales.

This is important for three reasons. First, it means that there should not be time for the lower energy processes to affect the “point” hard scatterings. Second, assuming all processes start occurring around the same time, an assumption justified by our phenomenological description of the previous chapter, it means that these “point” scatters occur at the very beginning of the collision, and in a sense offer a snapshot of the “initial state” which is then subjected to the later evolution of the situation. Finally, since the products of hard scattering are greatly differentiated in momentum compared to the other processes, they will usually escape the bulk medium and be easily differentiated at the end of the greater ionic collision. Furthermore, as luck would have it and we shall also show in a moment, before escape, they should generally be exposed to nearly the *complete* evolution of the ionic collision. All these points together mean that hard scattering is ideal for our purposes, offering an *accessible* probe that is present during nearly the entire evolution of the medium.

## 4.2 Quantifying Medium Effects

In experimental RHI physics, we generally must start by differentiating effects seen only in  $A+A$  collisions from the physics of plain  $N-N$  collisions. Being as unspecific as possible we can refer to these as *medium effects*: included in this term would be modifications due to fact that our nucleons are contained within the nuclear structure (*nuclear effects*, sometimes referred to as *cold nuclear effects*), potentially *QGP effects*, or any other differences from what we would try to extrapolate from plain  $N+N$ . Experimentally  $p+p$  and  $p+n$ , even  $p+\bar{p}$  collisions have been studied extensively, not necessarily always at all relevant energies though, and for the most part then  $N+N$  collisions are well understood within pQCD and the Standard Model. We shall like to compare then the basic production of particles. This amounts to literally scaling up the  $p+p$  production rates by some factor  $S_F$ , in a simple ratio called  $R_{AB}$  which can be defined with the following general form

$$R_{AB} = \frac{(d\sigma_R/d^n S)_{A+A}}{S_F(d\sigma_R/d^n S)_{p+p}} \quad (4.1)$$

where  $\sigma_R$  is some general cross section defining production for some process  $R$ , *e.g.* the production of some type of particle.  $d\sigma/d^n S$  just signifies that it can be some generalized *differential* cross section of some  $n$  component differential. For our purposes we will most often be comparing the Lorentz invariant cross section  $E d\sigma/d\vec{p}$  or some integration thereof. The scaling factor  $S_F$  mostly depends on the geometrical considerations, energy scales of the produced particles, and a number of other considerations. We will motivate and derive what is expected to be the correct  $S_F$  for hard-scattering production. However, in general the choice of  $S_F$  needs verified independently with experimental data if one is to glean significance from (interesting) deviations of  $R_{AB}$ . It is here that having two very different types of such hard probes, such as both direct photons *and* QCD partons in the form of jets, two probes which should be affected by the QCD medium in radically different ways, where the possibility of learning something from high- $p_T$  particle production is made even more promising. For by comparing production of EM direct photons,

which should be hardly affected by the QCD medium, to that of jet production which as we shall see *is* expected to be affected quite noticeably, one is able to learn something about this medium even without the need of separate  $N - N$  references. Also quite fortunately, photon detection can yield access to *both* species “at once” by looking at, in addition to the photons themselves,  $\pi^0$  mesons which decay into photon pairs for the jet component. Thus we can now restate the prime intention of this thesis more specifically than before: to measure, compare, and interpret both the  $\pi^0$  spectra and the direct  $\gamma$  spectra produced at RHIC with an eye towards what they can tell us regarding the potential formation of a QGP.

## 4.3 Scaling And The $R_{AB}$

### 4.3.1 AB Scaling

In the above section, we laid out a general formula for quantifying the study of nuclear collisions through comparisons with particle physics measurements and related it to hard scattering. It should already be obvious that we will wish to observe and compare the Lorentz invariant  $p_T$  spectra of particle production as discussed in section 4.2 so there is no ambiguity about what constitutes *high*  $p_T$ . Indeed, we’ll look at *all*  $p_T$  ranges we can. But what scale factor  $S_F$  should we use in 4.1? This is the general problem of how particle production *scales* in heavy ion physics.

For hard scattering, the most basic answer turns out to be quite easy. First, we realize that we want to compare to the *null* hypothesis, that is, the hypothesis that the fact nucleons in our nuclear collisions are bound makes absolutely no difference—meaning we want to compare to an equivalent number of single N-N “collisions”. I put collisions in quotes because perhaps crossings would be the better word—hard scattering collisions are rare even when the two nucleons are headed right for each other and essentially pass right through each other. This is actually why things become easy as promised. We can rely on the fact that hard scattering events (those that produce high  $p_T$  particles) are in fact *so* rare that for an equivalent number of  $N + N$  “collisions” to our  $A + A$  collision, we expect *at most* only **one** such event

to occur. We shall explain what we mean by “equivalent” soon below. Also, more generally let us consider two different nuclei  $A + B$ . What this means is that the total probability of the hard scatter occurring in the  $A + B$  collision is simply the same as the total probability of the equivalent number of  $N + N$  “collisions”.

The equivalent number of  $N + N$  crossings/“collisions” in this case is  $AB$  by the following logic. First consider a single nucleon as nucleus  $A$  in Figure 3.4 ( $Z=A=1$ , we have a hydrogen ion). As it passes through nucleus  $B$  (containing  $B$  nucleons) it is crossing all  $B$  nucleons there,  $i = 1$  to  $B$ , some at larger impact parameters  $b_i$  than others. The sum of all events includes all *nuclear* impact parameters  $b$ , from 0 to  $\infty$ . Under the supposition that the nuclear superposition makes no difference, this therefore includes *nucleon* impact parameters  $b_i$ . Extending  $A$  to a more complex nucleus, our supposition again tells us that we only need multiply the situation  $A$  times. To put this in a formula, keeping in mind that a cross section represents such probabilities, we have:

$$\sigma_{AB}^{\text{hard}} = AB\sigma_{nn}^{\text{hard}} \quad (4.2)$$

This is a general starting point. We could even use this formula as is, ( $S_F = AB$ ) if we were only interested in looking at hard production in the inclusive sum of all heavy ion events. Things are not so simple however and our triggers are not perfect. First, in general, ion collisions with large impact parameters are hardly different from  $N$ - $N$  collisions, so in addition to the integral over all impact angles, we wish to differentiate categories of impact parameter ranges corresponding to notions of *centrality* introduced in section 3.3.1. We will define these categories formally below. Furthermore, there are a host of other considerations which come into play that make the experimental observation of the above scaling paradigm much more complicated than it might seem from the straightforward logic above. For all these reasons we need to introduce some formal concepts.

### 4.3.2 Centrality

An nuclear collision is considered *central* if it has a small impact parameter. Large impact angle, glancing collisions, are called peripheral. To quantify this concept of centrality, the RHI field has chosen to represent it fractionally, most often in percentages with 0% Central corresponding exactly to  $b = 0$  and 100% Central (“perfectly peripheral”) corresponding to  $b = \infty$ <sup>2</sup>. In fractions, the concept of centrality (at the expense of overusing a word) becomes “scaleless” in the sense that regardless of the types and sizes of nuclei, centrality classes retain their proportional overlap as in Figure 4.1. The question is how do we fractionalize this infinite range,  $b=0$  to  $\infty$ ?

The answer is by mapping everything onto probability. As long as the probability of occurrence for any of the interactions or experimental event we are interested in decreases monotonically as  $b \rightarrow \infty$ , we can simply divide ranges of  $b$  into equal swaths of probability.

One might say that how this mapping is done has two solutions—one academic and one practical, which has to do with the fact that we are not practically able to experimentally fix  $b$ . The academic definition which is the “true” definition is in terms of fractions of the total scattering probability. The practical definition is in terms the scattering probability of producing different numbers of particles. The model that is used to make a relation between the two definitions is called the Glauber model [96].

The general theory of scattering defines the cross section as the event rate (for any certain process) divided by the luminosity. The total *geometric* cross section  $\sigma_{geo}$  (also written  $\sigma_{inelastic}$  or  $\sigma_{inel}$ ) is for occurrence of *any*<sup>3</sup> detectable interaction in a scattering collision between particles and so is defined as the integral over all impact parameter values.  $d\sigma_{inel}/db$  depends on  $b$ , so we define a general centrality

---

<sup>2</sup>remember that the nuclear wave function extends to  $\infty$ ”

<sup>3</sup> “any interaction” here essentially means any “non-diffractive” *inelastic* interaction. There are other types of events, such as “diffractive” and elastic collisions, but at these energies in most experiments such as PHENIX, these either have negligible rates or are easily vetoed rendering them undetected.

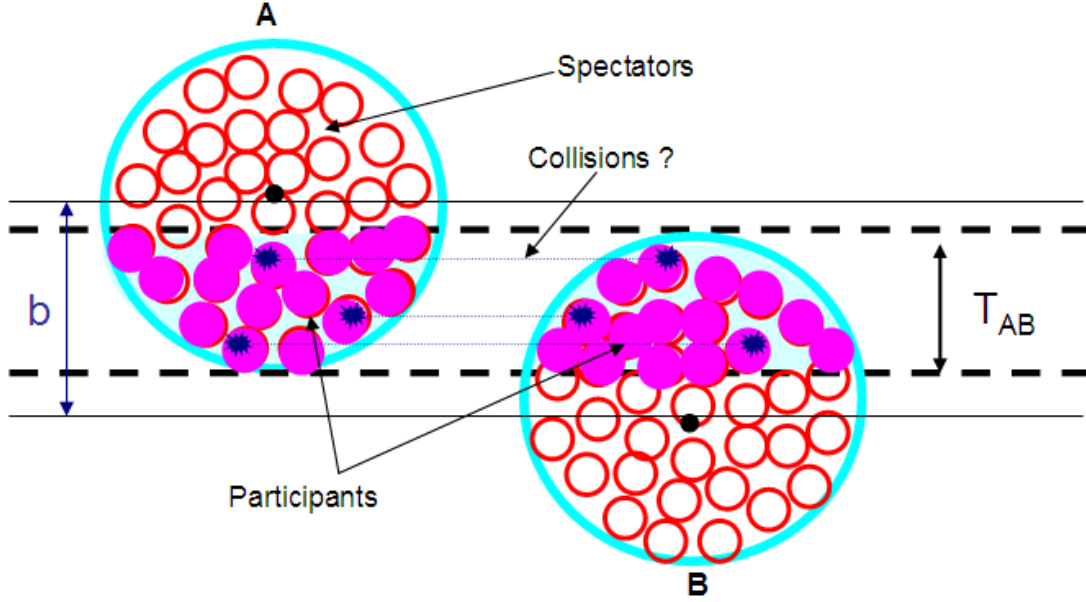


Figure 4.1: In this *semi-central* A+B event, with  $b \approx R_A(R_B)$ , the shaded overlap region corresponding to the overlap and approximately to the thickness integral  $T_{AB}$  defined below contains what are called the “participant” nucleons. All other nucleons are called *spectators*. *Binary* collisions can occur between a nucleon in A and one in B

fraction  $f$  of as the integral of  $d\sigma_{inel}/db$  between some range of  $b$ :

$$f = \frac{\sigma_f(b_{min}, b_{max})}{\sigma_{inel}^{AB}} = \frac{1}{\sigma_{inel}^{AB}} \int_{b_{min}}^{b_{max}} db \left( \frac{d\sigma_{inel}^{AB}}{db} \right) \quad (4.3)$$

For example the most central 0- $X\%$  fraction  $f_{0-X}$  has  $b_{min} = 0$  and  $b_{max}$  equals a some value of impact parameter determined by the distribution  $d\sigma/db$ . The nice thing about this definition is that theoretically it needn’t even assume anything about how a nuclear event relates to underlying nucleon-nucleon events.

Now for the practical definition, which arises from the fact that we cannot realistically fix  $b$  in experiment. Instead, what we can do in experiments is measure the number of particles produced when an interaction does occur. The Glauber Model [96], along with some other assumptions can relate  $d\sigma_{inelastic}/db$  to product particle multiplicities, so we can still use equation 4.3 as our definition. Instead of measuring the scattering probability at different values of  $b$ , we instead rely on the assumption

that on average the *multiplicity* or number of particles produced also increases with decreasing  $b$  just as  $\sigma_f(b_{min}, b_{max})$  according to the model. We shall discuss practical/experimental definitions of centrality more in section 6.1. Now we will introduce some of the basics of the more general Glauber Model, with more specific emphasis on how it describes hard-scattering production within nucleus-nucleus reactions.

### 4.3.3 The Glauber Model and Thickness Functions

In this section we will mostly rehash the explanations in [176], [164], and [79]. The Glauber model starts by defining some *thickness* functions of which there are three types.

The thickness function  $T_A$  for a general nucleus is proportional to the collapse of the 3-D wave function in the two dimensional space transverse the  $z$ -axis which will as usual be oriented  $\parallel$  to the collision axis:

$$T_A(\mathbf{b}) = \int \rho_A(r) dz \quad (4.4)$$

where  $\rho_A$  would in general have the form in section 3.3.1 like equation 3.2. This is not, however, exactly the same as the integration of the wave function, because it is just a weighting function which we can normalize to anything. In fact most authors choose to normalize it such that  $\int (T(\mathbf{b}) d\mathbf{b}) = A$  (however, this is not the normalization taken in the book by Wong [176]). In this way it represents the number of nucleons in an area  $d\mathbf{b}$ . More properly it represents the probability of finding  $1/A$  nucleons in the area element  $d\mathbf{b}$ .

Next we define an  $N - N$  thickness function  $t(b)$  which represents something different. It represents probability weighting for the occurrence of an inelastic event  $N - N$  event for a given impact parameter  $b$  where the total probability is  $\propto t(b) \sigma_{inel}^{NN}$ . As such it is most often normalized to 1. Note that  $t(b) \neq T_N(b)$ , at least not *necessarily*. With this definition we can define the *full* nuclear overlap thickness function  $T_{AB}$  for point-like interactions as

$$T_{AB}(\mathbf{b}) = \int d\mathbf{b}_A d\mathbf{b}_B T_A(\mathbf{b}_A) T_B(\mathbf{b}_B) t(\mathbf{b} - \mathbf{b}_A - \mathbf{b}_B) = \int d\mathbf{b}_A T(\mathbf{b}_A) T_B(\mathbf{b} - \mathbf{b}_A) \quad (4.5)$$

The reader will note that in the last expression, we have essentially set  $t(b) = \delta(b)$ . This is because for realistic  $t(b)$ , we can always just absorb the integral over  $t(b)$  into the definitions of  $T_A$  and, in turn, into the definitions of  $\rho_A$ . We shall discuss this ambiguity further in section 4.3.4.2 below.

Given the above normalization for  $T_A$ ,  $T_{AB}$  will then be normalized to AB, and  $db T_{AB}(b) \sigma_{hard}^{NN}$  represents the probability of having a single  $NN$  hard scattering around the impact parameter  $b$ . Referring to equation (4.2) where we are interested processes that will only in general happen a single time, it is easy to see that  $T_{AB}$  then represents the generalization of our AB scaling above and  $\int_f db T_{AB} \equiv \int_{b_{min}(f)}^{b_{max}(f)} db T_{AB}(b)$  represents the enhancement of a hard scattering cross section relative to its value in  $NN$  collisions. So we are already at the point of being able to write a more definite expression for  $R_{AB}$  for hard scattering:

$$R_{AB}^f = \frac{d\sigma_f^{AB,hard}}{\int_f d\mathbf{b} T_{AB} d\sigma_{hard}^{NN}} \quad (4.6)$$

To use equation (4.6) we still need to know how to determine our centrality fractions  $f$  from experimentally observable particle multiplicities. And as it will turn out, doing so experimentally will make it desirable to define  $R_{AB}$  in a slightly more complicated manner. However equation (4.6) does capture exactly the scaling situation we want to exploit for hard scattering. Notice that the scaling factor  $S_F$ ,  $\langle T_{AB} \rangle_f$ , [see equation 4.1] only depends on geometry and is not dependent on the cross section of the process. It therefore applies to all hard scattering processes and in fact all very rare inelastic processes.

$T_{AB}$  scaling has been verified quite solidly in hard scattering reactions involving a single nucleus. In  $l + A$  scattering where A is varied, hard production is found to be exactly proportional to A. In  $p + A$ , nearly the same result is found however there is a very small violation called the Cronin effect which will be discussed below

in section 4.4.2 and in the concluding chapter 8.

### 4.3.4 Binary and Participant Scaling

#### 4.3.4.1 Multiple Scattering and $N_{collision}$

If the scattering process is not so rare, there will in general more than one interaction likely in a single nucleus-nucleus collision. In this case, we must not consider each nucleon-nucleon pair completely independently but instead we must take into account that the nucleons are always grouped together in the nuclear superposition. The Glauber Model formalism will also allow us to determine scaling for these types of processes as well by making a *multiple-scattering* assumption. The Glauber multiple scattering assumption, well justified by experimental data [173], [176], is that even if a nucleon undergoes a collision, the cross section (that is the probability) for interactions after such collision are the same as for the initial collision. The best example of this is in the calculation of the total  $A + B$  inelastic cross section—the total probability for *any* inelastic interaction in a  $A + B$  collision. Under such an assumption the thickness function is applied with the same cross section throughout the nucleus so that  $dbT_{AB}(b)\sigma_{inel}^{NN}/AB$  represents the probability of any interaction occurring throughout the entire nucleus-nucleus crossing. As opposed to the hard scattering case, this time we must consider multiple interactions as well as single interactions in our probability. Given our  $T$  normalizations, the probability for  $N_{coll}$  interactions in an area  $d\mathbf{b}$  simply a binary probability with one factor the probability of  $N_{coll}$  collisions and one factor representing the probability of  $AB-N_{coll}$  crossings *not* resulting in a collision:

$$P(n \equiv N_{coll}, b) = \frac{1}{AB} \binom{AB}{n} [T_{AB}(b)\sigma_{inel}^{NN}/AB]^n [1 - T_{AB}(b)\sigma_{inel}^{NN}/AB]^{AB-n} \quad (4.7)$$

From this equation, we can derive several important relations. First, we go ahead and derive the Glauber Model estimate for the total  $A + B$  inelastic or geometric cross section by summing over all possible numbers of collisions:

$$\sigma_{inel}^{AB} = \sum_{N_{coll}} P(N_{coll}, b) = 1/AB [1 - T_{AB}(b)\sigma_{inel}^{NN}/AB]^{AB} \approx (1 - e^{-T_{AB}(b)\sigma_{inel}^{NN}}) \quad (4.8)$$

The exponential (Poisson) approximation in this equation is extremely accurate— which expression is used is numerically insignificant [78] and thus the exponential which is generally easier to work with is generally chosen.

#### 4.3.4.2 An Ambiguity

We mentioned that for realistic  $t(b)$  we can always just absorb the integral over  $t(b)$  into the definitions of  $T_A$  and, in turn, into the definitions of  $\rho_A$ . It should be remembered that this is what the  $\rho_X$ 's represent. Therefore one must keep in mind what kind of processes the  $\rho_X$ 's being used in various calculations were measured by, and whether these are believed to be representative of the actual density of *all* quarks and gluons in the nucleus or perhaps just the protons. Our  $\rho_A$ 's from section 3.3.1 and their exact parameters from various nuclei are determined from lower energy  $e + A$  scattering structure functions <sup>4</sup> [110], so one expects them to more likely reflect preferentially the (charged) protonic content of the nuclei and perhaps not completely the neutron content—the question of the "neutron skin". Luckily this uncertainty as high as 10% [157] is only important in very peripheral centrality bins. It also stresses the importance of being able to verify *in the same experiment* the validity of proposed scalings like  $T_{AB}$  with some control. Did we mention that this is one of the main purposes of the direct photon analysis in this thesis?

#### 4.3.4.3 Participant Scaling

The second important expression we can derive from (4.7) is the average number of collisions for a given centrality/impact parameter range  $f$  under that condition that at least one collision occurs (taking our definition from above for  $P(n, b)$ ):

---

<sup>4</sup>although the A normalization has been verified with much higher  $Q^2$  ( $\sim 8\text{GeV}^2$ ) processes. [39]

$$\langle N_{coll} \rangle_f = \int_f db \frac{\sum_{n \neq 0} n P(n, b)}{\sum_{n \neq 0} P(n, b)} = \int_f db \frac{T_{AB}(b) \sigma_{inel}^{NN}}{1 - e^{-T_{AB}(b) \sigma_{inel}^{NN}}} \cong \frac{\langle T_{AB} \rangle_f \sigma}{1 - e^{-\langle T_{AB} \rangle_f \sigma}} \quad (4.9)$$

Referring to Figure 4.1 we see the essential features of the Glauber geometry. Many features of the  $Au + Au$  collisions depend on  $\langle N_{coll} \rangle$ . Processes that scale this way, including hard processes<sup>5</sup> obey what is called “ $N_{coll}$ ” or *binary collision* or simply “binary” scaling. However, the *total* multiplicity of particles produced in the reactions does **not** follow binary scaling. This is because the vast majority of particles produced in an inelastic  $A + B$  collision are not produced by hard processes, but rather “soft” or low momentum ones. We’ve only tried to apply the Glauber model assumptions laid out thus far to relatively hard processes. For soft processes, one might expect naively that perhaps a different type of “multiple scattering” assumptions could apply, such as “single collision” scaling where only the first collision is relevant. [136]. Since soft processes in QCD are not in the regime of perturbative calculations, naively it may seem that we will be dependent on models to determine how the soft particle multiplicity scales with impact parameter.

Fortunately a large body of experimental  $p + A$  and even  $A + A$  tells us that the situation is simpler than that [120], [24]. Essentially, it is found in these results that the soft particle multiplicity scales with the number of “participating” nucleons (“participants”) shown in 4.1. This is called  $N_{part}$ -scaling or *Wounded Nucleon* scaling. The easiest way to understand this is to look in the Lorentz frame where one of the colliding particles is at rest. In that frame, the incoming projectile is moving so fast, that it simply does not have time to react (*i.e.* change) justifying the Glauber multiple scattering argument, and thus will soft-produce with each nucleon in the at rest target it encounters— $N_{participant}$ . Another more naive explanation of  $N_{part}$  scaling is that one expects the soft particle production to be proportional to the amount of energy deposited in the overlap region of the two nuclei. In terms of

---

<sup>5</sup>for hard processes we keep the zero in the sums which makes  $\langle N'_{coll} \rangle \cong T_{AB}(b) \sigma$ . Apparently hard scattering follows a different  $N_{coll}$  scaling. This other scaling is in fact what we are calling the AB scaling.

the thickness functions we have defined, since the probability for soft interactions is extremely high ([175] and see below), the number of participants,  $N_{part}$  is

$$\langle N_{part} \rangle_f = \int_f db (T_A(b) + T_B(b)) \quad (4.10)$$

Integrating over all impact parameters then,  $N_{part} = A + B$ .

Most models of particle production in high energy nuclear collisions [167] assume that the production at low  $p_T$  is proportional to  $N_{part}$  raised to some power  $\sim 1$ . An exception is HIJING [166], which is currently probably the widest used the best event generator for complex high-energy nuclear scattering situations. HIJING assumes higher  $p_T$  jet and minijet production proportional to  $N_{coll}$ , but is tuned such that  $N_{part}$ -scaling is implicitly obtained in the soft sector.

Whatever it scales with, the average multiplicity of soft particles either per  $N_{coll}$  or per  $N_{part}$  is in general of order unity. In an average  $Au + Au$  collision,  $\langle N_{coll} \rangle_f$  gets as high as  $\sim 1000$  in very central events and  $\langle N_{part} \rangle_f$  as high as  $\sim 350$ . A scale that ranges from 0 to hundreds of particles makes a very fine grained experimental centrality measure. Therefore as we will discuss in more detail in section 6.1. the way we experimentally determine our centrality for a sample of events is based on its average particle multiplicity. This in turn can be related back to  $\langle N_{part} \rangle_f$ ,  $\langle N_{coll} \rangle_f$  or  $\langle T_{AB} \rangle_f$  for that sample. Of course individual events are subject to fluctuations in  $N_{coll}$  and particle multiplicity, and even  $N_{part}$ .<sup>6</sup> For this reason, especially the fluctuations in  $N_{part}$  as well as the ability to flexibly study effects such as experimental biases, Monte Carlo (MC) simulations which model the numbers of nucleons, and probabilistically determine their position and numbers of collisions are generally superior to the analytic, geometric calculations we've used to define all the quantities in this section. The MC PHENIX uses to make these calculations is also explained in detail in 6.1.

---

<sup>6</sup>remember that  $\rho_A(\vec{x})$  on which  $T_A$  in 4.10 is based is a quantum weight according to which *on average* the nucleons are distribute themselves over space. In each individual collision, the nucleons take a random position according to this distribution.

### 4.3.5 Experimental $R_{AB}$ : $T_{AB}$ or $N_{coll}$ ?

We've already given two formulas for  $R_{AB}$ . Given ideal experimental circumstances we could use formula 4.6.  $T_{AB}$ , a seemingly purely “geometrical” quantity is the scale factor we want. However, usually the term “binary scaling” or “ $N_{coll}$  scaling” is used over “thickness scaling” and, as we have shown, (see footnote 5) the two scalings are not necessarily the same. While we wouldn't presume to provide a full explanation for this ambiguity in the common language here, the reasons most likely have to do with the limits imposed by experiment.

There are two main experimental difficulties to overcome in making comparisons via the  $R_{AB}$  quantity. First, there is the issue of centrality determination via number of charge particles per event. This is complicated by the fact that every experiment has a finite acceptance and efficiency so that measuring *all* particle products is impossible. However as it turns out, things are not so sensitive to this problem and we can be reasonably confident that we understand it, reflecting the relatively small systematic errors on our scaling calculations discussed in section 6.1.

The second difficulty is unavoidable given the experimental reality of measuring centrality via the products of the collisions: a collision must happen for the event to register at all, so all the probabilities we considered must properly take into account this bias. This is why we don't include the zeros in the sum in equation 4.9. This bias will make it desirable to use the following formula for  $R_{AB}$  in preference to 4.6 for a general hard process  $X$ :

$$R_{AB}^f = \frac{dN_f^{AB,X}/N_f^{events}}{\langle T_{AB} \rangle_f d\sigma_{hard}^{NN}} = \frac{dN_f^{AB,X}/N_f^{events}}{(\langle N_{coll} \rangle_f / \sigma_{inel}^{NN}) d\sigma_X^{NN}} \quad (4.11)$$

The reason this formula is preferable is because experimentally we can't *measure* the  $A+B$  luminosity of for a set fraction  $f$ , but rather only the number of events that occurred in that centrality bin. Although this is the normal form for an invariant cross section normalized to the total cross section, the way to view it in this case is that we are averaging  $dN_X$  over the relevant fraction of the total cross section since  $dN_X^{AB}/N^{events} = d\sigma_X^{AB}/\sigma_{inel}^{AB}$ . Therefore we are forced to correspondingly average

$T_{AB}$  over the centrality fraction, *i.e.* divide again by the total cross section fraction, which gives our definition of  $\langle T_{AB} \rangle_f$ :

$$\langle T_{AB} \rangle_f = \frac{\int_f db T_{AB}}{\int_f db \left(1 - e^{T_{AB}(b)\sigma_{inel}^{NN}}\right)} \quad (4.12)$$

With this definition, and combining (4.9) as equation (4.11) shows  $\langle N_{coll} \rangle_f / \sigma_{inel}^{NN} = \langle T_{AB} \rangle_f$ , so it turns out that our scaling factor  $S_F$  has turned out to be proportional to both what is commonly called  $N_{coll}$  and also  $T_{AB}$ . To make things more confusing, usually the  $\langle \rangle$ 's are not usually used for  $\langle N_{coll} \rangle$ . Both terminologies would then seem acceptable. It should be kept in mind however that fundamentally the hard cross section scaling factor itself is the purely geometric  $T_{AB}$ : In an average  $Au + Au$  event, as we will show in 6.1, (the average) number of collisions,  $N_{coll}$ , is 200. But the factor by which hard production is increased in  $Au + Au$  compared to the same luminosity for  $p + p$  is  $\int T_{AB} = AB = 197^2 \cong 40000!$

## 4.4 The Baseline: Review of Hard Scattering in Particle Physics

The history of “high  $p_T$ ” (although not necessarily what we would call “hard scattering”) hadron, meson and baryon, production studies is basically the history of particle physics itself. With the BNL Cosmotron’s discoveries of a zoo of particles, the cataloging of production of the various assorted particle species began, including the relatively late discovery of the neutral  $\pi^0$  [142] in 1950 by Jack Steinberger’s group, the very same type of studies we use now in our studies of high  $p_T$  suppression. Not too long after the discovery of jets in 1982, the shift in particle physics moved away to the measurement of inclusive spectra, indeed current Tevatron experiments at the highest world energy don’t even bother measuring inclusive meson spectra, instead concentrating on full jet reconstruction. This is natural since the basic physics that these particle physicist’s are trying to probe depends on the behavior of the whole jet and need not be clouded by details of fragmentation encoded

in the inclusive hadron spectra themselves. Since inclusive leading particle spectra are what we are presenting in this thesis our review will focus on these and issues surrounding them.

On the other hand, inclusive single prompt photon production remains a hot topic of measurement even at the highest energies, since with less complication from fragmentation issues, it offers the ability to more precisely test perturbative QCD. Even though as we shall see, the precision offered by the cleaner physical process is somewhat offset by experimental imprecision due to many difficulties in making the photon measurements, direct  $\gamma$ 's have been able to help to both provide evidence that confirms pQCD as the right theory of parton with their confinement and also push the envelope of theoretical calculations by pointing out many of their shortcomings.

#### 4.4.1 The Basics: $p_T$ $x_T$ Scaling, *Etc.*

It's easiest to study an interaction in a region where its relative effects are large, hence the desire to study large angle scattering where the transverse momentum  $p_T$  or  $m_T = \sqrt{p_T^2 + m^2}$  quantifies the amount of scattered (as opposed to input) momentum. For small momentum transfer processes at mid-rapidity, as we've already stated in our discussions of the general properties of HI collisions, the soft particle production,  $dn/dm_T$ , for  $p_T < \sim 5$  GeV/c obeys a Boltzmann-like functional form,  $e^{-6m_T}$ , universally for any  $\sqrt{s}$  at "high energy". Things are found to be different as higher  $Q^2$  hard processes are probed with higher  $p_T$  reach however, and this universality is found to be broken.

We could say "true" hard scattering experimental studies started at the CERN ISR in the 1970's, apparently soon after the basics of the quark and parton models were laid out by Gell-Mann, Bjorken, Feynman and others, but before QCD was fully accepted. The ISR ran at  $\sqrt{s}$  energies around 10-60 GeV, so we might take this as the minimum energies in which serious hard scattering studies are possible. During this period and following at later machines like the SppS, and Fermilab, different

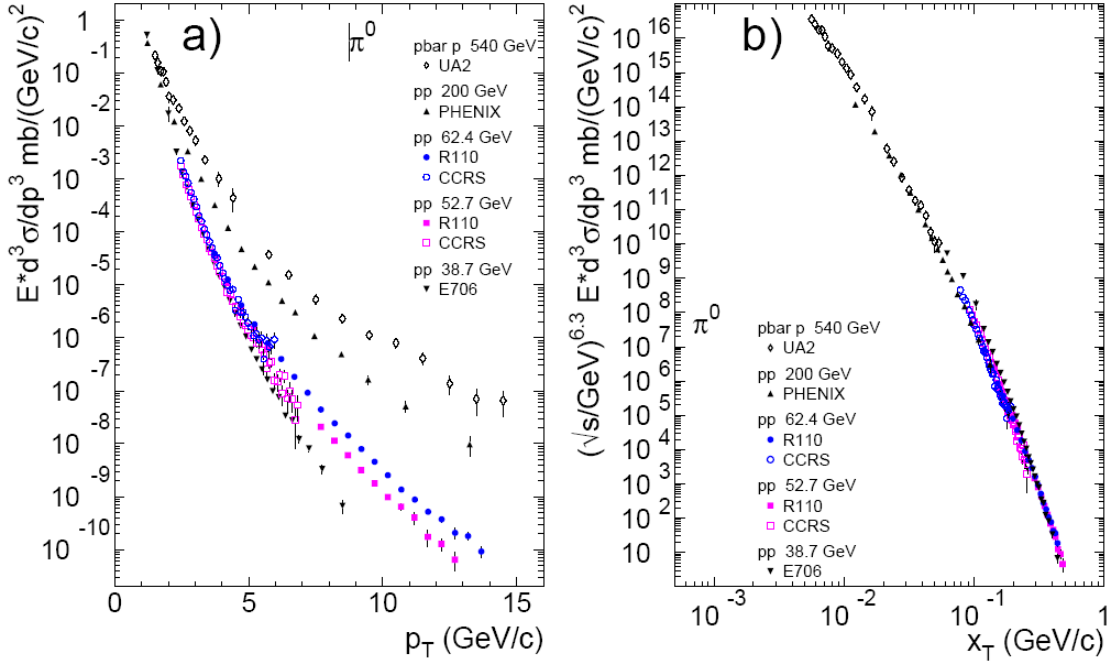


Figure 4.2:  $\pi^0$  Production vs.  $\sqrt{s}$  and  $p_T$  (a),  $x_T$  (b). figure from [118].

hadron species were measured at increasingly higher energies and  $p_T$ . A good way to summarize all these various measurements over several orders of magnitude in  $\sqrt{s}$  is through the principle of  $x_T$  scaling [52], [26]. In a more general description of hadron collisions called the *parton model*, Bjorken, Feynman, et. al. theorized about the behavior of very unspecific “parton” (as opposed to specific particles like quarks or gluons) which carried some fraction of its parent hadron’s momentum  $x$ . In his seminal paper [53] Bjorken proposed that the structure functions would scale with  $x$  due to the fact that the colliding partons were essentially free particles themselves. In turn, this  $x$  dependence for two colliding partons can be directly translated [8] into a scaling by the quantity  $x_T = 2p_T/\sqrt{s}$ —the scaling can also be derived through sheer dimensional arguments [140]—which is found to be the proper scaling variable.

An example of all these points is summarized in Figure 4.2 for  $\pi^0$  production across many different years and experiments. The functional form of the scaling naturally follows the following relation [52], [26]

$$E \frac{d\sigma}{d^3p_T} = 1/p_T^n F(x_T) = 1/\sqrt{s}^n G(x_T) \quad (4.13)$$

where  $n$  also depends on both  $p_T$  and  $\sqrt{s}$ . As demonstrated in the figure,  $G(x_T)$  is an approximately linear function on log-log axes with slope 8.4 and the deviations from this line (which is actually where the apparent curvature is coming from) in the figure are the low  $p_T$  Boltzmann exponential description becoming more important. Note that this figure includes our PHENIX  $p + p \pi^0$  measurement. The parameter  $n$  in 4.13 is slowly varying between 5 and 8, (in the figure  $n = 6.3$  gives the best description) which is mostly determined and predicted by general quantum field theory considerations of the interaction propagator's spin. For a gluon  $n$  should be 4, but refinements due to higher order/non-perturbative corrections cause the additional rise in  $n$ .

As we mentioned the “modern” study of hard scattering production of hadrons in particle physics is mostly the study of the full jet. Fragmentation functions are nailed down in  $e^+e^-$  experiments, the natural choice since things are not clouded by any incoming PDF. Such fragmentation studies have been performed in nearly every shape and form, and the properties, such as composition, of jets have been meticulously cataloged and used to constrain QCD. The jets themselves are identified on an event by event basis in full acceptance detectors by identifying groups of high energy particles with *jet finding algorithms*. The specific algorithms, which are very robust, introduce their own systematics into the measurements, but these are far outweighed by the cleaner physics interpretation without fragmentation [132], [134]. On the other hand, the rarity of heavy quark hadrons which are also produced by hard scattering makes basic leading particle measurements of these still interesting and necessary.

The story has a different beginning for high energy photons. Although photon detection had been around since the early days of particle physics, its purpose was to detect decay photons from other particles. This was the only known non-negligible source of photons with energies above a few hundred MeV/c until the discovery of

direct photons in the mid 1970's. Direct Photons were first proposed to explain an enhanced yield of direct leptons<sup>7</sup>. This allowed Farrar and Frautschi in 1975 [82] to guess their existence, though somewhat incorrectly attributing them to some sort of enhanced unknown Bremsstrahlung but they were more fully explained in 1977 by Minkowski and Fritzsche [90] and 1978 by Krawczyk and Ochs [130] after their understanding in QCD reactions had developed somewhat. Henceforth direct photon measurements were performed across at all hadron-hadron energy ranges, and have even been performed at  $e^+e^-$  and  $ep$  colliders where they allow some of the most precise tests of QCD yet.

Since  $\gamma_{direct}$  production depends on the same inputs from the parton model and pQCD, the exact same same type of  $x_T$  scaling at high  $p_T$  works as shown in Figure 4.3. This time taking  $n = 4$  does a much better job, as expected due to less sensitivity to the same effects which raise  $n$  for mesons discussed above, this being because there is one less power of  $\alpha_S$  and no fragmentation function [140]. However, some rise in  $n$  should be expected, and probably using somewhat higher values would even improve the scaling behavior in the figure somewhat. Again we find a  $G(p_T)$  that would be linear on a log-log plot, (demonstrated by the small fit function shown on the figure) this time with a slope of 5.8 instead of 8.4.

#### 4.4.1.1 Difficulties

Careful examination of the disagreements with the scaling expectation in 4.3 reveal that the deviations are actually within datasets from the same  $\sqrt{s}$  ranges, and in fact many times although not visible on the plot, the very same  $\sqrt{s}$ . This is an important message that must be interpreted about direct photon measurements. They have been fraught with difficulty especially in the earliest days. In Figure 4.4 taken from [144], we show data from four experiments all taken at the same  $\sqrt{s}$  energy of 19.4 GeV Some of the order of magnitude differences in the results, shape and normalization, may be attributable to the fact that some of the data in the figure is somewhat "older", relatively speaking, and many advances in calorimetry

---

<sup>7</sup>but this was not in fact the correct explanation of the direct leptons [172]

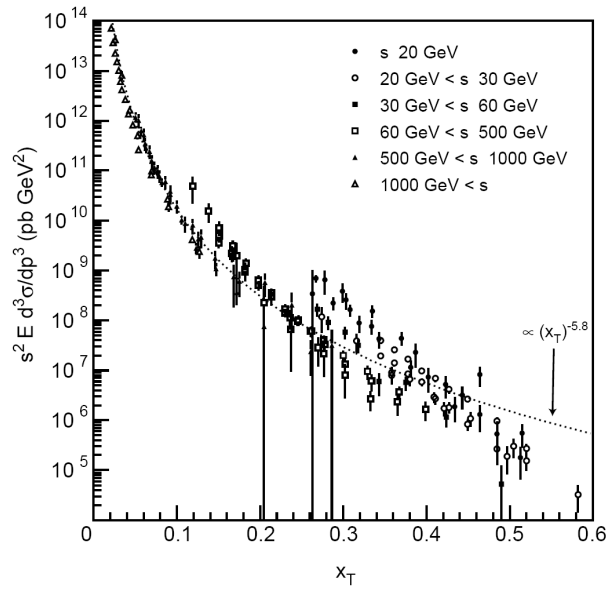


Figure 4.3: Direct  $\gamma$  Production vs.  $\sqrt{s}$  and  $x_T$ . figure from [144]

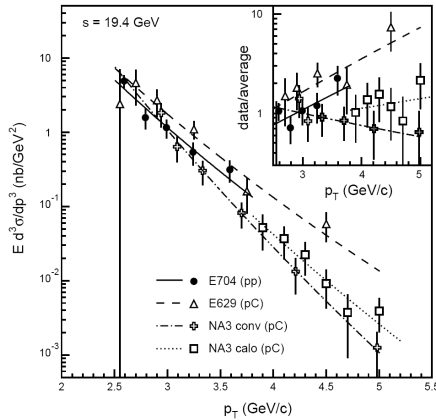


Figure 4.4: Disagreements between various  $\gamma_{direct}$  data sets at  $\sqrt{s}19.4$  GeV. figure taken from [144].

and other technologies have been made since—however even in the most state of the art Tevatron data of the past years 50-100% disagreements in normalization could be found between the competing D0 and CDF experiments [55].

Such disagreements (and therefore the identification of where the difficulties arise)

are commonly attributed to the worse energy resolution (and therefore scale uncertainties) relative to tracking for EM calorimeters, the smallness of the signal at low  $Q^2$  relative to decay photons from meson decay, and for the very highest energy experiments, the inability to distinguish on a cluster by cluster basis photons from two merged photons from a highly boosted  $\pi^0$ . In many of these respects, the RHIC energy of 200 GeV offers a window that that may lie in a "sweet spot" region for direct photon measurements, since accessible  $x_T$  ranges are where the signal to background is relatively high, giving confidence in statistical methods such as the ones we shall employ as described later in the analysis section (6.5), but still at low enough  $p_T$  that  $\pi^0$ 's are easily separated with reasonable modern calorimeter segmentation. We also note that 200 GeV also lies smack in the middle of a glaring gap in  $\sqrt{s}$  where direct photon measurements have not been made yet: there is an order of magnitude between the high end of the lower energy measurements at  $\sqrt{s}$  63 GeV (incidentally among the very first direct photon measurements) taken at the ISR and the higher energy CERN [25] / Fermilab "reduced energy" data at  $\sim$  500 GeV [180],[133].

#### 4.4.1.2 The Ratio $\gamma_{direct}/\pi^0$

Due to some of the difficulties cited in the last paragraph with  $\gamma_{direct}$  measurements, a helpful ratio to look at and preferably use to make physics statements where possible is the ratio of  $\gamma_{direct}$  production at a given transverse momentum to that of  $\pi^0$ . First, this ratio gives a very good handle on the signal to background level, since decay photons from  $\pi^0$  are the dominant background source. Second, many systematics cancel in this ratio since both particle measurements use the same photon calorimetry. For example the nearly factor of 10 differences between the two measurements at  $p_T > 3.5$  GeV/c in 4.4 are reduced to only a factor of  $\sim 2$  when  $\gamma_{direct}/\pi^0$  is compared.

Of course the ratio  $\gamma_{direct}/\gamma_{\pi^0 decay}$  would be even more direct, but this is easily converted mentally if one remembers the formula  $\gamma_{\pi^0 decay}/\pi^0 = 2/(m - 1)$  where  $m$  is the power law "slope" on our  $x_T$  scaling plots above, shown there to be  $\simeq$

8.4. The  $1/(m - 1)$  comes from one integration of that “source” power law shape necessary to obtain the distribution of decay photons—so to good approximation  $\gamma/\pi^0 = (8.4 - 1)/2 \times \gamma/\gamma_{decay} \approx 3 \times S/B$ .

The behavior of  $\gamma_{direct}/\pi^0$  becomes even more important and interesting in the context of *both* of the two QGP signatures we are after in this thesis. The already measured suppression (which we will show new data on) of the (meson)  $\pi^0$  will enhance this ratio to levels never before observed at these  $x_T$  values—a brand new phenomena, that would represent a way to quantify this signature without need of any  $N + N$  reference data. This effect will combine with other potential enhancements from the QGP in  $\gamma_{direct}$  including thermal and Jet-Plasma radiation (see section 4.7 below) driving the ratio yet even higher.

#### 4.4.2 Nuclear Effects

In high energy particle physics, one might say nuclear effects were discovered by accident. Using nuclei in fixed target experiments is convenient as the high density of heavy elements provides googles more effective luminosity than colliders. Of course, at very low  $p_T$  (the soft regime), the uncalculable nature of confinement-type effects allowed for just about anything to happen, but it was surprising when the high  $p_T$  production was found not follow the  $AB$  (in  $p + A$ , plain  $A$ ) scaling described in the previous sections (4.3). In the end both the high  $p_T$  and low  $p_T$  behavior are able to be explained, at least phenomenologically. For high  $p_T$ , we shall find that such deviations are fairly small in comparison to the expected QGP effects like suppression that we shall be looking for, however they still do play a role, so we must describe what is known about them. In the following sections we shall try to relate different scaling behaviors and nuclear effects to how they will be exhibited in our nuclear modification factor,  $R_{AA}$ .

#### 4.4.2.1 Low $p_T$ : $N_{participant}$ Revisited

For completeness we review that at low  $p_T$ , our nuclear modification factor  $R_{AA}$  is expected to be  $< 1$ . As we've already described in our discussions of the evolution of a RHI collision, and in detail above in 4.3.4, the low  $p_T$ , or more generally, the low momentum transfer  $Q^2$  (and therefore uncalculable within pQCD) the processes are known to also follow a scaling linear in the individual nuclei's  $T_A$  geometric thicknesses rather than the quadratic dependence of  $T_{AA}$ . This  $N_{participant}$ -scaling also applies to  $p + A$ . Due to this linear behavior, if we make  $R_{AA}$  in the low  $p_T$  region for either  $p + A$  or  $A + A$  we find that it is well below 1.

#### 4.4.2.2 High $Q^2$ : Cronin Enhancement, Shadowing, *Etc.*

Modifications from binary scaling for high  $p_T$  or high  $Q^2$  processes due to the nucleus can make  $R_{AA}$  deviate from 1 in both directions. The clearest example for our purposes of such a deviation is called the Cronin effect, first discovered in the mid 1970's ([31]). This effect, shown schematically in Figure 4.5 *a*), is an peaked enhancement starting just after the low  $p_T$  region and slowly going away back down to 1 asymptotically, the  $p_T$  borders of its shape characteristics changing with  $A$  and  $\sqrt{s}$ . Many other nuclear effects in hard scattering have been observed besides the Cronin effect as in Figure 4.5 *b*) [40]. More commonly these effects are displayed in terms of the variable  $x$  as ratios of the more cross section structure functions, as in the figure. But these enhancements are easy to translate since the scattering structure function are simply related to our PDF's  $G(x, Q^2)$  from formula 2.11, as  $F_2 = \sum_i e_i^2 x G_i(x, Q^2)$ . Such data will definitely play a role in the story at RHIC because whatever nuclear effects we wish to include any theoretical descriptions of  $p + A$  or  $A + A$  must be constrained by this experimental data, and most importantly/conversely the theoretical explanations of this data will lend insight into ways to account theoretically for any observed  $R_{AA}$  deviations we see.

Nuclear effects in comparison with LO pQCD expectations are understood as being limitations in the zeroth order factorization ansatz. For example, factorization

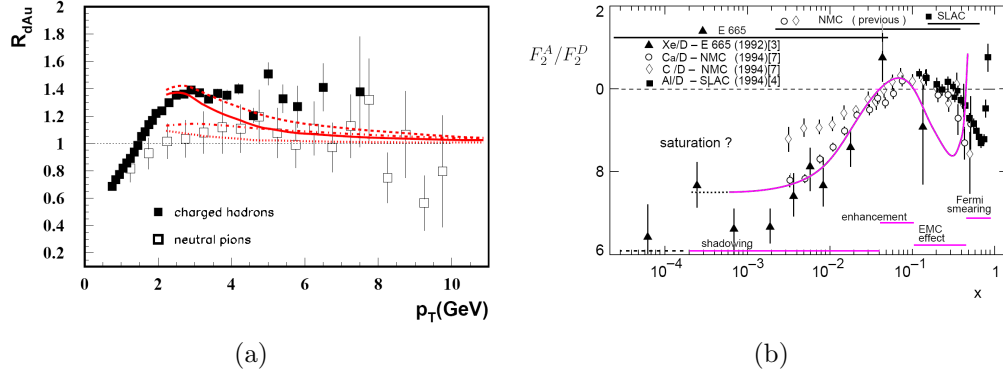


Figure 4.5: a) The Cronin effect as measured by PHENIX in d+Au reactions along with theoretical predictions b) Ratio of  $F_2$  scattering structure functions for various nuclei over deuterium. In both cases, deuterium is used as stand-in for proton, since deuterium is a very loosely bound and isospin symmetric.

assumes that the parton is completely static with respect to the parent hadron, since we always define our z-axis according to this hadrons' incoming momentum,  $\hat{p}_{hadron} = \hat{z}$  and therefore the child parton's momentum must also have  $\hat{p}_{parton} = x\hat{p}_{hadron} = \hat{z}$ — in other words there is no room for the the parton to move around transversely inside the hadron. As we shall show in a moment, that there is plenty of evidence that this assumption causes problems even with  $p + p$  factorization calculations. Of course this could be absorbed into the structure functions.

There are several current ways theorists generate a Cronin effect within factorization calculations [4]. The first most obvious way is to directly introduce an amount of intrinsic transverse momentum called nuclear  $k_T$  smearing for each parton. The  $k_T$  distribution is assumed to follow a gaussian as with most “smearing” endeavors, of the form

$$f(k_T) = K_n e^{k_T^2 / \langle k_T^2 \rangle} \quad (4.14)$$

which is applied by convoluting the normal PDF's (*e.g.* in equation 2.11 by this function [74]. In equation 4.14,  $K_n$  is a normalization constant.

More sophisticated ways in which Cronin is accounted for is through other more complicated modifications of the PDF which also naturally take into account various

other of the nuclear modifications shown in Figure 4.5 b) such as shadowing. For example in the *color dipole* or Generalized Vector Meson Dominance (GVMD) models [129], [56] the PDF is given an additional functional dependence factor  $dN/dk_T$  factor, not convoluted as in the  $k_T$  smearing case.  $dN/dk_T$  contains factors that also account for shadowing.

Shadowing itself is interpreted phenomenologically as a reduction in the magnitude of the parton or nucleon wave functions as the nucleus is traversed by an incoming probe due to destructive interference (as if the front face of the nucleus is shadowing the back face, hence the name) which then get translated into the PDF. As with any quantum interference effect, the net result can also be constructive, leading to the so called antishadowing. Despite many models like the color dipole example which can be successful across large portion of the world’s data, pure data driven parameterizations just as in the case of regular PDF’s are quite often resorted to, such as is EKS [77].

Finally we mention that the nucleons themselves can have further transverse momentum with respect to the nuclear center of mass this is usually referred to as “Fermi motion” enhancement and can cause an modifications in regions of large  $x$ .

### 4.4.3 The $k_T$ Smearing Debate

The oversimplification of  $k_T$  in factorization which leads to the Cronin effect in nuclei, can be viewed in another way which makes it clearer that it might also be an issue even in  $p + p$  collisions. In fact, the higher order scattering processes (e.g. higher order Feynman diagrams) are in fact conceptually the same as the resolving of a substructure in the parton scattering, where by the LO parton is actually multiply scattering and radiating soft gluons “before” (called initial state radiation–ISR) and “after” (final SR–FSR) the “main” diagram process. This causes the  $x$  and  $Q^2$  evolution of PDF’s and therefore structure functions to be altered, and the confirmation of such “scaling violations” was one of the early successes of QCD [111]. However, despite some success at *resummation* techniques [68], [66] “fully” accurate

all order pQCD calculation or approximations that would account for all ISR/FSR effects in  $\gamma_{direct}$  production have still not been accomplished either at all or in a way that is successful at all energies. One way to compensate for this problem is just as above we were able to explain nuclear substructure modifications by introducing additional  $k_T$  for partons, is to introduce the exact same type of phenomenological  $k_T$  smearing as in 4.14 into the hadron-hadron pQCD factorization too.

It is in fact soft gluon FSR/ISR which is known to add potentially significant effects to steeply falling cross section calculations. It should be noted that such shortcomings were recognized early on, e.g. in the seminal review by Owens in 1987 [140] and continually studied [47]. Nonetheless, in the late 1990's when inclusive direct photon and  $\pi^0$  production was revisited at large  $x_T$  by the E706 collaboration, extremely large disagreements with NLO pQCD [181] generated quite a stir which many would refer to as the "  $k_T$  smearing debate" since E706 was able to explain their disagreements with our by now familiar  $k_T$  method. Fingers were pointed in both directions, many experimentalists seemed to imply that perhaps QCD wasn't even the right theory, and theorists claimed that E706 was just making large systematic mistakes not accounted for in their published errors. Both of these viewpoints are unjustified however. First of all, in the many intervening years between E706 inclusive  $\pi^0$  results and earlier inclusive hadron measurements, QCD has had spectacular performance in predicting many non-intuitive properties of jet-jet, jet- $\gamma_{direct}$ , and  $\gamma - \gamma$  correlations in a wide variety of exclusive processes in both  $h + h$  collisions but also in precision  $e^+e^-$  LEP measurements and  $ep$  measurements at HERA. Implications that QCD isn't working are not justified. Equally unjustified is the claim that the E706 discrepancies are unbelievable given the level of agreement with pQCD of other experiments. This is demonstrated the following figures, 4.6 and 4.7. Since the E706 measurements *e.g.* [27], [50] were performed with more recent event generators, technology, methodology and much better statistics than ever before, we should probably even give them more weight. It should be noted however that the E706 measurements are fixed target  $p + A$ , but  $A$  is very small (*e.g.*

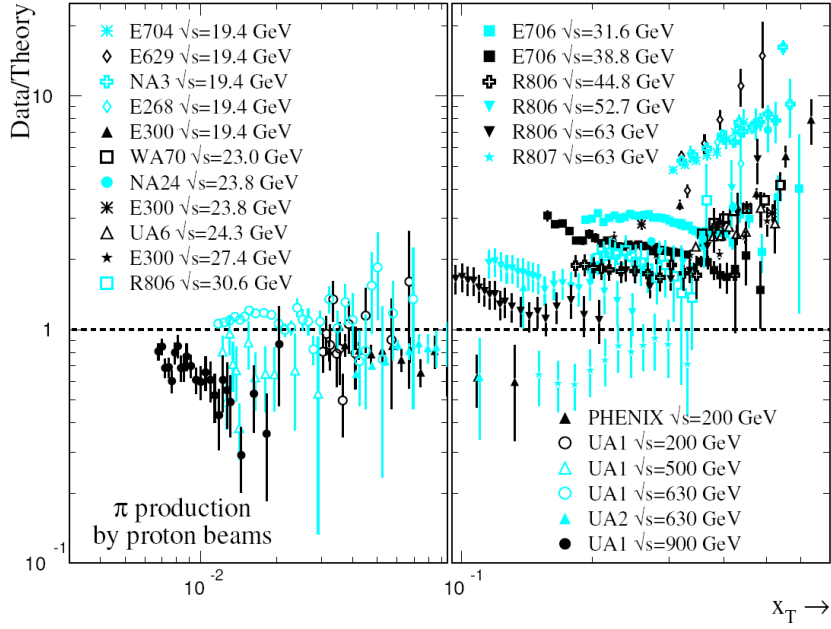


Figure 4.6: Disagreements between world’s inclusive pion data and NLO QCD. figure taken from [33]. Note that the initial data from PHENIX Run2 is included.

Be) and the miniscule expected nuclear effects have been corrected for. Nonetheless, some authors [177] have attributed some amount of the E706 disagreement to this source.

Part of the debate has also been about E706’s stressing of the  $k_T$  smearing phenomenological model as a way to improve the pQCD agreement. Although their  $k_T$  smearing methods are based on calculations from such prominent QCD theorists as J.E. Owens himself and Qiu, some question the usefulness of framing the question in terms of a new tunable parameter. [42]. Indeed, large differences in the NLO calculations can be generated within the factorization framework, without resorting to explicit inclusion of parton  $k_T$ : e.g. certain PDF choices can yield predictions that match the world’s data in this sector much better, at the expense of worsened agreement in other measurement sectors [95]. Also Vogelsang et.al. have shown that quite large changes can be generated by choosing non-equal, factorization, fragmentation, and renormalization scales [68]. It is not clear how this is any better than  $k_T$  smearing, for at least the  $k_T$  model tries to prescribe a way to at least

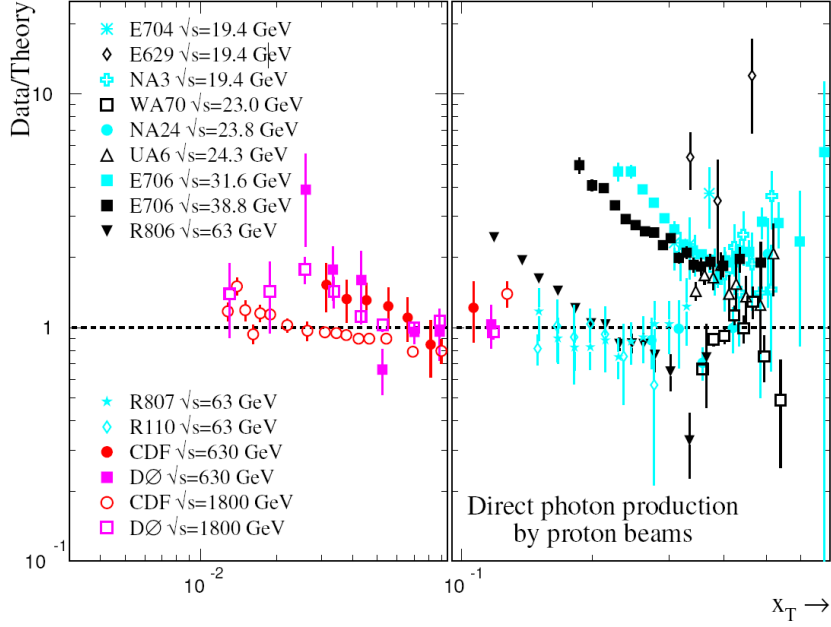


Figure 4.7: Disagreements between world’s inclusive  $\gamma_{direct}$  data and NLO QCD figure taken from [33].

”guestimate” expected disagreements.

Thus, the most important implication of this debate for us is that it puts doubt in the predictive power of pQCD in making inclusive spectra predictions. When  $p + p$  reference data exists, it hardly matters for our  $Au + Au$  data comparisons like  $R_{AA}$ . This is the case for our  $\pi^0$  measurements. But in the absence of having a  $p + p$  reference for direct photons at 200 GeV to compare our  $Au + Au$  direct photon measurements with, we should like to turn to pQCD. We shall find however that alas, the doubts raised in the  $k_T$  smearing debate must lead us to conclude that it is imprudent to do so at a quantitative level (see section 8.3 of the conclusions).

## 4.5 The Mechanism of High $p_T$ Suppression in the QGP

### 4.5.1 Gluon Radiation

As the energetic partons which are products of hard scattering move through the bulk matter created in the nuclear collision, they lose energy to the surrounding environment similar to the way charge particles lose energy through electromagnetic interactions with electrons and nuclei when passing through normal matter. In the case of these quarks and gluons however going through a QGP the most important microscopic process by which this energy loss proceeds is through gluon Bremsstrahlung radiation induced by the static gluon fields arranged with a particular (*e.g.* plasma) screening configuration [46]. In low enough ranges of energy for the radiated gluon, the Landau Pomerancuk-Migdal (LPM) effect is important and therefore must be included in the calculations. LPM occurs when the characteristic formation length ( $1/\Delta p$ ) of the gluon that is to be radiated becomes large enough that several gluon scattering centers in the medium can act coherently to destructively (or sometimes constructively!) interfere in the Bremsstrahlung process [168]. A similar process has been observed in QED Bremsstrahlung loss. A unique feature of QCD Bremsstrahlung, however is that this, other quantum interferences, and the fact that the radiated gluon interacts with the other gluons making up the color fields, lead to an energy loss (denoted ubiquitously as  $\Delta E$ ) per unit length that is proportional to the length the moving parton traverses in the medium, that is  $\Delta E \propto L^2$

We shall discuss three different approaches to quantifying the gluon radiative losses in the plasma. In all cases, the energy loss is realized as modification to normal jet fragmentation, although in some approaches this is made more explicit than in others. This is natural since the Bremsstrahlung processes, just as in the case of Bremsstrahlung direct photons discussed above, are higher order processes and are most naturally absorbed in the FF. Also, since vacuum effects are still assumed

to be present, the normal NLO Bremsstrahlung induced by the parton's own field must be included and this is most naturally done in terms of the normal parton to gluon FF. In order to calculate estimate the modified fragmentation function, different models of the energy loss itself are available.

The most basic initial attempts at modeling the parton energy loss were done with HIJING [166] where simple gluon splitting algorithms were employed to modify the parton fragmentation and effect the energy loss. The early work of Wang and Gyulassy (GW) for incorporating LPM followed the original work of Landau [168], and this idea was expanded upon by many authors. The approach taken by the BDPMS group [169], valid for asymptotic parton energies, starts by calculating an energy spectrum for emitted gluons  $dI/d\omega$  from a single scattering directly from, and as usual in such calculations [114], proportional to an effective current  $J$  squared. LPM is implemented by summing the products from  $N$  scatterings and including a quantum interference term  $e^{i\omega}$  for each scattering. This is a common way to account for the effect. BDPMS does not include any other nuclear effects such as Cronin and results in an energy loss that is approximately constant ( $\propto \log E$ ) causing a high  $p_T$  suppression pattern which diminishes with increasing  $p_T$ . As we shall see, this disagrees with suppression behavior at RHIC in the range that has been measured so far, but this prediction was not intended to be used in that region.

Perhaps the most successful model of high suppression models at RHIC have been the GLV model of Gyulassy, Levai, and Vitev. This model employs an operator product formalism in which a probability amplitude for gluon emissions is calculated. The individual single scattering amplitudes are based on the GW model, but are applied in an *opacity expansion* where the number of scattering centers is determined by the opacity  $\chi = L/\lambda$ ,  $L$  being the length traversed and  $\lambda$  the mean free path. The authors find that the expansion is able to be applied at all orders by a recursive algebraic formula starting from a simple set of lowest order single and double scattering *Born* amplitudes one of which is represented by the diagrams shown in Figure 4.8. The lowest term in the opacity expansion is however found to

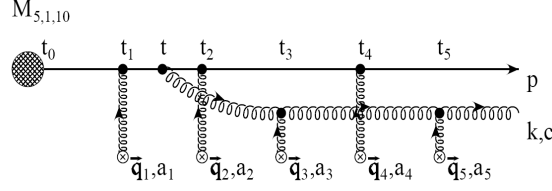


Figure 4.8: Lowest order diagram in the GLV opacity expansion.

be most important. The probability distributions for gluon emissions are then folded with an initial density  $\rho(z)$  of the gluons which can be translated into  $dN_g/dy$  for the scattering centers, and is made time dependent to account for Bjorken expansion. This again yields a double differential distribution of the emitted gluon energy which can be integrated over the collision volume to obtain the total energy loss. An analytic GLV leading log prediction for the energy loss using only the first terms in the opacity expansion yields  $\Delta E \propto \ln E$ , however the full calculation including the higher order terms turns out to have a much higher energy dependence  $\Delta E \propto E$  matching the RHIC results showing a  $p_T$  independent suppression. It should be noted that the Cronin effect naturally arises in the model from additional  $k_T$  fluctuations for each scattering in the expansion which may partly explain additional energy dependence inherent in the higher order terms. It also means that the model can correctly generate the proper Cronin effect for  $p + Au$  collisions.

Other important high  $p_T$  suppression work can be summarized in a similar manner. An important consideration is that of Wang and Wang who [165] stress the importance of including detailed balance between absorption and stimulated emission in a thermal bath of gluons as the QGP is expected to provide. We mention that this same type of detailed balance is invoked within finite temperature quantum treatments of thermal photon radiation described in the next section. In both a hard scattering lowest order calculation of gluon Bremsstrahlung and with the first order GLV result, these authors show an increase in the energy dependence of the energy loss from what would otherwise be nearly energy independent to something having increased energy dependence such that  $\Delta E$  is proportional to  $E$ . With inclusion of this effect (derived from the  $N = 1$  GLV result) other work by X.N. Wang, with

other collaborators the WOGZ [101] model can also provide a good description of the RHIC results. We note however that this does not necessarily imply that the effect would be as large in the full order GLV result (which does not include detail balance) and therefore that the GLV result is necessarily “missing” a similar sized enhancement. It would however lead to two different interpretations of the same effect. It may turn out that the amount of this stimulated emission and absorption can be constrained by other thermal information such as low or especially mid  $p_T$  direct photon enhancement. Getting back to the WOGZ model however, it is based on calculating a “multi-twist” (which in this case mostly just means higher order) “semi-inclusive differential hadron tensor”  $dW_{\mu\nu}/dp$  which is proportional to the fragmentation function convoluted with the higher twist scattering amplitudes. Modifying this amplitude based on larger numbers of scattering centers in the QGP or in a cold nucleus (analogous to higher terms in the GLV opacity expansion) then allows one to define a new effective fragmentation function which allows calculation of energy loss. A similar technique of directly modifying the gluon fragmentation function was used in earlier work by Zakharov [178]. The fragmentation functions are adjusted to fit HERMES  $e + A$  data in the WOGZ model.

Finally we note that all the models depend on a finite time  $\tau_0$  (a different  $\tau_0$  than ours from section 3.3) which is the formation time of the medium, the time it takes for the scattering centers with their associated screening to form and arrange themselves. The GLV model has been shown to be rather insensitive to this time [103]. The actual lifetime of the medium does not matter as the expansion of the volume rapidly degrades the radiative loss processes, such that the effects around  $\tau_0$  dominate.

### 4.5.2 Is it Really a QGP Signature?

Even though most of the quenching calculations originally assumed a plasma, it is not clear that they really do require the presence of such. In nearly all the models the important parameter is simply the number of scattering centers, i.e. the

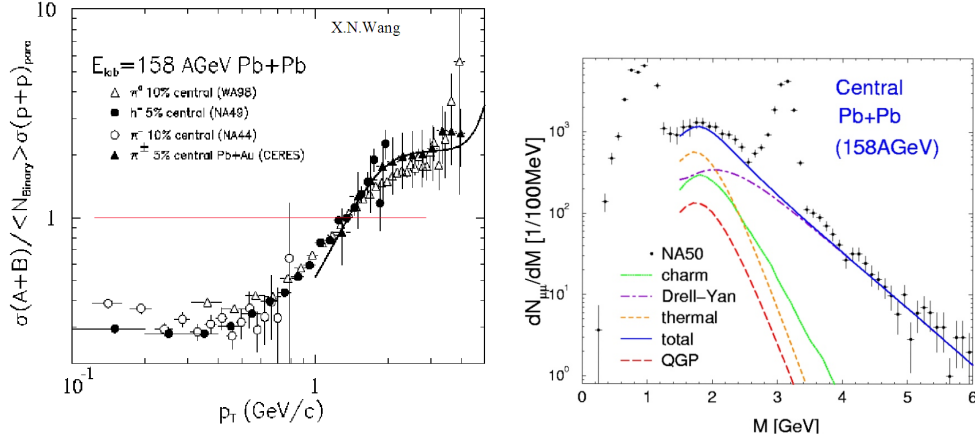


Figure 4.9: Hard Scattering Results at the SPS

number of color charges (gluons). In this respect they do not necessarily have to be free or deconfined. This is why this signature is not considered by itself a definite confirmation of QGP formation. It will be interesting if it can be shown that the detailed balance effects are unambiguously present in the RHIC data because this assumes that the individual gluon degrees of freedom participate thermally in an independent manner—which could be one definition of a true QGP. There are also other mechanisms which potentially could cause suppression of high  $p_T$  mesons, such as hadronic rescattering, although these have been all but ruled out. [104]

## 4.6 Review of Hard Scattering in $A + A$

### 4.6.1 pre-RHIC: SPS

The SPS was the first facility to collect data which could be considered within the hard scattering regime, but only just barely so. The  $p_T$  reach of the experiments for  $\pi^0$ , charged hadrons, and direct photons (not shown, but see the next chapter) sputtered out at about 4-5 GeV just above the soft to hard transition, but probably not reliably above it. This is shown in Figure 4.9 a). The center of mass energy was small enough that even mini-jet production was not expected to dominate even the soft particle production in the  $p_T < 3-4$  GeV region, no one was surprised that  $R_{AA}$

was much less than 1 (in contrast to RHIC expectations which we discuss in the next section). Basically we see that  $R_{AA}$  was one only at exactly one value of  $p_T$ , a bit below the hard scattering regime. At the highest  $p_T$  where hard scattering should be the dominant mechanism,  $R_{AA}$  was quite a bit larger than 1, which was interpreted as the Cronin effect. In other words, there was no sign of any suppression.

Other hard scattering results at the SPS can be found in the the di-lepton data. In Figure 4.9 *b*), we see that with fairly good statistics, the invariant mass distribution  $M^2$  which can be *directly* interpreted as  $Q^2$  (as opposed to  $p_T$  which is more like one component of  $\vec{Q}$ ) did resolve the  $J/\Psi$  at  $\sim 3$  GeV/c and even much higher mass Drell-Yan pairs were observed. As discussed in our brief introduction of QGP signatures, modifications to  $J/\Psi$  production is also a potential sign of QGP formation, and indeed at the SPS, solid evidence for modifications with respect to binary collision scaling was found. However this is not generally grouped together with other hard scattering. And even though the dominant mechanism for  $J/\Psi$  production is expected to be hard scattering, one may argue that  $Q^2 = (3\text{GeV})^2$  this is still in the soft range. But considering many of these leptons must also have had some momentum themselves, it probably puts it in the range. Above the  $J/\Psi$  the dilepton pairs are dominated by Drell-Yan production which proceeds via quark anti-quark annihilation into a virtual photon which then “pair produces” the dileptons. Interestingly enough, these pairs just above the  $J/\Psi$  peak ( $M^2$  3.5 - 4.5  $\text{GeV}^2$ ) are above the (binary scaled) prediction just like the Cronin region in the  $p_T$  spectra. However it was concluded that the total Drell/Yan yields did obey binary collision scaling [3], and thus a ratio between  $J/\Psi$  to the scaled Drell-Yan could be used to judge  $J/Psi$  enhancement or suppression.

### 4.6.2 RHIC

With the advent of RHIC, the first results well within the hard scattering  $p_T$  range were observed for charged hadrons and  $\pi^0$  in very fine centrality bins. As opposed to the SPS result, binary scaling was observed in the high  $p_T$  hadron spectra for

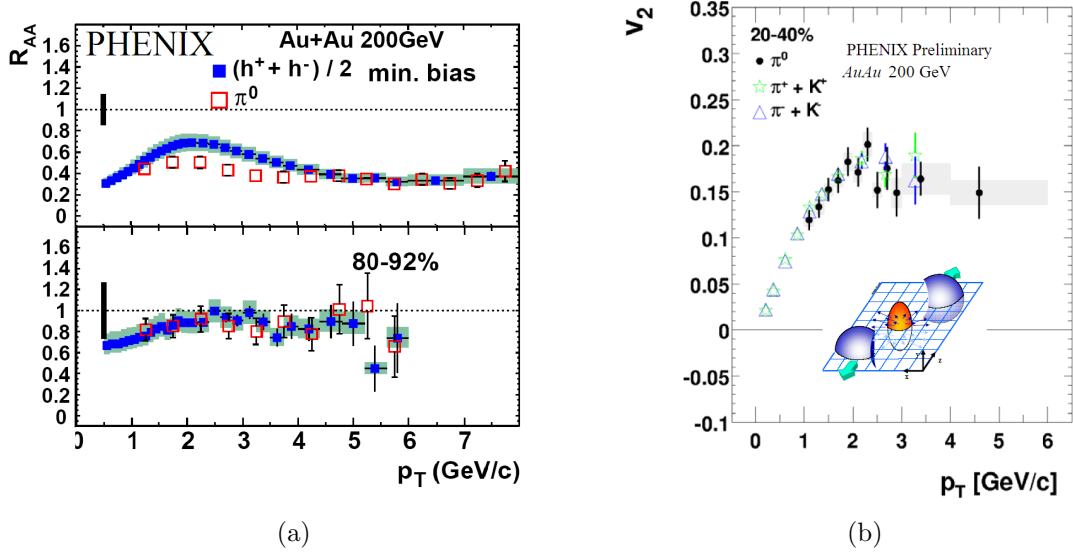


Figure 4.10: *a*) High  $p_T$  suppression pattern observed at RHIC by PHENIX. *b*)  $v_2$  is a measurement of the second Fourier harmonic present in the angular distribution of all particles with respect to the reaction plane. An positive anisotropy corresponds means more particles are produced in plane than out of plane.

the very most peripheral bins, across all  $p_T$  bins in the hard scattering range ( $p_T > 3-4$  GeV/c), but was found to be violated for more central events, in agreement with jet quenching predictions. This is demonstrated in Figure 4.10 a) for both particle species. Furthermore this behavior was also verified by multiple experiments independently [15], [6]. Surprisingly the suppression was found to be absent in the baryons in the mid  $p_T$  range, taken as signs for a new production mechanism distinct from fragmentation known as recombination [113], [88], where hadrons form by quarks already present which combine as opposed to being generated by confinement processes. While the bath of available quarks in this model is not explicitly a QGP, it could be interpreted this way; however, details of recombination calculations have been found not to be fully consistent with the data [20].

Further studies of  $d + Au$  collisions again yielded consistency with binary scaling taken as evidence that the  $Au + Au$  suppression was indeed a final state effect and not simply due modifications in the initial state PDF's as a relatively new competing explanation (gluon saturation) proposed. A clear Cronin effect was observed in the

$d + Au$  charge hadron data (see Figure 8.1). Incidentally the baryon enhancement relative to the meson suppression in  $Au + Au$  is also consistent in some ways with Cronin, known to be larger for baryons than mesons. [118]; however, the known mechanisms for Cronin cannot account for as dramatic of a difference as exists between the mid- $p_T$  mesons and baryons in RHIC  $Au + Au$ . We also note that the RHIC measurements have been done side by side with complementary  $p + p$  reference measurements at the same energy. We shall revisit issues of binary collision scaling and initial *vs.* final state effects in our concluding *Discussion of Results* section.

Perhaps even more exciting than the plain measurements of suppression in the high inclusive  $p_T$  spectra at RHIC has been the ability to actually resolve properties of the actual jet modifications. While event by event jet identification has still not been achieved (and would be beyond all initial expectations in the  $Au + Au$  environment) statistical measurements of jet angular correlations by both PHENIX and STAR as shown in 4.11 found that the suppression can be associated with a “disappearance” of the away side associated fragmentation from the leading particles. More specifically as is apparent in the figure, the disappearance corresponds to a reappearance or enhancement of lower momentum fragmentation—in other words a significant modification of normal fragmentation. This is as predicted in QGP quenching scenarios [171] discussed in the previous section describing gluon (fragmentation) radiation modifications, the interpretation being that the away side corresponds to back side jets which suffer energy loss going through the collision volume. This is not all—in semi-central events as shown in Figure 4.11, where the collision volume and hot medium is asymmetric, the suppression pattern is also observed to be similarly asymmetric corresponding to a larger energy loss in the out of plane, longer path length direction. This indicates sensitivity to the path length ( $L$  from the previous section) dependence of the energy loss and is also the cause of a high  $p_T$  “flow” pattern shown in 4.11 *c*), well above where hydrodynamic effects would be present.

We conclude the review by mentioning that again hard scattering information

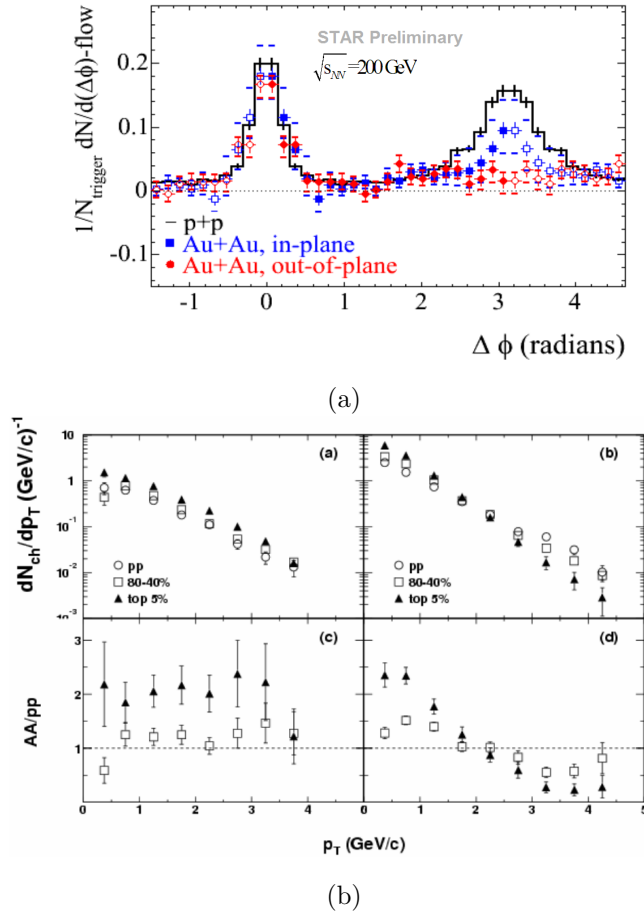


Figure 4.11: Particle Pair  $\phi$  Angular Correlations measured at RHIC. In *a*) the Jet Structure is obvious due to the correlations at small angle (near side) and at  $180^\circ$  (away side). Both STAR and PHENIX observe this Jet signal [135],[21] . In *b*) it shown that the away side correlation is reduced at high  $p_T$  (disappearance) but enhanced at low  $p_T$  (reappearance). As in *a*) this behavior is also shown to depend on orientation with respect to the reaction plane, explaining the high  $p_T$  portion of 4.10

has also been made available at RHIC in the heavy quark sector. Being collider experiments, statistics have not been good enough to resolve a significant  $J/\Psi$  signal let alone higher mass Drell-Yan dileptons, though for  $J/\Psi$  upper limits have been set. But "Open Charm" ( $D$  mesons) has been observed both indirectly in semi-leptonic decays by the PHENIX single electron measurements (as shown for  $Au + Au$  in Figure 8.10 of our concluding chapter) and directly in di-hadron decays by STAR.

## 4.7 Mechanisms for Direct Photon Enhancement and Measurements in $A + A$

One of the earliest proposed signatures of the QGP was in very low  $p_T$  enhancement of the direct photon spectra compared to binary scaled  $p+p$  due to thermal radiation from the extremely hot QGP matter. Recently new predictions of direct photon enhancement due to parton jet interaction with the QGP medium have extended to higher  $p_T$ , in the hard scattering range, meeting the rising normal pQCD signal level. Together this means that the photon signal in nearly every  $p_T$  range should be significantly above background enough that we should at the minimum be eventually be able to make the notoriously difficult  $\gamma_{direct}$  measurement over the entire  $p_T$  range.

### 4.7.1 Experimental Results

Summarizing the experimental results for direct photon measurements in HI physics will be brief because there have only been two experiments which were able to produce a result with any appreciable  $p_T$  reach prior to RHIC, and only one result which found a positive direct photon signal. Both measurements were done at the at the CERN SPS fixed target energy in the  $\sqrt{s_{NN}} \sim 20$  GeV range. The first attempt was performed with the WA80 experiment in  $\sqrt{s_{NN}} = 19.4$  GeV  $Sn + Au$  [44]. As this experiment was one of the first uses of calorimetry in Heavy Ions it was not possible to resolve a positive signal above the large background from decay mesons, but this implied that the signal was relatively small and upper limits were able to be made. It wasn't until 10 years later in the "grand-child" successor of

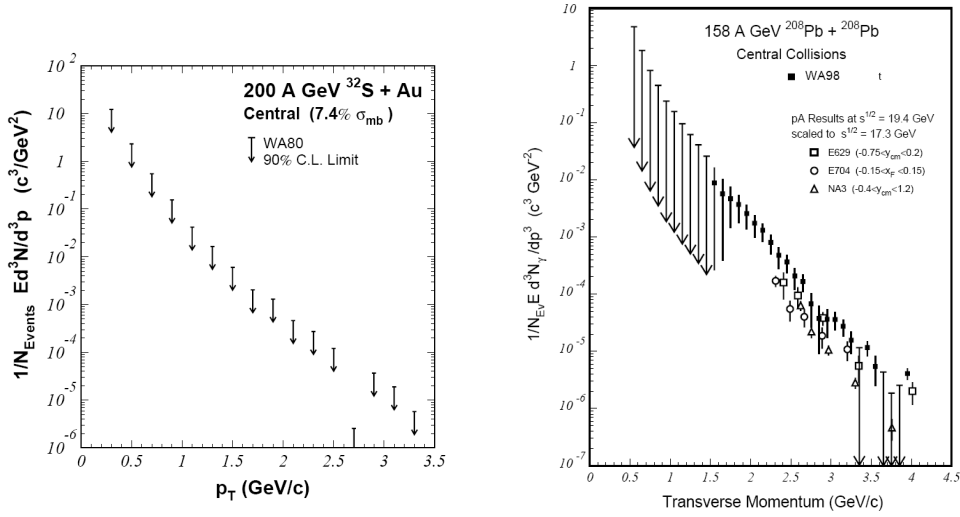


Figure 4.12: The two direct photon results in HI physics previous to this result, the upper limits set by WA80 [44] and the first measurements by WA98 [143]

the same experiment, WA98, in  $\sqrt{s_{NN}} = 17.3 \text{ GeV } Pb + Pb$ , that the systematics were reduced enough to make a positive measurement [143]. Both measurements are shown in Figure 4.12. The entire measurement is in the standard low  $p_T$  range typical of all inclusive leading particle measurements from the SPS where hard scattering and pQCD contributions should be low. This is the desirable range for studying thermal  $\gamma_{direct}$  enhancement.

## 4.7.2 Thermal Radiation

Both a high density of charged quarks in a high temperature plasma and also a high density of hot charged hadrons will produce black body thermal radiation, just like any other such matter. It is almost certain that the hot strong matter produced in RHI collisions will at least reach the latter phase, the so called *hot hadron gas* (HHG). Therefore, a calculation of the total thermal production of photons must include estimates from both phases in a dynamically evolving realistic treatment of the collision volume matter—preferably including the details of the phase transition. In fact all these pieces have been worked on by many theoretical groups, so we shall

discuss each separately.

#### 4.7.2.1 QGP Rates

There are two ways in which photon rates from a thermal QGP are calculated within perturbative QCD. In the end however a complete calculation has not been accomplished. Nonetheless, a large body of theoretical work has gone into the problem, and the hope is that the current state of the art rate calculation represent a good “educated guess” [144].

The first method of rate calculations employed is the most straightforward and easiest to understand. We start with the pQCD result for the microscopic partonic  $d\sigma/dt$  cross sections derived in section 2.3.1 which cause photon radiation such as gluon Compton and quark-antiquark annihilation. Similar to the factorization calculation, we fold them with distributions for the quark and gluon partons, but this time instead of PDF’s we use thermal distributions, Bose-Einstein for gluons and Fermi-Dirac for quarks. This result, derived by [?], has a characteristic temperature dependence given in the rate:

$$\frac{dN_\gamma}{d^4x d^3p} = \frac{5}{18\pi^2} \alpha\alpha_S \frac{T^2}{E} e^{-E/T} \ln \frac{ET}{\mu_{q0}^2} \quad (4.15)$$

The parameter  $\mu_{q0}$  is the quark mass. In the “chiral” ( $m_q = 0$ ) limit this expression diverges for zero parameter  $\mu_{q0}$ . For this reason, an effective quark mass  $\mu_{q0} = g^2 T^2/6$  in the plasma is used to regulate the expression. The effects of higher order diagrams can be accounted for by modifying the parameter  $\mu$  but in comparison to the more complete treatments we will discuss next, the rate 4.15 is found to be an overestimation. However the fact that we need to introduce the artificial plasma mass cutoff points to the fact that the treatment is not self consistently accounting for the presence of the non-zero temperature medium.

In order to improve the situation, a much more sophisticated and powerful general formalism is employed. With this formalism a resummation technique called the Hard Thermal Loop (HTL) approximation can be employed. The basis of this tech-

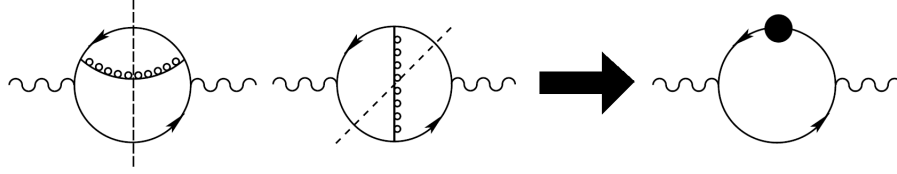


Figure 4.13: Photon self-energy diagrams in finite temperature pQCD [144]. The first two diagrams are the NLO contributions. The third diagram (farthest right) is the LO contribution (the 2-point correlation function) with the 1-loop Hard Thermal Loop (HTL) modified quark propagator—the HTL is represented by the blob.

unique is the identification that the photon production rate is related to the quantum field theoretical photon self energy  $\Pi^{\mu\nu}$  which follows from generalized field theory at finite temperature where the vacuum is temperature dependent and the distribution of initial states are density operator eigenvectors weighted according to Boltzmann weights and normalized by the partition function. Specifically, it can be shown [107] that

$$\frac{dN_\gamma}{d^4x d^3p} \propto \frac{1}{E(e^{E/T} - 1)} \text{Im}\Pi^{\mu\nu}(E) \quad (4.16)$$

where the self energy  $\Pi$  is evaluated from the normal QFT  $N$ -point correlation function represented by the diagrams in Figure 4.13 except now the coupling and propagators become temperature dependent. Virtually the same Feynman rules as in cross section matrix element calculations, apply to each aspect of the diagram and the integral which it represents. The advantage of the expression is that it is easier to apply all-order leading-log resummations to these  $N$ -point correlations functions than to the basic matrix element calculations used to derive 4.15. The HTL approximation represents one such resummation scheme where an effective propagator (which is the HTL and can be derived from first principle assumptions) replaces the normal *bare* propagators in the self energy vacuum expectation calculation. For each order however, the HTL has to be re-derived. The farthest this has been done *and* a rate extracted is to 2-loop giving the following *HTL 2-loop* expression:

$$\frac{dN_\gamma}{d^4x d^3p} = \alpha\alpha_S e^{E/T} \frac{T^2}{E} \left( a \ln \frac{0.2317E}{\alpha_S T} + b + c \frac{E}{T} \right) \quad (4.17)$$

where the  $a$  term is the 1-loop result, the  $b$  is from Bremsstrahlung and the  $c$  term is from annihilation. The reason for this was discovered by Aurenche. He showed that all loops contribute at the same order [43], similar to the way Bremsstrahlung for photons in NLO pQCD can contribute at the LO. Nonetheless, observing the change from including the 2-loop results into the 1-loop, higher order effects are expected to only add to the rate estimation 4.17 while other effects such as LPM suppression are expected to cause rate reduction. It is for this reason that HTL 2-loop calculations are hoped to be approximately correct within a factor of 2 to 3.

It should be apparent that QGP rates are not yet in a systematically predictable state. However, they can be trusted in so far as they prove that a QGP thermal enhancement *can* and in fact is likely to exist. They also give us some indications of where in  $p_T$  one might expect to see a QGP enhancement. It is therefore left to the experimentalists to go out and measure it.

#### 4.7.2.2 HHG Rates

The *really* crucial theoretical sector in being able to make an experimental measurement of thermal QGP radiation is not the QGP rates themselves, but rather those from the normal hot charged hadrons. The reason for this should be obvious: HHG rates represent the null effect baseline based on which we can make claims of deviations due to the medium. Fortunately, the state of HHG rate calculations seem to be in a much more hopeful state, though things are still not yet in a completely stable state either. The calculations of hadron gas rates can be done using *effective* quantum field theories in which mesons are the mediating fields. These types of effective theories can also be used quite successfully to calculate many nuclear properties [22], the nucleus with its many nucleons being a very similar problem, and can be constrained by many other measurements from basic particle physics, such as meson decay widths and branching ratios [162]. The principal of Vector

Meson Dominance (VMD) [138] which prescribes the introduction of vector mesons into the photon-hadron interaction terms causes these mesonic fields to be the most important mediators. The Lagrangian is chosen to respect basic QCD symmetries and is generally chirally symmetric. The large number of mesonic resonances leads to very large Lagrangians with many terms for which complicated programs must be employed to run the entire calculations.

Typical photon producing processes considered include the lowest order hadronic processes including “hadronic Compton” processes e.g.  $\pi\rho \rightarrow \pi\gamma$ , and hadronic annihilation  $\pi^+\pi^- \rightarrow \rho\gamma$ , but where the  $\rho$  can be replaced by any of the vector mesons. Indeed the  $a_1$ ,  $\omega$ , and more “exotic” VM’s are found to contribute the largest amplitudes. Form factors which account for the substructure of the meson in the rate calculations have also been found to make a difference. Deciding which final set of propagators to include has been one of the difficulties. In fact, it has been noted that there does not appear to be a unique way to write the Lagrangian. [92]—though more work in incorporating other constraints such as analogous low mass dilepton production is expected to be able to resolve the degeneracy[153]. Nonetheless, a fairly stable set of predictions for the lowest order effective theory HHG photon emission rates have been established. The following parametrization [155] matches most theoretical predictions at least in the lowest  $p_T$  region below 3 GeV/c:

$$\frac{dN_\gamma}{d^4x d^3p} = 4.8T^{2.15}e^{-1/(1.35ET)^{0.77}}e^{-E/T} \quad (4.18)$$

Yet other contributions to the rate are still under investigation. These include higher order Bremsstrahlung processes which originally were only expected to contribute at extremely low  $p_T$  on order of the critical temperature, but under similar, more sophisticated inclusion of the other VM’s as in the lowest order case, they were found to be non-negligible [108]. Many investigations into thermal modifications of the effective theories have also been investigated and have been found to differ from the basic predictions of *e.g.* equation 4.18 [144]. However, as one may

consider these as medium modifications, it is best to focus on a prediction for the most basic expectations. Nonetheless, we must say that there are still fairly large uncertainties in the HHG rate predictions within a factor of 2 to 3. However as opposed to the QGP case, the estimation of this uncertainty level is on much firmer ground and furthermore can be expected to be resolved in the next few years.

### 4.7.2.3 Evolution of Both Phases

The rates from the previous two sections must be applied over the distribution of matter produced in the collision. The evolution of this matter and the interplay between regions of one phase or the other, mixed phases, or regions of non-equilibrium are also extremely important in order to make true full estimates of expected thermal radiation in heavy ion collisions. Another source of uncertainty related to this are the initial conditions—since all the rates depend strongly on temperature, some temperature is usually assumed in the calculation, but until just recently (probably since the rates are to be taken more as estimations) systematic treatment of relating temperatures, initial conditions, and evolution to other HI observables and measurements has not been done. Several of the theoretical groups working on one rate calculation or other (e.g. HHG or QGP) will often put together their own calculation together with reasonable estimates of the other components from the literature within a basic evolution framework, but such models tend to be rather simple, while on the other hand the size of such effects may change the actual final predictions by quite a lot.

Work that has been done in this regard has been done by Renk [149]. He attempted to include the latest thermal rates together with a realistic fireball evolution which took HBT parameters, flow, and other parameters as inputs. He found that including hydrodynamical flow increased the rates from the HHG by a factor 2 to an order of magnitude. Boyanovsky and Vega [57] derive a new formalism which allows QGP rate estimates to include a finite lifetime, which in the usual approaches is assumed to be infinite, yet another problem with these rate calculations. They find substantial increases in the rates from higher order processes that become lower

order with the introduction of the finite lifetime. Other authors [155] [158] have investigated non-equilibrium effects and also found that these can enhance QGP radiation.

### 4.7.3 Jet-Plasma $\gamma_{direct}$ Production

Recently two authors have introduced a new type of enhancement in direct photon production within a QGP. The source of these  $\gamma_{direct}$ 's is from jet-forming partons as they traverse the plasma. The first prediction was from Fries et al. in 2002. [89]. In this calculation, once again only the simple 2 body scattering diagrams were considered, and in a manner analogous to the “straight forward” thermal or normal pQCD factorization calculations, these are folded with  $f(p)$  distributions for the partons. This time however, the distributions contained a thermal *and* “jet” term where the jet term is simply taken to be a power law parametrization from pQCD itself and can be ignored in the  $f(p)$  distribution representing the medium. However, this  $f_{jet}(p)$  in the “incoming” distribution when folded with the thermal medium distribution results in *jet parton to photon conversion*, just due to the kinematic structure of the cross-section, for some portion of the “jet” parton spectrum. The final expression for the rate is similar to the basic thermal prediction, and employs the same plasma mass  $\mu$  cutoff. The only difference is the replacement of the Boltzmann exponential with the sum of the  $q$  and  $\bar{q}$  distributions  $f_{q/\bar{q}}$  which are the power law parameterizations derived from LO pQCD

$$\frac{dN_\gamma}{d^4x d^3p} = \frac{5}{18\pi^2} \alpha\alpha_S \frac{T^2}{E} (f_{q/\bar{q}}(p_\gamma)) \ln \frac{ET}{\mu_{q0}^2} \quad (4.19)$$

Even though the relative fraction of jet partons which convert is small, it could be substantial compared with the number of ( $\alpha_{EM}$  reduced) normal pQCD direct photons. Using LO pQCD, as shown in Figure 4.14 that this source of photons actually dominates all photon sources in the range of  $p_T$  from 4 to 6 GeV/c. As we shall discuss further in our conclusions, the use of LO order pQCD may be a problem, but nonetheless, as a first step, (which authors themselves acknowledge)

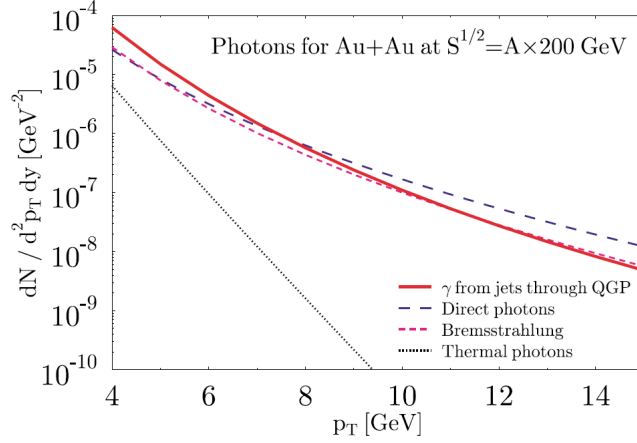


Figure 4.14: Prediction of Jet-Plasma or “Jet Passage” Photon Radiation from the QGP in [89]

the result demonstrates the exciting possibility that photons from this source could potentially offer a new QGP signature.

The second prediction like this came from Zakharov [178] in a treatment of photon (EM) Bremsstrahlung from these same jet forming partons. While for a long time it has been expected that the vacuum Bremsstrahlung coming from NLO and higher order QCD diagrams and accounted for in the photon fragmentation functions, would be suppressed just as the jets themselves are suppressed due to the gluon radiative process discussed above (section 4.5) [116]. However Zakharov argues that the formation time of the photons and gluons being similar means that quite often the Bremsstrahlung photon would be emitted before the gluons, and therefore the suppression of this photon source (nearly equal to the LO Compton contribution at our energy– see Figure 8.19 in the our concluding section 8.3.2) would be smaller than previously estimated. However Zakahrov goes on to calculate an “in medium” enhancement to the EM (photon) Bremsstrahlung analogous to the gluon Bremsstrahlung responsible for quenching and finds that this contribution is large, greatly overpowering the now reduced suppression effect, leading to a total enhancement similar in relative size as the [89] prediction in Figure 4.14.

In fact the similarity of the two predictions leads one to believe that there may

be a possibility of double counting between the two predictions. This is discussed further in the Discussions and Conclusions section 8.3.2.

# Chapter 5

## Experiment

### 5.1 RHIC: Trains of Trains

RHIC itself is essentially a more or less circular train of super conducting magnets placed in a tunnel 3.8 km in circumference. Beams of protons and nuclei/ions can be accelerated over almost three orders of magnitude. The normal running mode energy for protons is 200 and 500 GeV. Already Au ions have been accelerated to achieve  $\sqrt{s_{NN}}$  energies of 19.6, 56, 62.4, 130, and 200 GeV, and other energies may be explored in future runs. Other lighter ion species are scheduled for the next run of 2005, and operations were already extended to d+Au running in 2003. Another unique capability of RHIC is its ability to run polarized beams of protons for study of the nucleon spin structure. However its main focus remains the search for the QGP. For other published information about RHIC, consult the RHIC NIM article [2].

As with all particle accelerators at very high energy, RHIC is not capable of accelerating particles from rest. Instead, it is fed lower energy, but already accelerated, particles from a train of other accelerators. More or less, each of these has an energy range it is responsible for, and each often historically represented the “state of the art” at the time it was originally built. Some brief information regarding all these accelerators is compiled in Figure 5.1. The very beginning of the acceleration process depends on what kind of particle is being accelerated, whether it be proton,

or nucleus. Generally, the acceleration process starts by ionizing a gas of neutral atoms or by heating a filament of neutral atoms which causes ions to be ejected, and using an electric field to accelerate these ions. Generally, electrons are “stripped” from atomic ions by running the beam through foils of various sizes and materials. We shall discuss the specific steps involved in  $Au + Au$  acceleration at RHIC in the next paragraph. Towards the beginning of the process, the accelerated charged ions can be placed in a linear accelerator (*linac*) with a single continuous electric field or *cyclotrons* (though there are none of these at RHIC) which use a single large magnetic field to keep forcing the circular trajectory of the ions into small regions of electric field at regular intervals. Eventually the particles become so energetic that their trajectories become so large that a *synchrotron* “trains” of magnets which trace out a beam line in an accelerator such as RHIC must be employed.

For  $Au + Au$  running, the RHIC process is as follows. The Tandem Van de Graph starts with Au atoms with one extra electron so a unit  $-e$  electron charge. It accelerates these to 15 MeV (total) by a static electric field into a foil (its composition is not important) which causes a virtually random number of electrons to be stripped from some fraction of the ions. Therefore these are now positively charged. Again these ions are subjected to a static potential and therefore ions with different numbers of electrons left can be differentiated by their energies, e.g. by their bend in a magnetic field.  $Au^{+12}$  is selected and further accelerated to an energy of 1.0 MeV per nucleon. One more stripping occurs with foil bringing the ions to the  $Au^{+32}$  state. These then enter the AGS Booster which then accelerates them to 95 MeV after which they are stripped again till there are only the two highest shell electrons remain as  $Au^{+77}$ . All the while in the AGS itself, the Au is in this ionic state, and it is not until just before entry into the ATR Transfer line (please see the figure) at an energy of 9.8-10.8 GeV that the final 2 electrons are stripped. This defines minimum  $Au + Au$  energy of RHIC 9.8-10.8 GeV in each ring, resulting in 22 GeV  $\sqrt{s}$  collision energy. A relatively very small amount (about 1/1000 of the number of events used in this thesis’ analysis) of 22 GeV  $Au + Au$  data was taken at the end

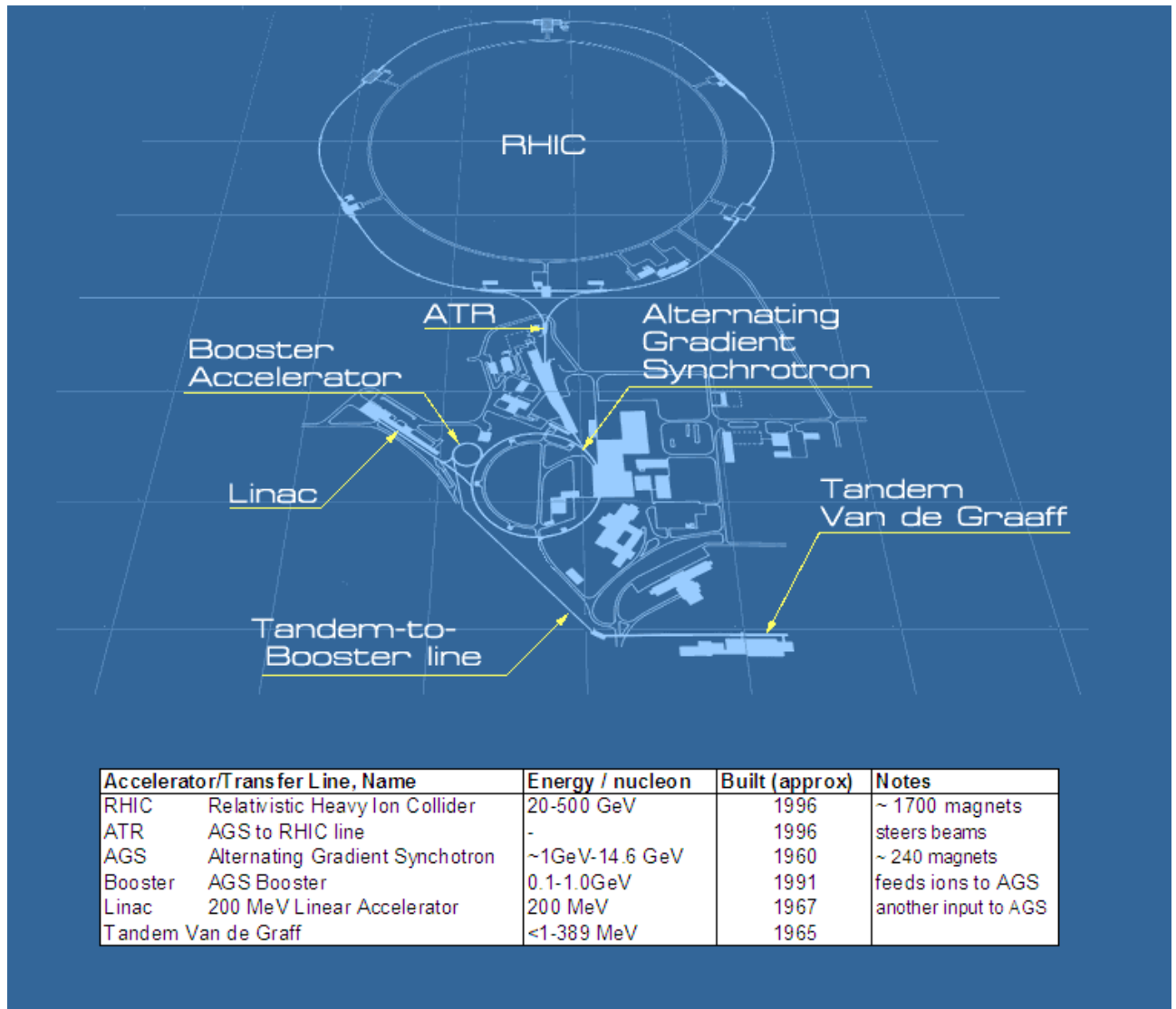


Figure 5.1: RHIC is fed by a train of several accelerators.

of Run2. From this energy

### 5.1.1 “Runs” and “runs”

RHIC is turned on for many months at a time in what constitutes a RHIC “Run” (with a capital “R”) which is really a run *period*. Different Runs correspond to different running modes of the accelerator. For example Run1 was a commissioning Run with  $Au + Au \sqrt{s_{NN}} = 130$  GeV, or Run3 focused on d+Au collisions which

will be discussed later in 7. Run2 was the subject of this thesis. Run4 was recently completed with a larger data set of Au+Au. All the Runs so far have also included some polarized 200 GeV  $p + p$  running time as well.

Particles are accelerated at RHIC in groups called bunches. *Au* bunches start in cycles of 4 coming into the AGS. They are usually injected into RHIC in 15 cycles resulting in 60 bunches of about  $N_B = 10^9$  ions spread over 10-22 cm ( $\sim 1$  ns) in horizontal length, grouped with regular spacing of 108 to 216 ns and  $\sim 0.01$   $mm^2$  in transverse area ( $A_T$ ). These are held in *stores* which can last approximately 10 hrs, but will vary in longevity based on quality. The luminosity degrades exponentially, so the majority total integrated luminosity from a store occurs right at the very beginning. For high-rate experiments like PHENIX this period of high luminosity is most desirable and therefore many short stores are optimal. On the other hand, for other experiments whose event taking speeds are still saturated by the low rates towards the end of store, the machine stability inherent in long stores is preferable. For this reason a voting system for the 4 RHIC experiments is used to determine whether the experiments like the quality of the store or want it *dumped*.

The effective average luminosity  $L$  crossing a plane perpendicular to the beam direction in this bunch configuration is then  $L = r_B N_B / (4\pi A_T)$  approximately  $10^{27} s^{-1} cm^{-2}$  since  $r_B$ , the average bunch crossing rate from the information above is 78 MHz. In actual practice for Run2, the average luminosity achieved was  $2 \times 10^{26} s^{-1} cm^{-2}$ . With a bunch spacing of 198 ns, the maximum bunch crossing rate is 1.2 GHz meaning that the maximal luminosity during this period is  $1200/78 = 15$  times as high. From the above information, the integrated luminosity during a single bunch crossing is  $\sim (10^9)^2 / (0.01 mm^2) \approx 10^{22} cm^{-2}$  and with a total *AuAu* cross section of  $\sim 7$  barn so the probability is extremely low ( $1/10^5$ ) that more than one event per bunch crossing will happen.

During each store the experiments take data. To keep data in smaller units over which constant calibrations can be assumed, the DAQ is started and stopped several times during each store. Each such starting and stopping is called a “run” (lower case

“r” – I will try to keep this notation throughout this thesis) which generally contain 100K to many millions of events lasting 20 minutes to an hour. For Run2 Au+Au, there were approximately 500 runs which were used for real physics analysis, totaling about 50-100M events depending on the trigger used explained below in 5.9.

### 5.1.2 RCF and PHONCS

In addition to the accelerator itself, a computing farm dedicated to RHIC data analysis exists at BNL called the RHIC Computing Farm. This farm contains nearly 1000 state of the art (2GHz processors) dual and quad processor machines along with 100's of TB of accessible disk space (important since it reduces the need to retrieve data from the tape storage system discussed below in 5.9). PHENIX also houses a smaller 75 single dual and quad processor machine farm (PHENIX Online Computing Systems: PHONCS) in its counting house for fast online analysis. The majority of the serious data crunching for the analysis of this thesis was performed in on these machines. Occasionally even more computing power has been necessary to meet the computing demands of the  $\sim 500$  collaborators of PHENIX. For this additional resources have been allocated for PHENIX use by the Riken Institute in Japan (CC-J) and at Subatech Research Institute in France (PHENIX-France).

## 5.2 PHENIX

When RHIC was in its embryonic stage, having been scheduled to built but not yet fully constructed, many separate collaborations of scientists mostly who had already been working on experiments at the Alternating Gradient Synchrotron (AGS) ring at BNL and elsewhere were competing for funding with proposals for different types of RHIC detectors. Some of these proposals went through the approval process relatively unchanged and were built, e.g. the STAR experiment. Most of other serious competitors found it necessary to merge into one experiment which by its nature then would be a somewhat motley conglomeration of many different types of detectors but with the advantage of providing access to many different technologies

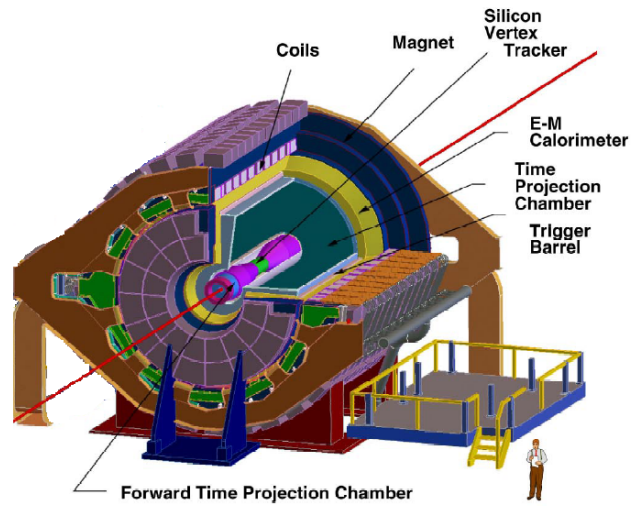
and probes simultaneously. The result of the merge was PHENIX. Figure 5.2) demonstrates this better than words ever could.

The benefits of having access to diverse probes and technologies should be obvious. Besides providing simply more kinds of measurements, each individual measurement can often benefit from more and higher quality cross-checks. The types of probes that many of the PHENIX sub-detectors are optimized for are *penetrating* probes like the direct photon of this thesis and leptons. The original idea was to measure these penetrating and rarer probes along with the other hadron based observables that were more mainstays of the other experimental proposals most importantly, in the **same** experiment [146]. Due to the rare nature of such probes, the rare-event emphasis and high rate capability of PHENIX was an integral part from the very beginning [146].

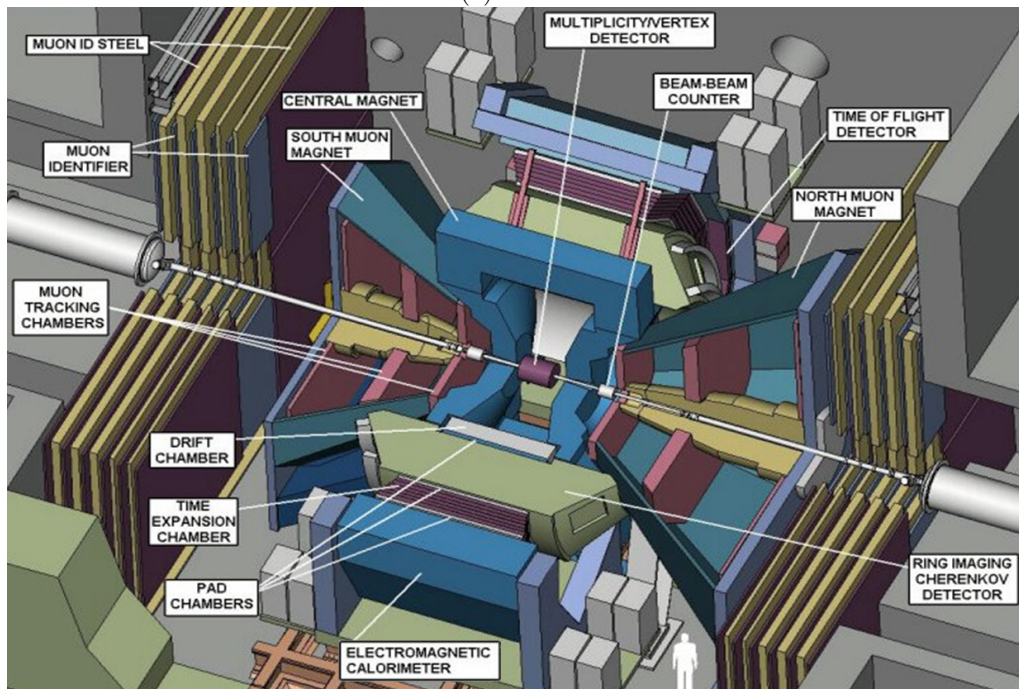
Most information explained here can be found in more detail in a series of *Nuclear Instrumentation and Methods* articles published together in a single volume [2]. PHENIX's skeleton is about 2000 tons of steel magnets which already define the two major divisions of the the detector: the central arm and the two forward/backward muon arms. The muon arm magnets and detectors are not used for any part of this thesis' analysis, so I will only describe the middle division of the central arm. For further reference about the muon arms, please see [2]. For completeness, we will just mention that they are a couple of very similar, large forward/backward rapidity detector-magnet systems ( $\pm 2.2 < \pm y < \pm 1.8$ ) with large acceptance designed mainly to study muons from heavy-flavor quark particle decays.

### 5.3 Central Magnet and Interaction Region

The Central magnet is made up of two energized coils which serve as magnetic poles creating field lines which go parallel to the beam in an azimuthally symmetric fashion with respect to the beam axis. This is shown in Figure 5.3. The central magnet's axial field therefore bends charged particles coming from the event vertex in the circumferential ( $\vec{\phi}$ ) direction, such that after tracking, their momentum can be



(a) STAR



(b) PHENIX

Figure 5.2: PHENIX vs STAR. figures are from both experiments' overview papers. Note that its EMCal was a recent addition to STAR while in the same time several more detectors not shown have been added to PHENIX. The single detector of the TPC has yielded the bulk of STAR's physics up until now. PHENIX on the other hand is a complex combination of many different detectors due partly to its "political" history. However, this inherent diversity has already provided many outstanding benefits.

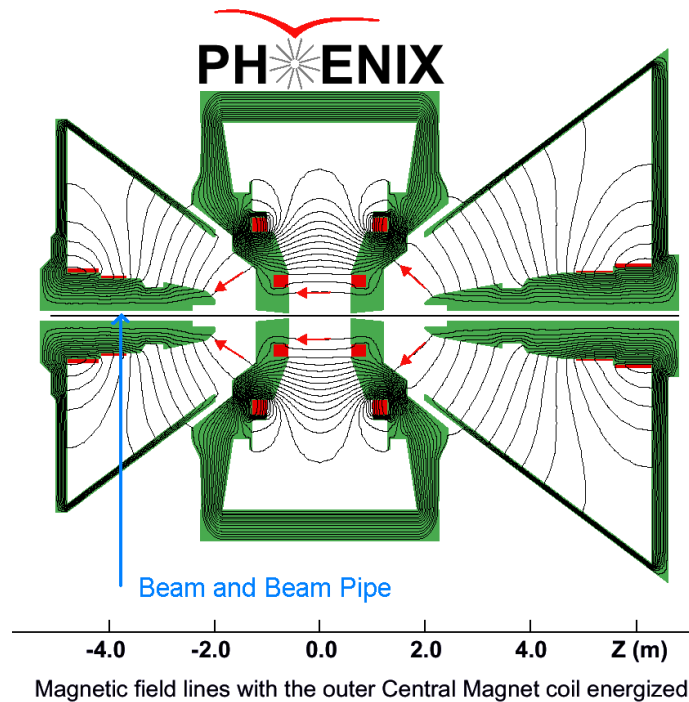


Figure 5.3: PHENIX Magnetic Field. Side View.

determined from how much their trajectories are bent. This will be discussed below in the charge particle tracking section. The field is quite uniform in the immediate region of the beam up to a distance of about 1 m and in this region the field reaches a value of  $\sim 5000$  Gauss. This imparts an  $\int Bdl$  of about 0.8 Tm: the typical  $p_T$ -kick for a charged track by the time it reaches 220cm (at which point it is in the middle of the PHENIX Drift Chamber (DC)) is  $86 \text{ MeV}/c = 0.236 \text{ Tm}$ .<sup>1</sup> After a distance of about 2.4 m from the beam (the start of the Ring Imaging Cerenkov [RICH] detector, the magnetic field is at a nearly negligible level with a field integral after that  $\leq 0.01 \text{ Tm}$ , an important requirement for the proper identification of electrons.

As demonstrated in Figure 5.2 and 5.3, the particle beams go right through the center of these two central field magnet coils such that their intersection is exactly in the center of the volume between the coils. An origin is defined by this interaction point, and a corresponding choice of axes start with a  $z$ -axis along the beam (the north direction is chosen to be positive  $z$ ), and  $y$  is chosen to point up, away from

---

<sup>1</sup>1Tm = 300 MeV/c

the ground. The interaction region between the central magnet poles, is therefore exactly centered around mid-rapidity and extends to a pseudo-rapidity of  $\pm 0.35$ , which also defines the rapidity acceptance of all the detectors in the central arm. The two counter-rotating RHIC beams themselves are merged into a single beam pipe before entry into the center of the PHENIX detector. This beam pipe itself has a radius of 10cm and is made of stainless steel and inside this pipe, the beams are further contained in a Be tubing with a radius 8cm. The total amount of material in the beam pipe in relation to interaction rates is discussed in more detail in our discussions of conversion rates in Chapter 6.7.1.

## 5.4 Introduction to Particle Energy Loss in Matter

High momentum particles generally pass right through of googles ( $\mathcal{O}(10^{20})$ ) of atoms in matter without interacting at all or hardly at all. Some feebly interacting particles (e.g. neutrinos) can regularly go through an quantities of matter the size of planets without interacting. Fortunately for “regularly” interacting particles there are just such googles of atoms in relatively small macroscopic portions of matter. The “probability”  $P$  for a general interaction is defined as  $P = 1 - e^{-x/L_X}$  where  $x$  is the distance traversed in the matter (always in units weighted by density) and  $L_X$  is some length characteristic of the basic interaction that is relevant. For actual out and out “stopping” collisions, generally high momentum particles have to smack into nuclei, as Rutherford’s alpha particles did. This generally only happens for hadrons, as other particles lose most of their energy through other processes before having a decent chance of doing this. For hadrons then, the  $L_X$  is called the nuclear interaction length,  $\lambda_I$  and  $P$  is a true probability. For charge particles, energy loss occurs in smaller more frequent interactions, mostly with atomic electrons. This is called *ionization* loss. Other losses are from e.g. Bremsstrahlung radiation explained below. These types of losses are generally described by the rate  $dE/dx$ . Very accurate analytic formulas based on reasonable statistical approximations have

been derived for all of these processes, for example, the Bethe-Bloch formula gives ionization  $dE/dx$ , the similar Bethe-Heitler formula gives Bremsstrahlung  $dE/dx$ , all such formulas depend on  $E$  itself. In this last case, our  $P$ , instead of a probability, is interpreted as a total energy loss factor, and the relevant  $L_X$  is called the radiation length  $X_0$ . For high-energy photons,  $P$  is a true probability, with  $L_X$  being the very same  $X_0$  (due to the related EM nature) multiplied by the curious cosmic factor of 7/9.

## 5.5 BBC/ZDC Detectors and Triggering

Perhaps the two most essential parts of PHENIX are two relatively small detectors: the Beam Beam Counter (BBC) and the Zero Degree Calorimeter (ZDC) whose locations are shown in Figure 5.4. These two detectors perform three essential functions: event recognition (that is, minimum bias triggering), event vertex location, and centrality determination. Both detectors work in very similar ways: they both consist of north and south portions, functioning essentially as counters, and providing timing information from both two portions. An event is recognized in both by coincidental signals in the North and South detectors. Both have fine enough timing resolution (BBC 50 ps, ZDC 100 ps) to differentiate the two N/S coincidental signals and the timing difference then gives the event vertex  $z$  location. This way PHENIX has two independent vertex measurements and minbias triggers. The BBC timing is special in that this timing is used as the start time for events and all other detector electronics are therefore synchronized to this detector.

The difference between the two detectors lies in their rapidity locations (ZDC at “zero degrees” completely forward rapidity, the BBC at  $3 < \eta < 4.0$ ) and the kinds of particles they detect. The BBC is essentially an array of phototubes each with a Cerenkov radiating piece of quartz wired to the front of it. It therefore detects charged particles with sizable deflection from the event collision—these will always be particles produced in the collision, as we have seen in section 4 these will be a function of the number of participating nucleons. The ZDC is a hadron calorimeter

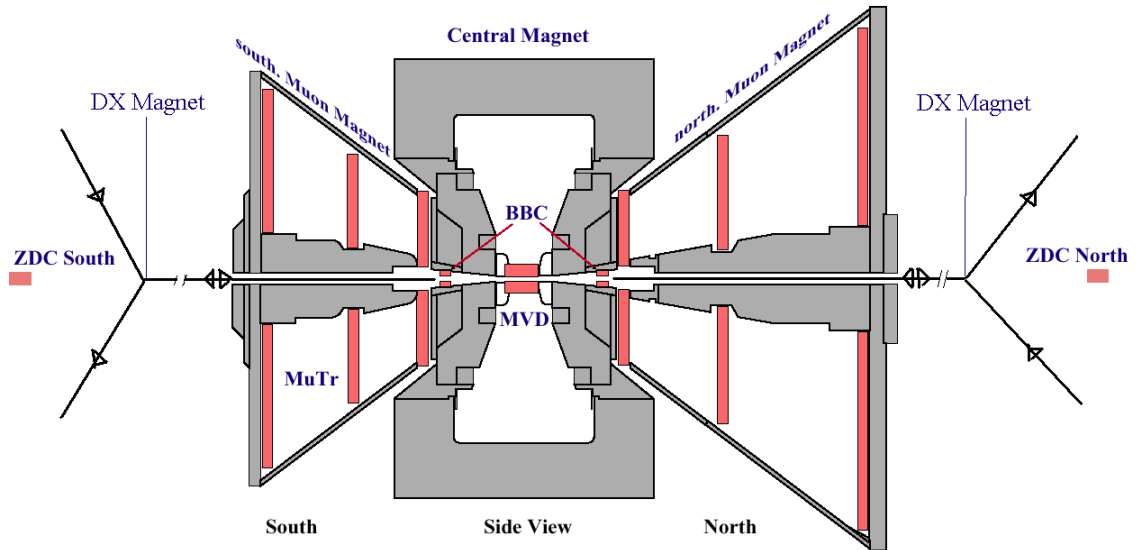


Figure 5.4: PHENIX side view showing the location of the BBC and ZDC detectors. (see below) which because of its location behind the steering DX magnets that sweep the charged beam particles back to and from the detector. It therefore detects only “spectator” fragments of collided nuclei, those neutrons whose momentum direction is essentially unchanged after the collision but are no longer bound to any charge.

Both detectors can quantify the number of different particles which hit them by the amount and locations of their energy response. This allows for a global multiplicity determination, which can ultimately be calibrated to a centrality determination. Originally the ZDC was intended to be used to make this determination by itself with duplicate ZDC’s installed in all four RHIC experiments such that all experiments would have a common centrality definition. However it was found that centrality was a double-valued function of the ZDC response. That is, the maximum ZDC signal occurs in semi-Central events. Both very central and peripheral events yield smaller signals, peripheral simply because the neutrons are more likely to still be bound to light charged fragments of the originally nuclei, and therefore deflected by the DX Magnets, central essentially because the nuclei in these events are “blown” completely apart. Because of this, the ZDC response is cross-referenced

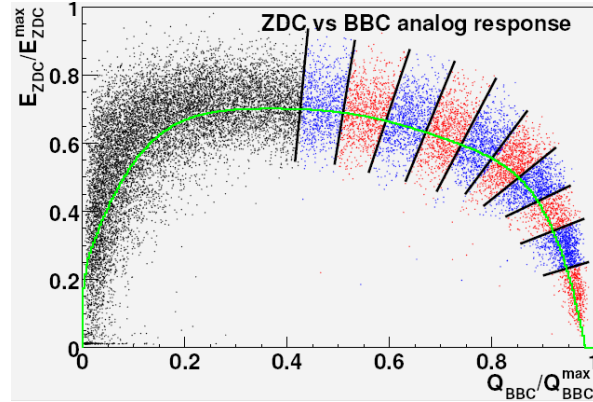


Figure 5.5: Examples of different centrality regions are shown by the shaded “slices”—please see the text for more information. The ZDC response becomes smaller both at high and also at low centrality in  $Au + Au$  collisions resulting in the “banana” shape.

with the BBC response in order to determine centrality. Therefore we have chosen different centrality regions to correspond to different regions in ZDC-BBC space as shown in Figure 5.5. In the figure the response of both detectors is shown for a large event sample. The double valued nature of the ZDC response is apparent. The lines superimposed on the distribution define different “slices” of centrality. We shall give more precise explanations of how these centrality bins are determined in the section 6.1.

Based on GEANT simulations the BBC detects particles meeting the the minimum bias trigger efficiency requirement (2 hits in both the north and the south units) for 93% of the total  $Au + Au$  geometric cross section. Requiring valid ZDC hits, reduces this efficiency to 92.5%, which defines the total percentage of the cross section and the total centrality range (centrality will be defined in 4.3) accessible to PHENIX with its minimum bias trigger.

Finally , we note that in the case of the BBC the position resolution is also fine enough to allow the reaction plane to be determined from the  $\phi$  locations of the its hits.

## 5.6 Charge Particle Tracking

Although the bulk of this thesis is based on measurements made by the PHENIX EMCal, we shall briefly explain the charge particle tracking system. Charge particle tracking and detection is used in this thesis to remove unwanted charge particle contamination from our photon samples—charge particle “vetoing”<sup>2</sup> Tracking is by far the most complicated measurement in PHENIX. Almost every central arm detector is used, including the EMCal. Most of these detectors provide location information around the three dimensional points where charge tracks went through them. Except for the calorimeter where hadronic showering is possible, this is in general from ionization energy loss through various materials on which the various detectors are based, each detector employing different specific technology. As is apparent from Figure 5.2, the Drift Chamber is one of the closest detectors to the interaction region. It provides many, many such points and it can perform its own tracking completely by itself. The many drift chamber hits are formed into tracks by a Hough transform procedure of pattern recognition. These internal Drift Chamber tracks then form a set of track candidates which are then validated by comparing their projections with the space points from other detectors. This procedure is called matching, and provides a powerful method of reducing the background from fake tracks formed by random combinatorial combinations of space point hits due to the lever arm created by the increasing distance from vertex point of the other detectors. Another such background reducing technique is to compare the energy measured in the calorimeter to the track momentum which comes from the drift chamber tracking procedure itself as explained in the next paragraph. Even though the combinatorial background is relatively small, its reduction is crucial for making measurements of tracks at high momentum since such tracks appear in events only very rarely so that at arbitrarily high momentum, fake background tracks can dominate real tracks. The tracks candidates which pass all the background cuts are called Central

---

<sup>2</sup>as explained in the later sections, for this analysis we don’t formally veto on an event by event basis, but rather we do a statistical subtraction based on cumulative information obtained from the tracking detectors.

Global (CGL) tracks.

Two important aspects of the tracking measurements are its momentum determination and the efficiency of our identification procedures. Momentum is obtained intrinsically from the drift chamber pattern recognition and track finding method. This is the purpose of the Central Arm Magnets: to give curvature to the charge tracks. The field created by the large dipole magnets is essentially in the  $z$ -direction causing the tracks to bend mostly in the  $r - \phi$  plane. By measuring the bend (and more importantly inferring the bend in the region just before DCH) an momentum estimate is obtained by the direct measurement of the curvature. Because the field is not exactly uniform though, a complicated look-up/ interpolation procedure must be then be employed, starting from the initial estimate and making several iterations with information obtained from a precise simulation based on the calculated full field map [2]. The final momentum resolution obtained for Run2 is

$$\sigma_p/p = 0.009p + 0.02[GeV/c]$$

Because of the momentum-dependent bending and many other effects the full efficiency of the full tracking system is a complicated function of the momentum and sets of cuts used, and must be determined from simulations. For example see, [12]. Most tracking detectors, including the drift chamber, have a very high probability of detecting the ionization they are designed to for a given track yielding a high “intrinsic” efficiencies of  $\sim >97-99\%$ . However due to dead areas in various regions, the actual average efficiency for different runs can be substantially less. For very high  $p_T$  tracks in run2 a ballpark estimate of the average efficiency including dead area effects is about 80-90%. See section 6.7. Related to our photon measurements and which makes up an integral part of the tracking system are the Pad Chambers (PC), three separate layers of detectors, each with the same finely segmentation in the  $z - \phi$  direction. The outermost Pad, PC3, whose front face center lies at a distance of 485 cm and whose thickness is 6cm places it just 15 cm in front of the PbSc (see below) portion of the EMCal. This makes the PC3 ideal for charge particle vetoing. The pad detectors have an intrinsic detection efficiency of 97% and

excellent position resolution.

One further detector to mention is the Ring Imaging Cerenkov Detector (RICH). This detector is considered part of the tracking system, with the sole purpose of identifying electrons. The RICH contains ethane gas which serves as a transparent Cerenkov radiator surrounded by a configuration of Photomultiplier tubes. Ethane was chosen because of its high photon yield per electron and its low atomic mass/density, in order to minimize photon conversions. Since electrons will be the only particles which can Cerenkov radiate below the  $\pi$  Cerenkov threshold momentum of about 4 GeV/c, electron ID is achievable by searching for Cerenkov rings with radius  $\sim 14$ cm in the PMT array. with additional matching in the Emcal, excellent electron ID can be extended to tranverse momentum  $\sim 6$  GeV/c. The RICH is important to photon analysis in this thesis because in theory, it can provide a clean sample of electrons with which to cross check the EMCal calibration. Because the EMCal response for electrons is nearly the same as for photons, energy measured in the EMCal for electrons can be compared to momentum measurements from the tracking system which generally has a better resolution, at least for low momentum particles.

## 5.7 EMCal Overview

The outer most detector in the central arms is the Electromagnetic Calorimeter called the EMCal. Calorimeters in general measure both hadronic and electromagnetic *showers*. PHENIX's calorimeter has been optimized to measure very preferentially the latter type, although it is impossible to construct a calorimeter that doesn't have some response to hadronic showers. To understand this let us begin by explaining both of these types of showering processes. This will be a very minimal introduction, since many excellent references abound, e.g., the very PDG handbook itself. [75].

## 5.8 Introduction to Showering

Electromagnetic Showers are produced by highly relativistic electrons or photons through the two fundamental processes of (EM) *Bremsstrahlung* radiation and *pair production*. Bremsstrahlung radiation occurs when a charge particle is accelerated and thereby must<sup>3</sup> emit a photon. Pair production is the process by which a photon collides with another photon and produces an electron-positron pair. Generally a very high energy photon collides with a photon with negligible energy whose origin is the EM field of the nuclei of regular atomic matter (most likely of fairly high density). Because of this, pair production is generally thought of more like a “decay” of the photon into the pair that can only occur in the presence of matter. Either way, conserving total energy, the high-energy photon must have a minimum energy of  $2m_e$  in order for this to occur. At sufficiently high energy a photon produced by Bremsstrahlung radiation will fulfil this requirement and the  $e^+e^-$  will each carry about half of its energy. Being still of such high energy, both charged particles will immediately Bremsstrahlung starting the process over again, but now with more particles involved. This exponential division of the original particle’s energy into more and more particles is what we call EM showering, and it continues until the last generation of photons no longer have sufficient energy to pair produce. During showering  $e^\pm$ ’s however still lose energy through the normal processes described above, so the shower development reaches a maximum at point when the  $n^{th}$  generation particles have an energy called the critical energy,  $E_C$  where the  $dE/dx$  from Bremsstrahlung equals that of ionization. This and most other EM shower properties, such as the lateral size parameter of the shower called the Moliere radius,  $R_M$ , are parameterized as a function of, and can be understood in terms of,  $X_0$ . Perhaps surprisingly, quantities like the shower depth and lateral size are only very

---

<sup>3</sup>that a charge particle must emit a photon when accelerated can be most simply understood as the fact that when a charge is moved, the EM field in the region around the charge (indeed filling all space-time) must correspondingly change. But because the speed of information transmission must be finite ( $\leq c$ ), this change must have a finite border that propagates at speed  $c$ . It can be shown that this propagation *is* in fact the emission of a photon.

weakly dependant on the initial energy of the incident particle which causes the shower [75].

In hadronic showering, the exponentiation occurs when the hadron strikes a nucleus and pops out two or more other high energy hadronic fragments, most often pions. For these showers then  $\lambda_I$  is the relevant length scale. Half of the produced pions will generally be neutral and since  $\pi^0$ 's immediately decay into two photons, EM showering then occurs simultaneously. This is why strict EM optimization for calorimeters cannot be perfect, and it is why sometimes hadronic showers will be falsely identified as EM Clusters, defining one source of background for our analysis. However as a large portion of energy is lost in the undetectable hadronic processes of the collision, the total EM energy released is generally a small fraction of the energy of the original particle, whereas for an original electron or photon, nearly all of the released energy is in principle detectable. Sometimes a calorimeter is designed primarily for hadron detection (the PHENIX ZDC and FCal are examples) : this requires much thicker calorimeter lengths, and is helped by something called *compensation*.<sup>4</sup> The PHENIX EMCal has very low compensation and is very thin, achieving EM optimization.

### 5.8.1 PbSc and PbGl

The PHENIX EMCal is really two different EM calorimeters. Six of its eight sectors employ one method for extracting the EM energy released in a shower, and the remaining two employ another. As shown in figure (5.6). The first method is the “Shish-Kebab” method: The six sector detector using this method is called the “PbSc” calorimeter, and its basic unit is a shish-kebab-like stack of alternating Pb and plastic scintillator blocks. The scintillator detects another type of electromagnetic radiation of charge particles in matter called scintillation. Scintillation radiation is visible or nearly visible light which can be measured by a photomulti-

---

<sup>4</sup>compensation can be achieved by allowing for some of hadronic energy loss to be released electromagnetically. This can be done by using an element such as Uranium, whose nuclei will become excited from hadronic interactions, and subsequently undergo an EM decay.

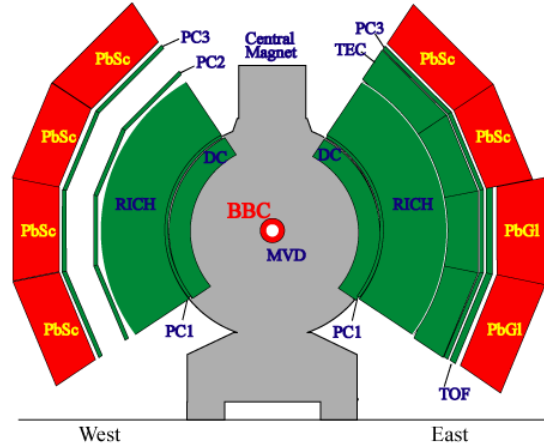


Figure 5.6: Side view of PHENIX showing the location of the PbSc and PbGl sectors of the EMCAL

plier (PMT) tube. PMT's work by Einstein's photo-electric effect and, held under very high voltage, output a current that is proportional to the amount of light detected (and the PMT voltage, a point which is important for understanding overall calorimeter calibrations. By *guiding* the light with other translucent materials from the scintillator's in the stack to the PMT's, some "sample" (to an excellent approximation, a constant fraction) of total shower energy is detected. For this reason, a calorimeter of this type is called a sampling calorimeter.

For many reasons, most importantly to obtain position information about showers, but also simplifying construction markedly, calorimeters are always segmented into small divisions, each an independent calorimeter itself, and placed in 2-D arrays. In PHENIX these individual segments are called *towers*, and it is in a single tower that the sampling shish-kebab is implemented for PbSc. In figure (5.7) this is evident. Each PbSc tower is 5.25 cm x 5.25 cm x 37.5 cm deep. Towers are arranged in the 72 x 36 tower *sectors* extending 4 m in the z-direction (parallel to the beam) and 2 m in the  $r - \phi$ , arranged symmetrically around the beam as illustrated in figures (5.6) and (5.2).

The PbGl calorimeter has a very similar overall structure to PbSc differing principally in its tower design. The energy collection method in this case, instead of the

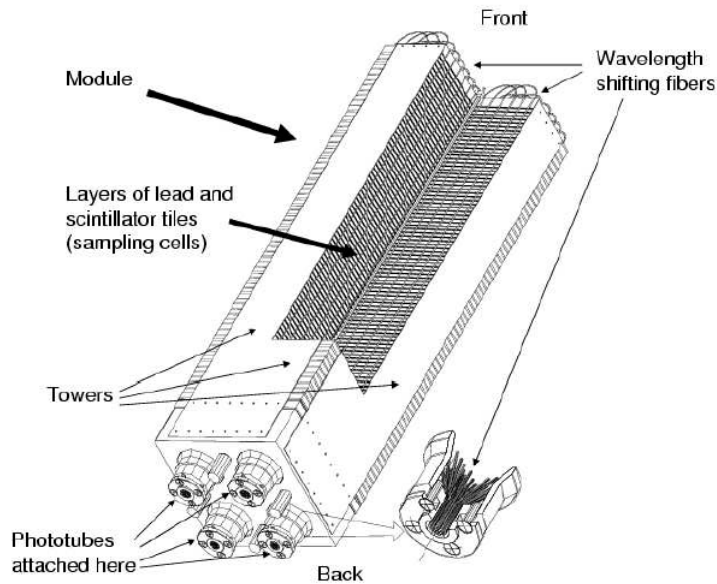


Figure 5.7: Cross section of PbSc towers, showing the shish-kebab structure. Note that in the picture, four towers are shown together, as they constructed into 2x2 units called modules.

Pb-Scintillator shish-kebab design relies on solid blocks of a homogeneous translucent mixture of Pb, glass, and Pb Oxide (Officially TF1 PbGlass 51% Pb-Oxide). Pb and Glass together is commonly known as “crystal”, though the mixture is not really crystalline in nature as is the case with the blocks in our experiment. Visible light output is again collected by PMT’s (the PMT choice is different for PbGl and PbSc) however in this case the source of the light is from the Cerenkov radiation of electrons traveling through the block compound. Cerenkov radiation is caused when a charge particle travels faster than the (reduced) speed of light propagation within a medium. Generally since the entire EM shower is contained within the light transmitting (“active”) portion of the calorimeter, such Cerenkov calorimeters suffer less statistical fluctuation and therefore have a better energy resolution than do sampling calorimeters. This will be discussed further in the Calibrations section. As is indicated in the Figure 5.8, no light guiding is necessary as the PMT can be nearly directly interfaced to the block. The PbGl towers are laterally smaller

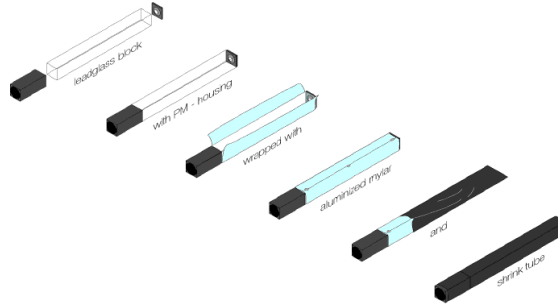


Figure 5.8: The internal structure of a PbG1 tower.

than PbSc towers: 4cm x 4cm with slightly more depth of 40cm. However the total sector size and distance from the interaction point is the same, resulting in a finer segmentation and better capability of resolving single showers.

### 5.8.2 Organization And History

As mentioned in Figure 5.7, PbSc towers are organized in 2x2 units called modules and then these modules are organized into 6x6 module *SuperModules* (SM). Each sector is made up of 18 SM's arranged 6x3. For PbG1, there are no “modules”, only 6x4 tower SM's which are arranged such that each sector contains 92x48 towers.

The PbSc calorimeter was constructed newly specifically for PHENIX, while the PbG1 calorimeter towers were used previously in several other CERN experiments including WA80 and WA98 ([44] , [143]) and simply repackaged into a different configuration for PHENIX.

### 5.8.3 Nominal Resolution

The energy resolution of a calorimeter usually has the form:

$$\sigma_E/E = A/\sqrt{E} \oplus B \quad (5.1)$$

with  $A$  and  $B$  usually given in percentages. The  $A$  term represents the poisson statistical fluctuations inherent in the showers and showering material. It is sensitive to how efficient the energy detection is, *e.g.* the sampling fraction in a sampling

calorimeter such as PbSc. In PHENIX the  $A$  term was determined with test beams of electrons with known momentum [37] as 8.2% for PbSc and 6.1% for PbGl. The  $B$  term, usually called the “constant term”, is mostly determined by the calibration quality. This is discussed in section 6.2. However there is an “intrinsic” amount of  $B$  that arises from detector effects such as geometry. From test beam this amount is 2.1% for PbSc and 0.8% for PbGl which represents close to an ideal calibration whereas in practice the calibration yields much higher values.

The position of a shower is obtained during the clustering phase using fits to the distribution of energy in the towers that were hit, described below in 5.8.4. It depends mostly on the segmentation of the calorimeter. This resolution was also measured quite accurately with the test beam. The results of this test [2] yielded the following empirical parametrization for the approximate 1 sigma RMS of position measurements  $\sigma_x$  in mm:

$$\sigma_x(E, \theta)[mm] = 1.55[mm] \oplus 5.7[mm]/\sqrt{E[GeV]} \oplus 19.0[mm] \sin \theta$$

$\theta$  here is the usual angle of incidence from the perpendicular to the calorimeter front face. The energy dependence comes from the improvement in the per tower energy resolution which translates to improved fits of the shower distribution as a function of position. The worsening of the resolution towards the edge the calorimeter exhibited in the  $\sin \theta$  term, is caused by larger fluctuations in the longitudinal shower development which negate any advantage gained by having the transverse information spread over more towers.

#### 5.8.4 Clustering

$R_M$ , the Moliere Radius, roughly defines a lateral cone in which 90% of the energy of an EM shower is contained. A empirical formula for  $R_M$  is  $R_M = 21 \text{ MeV } X_0/E_C$ , with  $E_C = 610 \text{ MeV}/(Z + 1)$ . For PbGl,  $X_0$  is 2.8cm, for PbSc, 2.1cm, so that our rough formula (the low  $Z$  elements dominating) yields  $R_M \sim 3\text{-}4\text{cm}$  for both calorimeters. Therefore it is quite probable that a shower will spread across several

towers. For a single photon or electron then, the *cluster* of towers corresponding to its sower must be identified. This process is called clustering, and being a common problem in many particle physics applications, there are many algorithms varying in speed and precision available. A single clustering algorithm is employed for both detectors in PHENIX, however with certain desirable customizations for each. Because we work in a high multiplicity environment, the algorithm must also be able to have some capability for separating overlapping clusters. In this aspect the PHENIX algorithm is optimized to separate photon showers. The shape of photon and hadronic showers in the PHENIX detector was first studied extensively using the a full hit level simulation that is used for studies detector wide called PISA which is based on GEANT [60]. Later shower response was verified and tuned using results from testbeam studies. PHENIX shower response will be discussed more in section 6.3

Once a contiguous two dimensional group of hit towers is identified, local maxima within the group are separated in “peaks”. A fit with a function  $F_i^\gamma$  containing a parameterization of EM cluster shape obtained from from test beam studies for each peak is then performed simultaneously for the whole group. This parameterization is an exponential in 2-D tower distance from the central max tower and partially takes into account the depth dimension as well, though only by constraining the 2-D fit parameters. In fact EM Showers can principally be distinguished in PbSc by the fact that most of the energy is deposited at a shallow depth. Parameters from the fit can then be used in particle identification (PID) cuts, as will be discussed later. The functional form of  $F_i^\gamma$  is

$$F_i^\gamma = P_1 \exp \left\{ \frac{-(r_i/r_0)^3}{P_2} \right\} P_3 \exp \left\{ \frac{-(r_i/r_0)}{P_4} \right\} \quad (5.2)$$

with  $r_0$  is the 5.54 cm shower size and the  $P_X$  are fitted with functions dependant on both the total energy  $E_{tot}$  and the impact angle  $\alpha$  defined as the complement of the angle of incidence. These functions are as follows:

$$P_1 = 0.59 - (1.45 + 0.13 \ln E_{tot}) \sin^2 \alpha \quad (5.3)$$

$$P_2 = 0.59 - (0.265 + 0.32 \ln E_{tot}) \sin^2 \alpha \quad (5.4)$$

$$P_3 = 0.25 - (0.45 + 0.036 \ln E_{tot}) \sin^2 \alpha \quad (5.5)$$

$$P_4 = 0.52 \quad (5.6)$$

The impact angle dependence arises due to the fact that as the impact angle increases for hits towards the detector edges, more of the shower depth is translated along the transverse direction, resulting in longer shower shapes. This is corrected for by finding an impact angle dependent parameterization from the testbeam results of the transformation matrix  $V$  that simply transforms via the matrix  $M$  representing all the cluster's tower energies back to a non-elongated shape  $M' = VMV^{-1}$ .

For simplicity during the fitting procedure, the cluster (energy) center of gravity is used as a determination of the cluster center. The impact angle dependence as well as that of the energy dependence must also be taken into account when making a final correction to the shower's position however, in order to take into account for effects due to the discrete nature of the center of gravity calculation.

### 5.8.5 Shower Merging

An important consideration of the fineness of each calorimeters segmentation is the ability to distinguish the two photons resulting from the decay of a high  $p_T$   $\pi^0$  ( $\pi^0 \rightarrow \gamma\gamma$ ). When the momentum of the  $\pi^0$  reaches a certain value, the decay kinematics are such that the minimum opening angle  $\theta_{\text{MIN}}$  between the  $\gamma$  pair, (which is near the maximum of the probability distribution  $dP/d\theta$  for the decay) is so small that the photons will hit the calorimeter such that they create only a single local maximum. In this case, a more sophisticated cluster splitting algorithm may be possible to develop to separate such photons, using a modified fit function which parameterizes well the merged photon clusters. More likely the merged photon shape can be compared and goodness of fit parameter stored for cutting. However, for the

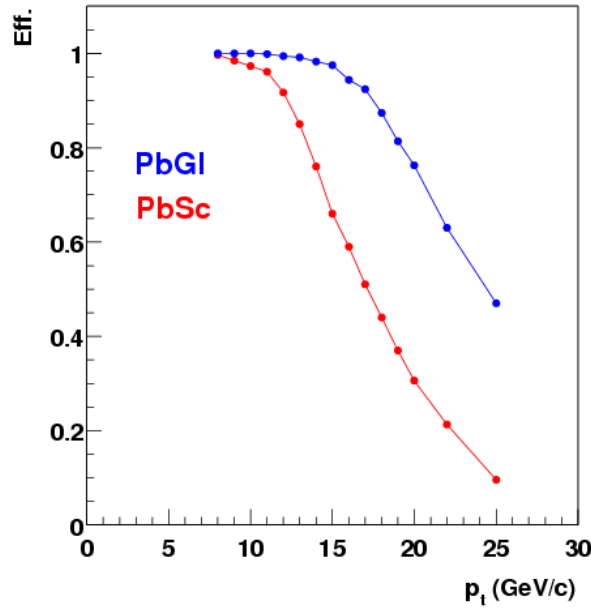


Figure 5.9: The probability that a  $\pi^0$  is lost due to the “Run2” merging inefficiency at high  $p_T$  [81]

reconstruction code used in this analysis, (Run2) this feature of the code was not necessary since these highest  $p_T$  values were just barely reached or not reached at all. Nonetheless there is a noticeable drop in the probability of separation due to this effect in high end of the  $p_T$  region we will measure. See figure (5.9). As will be shown in section 6.6, the  $\pi^0$  efficiency above  $p_T > 10$  GeV/c correspondingly drops in a noticeable fashion.

### 5.8.6 Photon Corrected Energy $E_{core}$

Besides the splitting of clusters based on the photon shape fit function, the photon shape is also used to make an optimized determination of the energy, assuming the cluster comes from photon sources. This procedure is based on the idea of defining a shower *core* and it primarily is introduced to reduce multiplicity effects of overlapping. If two photon showers do overlap they are most likely to do so only in their peripheries. Because of the fast fall of energy with distance apparent in formula 5.2, such regions of overlap should not contribute a large proportion of the

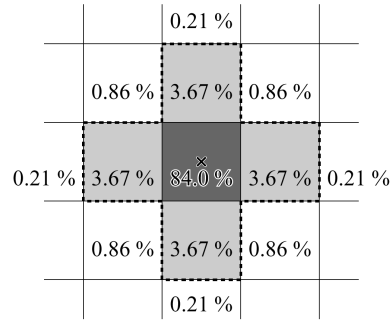


Figure 5.10: Typical distribution of the spread of energy in a cluster amongst surrounding towers, when the photon impacts a tower center. figure from [141].

cluster's energy anyway. As shown in Figure 5.10, fairly independently of energy, if a photon impacts a tower directly in its center, the shower shape is such that the towers directly diagonal to it only contain less than a % of the shower energy. The idea of the core energy, is that the low energy regions of overlap can generally be ignored. Specifically the corrected energy stored in a variable we call  $E_{core}$  ignores the energy of hit towers in the cluster peak area with energy less than 2% of the total in the cluster energy tower sum. The summed energy is then corrected back up based on the shape parameterization prediction of the total energy. This causes the energy resolution of the  $E_{core}$  energy to be slightly worse than the true total, since depending on where in the maximum tower the photon impacted, the total ignored energy can be up to  $\sim 20\%$ . However this increase, amounting to  $\lesssim 1\%$  increase in the resolution, is insignificant compared to what can be as large as (depending on the energy) a nearly 10% improvement of the energy determination for clusters suffering overlaps.

## 5.9 Data Acquisition and Triggering

Such a complex detector as PHENIX requires an even more complex data acquisition and triggering system, involving customized fast electronics and multiple *online* computer farms. figure (5.11) demonstrates this. This figure is obviously too busy to really understand so let me describe the basic different components and their

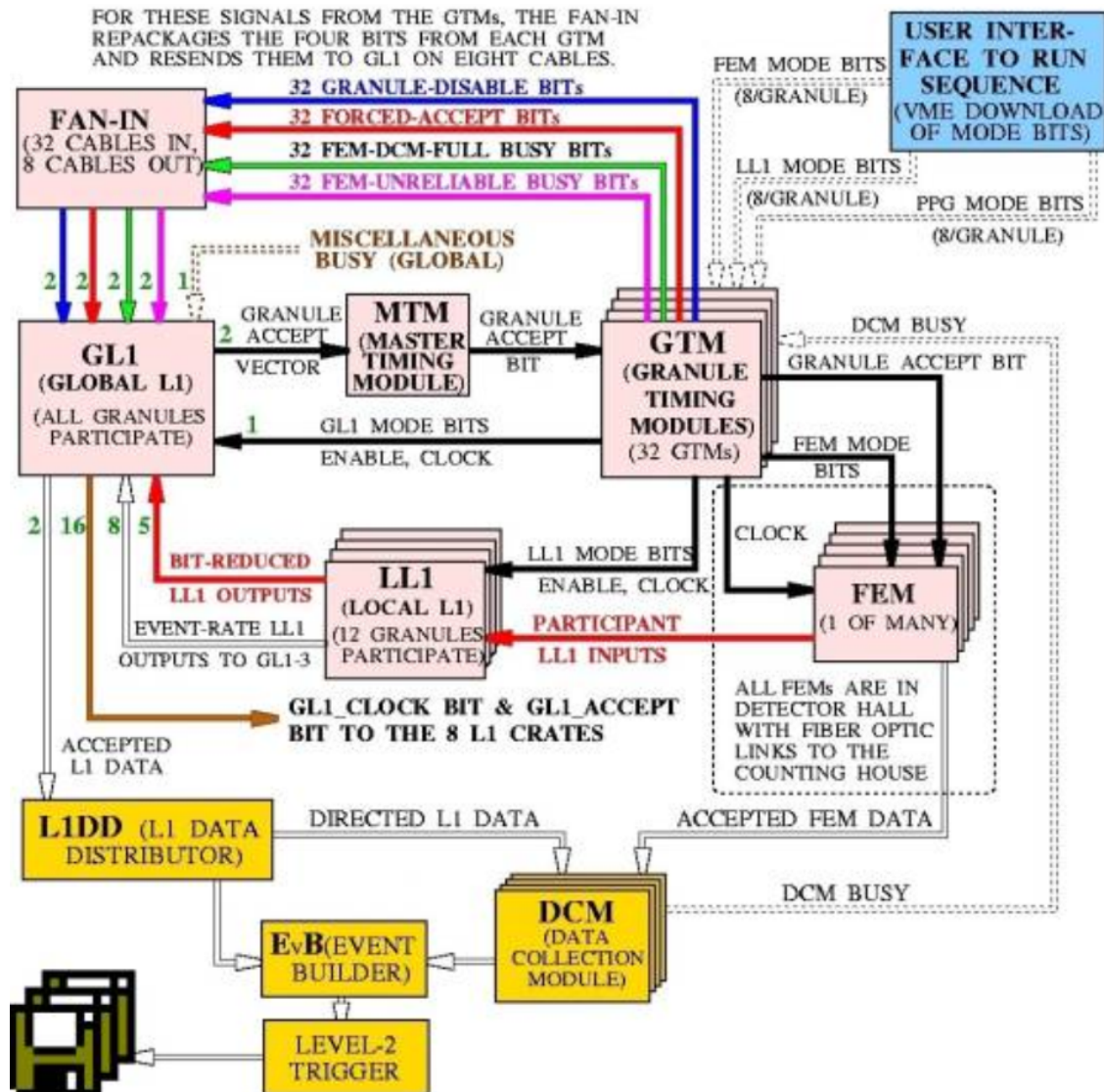


Figure 5.11: The PHENIX Triggering and DAQ system, one of the experiment’s most important aspect as principally a “rare-event” experiment, is insanely complicated. Fortunately some of us understand it.

workings here.

When Au-Au beams are circulating at full energy in the RHIC ring, it takes approximately  $20 \mu s$  for an ion to make the trip around. Beams of ions are split into  $N$  bunches where  $N$  varies but is  $\mathcal{O}(10)$ . Therefore in order to properly control the beam, RHIC electronics need to operate at a frequency on order of MHz’s. Indeed, the “Master Clock” of RHIC, an oscillator which drives all electronics of the

4 RHIC experiments cycles at  $\sim 25$  MHz. On the other hand, projected maximum luminosity of RHIC cause events that will trigger the BBC/ZDC triggers to occur at a rate on order of a tenth of this frequency, for Au+Au, even less, on order of 10 kHz. PHENIX has the fastest DAQ of the 4 RHIC experiments with electronics at the master clock speed that can sample certain detector signals, such that on average, many operations can occur in these electronics in between actual events. Also, the electronics sampling *all* detectors called Front-End Electronics (FEE) can digitize and store their signals in memory cells called AMU's at similar rates, high enough that many storages occur between each real event. This provides the basis of the idea of triggering: when the triggering electronics register something they deem interesting, e.g. a signal in the BBC North *and* South units, they can cause the data stored by the FEE's, themselves arranged in modules called Front-End Modules (FEM's), to be sent up for a given event.<sup>5</sup> The interesting signals along with the detectors and triggering electronics which process them are thus what actual constitute what are called *Level 1 Triggers*. These triggers can range from triggers that identify high- $p_T$  cluster candidates in the EMCal, electron candidates, muon track candidates, and basic combinations of such items—as described above, the BBC/ZDC provide the minimum bias triggering. The trigger signals interfaced with the FEE's with a set of electronics on called *Granule Timing Modules* (GTM's) which get their name because they also provide the clock signal which drives the FEM's. A list of the level1 triggers used in the *Au + Au* Run2, a representative group is given in Table 5.1

Many of the level1 triggers existed in two forms. The “LL1” triggers were designed to do more complex calculation (for example, the fast calculations with combinations of both EMCal and RICH data) with their own FEM's. The most complex of these algorithms are in the MUID which does a very primitive form of tracking

---

<sup>5</sup>the process of reading out the AMU's however, takes a non-trivial amount of time, and in “single event buffering” mode, no other data can be taken during this read-out time. This is the main source of *deadtime* for PHENIX, at the time of this writing, limiting the maximum event rate that can be processed to be less than the actual rate trigger events occur. In the (hopefully) near future, this limitation will be overcome by running in a “multi-event” buffering mode.

Trigger	Notes
ERT Gamma	EMCal High pT Tile trigger looks for high energy tower sums. ERT's not operational during Run2
ERTLL1 Electron	Match RICH rings to EMCAL clusters Make EMCAL energy threshold cut
MUIDLL1	Find "roads" through MuId panels Find two muon trigger candidates
BBCLL1, BBCNS	looks for coincidences in BBC signals cuts on primitive vertex calculation
ZDCNS	looks for coincidences in ZDC signals

Table 5.1: Overview of level 1 triggers

extremely quickly. Because of their complexity however, many of these triggers were not ready during the RHIC commissioning Run and the 2001  $Au + Au$  Run2. Therefore an alternative set of *Blue Logic* triggers was employed, based on a more direct analog connection to the detectors placed in an alternative DAQ route and logic provided by basic NIM and CAMAC units.

Once the FEE's are instructed, the *push* mechanism of the PHENIX DAQ is initiated. The next several steps of this "push" architecture are designed such that they handle everything the FEE's want to send them. The first component are the Data Collection Modules (DCM)'s, which were designed and built at Nevis. These receive the FEE data via standard fiber optic connections. The DCM's are designed in "Granules" and "sub-Granules" each responsible for a certain set of detector FEM's. The DCM's take care of formatting the digitized data into basic units called *packets*. They also can perform *zero suppression* in which channels with no data are "removed" from the data stream and thus do not incur any further overhead (caused by e.g. header information) on the DAQ. In the future, the DCM's may be upgraded to even perform basic calculations which could be used for decision making further downstream of the data flow. Despite their "push" design intention, with all this activity, the DCM's can become backed up, and appropriately send a *busy* signal via the GTM to the FEM's so that data flow is stopped temporarily. This is a normal operating condition and the entire DAQ is not stopped for this.

The next component in the DAQ however is not afforded the luxury of being busy in normal operating mode. This first part of the *Event Builder* (EVB), a farm of networked computers, are a set of computers called Sub Event Buffers (SEB's) which each receive the output of a DCM group. At this point then, data packets from a single event will be spread across many SEB's. Aptly, considering its name, it is the job of the EVB then to combine ("build") the various SEB packet groups into a single data structure called an event. This it achieves with another set of computers called Assembly Trigger Processors (ATP's) which each poll the SEB's (thus ending the "push" paradigm) and collect all sub-events and assemble them. The computers used in the event builder are standard PC's, in fact, in all running periods to date, running Microsoft Windows. Hence, the conceptual majority of the Event Builder is mostly its software, which is custom C++ code written also by Nevis/Columbia, employing multiple standard networking protocols.

At this point there can be two possibilities. Obviously the ATP's then need to send each event they've assembled (many ATP's working in parallel, and therefore processing many events in parallel) somewhere. The place they send events to is the "logging" system. The logging system is several more very fast multiprocessor computers called "buffer boxes" with extremely fast hard drive arrays. Therefore, the first home of fully formatted PHENIX raw data (PRDF files) is on a hard drive, where many events are collected into files. Actually because the amount of data flowed is so high ( $\mathcal{O}(100)$  MB/s, the buffer boxes are drained in a round robin fashion onto a tape storage system common to all the RHIC experiments called HPSS. Tape is still the only affordable way to store such large data volumes. For Run-2, the experimental run for this thesis, the total size of all files recorded was the better part of 100 TeraBytes. For the recently ended Run-4, the number was 1000 times this.

The other possibility for the ATP, is that before sending up an event, and while it is still in memory, another round of triggering can be performed. The level2 triggering system has its own section in the PHENIX Online-Systems NIM article

Trigger	Method
Single Electron	Match RICH rings to EMCAL clusters Make EMCAL energy threshold cut
Electron Pair	Calculate invariant mass of electron pairs Make invariant mass cut
Single Muon	Find roads through MuId panels
Muon Pair	Find two muon trigger candidates
High $p_T$ EMCAL	Find EMCAL clusters Make threshold cuts
High $p_T$ Charged	Match Pad Chamber and Drift Chamber Hits Cut on the bend angle
Coherent Peripheral events	Look for ZDC trigger with no BBC trigger Look for PC hits
Centrality Selection	Use BBC and ZDC to estimate centrality Make centrality cuts on selected triggers

Table 5.2: Overview of level 2 trigger algorithms.

[19] and in many ways functions as a separate sub-detector group within PHENIX, just as some of the Level1 trigger systems such as the EMCAL-Rich Trigger (ERT, which even has its own FEM's). As described above, the PHENIX DAQ is specially designed for biased trigger selection of rare physics from a high luminosity rate of events and this is accomplished by a set of base, also known as level1 physics triggers, which select or reject events based on interesting signals found in various detectors. After this initial event selection, which is limited in scope generally to single-detector or two-detector signals and performed by fast electronics, the level1 selected events can then be subjected to a second round of triggering in order to further increase the most interesting DAQ bandwidth, known as Level2. During the second half of the  $Au + Au$  Run2 on which this thesis reports, Level2 sampled all minimum bias events by partial reconstruction, kept a random portion as an unbiased sub-sample, and of the rest, kept only the fraction that fired any one of several level2 triggers. A review of these triggers is given in table 5.2. As much of the data in this thesis is based on the High  $p_T$  EMCAL Trigger, more details of the use of this trigger can be found in 6.4.

One final point about the PHENIX DAQ is that, as its many components have

themselves many pieces, it is very configurable. This of course was its design. New detectors are routinely added and some detectors are removed for certain running periods. Tests are run with the detector itself taken apart. Numbers of such diverse situations are handled by the same complicated yet extremely flexible DAQ design. This allows for convenience in upgrading. Also, its trigger integration and the quality of the triggering are PHENIX's single strongest point. Indeed, PHENIX rare-event capability makes up for what it lacks in acceptance by the ability to take many events and thus study extremely rare processes.

# Chapter 6

## Analysis

The history of experimental physics is self similar. As larger physical trends are observed, stops and sputters occur in the understanding of them. Such is more or less how Griffiths tells the history of the acceptance of QCD in [98] from its original proposed formulation by Gell-Mann in 1964 until its full acceptance by the physics community in the late 1970's. Progress is often halted because certain complicated phenomenon are not taken into account and the results are then hard to interpret. In the very same way, the details of an experimental analysis can go the very same way—through fits, stops and sputters as observed signals show non-intuitive behavior. Our analysis has been no exception—as we shall discuss, a large amount of time was spent trying to fix a faulty calibration which was ultimately abandoned and redone. Such hard work and long hours make the work all the more gratifying however, and improve our understanding's for the next time we encounter the same types of issues.

In the following chapter, we discuss the details of the analysis which yielded the results presented in this thesis. This analysis consist of at least three primary components: A PbSc  $\pi^0$  and direct photon analysis performed by the thesis author, a similar Au+Au analysis using nearly identical (in some cases identical) techniques, PbSc and PbGl analysis (the Muenster or PbGl analysis) performed by Christian Klein-Boesing of the PHENIX University of Muenster, (Germany) Group [127], and a similar  $Au + Au$  PbSc-only analysis (the Waseda-BNL analysis) performed by

Gabor David of BNL and Takao Sakaguchi of Waseda University, Japan [?] which used slightly different cuts and correction methods. The results of a further analysis of the same kind but using Run2  $p + p$ , also performed by Klaus Reygers also of Muenster will also be referred to. The focus of this chapter will be on the work done and methods used in the author's analysis. However when important or especially relevant, aspects of these other analyses will be pointed out. Since it was especially important to have the separate PbGl technology incorporated with its different systematics this will be done most often for the PbGl Muenster Au+Au analysis. However unless otherwise mentioned, it can be assumed that nearly the same methods or identical were used in the other analyses—that is, they are essentially the same analysis, but with the application of at least slightly different cuts and in the case of PbGl a wholly different detector. For the final results shown in the Results section (7), only the Meunster (because of the use of the PbGl) was included in the final average along with our results.

## 6.1 Glauber Model Calculations

In our discussions of the definition of centrality, we noted that although these can be defined analytically under the basic set of assumptions, due to certain ambiguities as to the effects of more complicated phenomena, such as fluctuation in the locations of the nucleons within the nucleus or the meaning of the nucleon thickness, it is actually more accurate and simpler to explore the effects of different physics assumptions with a fast Monte Carlo simulation based on distributions. Furthermore, Monte Carlo allows much a simpler connection to the real detector effects involved in making the centrality determinations.

The implementation of the Glauber model used by PHENIX starts with the population of each nucleus with 79 protons and 118 neutrons according to the Woods-Saxon density profile, equation 3.2. Different models of fluctuations in this population are tried (*e.g.* the inclusion of a hard nucleon “core” [139] which prevents nucleon overlap) and used to evaluate the final systematic uncertainties. According to the Glauber model assumptions already discussed in section 4.3, inelastic collisions are generated based on the probability of interaction in the  $N - N$  inelastic cross section, taken to be 42.4 mb, but this is also varied along with many other parameters in the final systematic uncertainty evaluation. The simulation is run in bins of impact parameter ranges. Based on the number of inelastic sub-collisions generated, the experimental response is then simulated. Since as discussed in section 5.5, PHENIX uses both the ZDC and BBC detectors in its centrality determination, this simulation has two corresponding parts.

During a central heavy ion collision, the nucleus is in some ways “blown apart” by all the inelastic collisions which occur. However it is found that the neutrons which do not suffer collisions, *e.g.* in the periphery of less central events, essentially do not go anywhere, but are simply disassociated from the nucleus and continue in the beam direction (at zero degrees). The Zero Degree Calorimeter (ZDC) response then depends on the number of *spectator neutrons* which do not participate in the any collision. Spectator nucleons are described visually in Figure 4.1. It is assumed

that to first order this is just the number of neutrons which weren't involved in a collision. However based on empirical measurements from the NA49 experiment's measurements in  $Pb - Pb$  reactions at the SPS it is known that a certain fraction of spectators will be diverted from zero degrees due to intrinsic nucleon Fermi motion or more importantly in our case because they will still be associated with charged fragments which will get swept out of the ZDC acceptance due to the DX magnets that steer the beam entry and exit to and from the PHENIX detector. Based on initial RHIC data and GEANT simulations [64] the following impact parameter dependent formula is used to parameterize the probability that spectator neutrons that will miss the ZDC,

$$p_{loss} = 1 - (1 - p^{swept}(b)) (1 - p^{acceptance})$$

where  $p_{swept} = 0.3305 + 0.0127b + e^{(b-17)/2}$  and  $p_{acceptance} = 0.2857$ .

The energy of the remaining spectators which hit the ZDC are smeared according to the ZDC energy resolution of  $\sigma_E = 218\sqrt{E[GeV]}$  and the total summed energy is used for the centrality determination.

As is apparent, the calculation of the number of spectator nucleons is conceptually quite straight forward and therefore expected to be quite accurate. This is why originally the ZDC's were chosen at RHIC to be good centrality determiners. The BBC response, on the other hand, is not quite as straight forward to simulate but does not suffer from the double value of the ZDC response discussed in section 5.5. Since total particle multiplicity is known to scale with  $N_{participants}$  (see section 4.3) assumption is made about the scaling of the soft particle production, consistent with RHIC multiplicity measurements, that  $dN_{charged}/d\eta$  is a monotonically increasing function of  $N_{participants}$ . This scaling is modified as being  $\propto N_{part}^\alpha$  where  $\alpha$  is deviated from one in order to test the uncertainty due to this scaling assumption. For each participant, a number of charged particles is thrown according to a Poisson distribution. The mean of this Poisson distribution  $\mu$  is chosen to be 0.5 based because this is the value that causes, with 93% probability, two hits per BBC. This

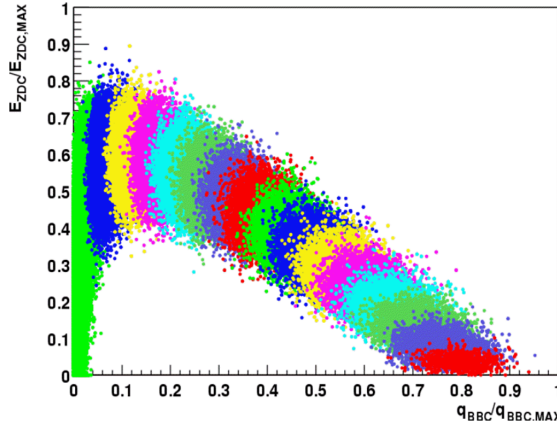


Figure 6.1: “Banana Plot” of Glauber Simulated BBC/ZDC Response. The different colored blobs correspond to different impact parameter ranges which in turn correspond to different centrality ranges. This is how the clock method slices in 5.5.

is equivalent to the real BBC trigger efficiency found in full GEANT simulations as discussed in section 5.5. Finally consistent with the real response of the BBC per charge track, a total amount of signal is assigned to the BBC.

For each centrality range, ZDC/BBC response for the corresponding impact parameter range is generated in the simulation, as shown in Figure 6.1. This is used to determine parameters (the slice boundaries) for the “clock method” of centrality determination from the data, already discussed in 5.5. Compare this figure to 5.5.

In order to determine the systematic uncertainties in the centrality and other related quantities calculated with the PHENIX Glauber simulation various assumptions of the simulation inputs were tested by variation. Variations considered included: varying to the  $p_{loss}$  parameterization, varying the  $N + N$  inelastic cross section  $\sigma_{NN}$ , varying the fluctuation model of the nucleon population, and varying the parameters of the Woods Saxon nuclear thickness distribution within very conservative ranges covering their systematic errors. In table 6.1, the results of the simulation are presented along with systematic errors. The final calculation of the total  $Au + Au$  cross section  $\sigma_{Au+Au}^{geo}$  is  $6847 \pm 542$  mb.

Class	$N_{part}$	sys.err	$N_{coll}$	sys. err.	$T_{AB}(mb^{-1})$	sys. err.	$\langle b \rangle (fm)$	sys. err.
0- 10%	325.2	3.3	955.4	93.6	22.75	1.56	3.2	0.2
10- 20%	234.6	4.7	602.6	59.3	14.35	1.00	5.7	0.3
20- 30%	166.6	5.4	373.8	39.6	8.90	0.72	7.4	0.3
30- 40%	114.2	4.4	219.8	22.6	5.23	0.44	8.7	0.4
40- 50%	74.4	3.8	120.3	13.7	2.86	0.28	9.9	0.4
50- 60%	45.5	3.3	61.0	9.9	1.45	0.23	11.0	0.4
60- 70%	25.7	3.8	28.5	7.6	0.68	0.18	11.9	0.5
70- 92%	9.5	1.9	8.3	2.4	0.20	0.06	13.5	0.5
0- 92%	108.4	5.1	233.1	34.7	6.30	0.87	9.4	0.4

Table 6.1: Table of Glauber Model Predictions with systematic errors.

## 6.2 EMCal Calibration

The general working of the PHENIX EMCal, including its divisions into towers is explained in 5.8.1. The PMT analog voltage signal is digitized by an Analog to Digital Converter (ADC) which discreteizes the voltage into 12-bit words representing an integer number of counts which make up the stored raw data. To be equated to an energy, the discrete ADC counts for each tower  $i$  must be multiplied by a gain factor  $g_i$ . The energy calibration is then determined by the accuracy of these gain factors. This is how all calorimeters work. There are generally many ways of doing this and many of them have been exploited at PHENIX. They generally fall between under two categories. First, “direct methods” measure the shower response to single particles of known energy. The particles used are generally electrons for EM calorimeters, but can even be charged hadrons or muons if the MIP Peak positions for those particles are known. The other class of methods are “statistical methods” where the response of many test particles are combined to make the gain determinations, and the emphasis is more on making the calibrations the *same* for all towers such that there is more uncertainty only on the absolute scale of the average tower gains. Realistically, because in a real experiment such as PHENIX, both the response and gains can fluctuate, statistical averaging must always used, so in a sense even direct methods are statistical. The final calibration used for this thesis’ analysis can be considered a mix of statistical and more direct methods.

### 6.2.1 Direct Methods: The Ideal “General Theory” of Calibrations

EM showers get higher in energy the showers get slightly bigger <sup>1</sup> and even low energy clusters take up more than one tower in a finely segmented calorimeter such as the PHENIX EMCal. Getting  $g_i$  for a single tower with direct methods is complicated by

---

<sup>1</sup>As discussed in 5.8, the “proportionate size” of showers are nearly independent of incident energy, and dependent mostly on the calorimeter material. For example 90% of the shower energy is laterally contained within  $R_M$ , which is a constant of the calorimeter material. However this means that in the small fraction of the energy found in the periphery of the space the shower takes up becomes more significant on an absolute scale.

*energy sharing*, the fact that calibration test particles will usually have showers that span more than one tower. Therefore ideally getting true gain factors from a particle involves solving a system of (at least)  $N_{towers}$  linear equations  $E_j = \sum_{i_{tow}} g_{ij} ADC_i$  where  $E_j$  is the known energy of the  $j_{th}$  test particle.

There are a number of reasons in practice why this idealized direct method is not used. For one thing, the number of towers is generally quite large (for PHENIX  $N_{towers} \sim 27000$ ) and the matrix  $g_{ij}$  is not *sparse* such that fast numerical methods for matrix inversion are amenable. So formally solving the system is generally not the preferred way to get the gain factors. If it were absolutely necessary to use this method, suitable algorithms for performing these matrix inversions with appropriate precision and speed probably do exist somewhere, or likely could be developed — - perhaps even the latest algorithms developed by the lattice community could be employed. But there is a more fundamental reason this method would not necessarily even always be adequate. The shower process has fluctuations, and the fluctuations can even be made worse by the ADC bit truncations. Therefore methods that represent a statistical average are used in PHENIX.

### 6.2.2 Averaging Methods of PHENIX

Another complication of gain determinations is that the gain factors actually change over time (called *gain drift*) due to instabilities in the PMT high voltage sources and sometimes transient electronic noise interference. Sharp changes in the gains can occur each time the voltage sources are turned off and on, as they must be sometimes (*e.g.* always at least between runs in PHENIX). It is impossible to track the instantaneous drifts so a suitable gain average is determined over periods where the voltages were continuously kept on. The PHENIX PbSc was designed with a complex gain monitoring system which used a laser with known intensity being frequently fired in the PMTs in order to keep the time over which the gain average was taken to be small. However due to technical problems, the monitoring system could not be used for PHENIX Run2. But as long as even a rough level of con-

stancy can be verified, averaging over much longer periods of time only results in an effective worsening of the calorimeter resolution constant term (see section 5.8.3) which is easily accounted for in MC. In effect the PHENIX EMCal calibration for this analysis was a very rough initial calibration that was improved incrementally through a series of gain *corrections* using a variety of test particles and methods and ultimately customized for three long running periods over which the gain averages were determined.

### 6.2.3 Test Beams, MIP calibrations, Energy Sharing

Before being placed in the PHENIX configuration, each SM of the PbSc EMCal was calibrated using cosmic ray muons in a test stand. Such a situation is most ideal for calibration, since these muons cannot shower either hadronically or electromagnetically, and, in the test stand it can be ensured that only a single tower will contain the ionization so there are no energy sharing effects. The energy at which the MIP peak appeared at was first approximated and all towers were adjusted such that the peak occurred in the same location, ensuring a uniform *relative* calibration. The correct absolute energy position for the MIP's was then determined from test beams. For PbGl the initial calibration situation was a different one as discussed in the next section, but the test beam was still used to verify the absolute calibration.

Two sets of test beam measurements of both electrons and hadrons, the first at lower energy at BNL using the AGS [1] and the second at higher energy at CERN using the SPS were used to establish basic performance parameters of the EMCal for both PbGl and PbSc. The resolution parameters discussed in section 5.8.3 were measured. Also, the absolute location of the MIP peak (280 MeV) was determined as shown in Figure 6.2. Together with the cosmic muons established a basic starting point from which the various gain corrections could be applied.

In the summer of 2000, a commissioning run (Run1) with a beam energy of 130 GeV undertaken at RHIC. During this run only the W0 and W1 sectors of PbSc and both PbGl sectors (E0,E1) were operational. An initial set of calibrations for

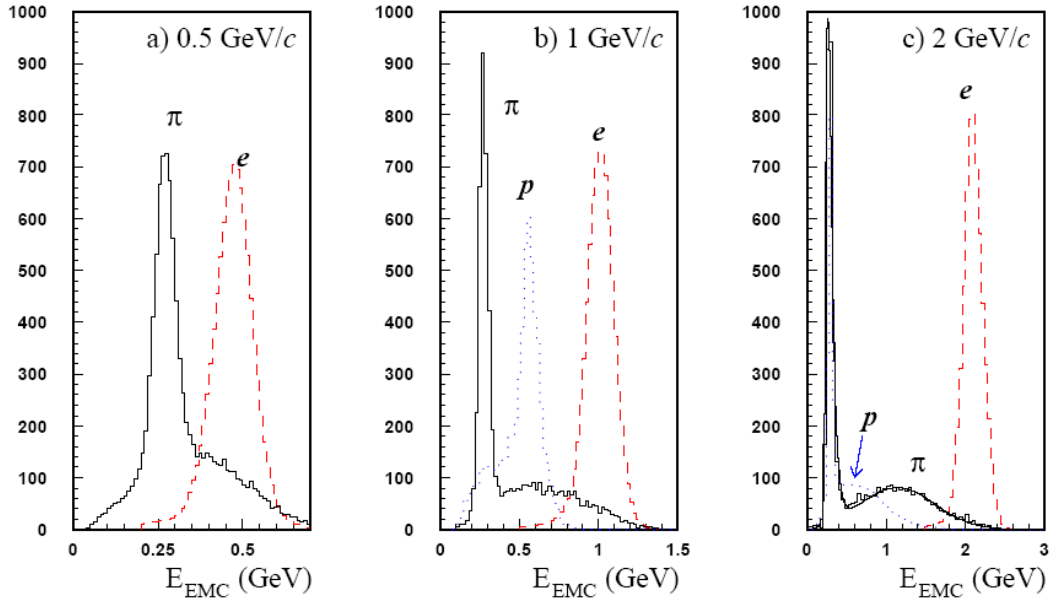


Figure 6.2: Test Beam Response of the PbSc EMCAL to various particle beams.

these sectors was determined again using MIP's, this time from physics processes in the collisions as described next, and also further corrected using a slope method similar to that described in 6.2.5. For the 2001 Run2 (this thesis data), an almost identical procedure was used to calibrate except that for the four sectors of Run1, the Run1 calibrations were used as the starting point. For PbSc, a second iteration of MIP peak corrections was first applied but then later found to be problematic as discussed below. For PbGl an additional method of slope corrections were also applied discussed in the next section. Finally a set of sector by sector corrections were determined from  $\pi^0$  invariant mass distributions. In this section we'll describe the two most important energy calibration corrections, the MIP and the  $\pi^0$ .

In a typical RHIC event, hundreds of charged particles are produced and traverse the EMCAL. The tracking system can be used to veto EMCAL clusters caused by neutral particles (the opposite of charged contamination removal discussed in 6.7). Therefore MIP peaks offer an good way to correct the gain factors and even monitor them. However things are more complicated than in the cosmic muon test stand conditions for which the initial calibration was determined. First, due to the non-

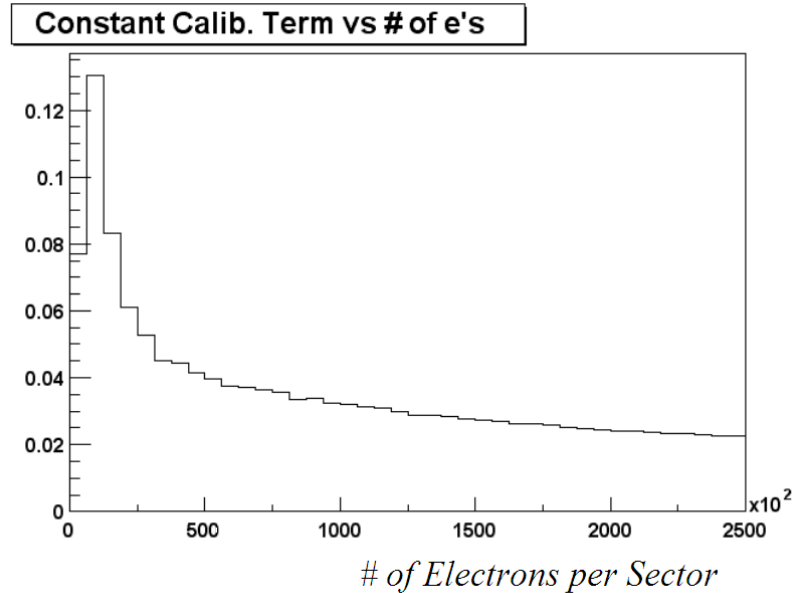


Figure 6.3: Improvement of calibration with an iterative “Kalman” method where for each electron, *all* towers contributing to the shower have their gains adjusted according to the (average) deviation of the *whole* shower energy from the input electron momentum. The true  $e$  momentum is obtainable experimentally from the tracking momentum determination. In this MC study the energy resolution of the calorimeter already has a constant  $B$  term of 2.1% so the convergence cannot go below this value, and the fastest part of the convergence has already occurred by about 25K electrons per sector.

radial configuration of the towers, just as with showers it is quite probable that more than one tower will share a single MIP leading to the same energy sharing problem with the direct method calibration above. A more practical solution to this problem is relying on successive iterations in a “Kalman” style averaging scheme. In this type of scheme a running average is determined from the test particles which improves as the number of test particles increases by effectively taking the cumulative history of all test particles into account. In Figure 6.3 a simple MC study shows that even for high energy electron showers which are usually spread over multiple towers, a convergence to nearly the proper gains with such a method can be obtained with only 25K to 50K electrons per sector. Such a correction scheme using electrons was actually implemented and used later in the 2003 Run3.

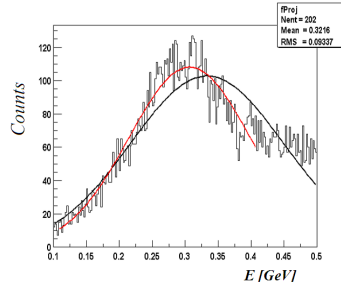


Figure 6.4: Typical Energy Distribution from which MIP-average correction is extracted. Please see the text for explanation of the red and black curves.

Even though Figure 6.3 is for electron showers, it in fact tells us that the effect of energy sharing in our MIP corrections should be small. Referring to the caption of the figure, energy smearing for MIPs is much smaller (at most 2 towers) so that we should expect the convergence for MIPs to be quite a bit faster. Since about 10 times as many MIPs were used in the MIP calibrations we may assume that a single determination using a similar cumulative averaging scheme (the averaging procedure is described in the next paragraph) will have only second order effects due to energy sharing.

A different averaging scheme is necessary when using MIP's (at least when using MIP's from particles that include hadrons) because some fraction of charged hadrons will leave much larger contributions than the MIP value due to hadronic showering as is obvious from Figure 6.2. Obviously the hadronic showers should not be included in the average, so these must be excluded statistically. As shown in Figure 6.4, for each tower the energy distribution is made, and iteratively fit first with a combination of an exponential and an error function (the black curve) and then using the results of this fit to cleanly fit the MIP peak area with a gaussian (the red curve). Corrections are then made such that the gaussian mean is manually moved to the proper value of 280 MeV for each tower. Typical MIP corrections were on the percent level.

In fact, both the energy sharing problem and the background subtraction both depend on the position of the tower in the calorimeter. These effects arise primarily from larger lateral spread of showers or MIPs as the impact angle on the front face

of the calorimeter changes with  $\phi - \eta$  (or equivalently  $y - z$ ) position. Therefore all calibrations which are based on single tower responses (as opposed to the ideal direct method above) have an impact angle dependence which in most cases is non-negligible and must be accounted for. This applies also to the slope methods discussed below 6.2.5.

The disadvantage of the MIP calibration is that it only probes a very low value of energy. As there could be detector effects that cause high energy measurements to be more sensitive to imprecisions at these lower energy values, it is necessary to verify the calibration at higher energies and if necessary further correct. This was accomplished by looking at  $\pi^0$  invariant mass peak location at high momentum, and cross checked with electrons for PbSc. The electron cross check will be discussed in 6.6.8.

#### 6.2.4 $\pi^0$ Corrections

The general idea of using  $\pi^0$ 's for the calibration is that decay photon pairs from a  $\pi^0$  will have an invariant mass  $m_{inv}$  (see 6.3) equal to the  $\pi^0$  mass.  $m_{inv}$  is proportional to the product of the two photon energies (equation 6.3) so if we use pairs only very symmetric in energy ( $E_1 \cong E_2$ ) we can derive an average correction for both photons  $\propto \sqrt{m_\pi/m_{inv}}$ . Energy sharing is even more of a problem in this case since we are the correction is shared across two separate showers. Naively we might also expect its effect to be quite different since in this case the sharing comes in the form of a product of energies and not just a sum. However, interestingly enough due to the energy symmetry requirement, we should actually expect the overall effects from energy sharing to be very similar to the case of the electrons.<sup>2</sup> Since we look at such high values of energy where the production rate of pions is greatly reduced, we practically do not have enough statistics for individual towers that we

---

<sup>2</sup>If  $E_1 \approx E_2$  then  $E_1 = E + \epsilon_1$  and  $E_2 = E + \epsilon_2$ .  $m_{inv} \propto \sqrt{E_1 E_2} = E \sqrt{(1 + \epsilon_1/E)(1 + \epsilon_2/E)} \approx E(1 + \frac{1}{2}\epsilon_1 + \frac{1}{2}\epsilon_2) = E_1/2 + E_2/2$ , dropping terms quadratic and higher in  $\epsilon/E$ . Therefore to first order it is just like we are looking at the sum of the two shower energies and therefore the sum of all tower energies involved. Since there are two showers however, there are more total towers in the sum.

can safely ignore the effects of energy sharing or even find a  $\pi^0$  peak. Therefore we must combine the statistics of many towers and therefore can only derive an average correction that applies to the whole tower group. For the final calibration, the  $\pi^0$  calibration method was only used to derive sector by sector average energy scale corrections.

One further complication of using  $\pi^0$ 's for calibration adjustments is that, due to energy smearing effects, the position of the  $\pi^0$  invariant mass peak is shifted according to the energy of the  $\pi^0$ . Therefore the amount of energy smearing must be known. However the amount of constant ( $B$ ) term energy smearing is itself dependent on the calibration. Therefore the calibration and the smearing determination become linked and therefore correlations in the systematic uncertainties due to these two sources can exist. This is discussed further in section 6.6.10.

### 6.2.5 PbG1 and the Slope Method

Electron, MIP corrections, have the disadvantage that a different (in the case of MIP, *very* different) physics process is generating the energy loss, difference which lead to slightly different calorimeter response. For example electrons will generally start showering earlier on average than photons. Such differences mean that systematics for calorimetry of these particles can be slightly different than for photons (which we are primarily interested in studying) which could lead to the optimal calibrations for photons not being realized. Using the  $\pi^0$ 's has its own set of issues to contend with as mentioned above. Therefore a calibration using only photons is desirable. The slope method is one such method. A set of corrections based on this method was used both in the final Run2 data for PbG1, and also in the initial Run1 PbSc calibrations for W0 and W1 previously mentioned. The slope method is the most statistical of all the methods and relies on the idea that the shape of the hit tower spectrum at low  $p_T$  should be approximately constant over all towers. We expect this for a small  $\eta$  acceptance, mid-rapidity detector like PHENIX since all particle is very nearly flat with rapidity there. As the true spectral shape is one of the things

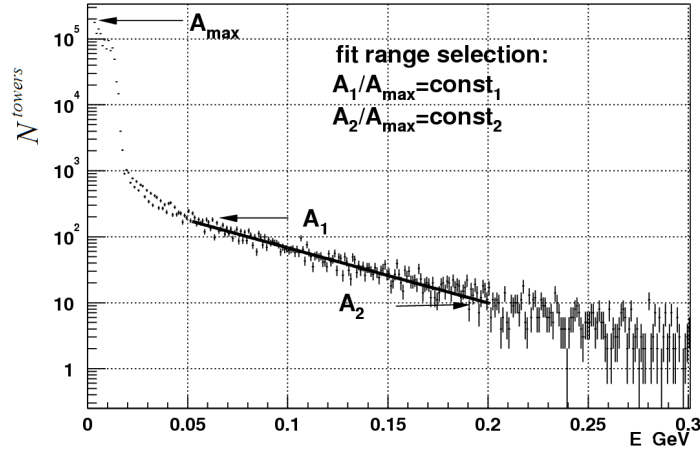


Figure 6.5: Demonstration of the Slope Correction for the energy calibration.

we are trying to measure, as with the initial cosmic muon MIP peak correction, only a relative calibration is possible with this method.

A typical tower spectrum with the method indicated is shown in Figure 6.5. Since this spectrum is fit very well at low  $p_T$  by a simple falling exponential (on logscale, slope) of form  $dN/dE = e^{\frac{E}{k_i}}$ , all towers are fit and a scale correction  $K = k_{ref}/k_i$  is then applied to each tower  $i$  energy. The slope method used for the Run1 PbSc corrections was slightly different and used the total number of towers integrated above 100 MeV to generate the corrections since with an exponential, the integral is also another exponential. However this method is not as accurate because it cannot account for an inefficiencies that are constant with energy (like dead areas) and is more sensitive to the true gradual rise with rapidity that photon production really has. One operational complication in the PbGl slope method is determining a good algorithm for choosing the fit range as hinted in the figure caption, since initially the spectra can be quite distorted over the very low energy range considered. This is another disadvantage of the Run1 PbSc slope corrections, since 100 MeV is used for all towers. Despite these imperfections, the Run1 corrections did improve the relative calibration and any shortcomings would have then been re-corrected in the Run2 methods described above for the data in this thesis. For PbGl, two correction iterations were performed for PbGl and the outcome is shown in Figure 6.6.

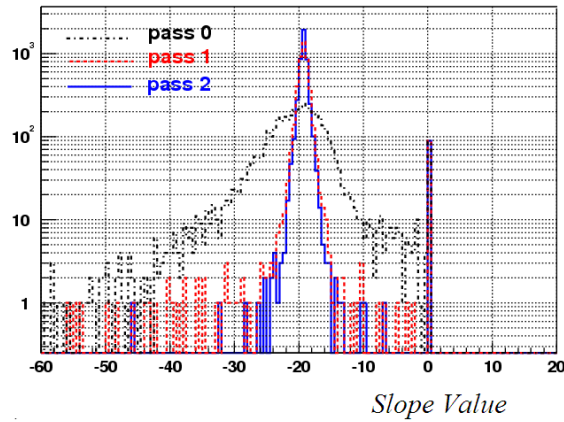


Figure 6.6: Improvement of relative calibration for PbGl towers from Slope Correction.

The story of the PbGl calibration is much different than PbSc calorimeter since its tower modules were already used in several previous experiments at CERN (see section 5.8.2). Because of this, well tested methods of keeping the calibrations constant between repackaging meant that a rough calibration (within  $\sim 10\%$ ) already existed before construction into the PHENIX PbGl form. In fact this slope method was the first correction/calibration performed while the units were actually part of PHENIX. The  $\pi^0$  correction above with a (with an additional MIP cross-check) provided the final absolute calibration corrections.

### 6.2.6 Calibration Quality, Final Resolution

Both relative and absolute calibrations are performed on as short of time period as possible down to specific runs, meaning that above methods are done many many times possibly for each run. If a period of runs cannot be calibrated for some reason it is not used as discussed in 6.3.2.

In general the quality of calibrations and corrections were checked by looking at  $\pi^0$  mass plots and for PbSc it was further verified by observing the electron energy to momentum ( $E/p$ ) ratio where the  $e$  momentum is from the higher resolution tracking determination.

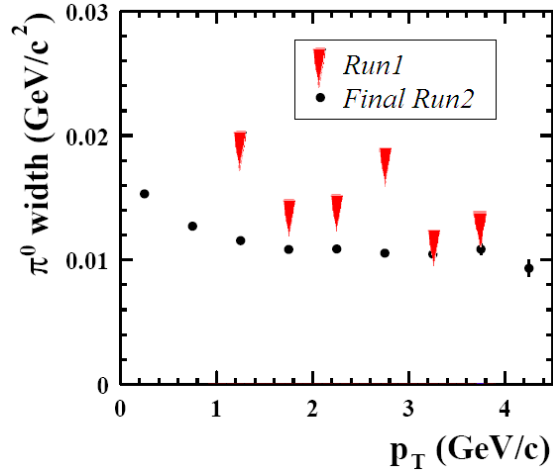
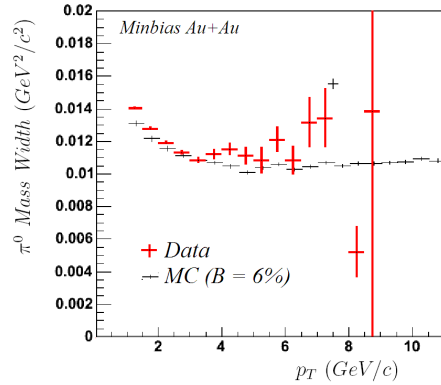
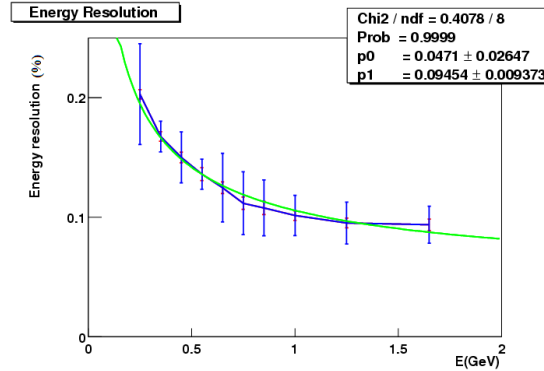


Figure 6.7: Overall reduction in  $\pi^0$  mass resolution due to calibration improvements between Run1 and Run2 for PbSc

The quality of the *relative* calibrations/corrections can be checked by observing the widths of the various calibration distributions. For example, relative calibration improvements are immediately apparent as reductions in the width the  $\pi^0$  invariant mass peak for a given  $p_T$  bin as shown in 6.7. The quality of a relative calibration directly determines the effective final resolution of the detector, specifically the constant  $B$  term in the resolution from section 5.8.3. Using the electron  $E/p$  width can also be used for this with the advantage that the actual resolution is more transparent than in the case of  $\pi^0$  widths but with the caveat of the slightly different showering process and the additional complication of the resolution. In general peak width for either  $\pi^0$ , electron  $E/p$  or even MIP peaks, information can be viewed fairly independently from peak location, which is determined by the absolute calibration. However, it is always necessary to study peaks as a function of absolute energy, since background effects are generally larger at low  $p_T$  and this can distort the widths. Because of energy smearing, this finite energy (or often  $p_T$ ) binning results in altered widths for different bins. Since the smearing is determined by the resolution, there is thus always a link between the absolute and relative calibration determinations. This problem is discussed further for  $p_i^0$  in section 6.6.8. However it mostly just amounts to needing to tune a simulation to describe a self consistent set of peak



(a)



(b)

Figure 6.8: In (a) a MC constant  $B$  term of 6% shown to reproduce the  $\pi^0$  mass widths. In (b), electron  $E/p$  resolution: the blue points are the width over energy, the green curve is an  $A/\sqrt{E} \oplus B$  fit with the  $B$  fit parameter given as  $p_0$  in the plot. Note that (b) is for the Run2  $p + p$  calibration (taken from [160]) which is almost identical to the final Run2  $Au + Au$  calibration used.

location and width plots. When this is done for  $\pi^0$  for PbSc, it is found that the effective resolution constant term that describes the data in the calorimeter best for the final Run2 calibration is between 4 and 6%, a value which is also consistent with the electron  $E/p$  peaks as shown in 6.8. The exact value depends on the details of the simulation tuning which is of course a source of systematic uncertainty. Therefore it is discussed further in section 6.6.10.

The quality of the absolute calibration is simply a statement of confidence in the energy scale and is therefore discussed in below in section 6.6.8.

### 6.2.7 A Problem

As discussed in 5.8.1, usually the source of the extra amount of the constant  $B$  term in the resolution is assumed to be mostly due to imperfect fluctuations of the gains around their true values. Of course things can go wrong if care is not taken when applying a set of corrections. When one only looks at the behavior of the peaks averaged over the whole detector to judge the quality of a calibration, systematic problems can exist that break the fluctuating gain assumption. Such was the case with one set of corrections that was originally applied to the Run2 data but was found to be faulty. We describe it here both as a historical lesson of what can go wrong when basic checks are not performed and but also as a demonstration of how PHENIX's diverse nature and sensitivity can be exploited when a problem is identified.

The faulty correction was one of the corrections applied after full DST production in the “afterburning” phase. These were applied during the rush for a major conference (*QuarkMatter* 2002) and since the problem was fairly subtle it was not discovered immediately. It was first noticed as an observation of a dramatic positional anisotropy in the yields at high  $p_T$  (only the inclusive distributions were previously checked), where towards the sector corners the photon yield differed from that of the center by approximately a factor of 2 as shown in Figure 6.9. A similar dependence was observed in all PbSc sectors.

The most obvious place a difference in yields can crop up is energy scale differences in different parts of the sectors, which ultimately reflect upon the calibration. In this case it was verified both by looking at the electron  $E/p$  peak location and also the  $\pi^0$  location as shown in 6.10. As we shall see, energy scale differences of this size ( $\sim 15\%$ ) can easily account for the  $\sim 100\%$  increase in yield for high energy or  $p_T$  bins, due to the steeply falling nature of the spectra. As the figure also shows, the corrections applied in the Au+Au afterburner were quite obviously the culprit. Unfortunately, all files related to the work that generated the correction were lost in the failure of a disk on the RCF computing farm so the source of the problem

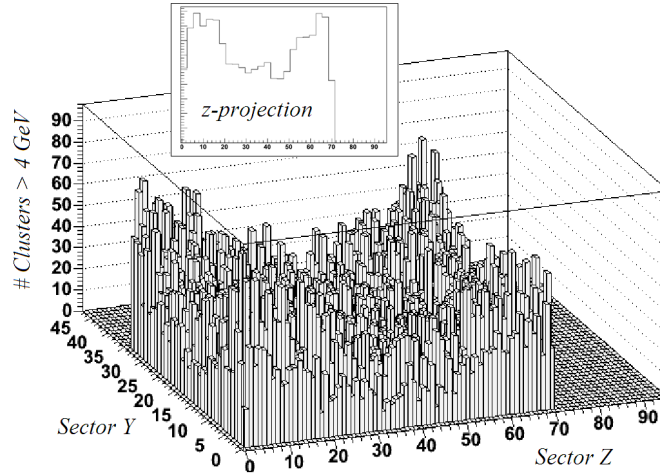


Figure 6.9: Cluster  $z - y$  position for clusters with energy  $> 4$  GeV for a single PbSc sector with the faulty afterburner correction applied. All PbSc sectors showed similar behavior. The problem was due to this correction and was subsequently removed

could never be identified exactly. However, we know the correction was generated with MIP peaks, which narrows down the source to either one of two sources: either the positional dependence of the MIP peak discussed above in section 6.2.3 was not accounted for properly, or, since it is known that minimum bias data was used (preferably one wants to use a low multiplicity event sample) it may have been simply due to multiplicity effects.

### 6.2.8 Timing Calibrations

When a shower or ionization occurs causing the scintillators in an EMCal tower to emit light, the quickly rising current in the PMT's are what trigger the electronics to record their signals. To do this the electronics must already be sampling with a fine grained clock so it is quite easy to also store the timing information of when the pulse occurred. This measurement is done by a Time to Digital Converter (TDC) which stores a discretized bit representation of the elapsed time. By using this information to calculate the *time of flight* (TOF) of particles hitting the calorimeter, an effective means of particle ID at lower momenta is realized, since more massive particles hit the detector later (for a given momenta) due to their reduced velocity.

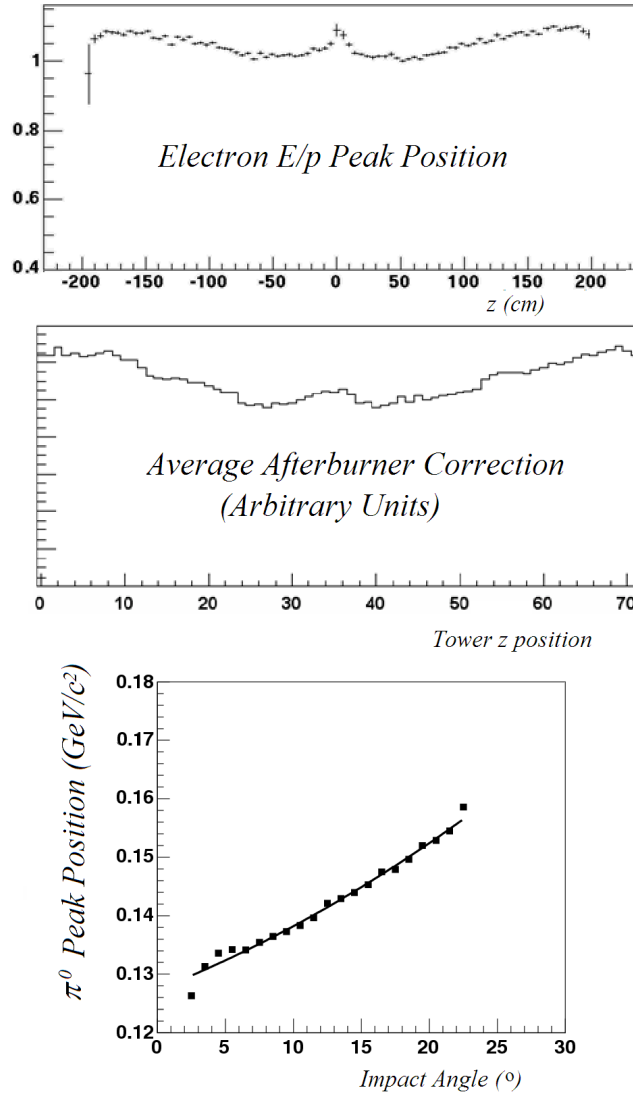


Figure 6.10: Identification of the problem with the Afterburner Correction.

Timing measurements are made with *leading edge* discrimination, so energy dependent *slewing* corrections must be made to account for earlier arrival of higher energy signal peak edges. This defines one part of the calibration: the accuracy of the  $t_0$  defined as the time the cluster started being formed in the calorimeter. This  $t_0$ , and as with ADC gains, the TDC's conversion factor  $f_t$  of bits to time is also subject to fluctuations and can drift—in this case, drift can come from not only the tower electronics but also from the timing modules that drive them. In the case of timing

measurements the laser monitoring system mentioned above for gains was able to be applied for  $f_t$  and less successfully,  $t_0$  monitoring for Run2. However the  $t_0$ 's still needed further corrected using physics data in order to achieve an overall timing resolution close to design for PbSc.

This is done for a single tower by observing the path-length corrected TOF distribution. Photons, being the fastest particles, will form a *flash peak*. The center of this peak should represent the same amount of time delay for all towers, so it is possible to calibrate all towers both relatively and absolutely in one step. For each tower and for multiple time periods as small as statistics allow for, every TOF value is adjusted according to the sample average. Observing the entire distribution of TOF for the entire detector over the whole run as in Figure 6.11, the overall average timing resolution for PbSc is about 450 ps for the Run2 sample used in the final results. For PbGl which has less precise timing electronics, the resolution was about 700 ps for Run2. From the figure we can also see the characteristic “asymmetric gaussian” shape of the distribution which occurs from the inclusion of the slower particles in the right hand side of the peak. It is the left hand side which should represent the intrinsic resolution of the timing measurements.

Using this correction method the timing resolution of the PbSc was close to the design of approximately 300 ps. However the resolution was found to be sharply dependent on the energy of the tower. Since the slewing was already accounted for, the cause of this dependence was unknown. It was suspected either to be due to fluctuations in shower locations due to material not accounted for in the GEANT simulations, but could also be due to the lack of consideration of the TDC conversion factor  $f_t$  in the timing calibrations, which can change the  $t_0$  peak location. No matter the source, the energy dependence was able to be accurately parameterized, as shown in Figure 6.12, and added to the simulation which resulted in consistent corrections. However due to the lack of statistics the very high energy behavior could not be trusted and so timing information was ignored above  $\sim 7$  GeV, which is where it becomes less useful anyway.

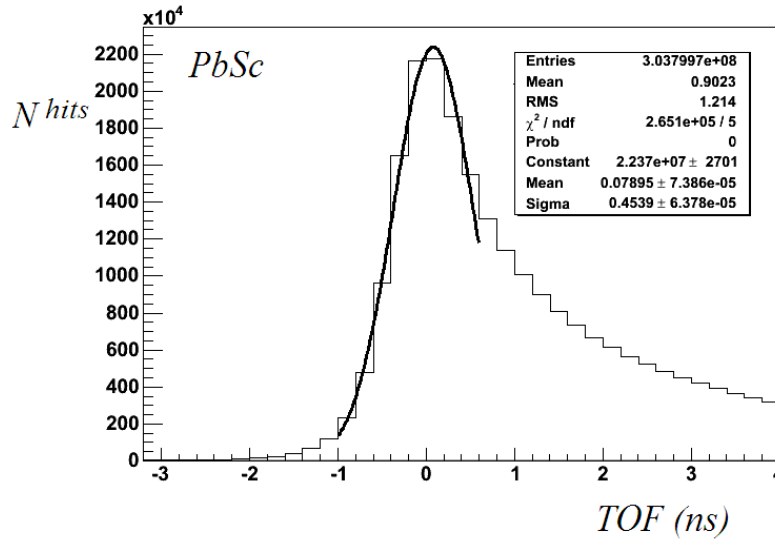


Figure 6.11: TOF distribution for PbSc Clusters. One out of every  $\sim 10$  clusters were sampled across all runs.

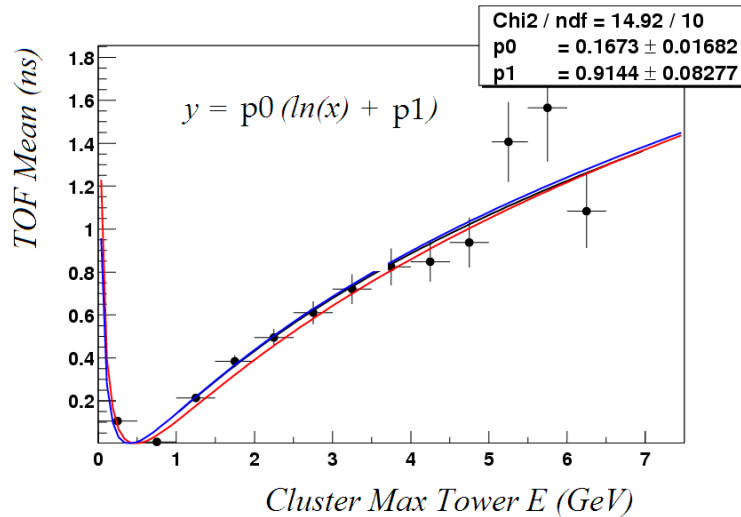


Figure 6.12: Clusters get their single TOF value from the tower with the maximum energy. This energy is referred to as  $E_{cent}$  in PHENIX. The dependence of this TOF value on energy was parameterized according to the function in the figure and added to the simulation. However above  $\sim 7$  GeV, the parametrization cannot be trusted due to lack of statistics. Therefore no timing information was used above this energy.

### 6.2.9 Systematic Uncertainties

The systematic uncertainties which arise from the calibration are mostly reflected in the energy resolution. As explained above, using the  $\pi^0$  mass peaks as the primary determination of the final resolution parameters obtained by tuning the simulation, means that the energy smearing corrections and the energy scale uncertainties become linked. Therefore we defer the discussions of the calibration and energy scale uncertainties to section 6.6.8.

## 6.3 Raw Data Extraction

### 6.3.1 Offline Reconstruction and Software

As described in section 5.9 raw data is first stored in PHENIX Raw Data Format files in which raw data signals are stored in their maximally compressed form. It is the job of the *offline reconstruction software* to turn the raw signals such as drift chamber hit collections or EMCal tower signals into physics usable objects such as charge particle tracks or clusters. The general flow of the offline reconstruction starts with the production of Data Summary (DST) files which store uncompressed, data with calibration constants applied. Unimportant data is thrown out and the results of many complex calibrations are also stored. Already at in this form all the raw physics objects are constructed such as tracks and clusters, though not necessarily in their final usable form. The basic storage unit in both PRDF and DST files (and in fact nearly all particle or nuclear physics data files: DST's for short) is the *event*. In PRDF files, a custom set of very simple formats containing minimal header information is used. For all files from various reconstruction phases after that, including the DSTs, PHENIX has chosen to use object-oriented (OO) data structures and a corresponding program language (C++) to manipulate them.

In this paradigm, the current technology standard which is pervasively used in nearly all aspects of computing worldwide, a uniform hierarchy of “header” information and meta-data<sup>3</sup> which can include even abstract machine instructions is stored together with raw data in as a single unit of bit patterns. The philosophy is that the data will be more easily extracted from such bit patterns, but more importantly, in being packaged this way, the object units are then capable of supporting the ability to make conceptual models of the real world where objects interact with each other. Being able to model problems in such a way often is often logically easier than traditional types of programming and therefore often less error prone. A strict set of programming conventions have been developed to “enforce” the OO philosophy, some even inherent in the programming language itself. Some people would even

---

<sup>3</sup>data about data

argue that programming in such a fashion represents a whole new outlook on life itself and that the OO philosophy with its sometimes arduous rules, has nary a place where it doesn't belong in programming. But in reality it is often good to realize the limitations of OO programming and choose expedient alternatives to following OO conventions especially in very complex applications as present themselves in scientific fields.

C++ is a very basic computer language which provides hardly any “vocabulary”, but rather just the basic structure of how “words” can be put together in statements and ultimately algorithms. The language provides only 6 kinds of basic 1 to 64 bit pattern data structures on which a limited set of basic logical operations like addition or value replacement can be performed. All more complex data structures and operations must be defined by the user “from scratch” in ways specified by the language. The particle and physics community has stored a repository of such definitions (which in OO programming called *classes*) in a *library* together with a fully functional analysis application called *ROOT* [61]. All PHENIX objects stored in data files are derived from the ROOT object standard and use the default ROOT data storage method.

The conversion of PRDF event to a DST event is on average about one to one in bit size. Both types of files are therefore about the same size which is chosen to be the maximum allowed by the Linux computer operating system (OS), the PHENIX OS of choice (currently the RedHat Linux) of 2 GB. Since the collection of all files for a Run2 is too large to be kept on actively accessible computer disks, after DST production, a series of refineries are performed, where only more specific information is filtered from the DSTs into smaller files. These are called microDST's ( $\mu$ DST's or more commonly notated uDST's). Even more finely filtered set of files are produced from the uDST's called nanoDST's, or picoDST's.<sup>4</sup> It is PHENIX policy that all analysis must be performed from some set of DST's produced in an *official production pass* where the reconstruction code is verified and cross checked for basic

---

<sup>4</sup>in this language, I suppose the smallest DST achievable would be the yoctoDST, which would be a single bit: *e.g.* were there direct photons or not?

programmatic mistakes (*bugs*) by a committee of coding “experts”. Algorithmic or calculational bugs cannot be reasonably checked and the bug finding system is not perfect as section 6.2.6 indicates. All results must be cross checked in any case, but this system avoids many obvious problems.

### 6.3.2 Data QA

A certain basic level of data Quality Assurance QA occurred from the production process itself. The event characterization data from the BBC and ZDC needs to be OK for a given run for it to even be considered for analysis. However cross checks need to be performed especially for this analysis, as to the quality of the EMCal gains and timing. As long as these can be calibrated over a time period, runs are kept. The following basic steps were performed in order to ensure good data quality for all runs used in the analysis:

- Nothing unusual about the run conditions or the state of the detector was remarked in the online logbook for runs. General Quality Assurances of the BBC and ZDC distributions showing normal looking response and timing functions were also required.
- A MIP peak in all towers in each sector was required to be found. In addition to MIP enhancement with non-photonic shower shape cuts, (see section 6.3.4) MIP’s were selected by requiring matching to charge tracks, so this in effect also implied a level of QA in the tracking system, however it’s not a very strong check since for central events combinatoric random matching is frequent and the peak can be visible even without this requirement.
- EMCal TOF distributions were required to have a well defined peak whose mean was within 1 sigma of 0. Examples of these distribution are shown in Figure 6.13
- After hot towers were removed (see Section 6.3.3 below), the total event normalized number of clusters for each sector above 0.1 GeV was required to be

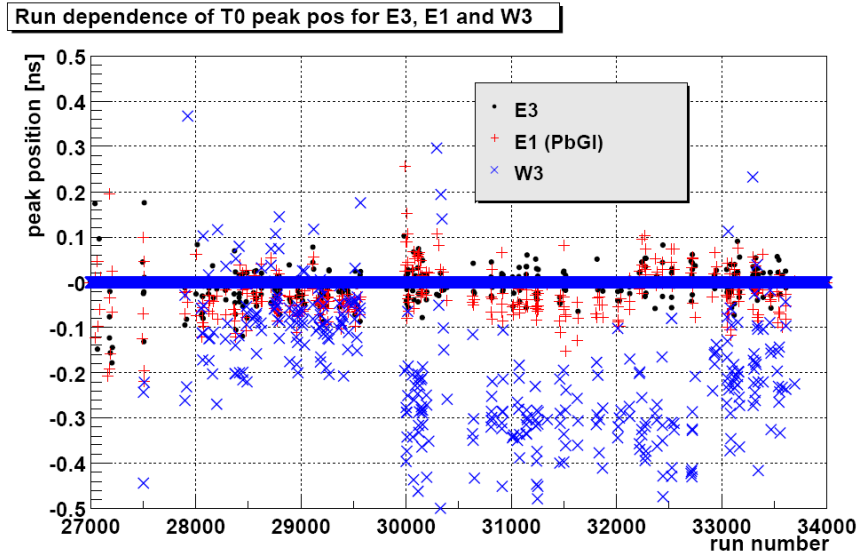


Figure 6.13: TOF distribution mean ( $t_0$ ) for three sectors. The best (E2) and worst (W3) sectors are shown along with one PbGI sector (E1). The PbSc W3 was not used in the final analysis for other reasons.

uniform within the statistical 5 sigma of the mean. The total event normalized number of clusters for all PbSc sectors above 3 GeV and 5 GeV was required to be uniform within 5 sigma. This together with other information also constrains the amount of intra run gain fluctuations as discussed in Section 6.6.3

- For the level2 events, the rejection rate was monitored for each run by eye. No anomalously high or low rejection rates were observed. Also basic requirements of normal functioning was required, such as no runs were used where the rejection was on, but the forced accept (see section 6.4) was set such that all events would be kept anyway which represents a nonsensical situation.

In addition to these basic check of runs, some checks were performed on EMCal data from larger time periods in order to make sure no odd biases existed in the EMCal data sample.

- Distribution of very high  $p_T$  (5-7 GeV) hits as a function of calorimeter  $z - y$  position showed no unusual fluctuations overtime periods of various lengths. Some of these checks fall under the guise of hot tower removal (section 6.3.3)

but the check was performed over longer periods of time (e.g. over  $\sim 1\text{M}$  events,  $\sim 10\text{M}$  events and the whole data sample) to check for so called “warm” towers. This was checked both for clusters and cluster pairs which fell within the  $\pi^0$  invariant mass peak.

- The ratio of the normalized cluster  $p_T$  spectra divided by the average for the whole detector were checked to be consistent in shape by eye for each sector over 3 run periods.

### 6.3.3 Dead and Hot Towers

Dead and Noisy towers for PbSc were identified online before reconstruction started by observing some basic quantities over multi-run periods: the total number of hits per tower above 100 MeV, the integrated energy per tower, and the average per event energy per tower.  $5\text{-}\sigma$  low outliers were flagged as dead and were treated as thus during reconstruction.  $5\text{-}\sigma$  high outliers were considered noisy, and were similarly marked as dead during reconstruction.

“Hot Towers” are noisy towers which passed these basic checks because they only produced abnormally high numbers of hits at higher  $p_T$  values. They are especially dangerous for high- $p_T$  data analysis, because the average production rate of such clusters is already so low that just a rate of noise can add substantial numbers of high- $p_T$  hits and completely dominate the true physics signals in those regions. Therefore it is of paramount importance that they be identified and removed. It is not as much of an issue for  $\pi^0$  analyses in more central heavy ion events because the already large background must be subtracted, Since hot towers will generally show up in the background, they will be subtracted for the most part. However they can still bias the subtraction procedure. For single photon measurements, however hot tower removal is absolutely crucial.

The method for identifying hot towers in the PbSc EmCal sectors was a simple one based on hit frequency. The general method was as follows. First, on a run by run basis, the number of hits above a certain energy threshold were histogrammed

for each tower. Second, again on a run by run basis for each of these thresholds, a histogram was made of the number of towers hit, and a Poisson or Gaussian was fit around the mean value. Third, one of the thresholds was chosen for each run, and all towers whose number of hits were above a certain number of standard deviations, defined by the fit function in the second step, were recorded for each run in text files based on the QA EMC extra reject list format. Last, the text files for all processed runs were combined into one large file containing the union of all identified hot towers.

### 6.3.3.1 Histogramming

On a run by run basis, the number of hits above a certain energy threshold was first histogrammed for each tower. Four thresholds were studied: 0 GeV (no threshold), 0.5 GeV, 1.0 GeV and 1.5 GeV. figure 6.14 shows an example of these histograms for run 30009.

### 6.3.3.2 Fitting

For each of these thresholds, a histogram was made of the number of towers hit, and a Poisson and a Gaussian were fit around the mean value of number of towers hit. One other distribution was studied to use as fitting function: a binomial distribution, where the standard probability  $p$  and number of trials  $n$ , and the scale factor were the fitted parameters. However this distribution was found generally not to have a significantly better  $\chi^2$  fit value, even for higher thresholds. Whether to use the Gaussian or Poisson results was decided upon run by run according to the  $\chi^2$ . In most cases, the results of the Gaussian fit were used. An example of the Gaussian fit is shown in Fig. 6.15.

### 6.3.3.3 Hot Tower Identification

Based on the results of the fit, a limit was chosen as the maximum number of hits a tower could have for the run and not be considered hot. All towers with number of hits above this limit would then be identified as hot. The limit and its definition

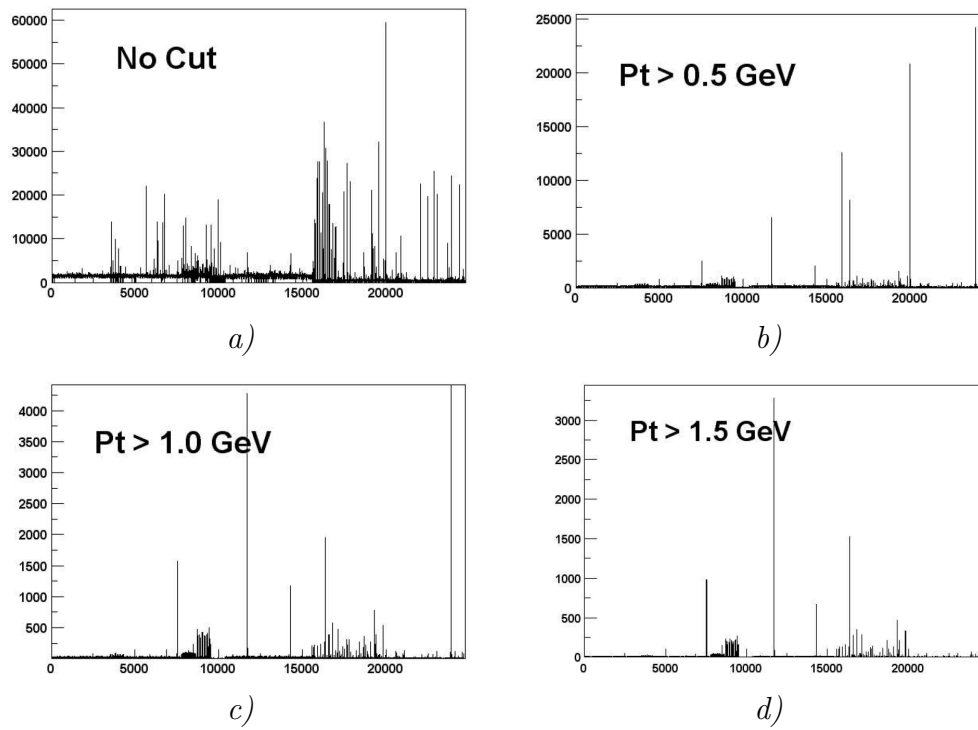


Figure 6.14: Number of hits vs EMCAL tower index with 4 different  $p_T$  cuts for run 30009.

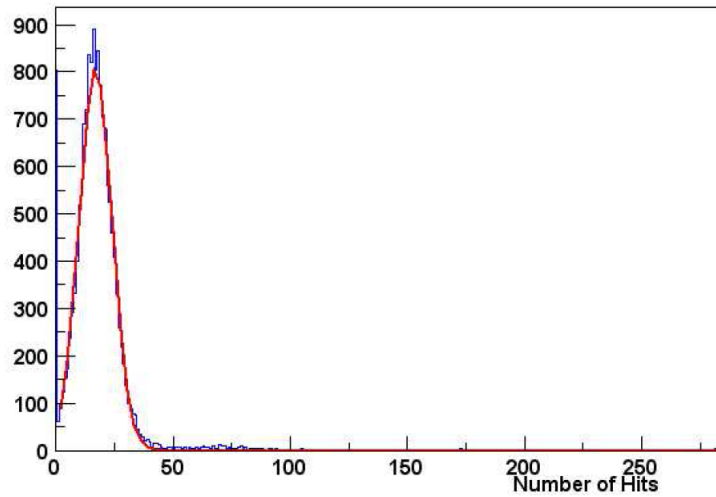


Figure 6.15: Gaussian fit to the distribution of number of hits with the cut  $p_T > 1.0$  GeV for run 30009.

Table 6.2: Number of hot towers in the PbSc reject list.

sector	hot towers
W0	1
W1	12
W2	3
W3	400
E3	6
E2	4

were studied extensively: limits of 3–12 standard deviations (defined by the fitting functions or the raw RMS), as well as limits based on the statistics in a certain sample were studied and appropriate limits were chosen on a run by run basis. Four standard deviations was the value used most often. All towers with numbers of hits above the limit were written to files formatted according to the QA EMCal extra reject list format. The processed runs included approximately 30% of the runs and 50–60% of the v03 dataset. Then, for the PbSc this run by run information was merged into a global (i.e. run-independent) reject list as follows. A tower was considered globally hot (and, consequently, made it into the global reject list) if it was hot in at least 10% of the runs processed. This conservative threshold still resulted in a relatively low number of hot towers outside W3, as shown in Table 6.2. The 5 good PbSc sectors have 26 hot towers (0.2%) out of a total of 12960.

#### 6.3.3.4 Afterburner

Finally, a single compiled list was combined with a PbGl list which included 52 PbGl hot towers (determined separately in a similar procedure) into a final single list. The single list was used for all runs at the expense of losing some data in runs where the towers did not misbehave, but this cost was small in comparison to the great simplification it allowed for in acceptance and efficiency corrections. The same philosophy was applied for the dead towers. However because of time and resource limitations, the hot towers were not able to be simply marked as dead *before* the initial DST production was completed as the dead towers were, but only

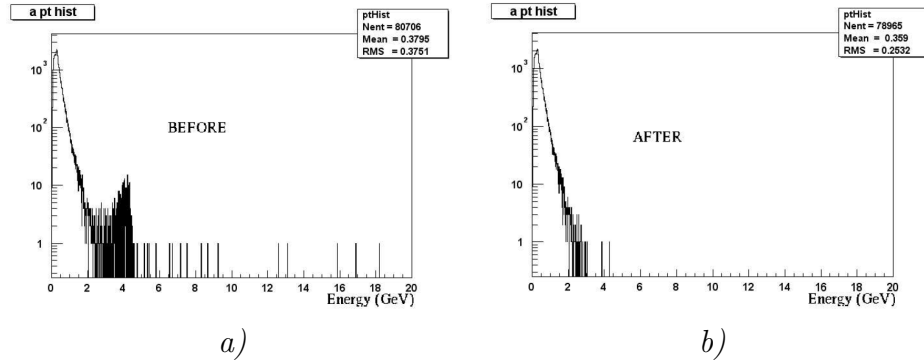


Figure 6.16: Energy spectrum *a)* before the hot tower removal; *b)* after the hot tower removal. Notice how the erroneous high energy tail of the distribution is gone.

*after* reclustering was no longer possible, as an “afterburner”. Because of this it could not be explicitly checked whether a cluster actually included a hot tower or not, so as a conservative alternative to this explicit check, all clusters with centers located in a  $3 \times 3$  square around one of the identified hot towers were also removed.

### 6.3.3.5 Results

An example for run 32123 is shown in Fig. 6.16 revealing the resulting improvement in the high energy cluster spectrum. Notice the dramatic reduction of the spectrum at high energies, which brings it in line with the expected exponential/power law drop off.

A very similar method of hot tower removal and dead tower identification was performed for the PbGl calorimeter. Because the PbGl modules were older due to their history (see section 5.8.2) a large percentage of the PbGl acceptance was unusable.

### 6.3.4 Cluster/Single Photon Extraction: Cuts

The extraction of the raw single photons is simply counting the number of clusters reconstructed and satisfying many of a large set of cuts at a given  $p_T$ . These cuts are introduced both to obtain both a clean sample of clusters, avoiding noise, faulty or poorly calibrated parts of the detector and also to reduce the propor-

tion of non-photon clusters in the sample. Corrections for the non-photon clusters still remaining in this sample are then applied convert the raw cluster sample into true photon sample. These corrections are discussed in section 6.6. They include a *measurement* of the charge particle contamination using PHENIX charge track identification system and subsequent subtraction of it. Therefore it is not entirely necessary that the cuts themselves remove all contaminations. Using several different cuts which will remove different levels of contamination allows us to test the systematic biases and quality of our contamination removal.

#### 6.3.4.1 Selection Cuts

A number of cluster selection cuts were applied in ALL cases (as opposed to some others which were tested by doing the analysis completely with and without, discussed below) in order to maximize the probability of clusters being from a photon and for other reasons, such as A summary of these cuts are as follows:

- Fiducial cuts, sector by sector: clusters center of gravity had to be inside 7cm from any edge of the sector in which it lied. For pbsc, this corresponds to about 1.5 towers, for pbgl, about 2 towers. This was to avoid edge towers which are poorly calibrated due to edge effects. Theoretically edges between adjacent sectors should not suffer from such edge effects, but because the PHENIX clustering is done only on a sector by sector basis, this is not the case.
- Deadmap/warnmap: a “3x3” vicinity cut around each tower “map” was applied as discussed above.
- No W3: the W3 sector was not used
- Hot Tower/Warm Tower based on the evaluations in previous section
- Minimum energy  $< 0.1$  GeV: even though we generally show only results above 1GeV for the single photon spectra, a cut to remove clusters with corrected energy less than 0.1 GeV. This is relevant to the  $\pi^0$  analysis, discussed later.

Table 6.3: Cut Names

PID0	No PID cut
PID1	TOF cut
PID2	Shower Profile (SP) Cut
PID3	TOF and SP cuts together

### 6.3.4.2 PID Cuts

In addition to these minimal set of cuts, two other particle identification cuts were tried in parallel, in combination, separately, and without:

- TOF Cut. In order to cut slower massive particles, the timing value recorded by the PMTs in each Emcal tower is flash-time/path-length corrected and used to make a cut. The final PbSc cut was chosen as 1.2 ns. We refer to this cut as PID1.
- Shower Profile/Dispersion Cut. This cut will be discussed next, referred to as PID2.

Both of these cuts were chosen to be loose and simple. The "χ<sup>2</sup>" was particularly loose. We will refer to these cuts throughout this work as "PID0" through "PID3". PID0 being no cuts, and PID3 being the two cuts in combination.

The different nature of the hadronic and EM showering processes discussed in section 5.8 lead to very different shower shapes. By studying the realization of these shapes in our calorimeter with testbeam and GEANT studies, and real physics data studies with identified charged particles from Run2 data, two related quantities were used for discriminating hadronic and photon showers: the difference between cluster shape the parameterized photon shower shape response quantified with the results of a χ<sup>2</sup> fit procedure and the plain transverse dispersion of energy in the towers making up the clusters.

Dispersion is simply the second moment of the energy weighted position averages in two perpendicular transverse directions:  $D_i \equiv \langle x_i^2 \rangle = \sum E_k (x_k - \bar{x}_i)^2$  where  $\bar{x}_i$

is the energy center of gravity average in the  $i^{\text{th}}$  direction and the sum is over all towers  $k$ . The PbGl analysis uses the plain  $z$  and  $y$  dispersions with corrections for tower discreteness and impact angle effects, but the dispersions about the principal axes of the distribution are also calculated.

The  $\chi^2$  fitting procedure is as follows. From the testbeam and GEANT the photon shower shape in the transverse direction is parameterized with an exponential function in distance from the shower center which gives a predicted energy for each tower in the cluster, once its center of gravity is calculated. Another complicated empirical function  $\sigma_F^i$  gives the expected RMS  $\sigma$  from this value. Then calculation of  $\chi^2$  is straight forwardly as the square of the energy difference between the measured and predicted values divided by  $\sigma^2$ . The probability of  $\chi^2$  (" $P_{\text{photon}}$ ") is also calculated given the number of tower degrees of freedom. Both variables are in practice used to discriminate showers by making cuts. The functional form of  $\sigma_F^i$  is given by in formula 6.1:

$$(\sigma_F^i)^2 = E_i \left( 1 + k \sqrt{E_{\text{tot}}} \sin^4 \alpha \right) \left( 1 - \frac{E_i}{E_{\text{tot}}} \right) + q_0^2 + q_1^2 E_{\text{tot}}^2 \quad (6.1)$$

where  $\sigma_C$  and  $k$  are tuned from the test beam tower energy distribution.

Since we've already stated that showers hitting the calorimeter at larger impact angles (towards the sector corners) will be more spread out, it might naively seem that  $P_{\text{photon}}$  would be necessary to use in order to avoid a positional dependence of this cut. However, since the shape and RMS parameterizations are tuned on impact angle, this is not in practice true. Nonetheless, the energy dependence of the number of towers kept in a shower also makes  $P_{\text{photon}}$  the more desirable variable to cut with in general. But even this dependence is quite small far out on the tails of either distribution. Therefore if only a very loose cut is desired to cut only the largest outliers away, it turns out that it is slightly more convenient to use that the plain  $\chi^2$  distribution in order to determine where to place the cut as shown in Figure 6.17.

In the BNL-Waseda analysis much tighter cuts, based on a principal component optimization of available shower shape information recorded for each cluster and

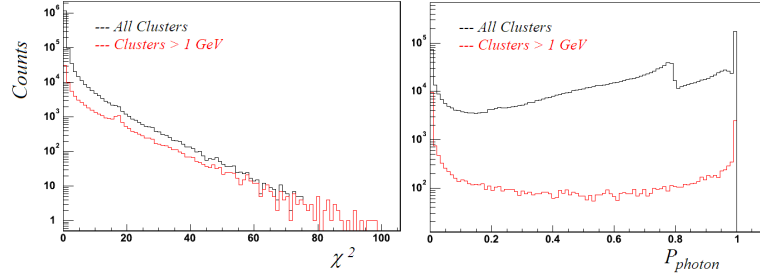


Figure 6.17: The  $\chi^2$  distribution is a smooth distribution extending to very large values. Therefore, if one wishes to make a *loose* cut (without removing *all* hadronic contamination) it is easier to place the cut in the  $\chi^2$  distribution than the  $P_{\text{photon}}$  distribution since  $P_{\text{photon}} \rightarrow 0$  as  $\chi^2 \rightarrow \infty$ . Furthermore, the  $P_{\text{photon}}$  distribution for lower energy clusters has less well behaved shape in the  $Au + Au$  environment.

many other cluster properties were explored. For final results a *stochastic cut* of the form

$$0.3 + 4e^{-E/E_{\text{cent}}} (1.9 - 0.67\chi^2) > 1.4 \quad (6.2)$$

was found to provide the optimal photon hadron separation and was employed. For the PbSc analysis used in this thesis however a simple  $\chi^2 < 3$  was employed.

### 6.3.5 $\pi^0$ Yield Extraction

$\pi^0$ 's are obtained from the distribution of cluster-cluster pairs in an event. All cluster pair combinations are considered and the pair invariant mass calculated with the usual invariant mass formula 6.3:

$$m_{\text{inv}}^2 = p_1 \cdot p_2 = E_1 E_2 (1 - \cos \theta_{12}) \quad (6.3)$$

where  $\theta_{12}$  is determined from the cluster spacial location (center of gravity) in the calorimeter and the event vertex is assumed to be the origin of all clusters. Invariant mass distributions are put into histograms in bins of cluster pair  $p_T$ .

### 6.3.5.1 Mixed Background and Peak Integration

In a typical central  $Au + Au$  event there are hundreds of clusters so the vast majority of cluster pair combinations are not from the same  $\pi^0$ . This *combinatoric background* shown next to the foreground distribution in 6.18 (a) is very large for low  $p_T$  bins and must be subtracted. Fortunately there are large statistics and it is not difficult to reconstruct this background using a *mixed event* procedure. The procedure is as follows.

Events are buffered in bins of similar vertex and centrality. The size of these bins were studied by choosing smaller and smaller bin sizes until no observable improvement was observed in the background to foreground matching. The largest such bin sizes were chosen in order to maximize background statistics and computational speed. It was found that 10% centrality bins and 15 cm vertex bins were sufficient by verifying that results did not change with smaller vertex binning. Since the event vertex for every event was required to have  $z \leq 30$  cm, this meant that 4 vertex bins and 9 centrality bins (see 6.1) for a total of 36 buffers. Data was processed in  $\sim 40K$  event (14 file) segments. Once all buffers are filled, each cluster in the current event is paired with every cluster from each of the events stored in the matching buffer for the current event. We call such a buffering scheme a “rolling buffer” scheme, and is very practical. It offers the advantage that events are only mixed with other events from within the same run, where all calibrations and other detector effects should be the same.

In addition to centrality and vertex bins, since the reaction plane 3.3.2 is measurable, we can also create buffer bins in angle ( $\phi_R$ ) with respect to the reaction plane. This is necessary since the combinatoric background is slightly different for different  $\phi + R$  bins. However, it was found that such binning made no observable difference in the foreground to background matching for the entire reaction plane averaged centrality-vertex binning.

Generally the buffers contain about 5-15 events which has two consequences. So first, the mixed background must be normalized to match the foreground. In most

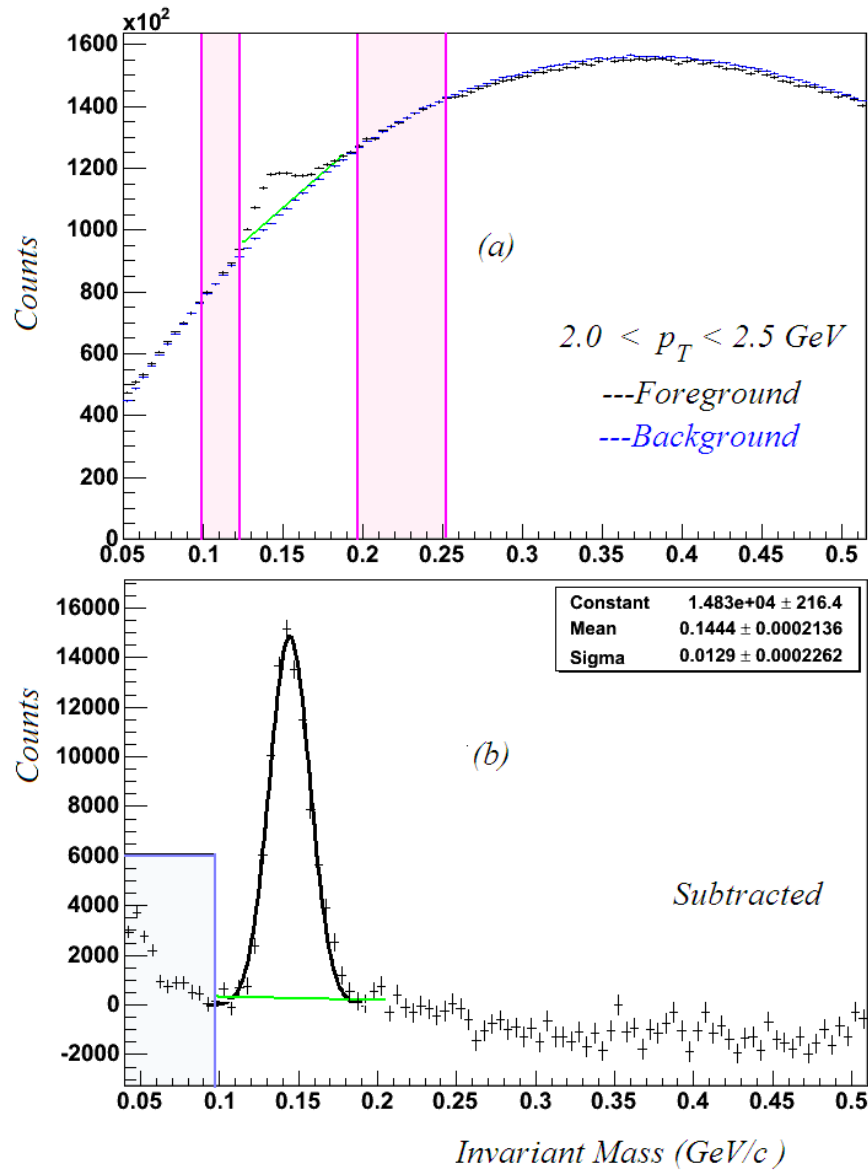


Figure 6.18: An example of foreground and background in the cluster pair invariant mass distributions. Details are explained in the text. The green line is explained in 6.3.5.4.

particle physics experiments this is best done by a manual *matching procedure*. This involves integrating the counts in *side band* invariant mass regions near the peak (demonstrated in Figure 6.18 by the pink regions) in the mixed distribution and scaling the entire distribution so that the number matches that of the foreground distribution. The scaling can be performed with a constant function or by fitting a linear function to the ratio of the foreground and background in the matching regions. Both methods were tried as discussed in the systematic error studies section below (6.3.5.4). The final method used for PbSc was the constant fit ratio. Once matched the background is subtracted from the foreground and a gaussian function + polynomials of varying degrees (several were tried) are fit to the peak. The yield of  $\pi^0$ 's for that bin is then obtained by integrating the counts (or for systematic studies, sometimes the gaussian fit function itself) in some *integration region* containing the peak. The gaussian function is also used for selecting the matching and integration regions and the systematics associated with this will be discussed below. One thing to note is due to smearing effects discussed in 6.6.8, the  $\pi^0$  peak's width gets smaller and its location moves up with increasing energy or  $p_T$ . Therefore the matching and integration windows must be determined separately for each bin.

The second consequence of the mixed background having substantially more statistics than the foreground is that its statistical errors are small compared to that of the foreground. This means that the statistical errors are dominated by the foreground, that is the signal. This is, of course, always desirable. The situation for this analysis is made even better since at low  $p_T$ , the statistical errors are negligible anyway, and at high  $p_T$  the background level becomes very small because the overall number of such high  $p_T$  clusters (after the application of pair cuts discussed below) is greatly reduced.

For the  $\pi^0$  analysis, no attempt to remove conversion electron was made. As will be discussed in section 6.7.1, most photon conversions occur outside the magnetic field region and the conversion electron positron are usually asymmetric in energy. Furthermore the shower is still EM so will mostly pass all photon PID cuts. The

higher energy electron will still leave nearly the full photon energy in the calorimeter so only a small conversion loss correction is necessary if these are included. However since the lower energy electron or positron will also generally leave a cluster, a foreground correlation is present around the photon mass of 0 in lower  $p_T$  bins. It is visible in the light blue shaded region in the lower left hand corner of Figure 6.18 (b). This foreground correlation will not be present in the mixed background. However it is obvious from the figure that it is at a nearly negligible level by the time we get into the  $\pi^0$  mass peak region. Nonetheless, different background subtraction and matching region selection techniques were evaluated as discussed in the error section below, but no indication of a systematic bias or larger systematic uncertainty was justified.

### 6.3.5.2 Pair Cuts

In order to reduce the combinatoric and other backgrounds in the invariant mass distributions, certain cuts are applied to remove unwanted clusters pairs. The most important of these cuts is the *energy asymmetry* cut, or  $\alpha$  cut. The quantity  $\alpha$  is defined by the following equation:

$$\alpha_{12} = \frac{|E_1 - E_2|}{E_1 + E_2}$$

An  $\alpha$  value of 0, means the two clusters were symmetric in energy whereas a value of one indicates that 1 of the clusters carried nearly the entire energy of the pair. Consider the  $\alpha$  in the case of  $\pi^0 \rightarrow \gamma\gamma$  decay. Since the  $\gamma$ 's are massless and are perfectly symmetric in the center of mass frame under the lorentz transformation  $E_\gamma^{lab} = E_\gamma^{CM} (1 \pm \cos\theta_{CM})$  and therefore  $|E_1^\gamma - E_2^\gamma| \propto \cos\theta_{CM}$ . Since the decay is isotropic the distribution of  $\cos\theta_{CM}$  is obviously flat and thus the laboratory  $\alpha$  distribution is too. On the other hand because of the steeply falling production of all particles as a function of energy, the vast majority of clusters in EMCAL are of low energy, equal to the average  $p_T$  which is about 500MeV (see section 3.3 of the last chapter). Therefore most combinatoric pairs contain one of these low energy

clusters and the  $\alpha$  distribution of combinatoric pairs are strongly peaked at 1. Thus, if we are interested in cluster pairs ( $\pi^0$ ) at higher energy or  $p_T$  we can exclude a large majority of combinatoric pairs by requiring only a mild  $\alpha$  cut, while such a cut will have an easily understood effect and proportionately small effect on the true  $\pi^0$ . This is why asymmetry cuts are nearly always used in  $\pi^0$  (and  $\eta$ ) analyses. For the analysis of this thesis, an cut requiring  $\alpha_{12} \leq 0.8$  was applied and for the PbGl analysis, the value of 0.7 was used.

Another pair cut which makes mixing easier is to require that the minimum opening angle is larger than some small value (in our case  $> 0.01$ ) in order to avoid mixing pairs overlapping clusters. Other trivial pair cuts ensure. only PbSc-PbSc, same arm pairs are considered.

Finally, all the cluster selection cuts from above are explicitly required of both pairs.

### 6.3.5.3 Trigger Data

There are many options for generating the mixed backgrounds discussed above. With the “rolling buffer” mixing scheme described above, one must be careful when working with triggered events. Triggered events cannot be mixed among themselves since this would result in a bias not found in the real foreground, since high- $p_T$  events which fire the trigger are rare. Fortunately in our case with the level2 trigger, the triggered events are interspersed with the other minimum bias events, so that each triggered event can simply be mixed with the current minimum bias buffer. However, one complication arises in our specific case, because, as discussed in the next analysis section 6.4.6, we desire to make a “software cut”, and only use clusters above the threshold where the trigger is fully efficient. As long as we are sure to apply the same software cut on mixed pairs, we should have no problem matching the trigger foreground. But this implies that the foreground *and* background for the triggered data will be different, and we may worry that the trigger cut introduces a bias that will effect the peak integration. After systematic studies, it was determined that there was no such bias. In fact as 6.19 shows the trigger background and minimum

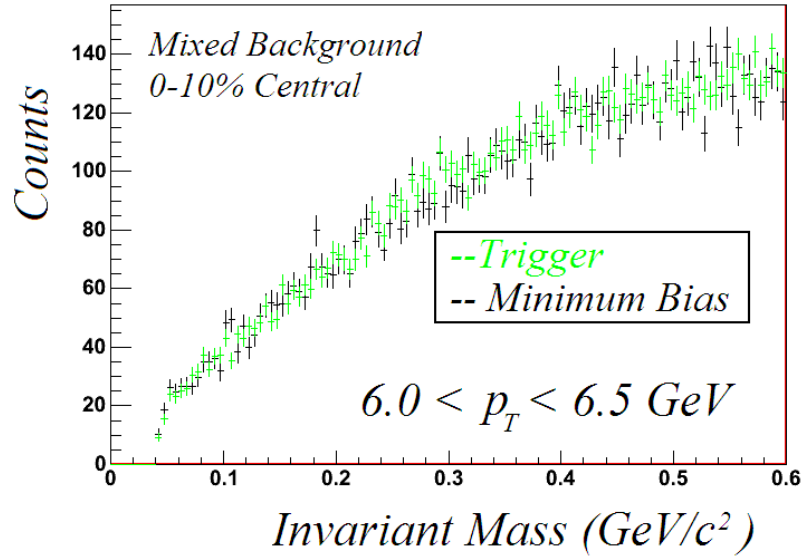


Figure 6.19: The mixed background from triggered events is virtually indistinguishable from the mixed background from minimum bias events.

bias backgrounds are virtually indistinguishable.

#### 6.3.5.4 Systematic Errors on the $\pi^0$ Yield Extraction

Despite our ability to reduce systematics with cuts and mixing techniques, due to the nature of high multiplicity  $Au + Au$  environment the peak integration extraction of the  $\pi^0$  yield is one of the largest systematic uncertainties in the  $\pi^0$  analysis. Fortunately the systematic uncertainty from yield extraction can be determined from data in several different ways and quite accurately estimated. This is because we have many different centrality bins (as well as  $p + p$  measurements) and different sets of PID cuts, for which the effects of multiplicity, background, and intrinsic imperfections of various methods can be compared systematically. Therefore a number of comparisons were performed to evaluate the systematic errors associated with the total procedure. A number of peak integrations techniques, background matching, and fitting techniques were evaluated by comparing the yields obtained with the four different PID cuts. The peak integration and matching technique combinations with

the smallest overall uncertainties of those were chosen. The different techniques are summarized here:

- The background matching was done with a polynomials of varying degrees from degrees 0 (constant) to 3.
- The integration region and matching band limits were varied.
- The peak area was fit with a plain gaussian plus, in different attempts, polynomials of degrees 0 (constant) to 2.
- The raw number of  $\pi^0$ 's were counted by integrating the number of counts in the integration region and by integrating the gaussian function.
- Asymmetry cut was varied. In particular a very symmetric ( $\alpha < 0.2$ ) sample of cluster pairs was evaluated. This was to study the effect of energy scale on the yield.

In each case, ratios were taken and compared. An example for MinBias is shown in Figure 6.20

Some errors were systematically correlated with  $p_T$  and some fluctuated from point to point. For example, when compared to a values from a fit to the spectra, the point by point fluctuations from the fit due to yield extraction gave an indication of yield uncertainties from these type of fluctuations in the peak extraction process.

The results of all these comparisons lead to an estimate of the systematic error on the peak extraction in the 10 % range slightly higher at low  $p_T$  and lower at high  $p_T$ . The exact errors used are shown in Figure 6.21.

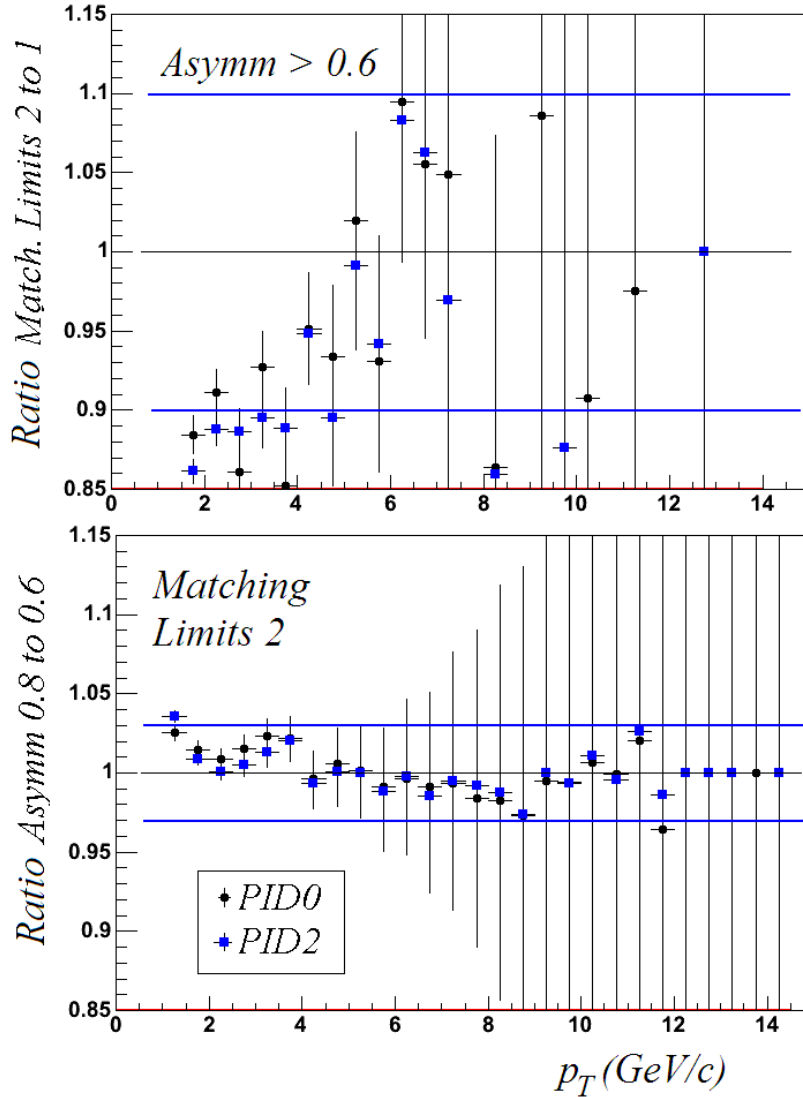


Figure 6.20: Example of Peak Extraction Yield Ratios. Many such ratios for different centrality bins and PID cuts in order to infer the systematic error on the peak extraction and background matching. In this example changing the matching region boundaries was found to cause deviations on the order of 10% while changing the asymmetry cut from 0.8 to 0.6 caused only  $\sim 3\%$  deviations. In many cases, imposing a PID2 cut caused the yield extraction to be less sensitive to deviations, since this reduced the combinatoric background.

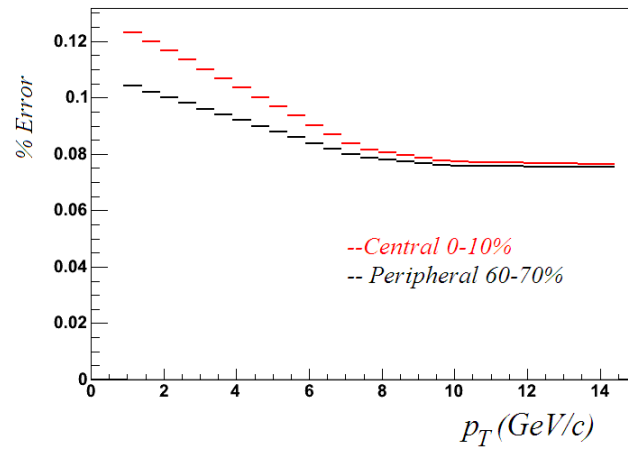


Figure 6.21: Peak extraction errors for Peripheral and Central Events

## 6.4 Level2 High $p_T$ Tile Trigger

The level2 triggering system was introduced in section 5.9. In this section we will explain how data from the Level2 High  $p_T$  Tile Trigger was incorporated into the minimum bias data set to yield the data used in this thesis.

Level2 was developed during the first part of run2  $Au+Au$ , and started rejecting events on November 2, 2001, which corresponds roughly to run 31400. Therefore only runs above this number were used for triggered data. Data extraction was done from the burnt microDSTs. Specific run information is in appendix A.

### 6.4.1 Event Counting

The level2 triggering system does not suffer from any dead time bias because of the parallel structure of the Assembly Trigger Processor portion of the Event Builder—if a certain type of rare event takes longer to process, it does not hold up the rest of the ATPs, and events are queued before large scale backups can affect their ordering. However because dead time limits the overall DAQ throughput, the mix of events kept as true minbias or kept for any of the level2 triggers is important for ensuring optimal balance of the minbias “control” data and rare physics. This mix is controlled by the level2 trigger system’s ability to *force accept* a certain fraction of events as minbias, and to prescale away a certain fraction of each individual trigger’s selections, in order to keep triggers with low rejection to not dominate the data throughput. These fractions are controlled and adjusted on a run by run basis, based on the overall machine luminosity, which can vary by an order of magnitude or so during the course of a single store.

### 6.4.2 Trigger Efficiencies

The best way to study trigger efficiency is to have a large min bias control data set from which one can extract the sub portion of this data set that also fired the trigger. In this way efficiencies and biases are actually *measured*. Such is the case for this study. However this implies that it is only a relative determination

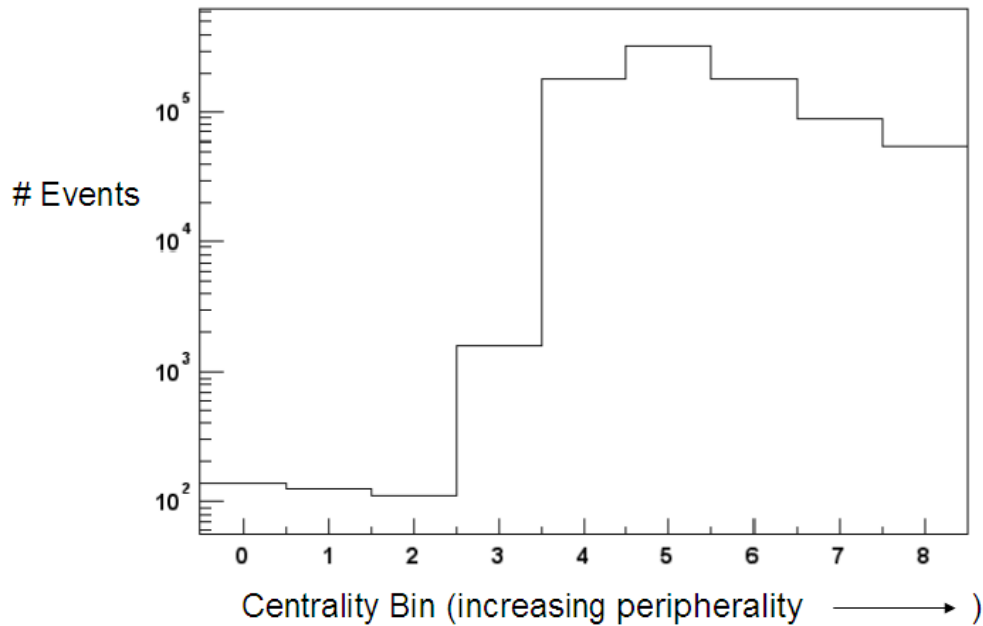


Figure 6.22: Number of triggered events per centrality bin for trigger 2. The trigger fires preferentially on peripheral events, in fact, the triggered events in the three most central bins are due to malfunctioning and poor centrality resolution by the trigger. Above bin 4, the # of events per bin decreases as expected due to the decrease in multiplicity per event: the greater the multiplicity, the higher probability the event will contain a high  $p_T$  trigger photon.

compared to the minbias trigger itself: all efficiency correction will normalize the resulting quantities to be the same as min bias. Therefore any bias inherent in the minimum bias trigger will still be present. This is just an example of something that is generally true for use of level2 data. In our case the input to level2 was the minbias, but in the future other level1 triggers may be used as inputs, even perhaps several different level1's may be input for the same level2 trigger. In this case it is still sensible that that biases from level2 first be removed/corrected for for each level1 trigger individually, such that the level2 output is normalized to match the level1 input, and then biases from level1 be dealt with separately.

Along these lines, something else that will apply to all of the following trigger efficiency determinations is that those corrections will only be derived to correct the *raw*, but uncorrected otherwise, yields for all particle species such that they match

the minimum bias *raw* yields. Any other efficiencies (e.g., photon reconstruction efficiency) will be accounted for by the same methods used to account for them in the minimum bias analysis, which is described in section 6.6. Except for one exception discussed below which turns out to have a negligible effect, (the influence of the input spectrum shape to the finite  $p_T$  bin averaging method) this introduces no additional systematics—that is, the two sets of corrections can be and are factorizable and therefore treated independently. Finally, the methods used here except where hence noted, including the comments in the last two paragraphs, as they should be are very similar to those described for accounting for the level1 ERT trigger in later run periods where that trigger was operational.

### 6.4.3 Photon Efficiencies

Because the calibration database gains are not perfect, but rather tend to fluctuate tower by tower about their true values, the trigger has finite efficiency even below the online trigger threshold and a corresponding “turn-on” region where the trigger rises from very small efficiency to a constant “plateau” value. The most important aspect of understanding any triggered data is to understand this turn on at which the trigger starts being as fully efficient as possible for clusters. Then from the high  $p_T$  cluster efficiency, efficiencies for other mesons detected through reconstruction of decay photons, the  $\pi^0$  and  $\eta$ , can be derived.

For trigger 1 and 2, in pbsc the cluster efficiency is shown in Figure 6.23. As is evident from the plot, the trigger reaches a plateau of about 100% at about 5 GeV, while trigger 2 reaches a plateau of about 95% at 2.0.-2.5 GeV. The 95% plateau value is strictly due to the miscalculation of the centrality as discussed above

If one only considers minimum bias triggers for which the l2 centrality determination was correct (within the same centrality bin), the plateau matches the  $\sim 100\%$  efficiency of trigger 1. This is shown in Figure 6.24:

In reality, the triggers are not 100% efficient. They should be slightly less

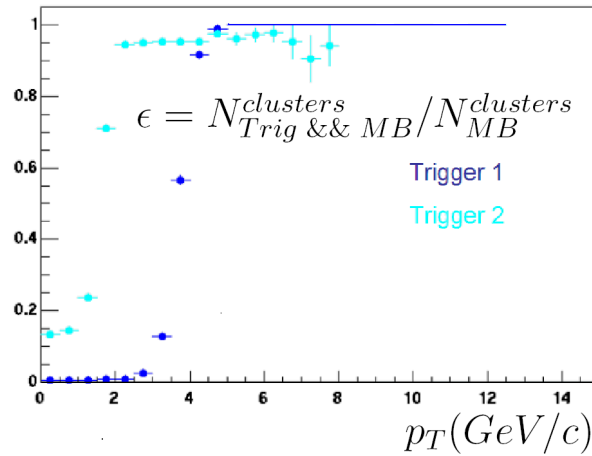


Figure 6.23: Trigger Cluster Efficiency compared to min bias as a function of transverse momentum for pbsc.

efficient than that by no more than  $\sim 0.5\%$ . This is consistent to what is measured within statistics. We know this because as a cross check the bad tower list used online was compared to the corresponding offline list used offline to reject clusters. There were 10 (out of  $>10000$ ) towers in pbsc that appeared in the online list but not in the offline list.

Theoretically then, the trigger should be fairly inefficient around such towers, but not necessarily completely inefficient, since the other towers around them may have still retained enough energy to fire the trigger, and the corresponding offline reconstruction of clusters would not exclude those towers in the cluster. However, if we assume the trigger is completely inefficient for clusters whose tower with maximum energy is one of those towers as a conservative estimate, then dividing this number by the total number of non-bad towers  $\approx 40$  (number of dead “areas” from the number of dead towers with area effects) /  $[36 \times 72 \times 5 - \sim 20 \text{ Pbsc (bad as determined by the offline)}]$ , we see that at most it could result in a  $0.5\%$  inefficiency.

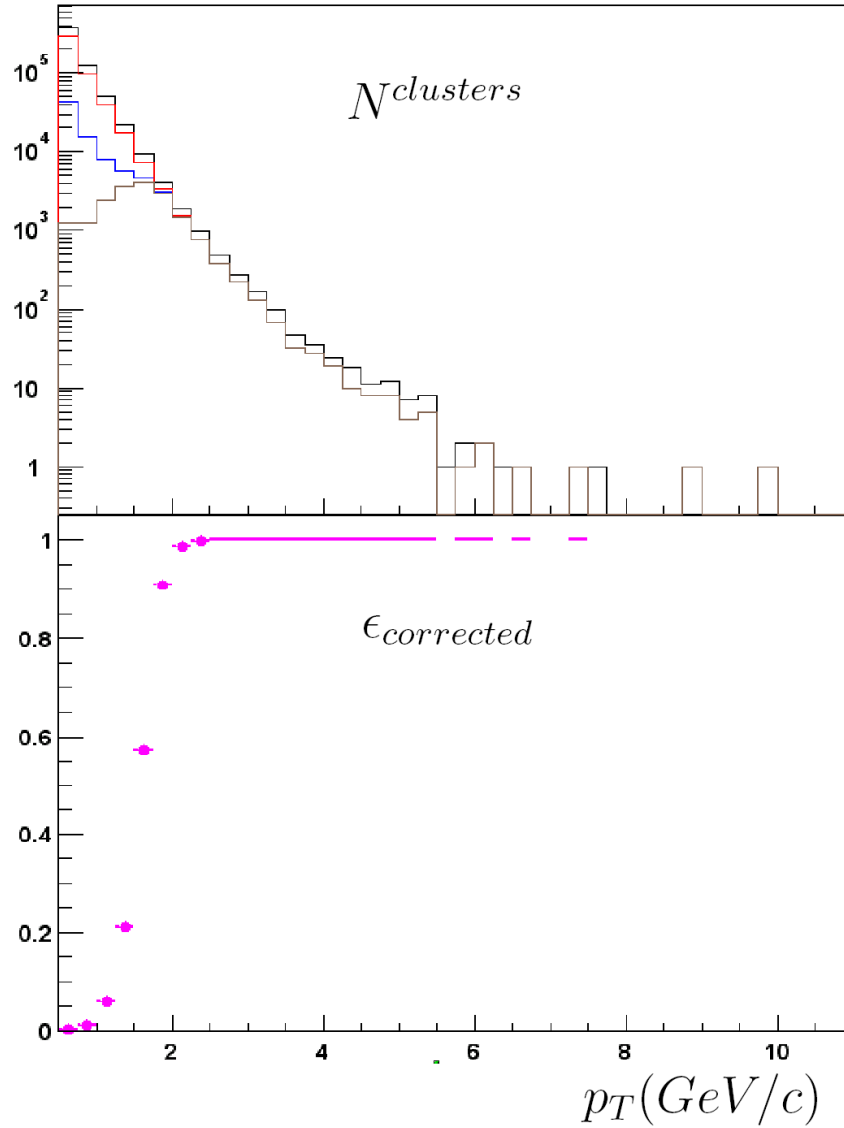


Figure 6.24: In the top plot the cluster spectrum is shown as a function of  $p_T$  for: minbias (black), minbias where the lvl2 centrality bin matches the offline centrality bin (red), trigger 2 where the same condition holds (blue), and trigger2, same condition but with the random benefit removed (tan). The bottom plot shows the cluster efficiency in cases where the level2 centrality matched the offline centrality determination, from the above plot, tan over red.

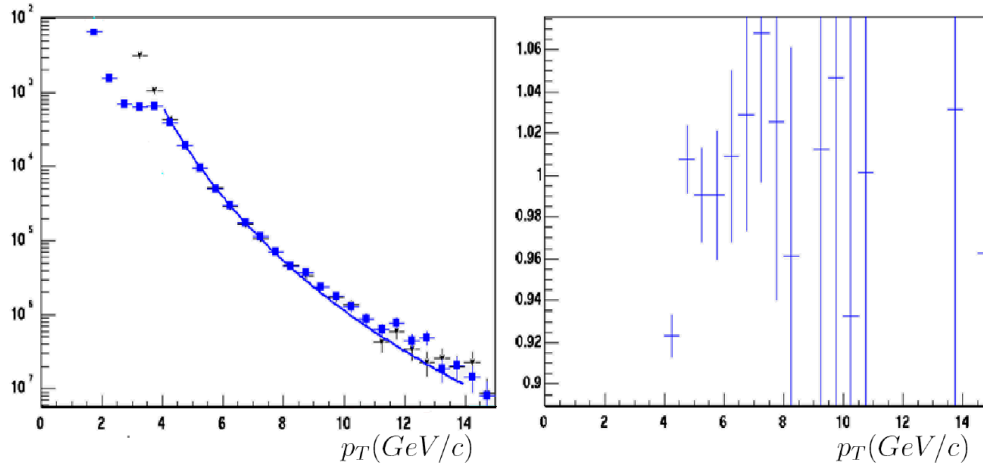


Figure 6.25: Event normalized yields with no corrections for the trigger 1 match well those for MinBias (no lvl2 trigger) above 5GeV. In blue is the corrected triggered photon spectra and in black is the minimum bias. To the right is the ratio corrected trigger to minbias.

#### 6.4.4 Photon Matching

In order to remove systematics involved in using photons *for the single photon yields only* the triggered data was added to the minbias only above 5 GeV for trigger 1, and 2.5 GeV for trigger2 in peripheral bins. Therefore there is no  $p_T$  dependent correction after normalizing to the number of equivalent sampled min bias events for each trigger, and only a  $p_T$ -independent efficiency factor of 0.95 to apply for trigger 2. Figure 6.25 shows the resulting match between the minbias event normalized yields to the that of the triggers (with the 0.95 correction for trigger2) and it is clear that within the statistics the two samples match perfectly. This is done with noPID cuts but results are the same for cuts.

#### 6.4.5 PbG1 Efficiencies

The same exercises can be repeated for the pbg1 sectors of the EMCAL. However it was found that, the pbg1 online gains were statistically spread around there true values such that the turn-on of the trigger in PbG1 was very broad in comparison to PbSc, not reaching plateau until  $\sim 7$ GeV. This means that there cannot be good

overlap with the min bias statistics, which run out in MB at even smaller  $p_T$  than for pbsc due to the much smaller pbgl acceptance. Also, because of this smaller acceptance the pbgl would not contribute much statistics at the highest  $p_T$  bins, which was really the whole purpose of including the level2 trigger sample in the first place. Therefore, the trigger performance in pbgl was not investigated further and the triggered data was not used for pbgl. The previously mentioned circumstance of online bad towers for which the offline reconstruction considered valid was also worse for pbgl.

#### 6.4.6 $\pi^0$ Efficiencies: The Software Cut

Given the above photon efficiencies, one can derive how this will translate to the  $\pi^0$  efficiencies. For the least systematic error, we can, as in the photon analysis, make a *software cut* and only use the triggered photons above the plateau threshold. In fact, since the gamma turn-on is then a simple theta function, ignoring detector acceptance effects, we can actually derive an analytical expression for the  $\pi^0$  energy turn on. A schematic of this situation is shown in Figure 6.26:

The red area represents the  $\pi^0$  photons cut away by the trigger, since the photons from the decay for a given energy are symmetric about half the pion energy, and cutting one results in the other to be cut away, so the geometrical area of the red to the total is the inefficiency percentage for the trigger. Therefore the formula is easily derived as formula 6.4:

$$\epsilon_{\pi^0} = 2 - 2 \left( \frac{E_{trig}}{E_{\pi^0}} \right) \quad (6.4)$$

or if an asymmetry ( $\alpha$ ) cut is used:

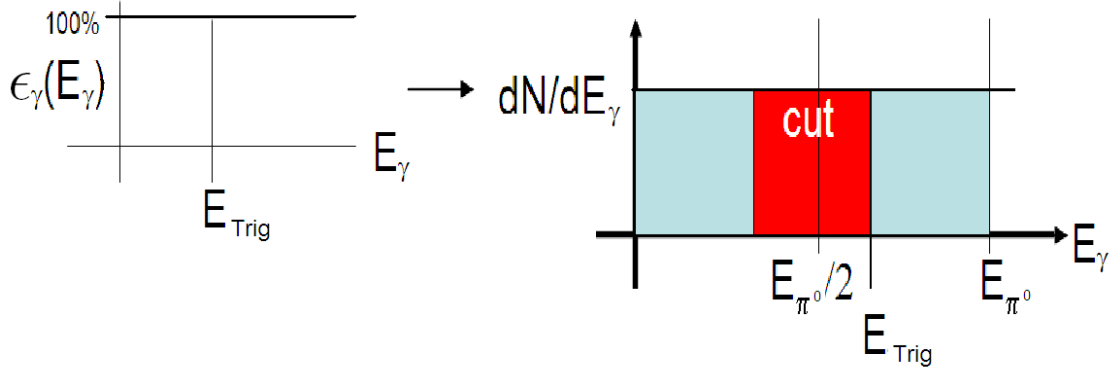


Figure 6.26: If a software cut above the 100% plateau is used such that the photon efficiency turns on as a perfect theta function, then then the  $\gamma$ 's from  $\pi^0$  and hence the  $\pi^0$ 's themselves that survive (light blue) and get cut (red) by the software cut are symmetric around  $E_{\pi^0}/2$  because of simple energy conservation in the decay. This allows the efficiency of the cut to be derived analytically as a function of  $E_{trig}$  and  $E_{\pi^0}/2$  by simply taking ratios of the colored regions.

$$\epsilon_{\pi^0} = \left(1 + \frac{1}{\alpha}\right) - \left(\frac{2}{\alpha}\right) \left(\frac{E_{trig}}{E_{\pi^0}}\right) \quad [E_{trig} \leq E_{\pi^0}/2] \quad (6.5)$$

Physics wise, what we are really interested in is the turn-on curve as function of  $p_T$ , not energy, so we can check things with a very simple decay kinematics monte carlo. It turns out that whether one makes the cut in  $p_T$  or energy, especially considering that our detector acceptance restricts  $p_T$  to be approximately the same as total energy. Eventually one must take into account the true acceptance effects, so a fast MC replaced the formula, but still yielded a very similar turn-on as shown in Figure 6.27.

One thing that is apparent from the plot is that the trigger has efficiency = 0 at the photon plateau value, which for trigger 1 is already at 5GeV. Especially for the direct photon analysis, where we divide the photons by the  $\pi^0$ 's, we'd like to use trigger data at the lowest  $p_T$  possible to reduce the statistical errors on the ratio of the two quantities. Therefore, photons in the region of energy turn-on

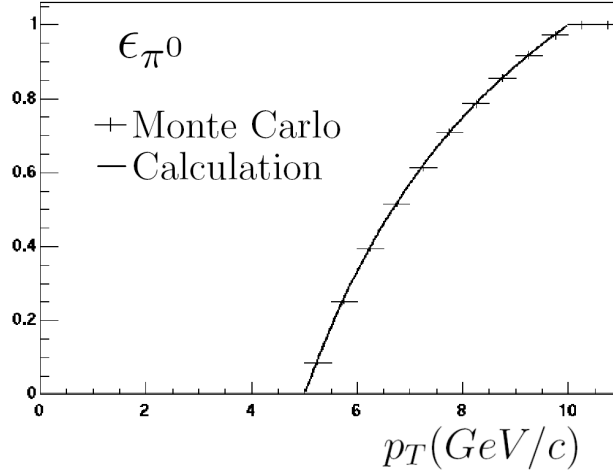


Figure 6.27: Monte Carlo results with and without taking into account the detector acceptance.

were used. However then the turn-on curve itself needs accounted for, which our derivation above does not do. This is most simply done by inputting the photon energy turn-on to a simulation. It could be done by fitting the photon turn-on with, for example, a cumulative gaussian, however since we have a large enough minbias sample that statistical errors are small with small bin sizes, we can use the measured turn-on histograms as input to the monte carlo. The finite width of the bins has an effect, but this is assumed to be small, as long as the  $p_T$  bins in the photon turn on are at least half of each desired  $\pi^0$   $p_T$  bin, which was done in this analysis. The systematic from not using a continuous function can be deduced to be negligible from the systematic studies in Systematics: Random Benefit Effects, where turn-on curves of varying width are shown to make a difference of only one percent amongst each other.

In the following figures, the derived efficiency for  $\pi^0$ 's is shown for both triggers, given the photon efficiency turn-on similar to Figure 6.23. The photon efficiency turn employed for this study used 0.25 GeV  $p_T$  bins.

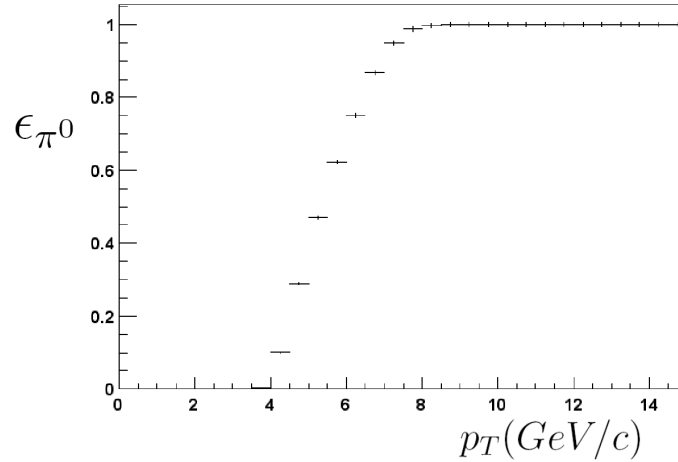


Figure 6.28: Trigger efficiency for  $\pi^0$  for trigger 1. The trigger data is only added where the efficiency is greater than 0.35, namely 5 GeV to keep systematics low.

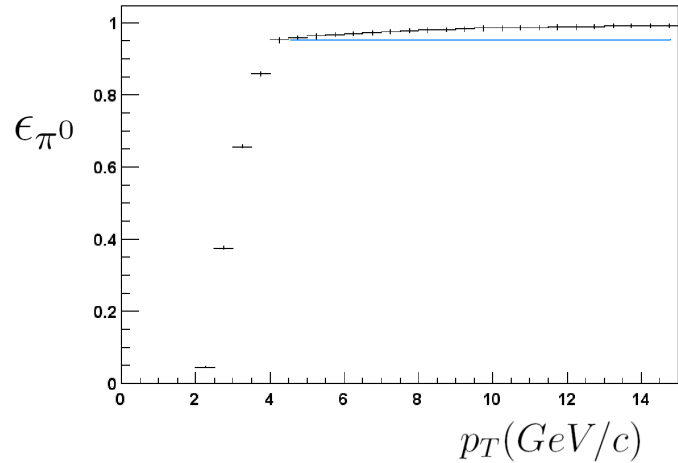


Figure 6.29: Trigger efficiency for  $\pi^0$  for trigger 2. The trigger data is only added where the efficiency is greater than 0.35, namely 2.5 GeV, to keep systematics low. The efficiency plateau at  $\sim 4$  GeV starts at 95% then increases at higher  $p_T$  because as  $p_T$  increases, because in the MC, *both* photons have a finite probability of being accepted by the triggers, reaching a maximum at  $1-(5\%*5\%) = 97.5\%$ . However, this small rise at high  $p_T$  is not consistent to what really causes the 95% plateau in this photon efficiency, since that inefficiency is really caused by the trigger missing whole events for the reasons discussed above. Therefore above 4.0 GeV, a constant 95% was used. Such a rise must be considered however, for cases where the per event single  $\gamma$  efficiency  $< 1$ . In subsequent PHENIX analyses using the ERT where this was the case, an algorithm to remove this rise was employed.

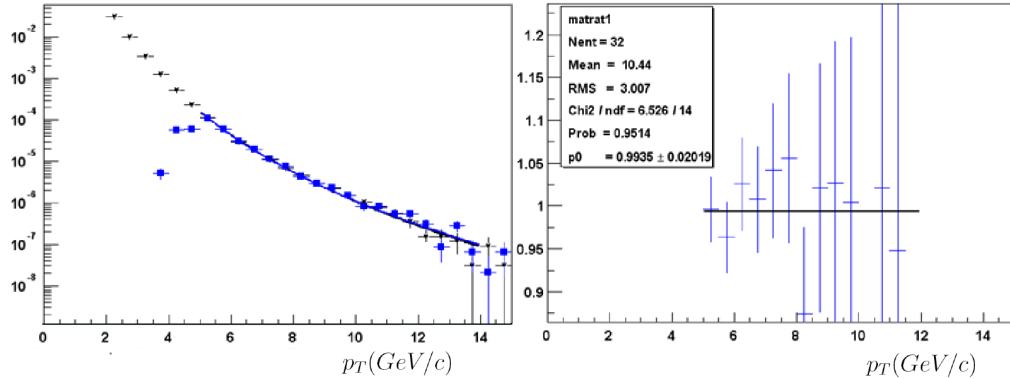


Figure 6.30: As in Figure 6.25, the triggered data sample is corrected with the derived efficiency and compared to the minimum bias sample in the overlap region for 0-100% centrality. The two spectra compare well.

### 6.4.7 $\pi^0$ Matching

As with the photons, the derived  $\pi^0$  efficiency can be tested by applying the efficiency correction to the raw yields and comparing these trigger corrected raw yields to the minimum bias this is shown in the following figure. 6.30

### 6.4.8 Systematic Errors

In the above plots, we fit a constant to the point-by point ratio which can be compared to the same ratio made with a different  $\pi^0$  efficiency turn-on with a different choice of photon turn-on software cut-off. This is shown in the following plots for the above analytical efficiency correction for the hard plateau software cut such as in 6.27:

As is shown, the constant fit to the point by point matching ratio again is within a couple percent of unity. We will take the difference of these fits as an estimate of the systematic bias in deriving the  $\pi^0$  efficiency. The fit for both cases and other fits where the fit range is reduced to cover only the range of the  $\pi^0$  turn-on to study

this systematic. Based on these values we assign a systematic from the trigger efficiency of approximately 3% in the turn-on region and 2% above that.

#### 6.4.8.1 Random Benefit

An observer with a careful eye would notice that the trigger efficiency of all the triggers is non-zero well below the trigger turn-on region. This is shown on a log plot in Figure 6.31. This is a result of the fact that using the ratio of  $N_{MB}^{clusters}$  over  $N^{clusters}$  to determine this efficiency is sensitive to picking up random benefit effects. Random Benefit for a trigger is roughly defined as any time extra rare trigger data is gained for reasons that were not designed into the trigger. For example if noise were to fire the trigger, you would still gain photon statistics from this event. Under this definition the small amount photons that are gained below the trigger turn-on are random bias. However in this case our extra photons at low  $p_T$  are a well understood source of random benefit. They are simply the other photons that in the high multiplicity event that tag along. Generally random bias is to be avoided because there is a fear that this data is biased in some way that is not understood. These random benefit photons can however be considered to have a negligible bias. To first order they are just the same as photons from a min bias event, an assumption that is verifiable and in fact in has even been exploited for the PHENIX ERT  $d + Au$  analysis [14] to allow event mixing within triggered events. None the less we need to study this random benefit, in order to make sure the random benefit is not increasing the trigger efficiency falsely.

Random benefit can be studied by accessing the lvl2 trigger primitives, and selecting only those photons which are associated with trigger tiles. This was done, and the results are shown in Figure 6.31. As is evident in the plot, the random benefit does not affect the plateau efficiency, and is only significant in the lower portion of the trigger turn-on. It does change the shape and steepness of the turn-on by different amounts for different centralities, and therefore, shown in more detail in Figure 6.32, since we use photons from this  $p_T$  region, we must estimate the bias

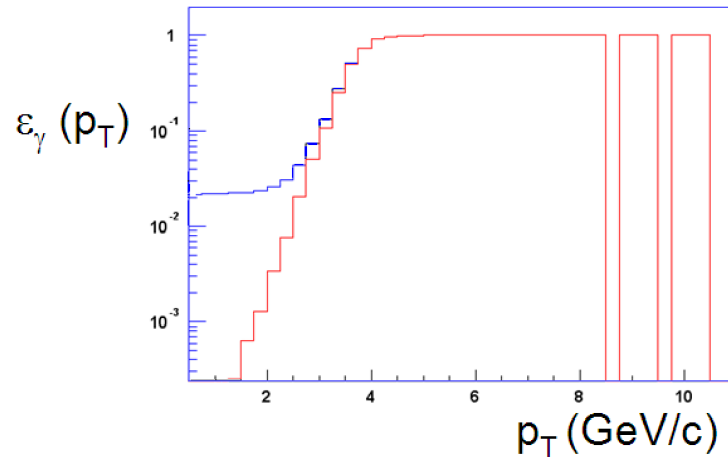


Figure 6.31: Trigger 1 efficiencies with (blue) and without (red) random benefit. To remove random benefit, the trigger primitive tiles that fired the trigger were associated with clusters.

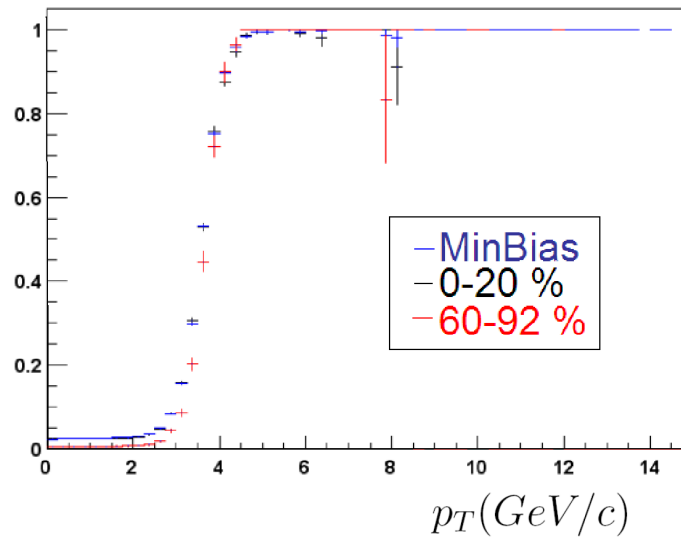


Figure 6.32: The Trigger 1 efficiency turn-on for photons is different for different amounts of the random benefit discussed in this section. Since this random benefit is simply a reflection of event multiplicity it is dependent only on centrality.

and systematics introduced by such use.

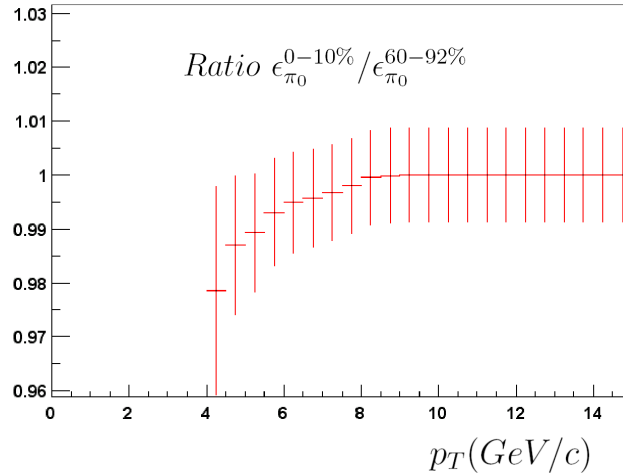


Figure 6.33: For Trigger 1, the maximally different efficiency curves of  $\pi^0$  efficiency curves are made into a ratio as explained in the text. Since the ratio is to good approximation equal to 1, it can be assumed the errors and systematic uncertainties discussed in the text are negligible above 5 GeV/c.

In the case of  $\pi^0$ 's, in order to gain greater statistical benefit, photons from “the middle” of the the photon turn-on were used. As is evident, the efficiency in this region was different for peripheral events compared to central or minbias. However, to make things simpler in the analysis only a single efficiency curve as shown in e.g. 6.28 was used for all centralities, determined from all centrality bins available. Although this introduces an error, figure [figRanBenRat], shows that for Trigger 1, this error must be on the percent level between 5-6 GeV, and negligible at higher pt's. In the figure, the two maximal extremes for the photon turn-on, 0-10% and 60-92%, shown in Figure 6.32 were used to generate  $\pi^0$  efficiencies, creating the ratio plotted in Figure 6.33.

#### 6.4.8.2 Input Spectrum Weighting

As with virtually all corrections that take a raw  $p_T$  (e.g. cluster) spectrum and turn it into a physics (e.g. photon) spectrum, we must assume a shape for the

true spectrum which are trying to measure. This usually results in an iterative process as in section 6.6. In fact all types of corrections which need this input should be included in the iterations including the trigger efficiency. However, since this is a “second order” effect, if we can show that the trigger efficiency correction is relatively insensitive to the input spectrum over some regime close to the correct answer, then we can separate it from the other corrections, that is *factorize* it. In the case of this trigger correction, from the minimum bias data, we can determine the “final” answer fairly accurately to begin with for each centrality. However if the correction is insensitive enough, then even the differences in shape between different centrality bins will not matter. Then a single trigger efficiency correction could be used for each spectrum. But besides just ease of analysis, using a single efficiency also has advantages when one wishes to take ratio of different centrality bins as we will for PHENIX.

For  $\gamma$ 's, the constant ( $\epsilon = 1$  null) correction means that the input spectrum weighting doesn't matter at all. For  $\pi^0$ 's, in the 4-6 GeV/c range the spectrum is fit well by a modified Hagedorn power law function (see section 6.5.4) of the form  $1/(p_T + p_0)^n$ , We can consider  $n = 10$  and  $n = 12$  as the extreme values for this fit parameter, because the  $\pi^0$  spectra from Minimum Bias (no trigger data) had values for  $n$  all at least  $2\text{-}\sigma$  in between. So as a dramatic demonstration of how small of an effect this is, we compared the efficiency calculation (for the same  $p_T$  binning size used in the  $\pi^0$  analysis since this effect is also sensitive to that) for  $n = 0$  (flat) and  $n = 12$ . Taking the ratio of of the two calculations we see in Figure 6.34 that for trigger 1 above the 5 GeV, the difference is smaller than a percent.

For the efficiency curves used for the final analysis (shown in figures 6.28 and 6.29), an input was used having  $n = 11$ . We can therefore safely assume that the error introduced from using this constant value for all centralities is completely negligible at  $\ll 1\%$ . Since this is already much smaller than our other main systematics, we stop here.

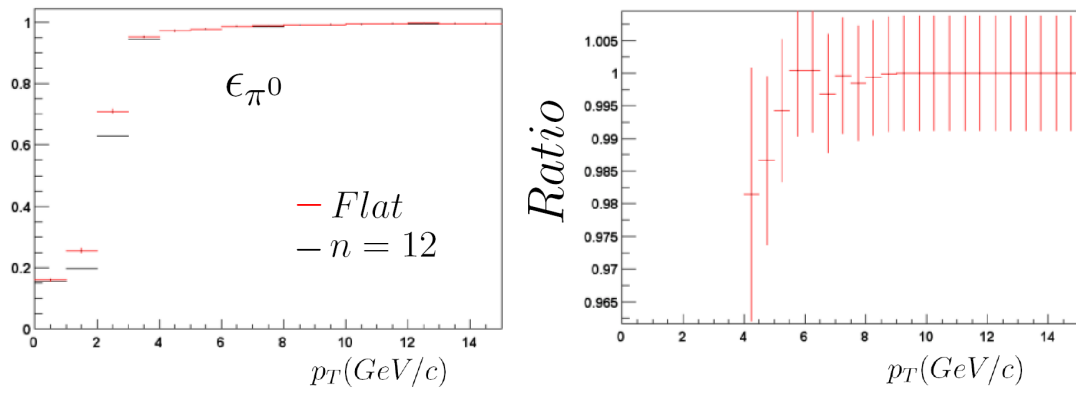


Figure 6.34: Explained in text.

## 6.5 Introduction to Corrections

### 6.5.1 Invariant Yields and Cross Sections

As discussed in 4.4 some high-energy experiments are performed with a single beam focused at a stationary *fixed target* with the laboratory frame highly lorentz boosted, and some are collider experiments, like RHIC where detectors are generally in the center of mass frame. However some colliders like HERA run in *asymmetric* mode where the CM is still slightly boosted in reference to the laboratory detectors. It is therefore convenient to measure lorentz invariant quantities. Since  $p_T$  and rapidity differences are both lorentz invariant, the quantity

$$\frac{d^3 N_X}{dy d^2 \vec{p}_T}$$

where the  $\vec{p}_T$  are the momentum components in the 2 transverse dimensions, is a lorentz invariant yield. Since the total number of events or particles  $N$  is dependent on the effective luminosity  $L$ , which will be different in different experiments, we must normalize to obtain the invariant cross section:

$$\frac{d^3 N_X}{dy d^2 \vec{p}_T} = \frac{1}{L} \frac{d^2 \sigma_X}{dy d\vec{p}_T^2} \quad (6.6)$$

$$= \frac{1}{L} \frac{d^2 \sigma_X}{2\pi dy dp_T} \quad (6.7)$$

where the last equation holds with the usual azimuthal symmetry. As we've already discussed, individual A+A events are not azimuthally symmetric due reaction plane dependent flow. However when looking at the inclusive  $p_T$  spectra, we will be averaging over all reaction planes the distributions of which obviously are azimuthally isotropic. The invariant cross section can be directly compared across experiments at the same  $\sqrt{s}$  energy.

In PHENIX our minimum bias trigger is sensitive to the entire 0-92% central portion of the  $Au + Au$  cross section. Therefore when measuring production in fractions within this range, as mentioned in section 4.3.5, it is experimentally more accurate to normalize by the number of total events observed than by the luminosity.

Therefore what we will present as results will be the *normalized invariant cross section* for the various centrality fractions:

$$\frac{1}{2\pi dy N_f^{events}} \frac{d\sigma^{Au+Au \rightarrow X}}{dp_T} = \frac{1}{\sigma_f^{AuAu}} \frac{d\sigma^{Au+Au \rightarrow X}}{2\pi dy dp_T} \quad (6.8)$$

### 6.5.2 Formulae

The methods used to obtain the “raw” yields (the portion of the yields that the PHENIX detector observes) for  $\pi^0$  and  $\gamma$  were discussed in previous section 6.3. Once the raw event normalized yields were extracted from the data, a number of corrections were applied to turn them into true invariant yields equivalent to cross section measurements. The form of these corrections is as follows. For  $\pi^0$ 's the formula for a centrality bin  $f$  is:

$$\frac{1}{2\pi p_T N_f^{events}} \frac{dN_f^{\pi^0}}{dp_T dy} = \frac{C_{trivial}}{a\epsilon_f} C_{conv} C_{bin\ shift}^f \frac{dN_f^{raw\pi^0}}{dp_T} \quad (6.9)$$

For the inclusive single  $\gamma$  spectrum (including meson decay and other background photons,  $\gamma_{bkg}$ ) which we will refer to as  $\gamma_{all}$  or sometimes  $\gamma_{direct}^{cand}$ , the formula is:

$$\frac{1}{2\pi N_f^{events}} \frac{dN_f^{\gamma_{all}}}{dp_T dy} = \frac{C_{trivial}}{a\epsilon_f} C_{conv} C_{bin\ shift}^f (1 - X_{ch}) (1 - X_{n\bar{n}}) \frac{dN_f^{raw\gamma}}{dp_T} \quad (6.10)$$

These are related to the cross sections by the formulas in 6.5.1. Many of these factors are similar between both photons and  $\pi^0$ . The factors are:

- Acceptance and Efficiency Calculations,  $a$  and  $\epsilon$ . These will be discussed in section 6.6 for both  $\pi^0$  and  $\gamma$ .
- $C_{trivial}$ . This are the trivial factors of  $2\pi$ ,  $dy = \Delta\eta = 1$ ,  $1/p_T$ . The pseudorapidity  $\eta$  distribution of virtually all measured mesons is a wide enough gaussian [10] that to an excellent approximation we can assume the distribution is flat over the mid-rapidity central arm acceptance, and therefore  $\Delta\eta$  is

the same as that acceptance. For the PHENIX central arm and the EMCal,  $-0.35 < \eta < 0.35$  which if all events occurred at a z-vertex of 0, would yield a  $\Delta\eta$  of 0.7. However since we consider event vertex's out to  $\pm 30\text{cm}$ , from fast MC and simple simulation checks, it was found that particles with pseudorapidity between  $+/- \sim 0.5$  contribute. This number then really comes from the acceptance calculation input also discussed in section 6.6.

- $C_{conv}$ . A certain number of  $\pi^0$ 's and  $\gamma$ 's are lost due to photon conversions. Obviously the correction is different for the two cases. Discussed in section 6.7.
- $X_{n\bar{n}}, X_{ch}$ : Fractions of hadron/electron contamination. Charge particle contamination is measured both using the full PHENIX tracking and separately PC3. Neutron contamination is determined from simulation. Discussed in section 6.7.
- $C_{bin\ shift}$ . Because it is important to be able to reliably take ratios between spectra, *e.g.* for  $R_{AB}$  comparisons (see section 4.3.5) in PHENIX we do not *measure* the average  $p_T$  of each bin and *shift* the  $p_T$ -axis point locations of the bin result to these values as is often done in cross section measurements in particle physics. Instead we use an iterative procedure to determine the corresponding shift in the yield-axis direction and simply use the experimental bin center as the average  $p_T$  value for each bin. This is discussed below in section 6.5.3. Note that this does not introduce any additional overall systematics compare to  $p_T$ -axis shifts.

Once these basic invariant yields/cross sections are in place, we construct the *Direct Photon Ratio*  $R_{\gamma_{direct}}$  which reduction of systematic errors is a “double ratio” representing the fraction of the inclusive photons ( $\gamma_{all} \gamma_{direct} + \gamma_{bkg}$ ) which come from direct photons:

$$R_{\gamma_{direct}}(p_T) = \frac{dN_{\gamma_{all}}/dp_T}{dN_{\gamma_{bkg}}/dp_T} = \frac{1}{F_{bkg}^{\gamma/\pi^0}(p_T)} \frac{dN_{\gamma_{all}}/dp_T}{dN_{\pi^0}/dp_T} \quad (6.11)$$

$F_{bkg}^{\gamma/\pi^0}$  is the ratio of background photons (from meson decay) to  $\pi^0$ ,  $\gamma_{bkg}/\pi^0$ , at each  $p_T$  bin, hence the reason we call  $R$  a double ratio. It is determined from a simple physics decay simulation discussed in section 6.8.

Finally, once we have all these components in place, we combine  $R_{\gamma_{direct}}$  with equation 6.10 to produce the invariant yield of direct photons:

$$\frac{1}{2\pi N_f^{events}} \frac{dN_f^{\gamma_{direct}}}{dp_T dy} = (1 - R_{\gamma_{direct}}^{-1}) \frac{1}{2\pi N_f^{events}} \frac{dN_f^{\gamma_{all}}}{dp_T dy} \quad (6.12)$$

### 6.5.3 Bin Shift Correction

In this analysis we use  $p_T$  bins of varying size but as a minimum 0.5 GeV/c. Even with this smallest of bin sizes the steeply falling nature of the spectra means the bin center for each bin is a poor approximation for the average  $p_T$ ,  $\overline{p_T}$  in that bin, defined as

$$\overline{p_T} = g(\overline{f(p_T)}) \equiv g(f(\overline{p_T})) = g\left(\frac{1}{\Delta p_T} \int_{\Delta p_T} dp'_T f(p'_T)\right)$$

where  $f$  is the true (continuous) functional form of the spectra and  $g$  is its inverse. Since we are by definition summing over all photons or pions in a bin and as we shall see deriving corrections only for these sums, our final result for each bin is just the average over the bin,  $\overline{f}$  (e.g.  $\overline{\sigma}$ ). Therefore one would intuitively like to associate it with  $\overline{p_T}$ . Often this is done formally in particle physics and the measurement of say,  $\sigma(p_T)$  is given only at these  $\overline{p_T}$  values where the  $\overline{p_T}$  values are calculated by some method.

One might naively think  $\overline{p_T}$  is *measurable* itself, in calculating the average  $p_T$  value for each bin by summing, just as the spectral contributions (particle numbers) are summed, and dividing by the bin width. Of course this average  $p_T$  is not the same as our  $\overline{p_T}$  from above, since the raw number of particles at each  $p_T$  value actually needs corrected by all the correction functions that go into the final spectra. This requires nearly continuous and very accurate correction functions of  $p_T$ , which

in reality can only be approximated from the usual finite statistics, Monte Carlo-generated calculations.

In practice [29] it is better to assume a functional form for the shape of the entire final spectra and calculate  $\overline{p_T}$  a correction to the bin center that depends on local functional form of the true function which is attempted to be measured. As we shall see, this situation is common in spectral measurements: often a correction depends on the final answer, which paradoxically one is trying to measure. The solution is to iterate. In this case it is best done by an iterative procedure (described in more detail below) in which a trial functional form that describes the data is fit and used to determine  $\overline{p_T}$  for each point, the data points are modified on the  $p_T$  axis, and process is repeated until convergence is obtained.

In Heavy Ion and nuclear physics we often want to take ratios of the different spectra that we measure, and we'd like to make *point by point* ratios. If we were apply the above iterative approach and modify the  $p_T$  values of our data points, since presumably all the different spectra do not have the exact same shape, we would arrive at different sets of  $p_T = \overline{p_T}$  values for each spectrum which would make things inconvenient. Therefore we choose to use the same iterative procedure, but instead of modifying the  $p_T$ -axis values for each data point, we simply correct the spectral *yield* for each bin appropriately. We start with the data points with all corrections applied but  $C_{bin\ shift}$ , we fit a function  $f(p_T)$  whose form will be discussed in section 6.5.4, and then repeat the newly corrected data points. For each bin the fit is integrated and evaluated to make the ratio:

$$C_{bin\ shift}^i = \frac{\overline{f(p_T)}}{f(p_T = \text{bin center})}$$

The final correction  $C_{bin\ shift}$  then, is that of the final iteration  $i$ . For fitting functions that match the data well, the convergence is very fast. For example, for the spectra in this analysis, already within the first two iterations the fluctuations are at a negligible level compared to the first previous iteration as shown in Figure 6.35.

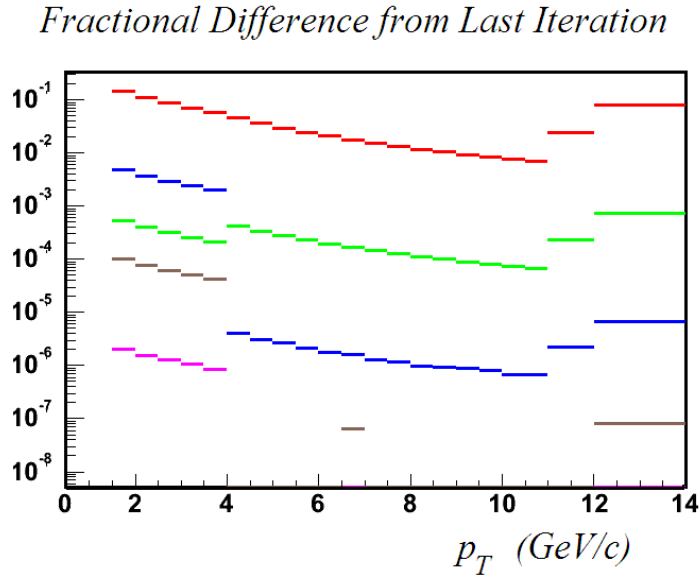


Figure 6.35: In the plot, 6 binshift iterations were performed. The absolute value of the fractional difference of each from the 6th iteration are shown in different colors. Mauve (5th), Brown (4th), Blue (3rd), Green (2nd), Red (1st). Note that the break at  $\sim 4$  GeV/c is due to the two component fit structure discussed below in the next section which is also explains the at low  $p_T$  momentary slight divergence of the blue in the third iteration. Nonetheless by the second iteration, the convergence is already at a negligible level relative to the other systematic errors of the analysis (section 6.9) By the fourth iteration much of the data points have converged within a level smaller than the numerical precision. Also note that the convergence is worse at different  $p_T$  values, determined by the local quality of the fit and especially the bin size.

### 6.5.4 Power Law Fitting

As already encountered above, in order to *produce* a fully corrected  $p_T$  spectrum, it is first necessary to be able to *fit* the spectrum you are trying to measure. The need for a fit which provides a continuous parametrization of the measurement, arises in the following applications discussed in other parts of this thesis:

- Bin shift correction iterations discussed in the previous section.
- Input to acceptance and detector efficiency corrections. Discussed in section 6.6.

- Input to the  $\gamma_{bkg}$  from decay mesons which is based on a fit to the measured  $\pi^0$  spectrum. Discussed in section 6.8
- Input to the Level2 Trigger efficiency corrections. Discussed in 6.4

In early nuclear, particle, and Heavy Ion ventures, production was limited statistically to the soft regime at relatively low  $p_T$ . As discussed in section 3.3 and 4.3.4, soft particle production is described well phenomenologically as a thermal equilibration of particle states and a simple Boltzmann exponential fits most particle spectra very well. [99]. Later Heavy Ion experiments up until the first RHIC data, even the published 200 GeV data before this thesis result entered into the hard scattering regime where power law behavior dominates. For this low and “mid”  $p_T$  data, a “modified power law” fit function generally attributed to Hagedorn [62] of the form fit the data quite acceptably:

$$f(p_T) = \frac{A}{(p_0 + p_T)^n} \quad (6.13)$$

However, this function, used to describe the previously measured  $p_T$  regions of most PHENIX particle spectra is not accurate at high  $p_T$ . For example there was a noticeable mismatch of the very highest  $p_T$   $\pi^0$  spectra from the fit with this function as shown in Figure 6.36 and the mismatch is worse in the highest  $p_T$  data which includes the level2 trigger statistics.

At very high  $p_T$ , a pure power law:

$$f(p_T) = \frac{A}{p_T^n} \quad (6.14)$$

is known to fit the data better.

This functional form does not, however describe the low  $p_T$  region very well. Much thought in PHENIX has been devoted to finding a single function that fits the data well in both regions. So far none have done better than the two above functions do in their respective region. So for this analysis, both functional forms

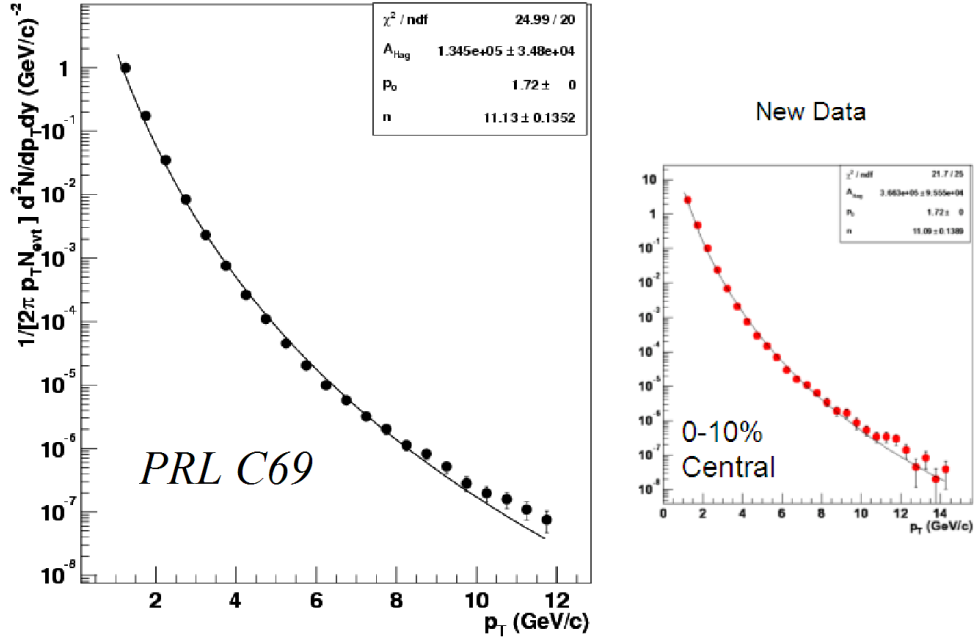


Figure 6.36: Both in the published PHENIX 200 GeV data ([15]) and continuing to higher  $p_T$  with the new data, we see that the modified power law consistently underestimates the data points at the high end.

were used in combination to describe the data. The way this was achieved was that 6.13 was fit in the region of 1.0 to 6.0 GeV, while 6.14 was fit in the region of  $p_T \geq 4.0$  GeV. Then a weighted average of the two functions, of the following form was used

$$f(x) = T(x) \frac{A_1}{(p_0 + p_T)^{n_1}} + (1 - T(x)) \frac{A_2}{p_T^{n_2}} \quad (6.15)$$

where  $T(x)$  was chosen to have the following fixed Woods-Saxon form, which essentially turns off one or the other functions depending on which region of  $p_T$  is relevant, determined by the parameters  $w, s, t$

$$T(x) = \frac{1}{(1 + \frac{e^{sx-t}}{w})} \quad (6.16)$$

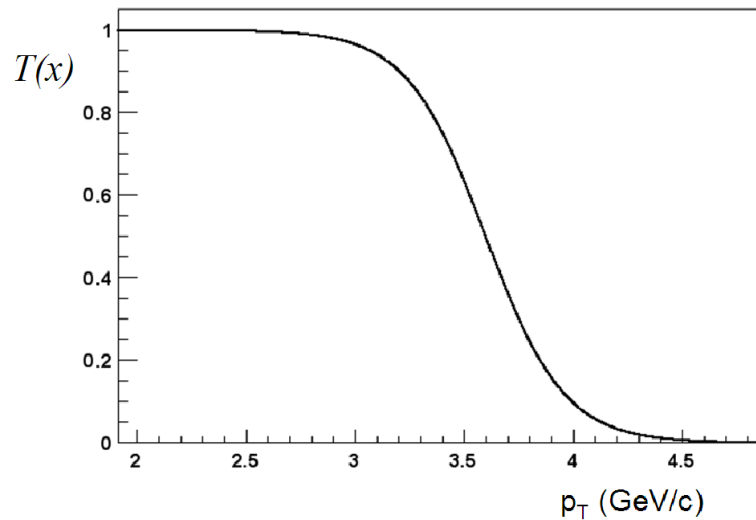


Figure 6.37: The actual function used to transition the two fit functions used in the two different  $p_T$  regions. This function multiplies the region 1 fit function and its complement multiplies the region 2 fit. As is visually apparent, below  $\sim 2.8$  GeV, the total function 6.15 is negligibly different from the region 1 fit function, while in contrast, region 1 fit function makes a negligible contribution in the  $p_T$  region above 4.5 GeV. In that region, the total function 6.15 is, to a high degree of precision, purely the region 2 fit function.

The values of  $w$ ,  $s$  and  $t$  were chosen in order to control the transitioning such that by 4.5 GeV the function has only a negligible admixture of the 6.13 fit, and vice versa below about 3 GeV as shown in the following figure:

Even though the new function 6.15 is continuous in all derivatives, occasionally we see systematic evidence of the rather drastic transition between the two functions such as in 6.35 from the previous section. However, it is not clear from the data whether or not the real data has this quality or not. As stated before, no functional form has been found which matches the data better. Nonetheless in situations where it was suspected to introduce an undesirable systematic, other functional forms were tried for systematic error evaluation discussed in 6.9.

## 6.6 Acceptance and Efficiency Calculations

As the formulas in Section 6.5 represent, we are interested in extrapolating the raw yields of clusters and cluster pairs that we measure in our detector to the true production of photons and  $\pi^0$  over the whole azimuth and “differential” rapidity interval. The bulk of this involves calculating the geometric coverage or *acceptance* of our detector and the probability that when a particle indeed strikes our detector that we actually detect it. The latter we call the *efficiency* in which we include other corrections: we will define what we call efficiency below.

### 6.6.1 Geometric Acceptance $a$

We calculate the geometric acceptance for particles by using a MC simulation of single particles thrown with a flat vertex distribution (which corresponds to the observed vertex distribution of events) between  $-30 \text{ cm} \leq z \leq 30 \text{ cm}$ . For neutral single particles which therefore have straight line trajectories (as opposed to charge particles which can be bent by the magnetic field) this simply corresponds to the fraction over the whole azimuth and rapidity interval which head from the vertex and intersect the vertex. Therefore it is constant with  $p_T$ . For a rapidity range of  $-0.5 \leq y \leq 0.5$  the constant acceptance of the PbSc detector is 0.287. Note that this factor does **not** account for **all** acceptance effects in our detector. Some acceptance affects cannot be separated from other detector effects, *e.g.* the effects of *dead* and faulty towers removed from consideration, and thus are included as part of the efficiency calculation, discussed in the next section.

For  $\pi^0$ , we calculate the acceptance only for those  $\pi^0$  where both photons intersect the detector or Dalitz decays ( $\pi^0 \rightarrow \gamma e^+ e^-$ ) where the photon and at least one electron intersects. The opening angle of decay particles depends on the lorentz boost of the pion so the distribution depends on  $p_T$ , and at high  $p_T$  approaches the single photon acceptance. The result of the calculation for the PbSc portion of the detector is shown in 6.38. This function is fit with the following smooth function, with the results for the parameters shown in the figure.

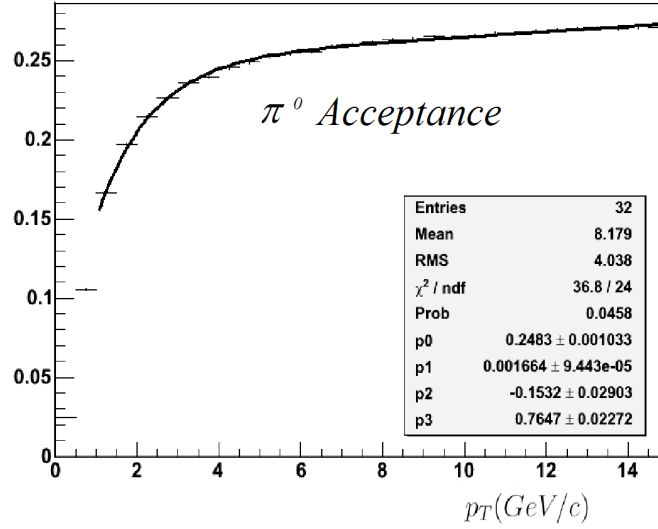


Figure 6.38: Acceptance for  $\pi^0 \rightarrow \gamma\gamma$  (including internal conversions) for the PbSc Calorimeter.

$$A(p_T) = (p_0 + p_1 p_T) (1 - e^{(p_2 - p_3 p_T)})$$

Above 1 GeV, the acceptance is always of the same order of magnitude. Below 1 GeV, the average opening angle becomes large enough that the correction  $1/a$  becomes large. This is the main reason we do not show results below this  $p_T$ . We note again that that this is factor does **not** account for **all** acceptance effects in our analysis, since dead towers are not included in this calculation, but instead in our correction  $\epsilon$ . We also note that since we use finite sized  $p_T$  bins (generally 0.5 GeV/c or larger) for the final  $\pi^0$  measurement and since  $\alpha_{\pi^0}$  is not constant with  $p_T$ , we must take into account the proper weighting within each bin due to the steeply falling shape of the real  $\pi^0$  spectra. We do this by using a power law fit as in section 6.5.4 which approximates the final  $\pi^0$  spectra—iteration in this case is not necessary since variations are small ( $\ll 1\%$ ) for all spectral shapes with power-law exponents  $n$  (see section 6.5.4) over a large range ( $\pm 5$ ) covering our final results within several orders of magnitude.

### 6.6.2 Efficiency Calculation $\epsilon$

After raw yield extraction (section 6.3), we have a measurement of EMCal clusters and clusters pairs falling within the  $\pi^0$  invariant mass window. Once we remove from these all background contamination contributions (for  $\pi^0$  this is the combinatoric background discussed in section 6.3, and for inclusive photons, this is hadron contamination discussed in section 6.7), the resulting yield is still not yet the true physics quantity we are after since its absolute value is still depends on non-interesting detector effects. For one thing, we must apply the acceptance correction  $\alpha$  described in the previous section. We lump together all remaining such corrections into a single factor  $\epsilon(p_T)$  which is also a function of centrality. The two main contributors to this factor are the effects of imperfect energy resolution (smearing) and occupancy degradation due to the high multiplicity of the Heavy Ion collisions.

The way we have separated the corrections  $\alpha$  and  $\epsilon$  is often called “factorizing” the corrections. In the case of  $\alpha$  and  $\epsilon$  in the way we’ve defined them, factorizing is exactly correct. For other effects such as smearing and occupancy, it is not possible to separate them by factorizing. So the way we must calculate  $\epsilon$  is with a single simulation which includes all such effects, and is therefore as realistic as possible. In the simulation, we know the “truth” information, the real photons or  $\pi^0$  we input, say  $N_p^{true}(p_T)$ , (where  $p$  is either  $\gamma$  or  $\pi^0$ ) and if we are careful that we extract the raw data, that the simulation generates in exactly the same manner (*i.e.* applying all the same cuts, *etc.*) we can calculate  $\epsilon$  with the following formula:

$$\epsilon(p_T) = \frac{N_p^{reconstructed}(p_T)}{N_p^{true}(p_T)} \quad (6.17)$$

where  $N_p^{reconstructed}$  is the raw data counts extracted in the simulation.

The effect of energy smearing, which we shall formally define as the modification of the true energy in the energy measured, causes shifts in the number of counts from one  $p_T$  bin to another. Therefore  $N_p^{reconstructed}(p_T)$  is a *functional* of  $N_p^{true}(p_T)$ , that is, it depends on the value of  $N_p^{true}$  at *all*  $p'_T$ . Starting with a *flat*  $p_T$  distribution of input particles allows arbitrary weighting functions to be applied which are equiva-

lent to starting with a real input distribution with the same shape as the weighting function. Therefore we must be careful that we use an input distribution/weighting function for  $N_p^{true}(p_T)$  that is as close as possible to the true particle spectra—the final result which we are paradoxically generating the correction in order to obtain in the end. We’ve encountered this problem several times already, and the solution is iteration. We start by using the observed raw cluster spectrum as the weighting function and generate a fully corrected candidate, which is used in a subsequent iteration. Iterations are performed until the final corrected spectrum converges. Just as with the bin shift correction discussed in section 6.5.3, it was found that only a small number of iterations are necessary: for the final  $\epsilon$  calculation, we use 4 iterations.

### 6.6.3 Simulation and Embedding

It should be apparent from the way we’ve defined our efficiency above, that a good simulation with good statistics is necessary if we are to believe the  $\epsilon$  calculated with formula 6.17. Since smearing and occupancy are such dominant effects, usually a so-called fast Monte Carlo (MC) which abstracts such effects into a finite (and small) number of well-defined modifications would be sufficient. The advantage of such fast MC’s are that they are simple and can quickly generate large statistics. However, it is safest to use a *full* simulation, as we have done in this case. Fast MC however, remain an indispensable tool for cross checks, and many effects observed in the full simulation were verified with fast MC checks.

#### 6.6.3.1 GEANT and PISA

A GEANT simulation [60] was employed to ultimately calculate efficiency and other corrections. GEANT is a program in which a (detector) geometry can be specified as input, including its materials, to nearly arbitrary precision, along with particle trajectories starting from arbitrary points. Once these are specified, GEANT will follow the particle and will generate and recursively follow the products of, interactions

with the specified matter configuration based probabilities which take into account nearly all known world knowledge of such propagation. A very general program, this data that it generates can be used make very realistic full scale simulation of detector responses. PHENIX interfaces GEANT to a larger application which converts the generated data into digitized detector signals segment by segment that mock the real data flow from the detector. This fake raw data can then be run through all normal reconstruction code which makes the simulation as real as possible. We call such a fully complete simulation an *full hit-level/response* simulation.

In the example of the simulation of EMCAL showers, the normal GEANT recursive following of every single product of every single interaction can quite often lead to unmanageable numbers of particles. In this case parameterizations are used. These parameterizations have been worked on for decades and are continually being updated by the physics community. The hardest showers to replicate in the simulation are hadronic showers. For this, several “flavors” of GEANT packages exist, for example FLUKA and GCALOR. [83] [91]. These will be discussed further in our discussions of charged hadron contamination in section 6.7. Even for EM Showers however, it is difficult to get *e.g.* the exact shower shape parameters right, and in general much tuning is input from test-beam measurements. The most accurate aspects of the full simulations should be macroscopic aspects such as the effects of acceptance and dead towers.

Even with a nearly perfect simulation and nearly perfect tuning, another difficulty with using a simulation simulation lies in *de*-tuning the response to reflect realistic imperfections. The place where this is most important is in properly capturing the inherent imperfections in the calibrations, since the GEANT/PISA program responses will be completely uniform. For many cases like this it is preferable to directly use real data in some way in order to ensure realistic situations.

### 6.6.3.2 Embedding

One place this is especially true is for simulating the effects of occupancy. Doing this completely from simulation is impossible, since even the best full event generators

on the market, such as HIJING, have problems predicting many exact details, such as the exact total multiplicity of charged and neutral hadrons—these are things we are setting out to measure. Therefore we employ a method of *embedding* where real EMCal hit data is combined with simulated hit data. In the case of our EMCal, this means we simply add simulated tower energies directly to real tower energies, and re-cluster. Timing information is taken from the tower with maximum energy as usual (indeed the exact same clustering code is employed as for real data), which for high  $p_T$  clusters will be tend to be simulated, but can be real for low energy embedded clusters.

Single photons and  $\pi^0$  are generated with the PISA simulation. The response data from a single such simulated particle is added to an event from the real data with a matching vertex, chosen from random. Vertex matching was done with fixed vertex bins similar to the  $\pi^0$  mixed event background generation discussed in 6.3.5.1 except that much finer 5 cm vertex bins were employed. That this tolerance was sufficiently small was checked by verifying that further reduction of the tolerance made no difference in the final efficiency calculations. In order to ensure realistic centrality weighting within centrality bins, events were additionally weighted with the original EMCal multiplicity from the real event.

To determine which centrality bin an embedded particle should be used for, the original real event centrality was used. Since we are embedding single particles into the central arm only, re-evaluating the centrality from BBC/ZDC information is obviously useless. Therefore in principal a hit or hits should be removed from an event before the embedded particle energy is added so that the distribution EMCal multiplicity for the new merged events is the same as that for all the real events in the same centrality bin. However, it is difficult to come up with an algorithm to decide how hit information should be removed. Therefore no clusters or tower information was removed from events before embedding and this effect was ignored. Such an effect should be small in all cases: for high multiplicity central events, the addition of a single particle represents a small proportion of the total— in central

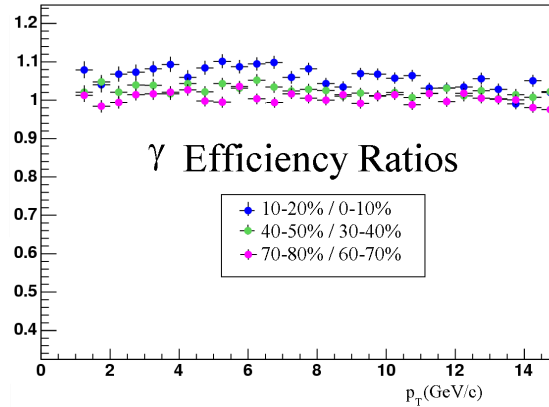


Figure 6.39: Ratio of efficiencies for different centrality bins. Since multiplicity is already a small effect between adjacent centrality bins, we can safely neglect removing hits from an event before embedding a particle.

events the EMCal cluster multiplicity is approximately 300, so we are talking about roughly a 1 part in 300 effect. On the other hand, for peripheral events where the multiplicity can be much lower ( $\langle N_{clus} \rangle \cong 4.5$  in the most peripheral 80-92% bin) the probability of overlap becomes so small that the additional multiplicity becomes insignificant. This logic can be verified by comparing the actual efficiency calculation between adjacent centrality bins, since as a ridiculously high upper limit of how much a single in could be off. As Figure 6.39 shows, these differences are on order  $< 5\%$ . This would be the size of the effect if *every* embedded cluster were being placed in the wrong centrality bin—therefore since we know this is really only an extremely small portion of the clusters ( $\propto (1/\langle N_{clus} \rangle) \times P_{overlap} \ll 1$ ) it is perfectly safe to ignore this effect.

#### 6.6.4 Smearing

Not surprisingly, the calibration of the full EMCal was found to have worse resolution than the “intrinsic” resolution determined from test beam. The  $A/\sqrt{(E)} + B$  functional dependence in formula 5.1 was found to have the same  $A$  as determined from the test beam, as it should since this term is determined by the physical geometry of the tower units due to the Poisson statistical nature of the showering process.

However the constant” term  $B$  was higher than in the test beam case due to gain fluctuations. In order to de-tune the simulation to this worsened resolution, an extra smearing amount was given to each simulated tower in addition to the  $B = 2.1\%$  smearing already in PISA based on the test beam. A random gaussian distribution of smearing with root-mean-square equal to  $BE$  was added to each tower energy. For each simulated photon the smearing was thrown randomly for each tower, simulating the gain drifts and fluctuations inherent in each. After an initial production additional such random smearing was also applied at the cluster level, as this was found to generate the best agreement between real data and simulation. The final amount of extra smearing chosen was  $B_{clus} = 4.5\%$  for clusters and  $B_{tower} = 3\%$  for towers based on the match between the simulation and real data. However, as discussed there and further below, with this choice also went along a final calibration scale choice as the  $\pi^0$  peaks were ultimately also used to fine tune the calibration itself. Correlations inherent in this procedure are discussed in the section after the next, 6.6.10.

### 6.6.5 Final Efficiencies

In the following figures, we show the result of the efficiency calculations for each centrality bin. Statistical errors on the simulation are at the 3% level and are reduced to 1% by smoothing [86] at high  $p_T$ . The rising trend of both the photon with  $p_T$  is due to the smearing effect which moves photons and  $\pi^0$  out of their true  $p_T$  bin and into neighboring bins. Since the spectra is steeply falling, the particles “moved up” into a  $p_T$  bin from lower  $p_T$  are proportionately much larger than those lost. This results in an effective efficiency that can be  $> 1$ —in this case it is still less than 1 because of dead tower effects included in the calculation.

### 6.6.6 Systematic Uncertainties: Simulation/PID

How can we verify that the simulation is in fact reproducing the real world situation with the electromagnetic calorimeter and to level of uncertainty can we verify this?

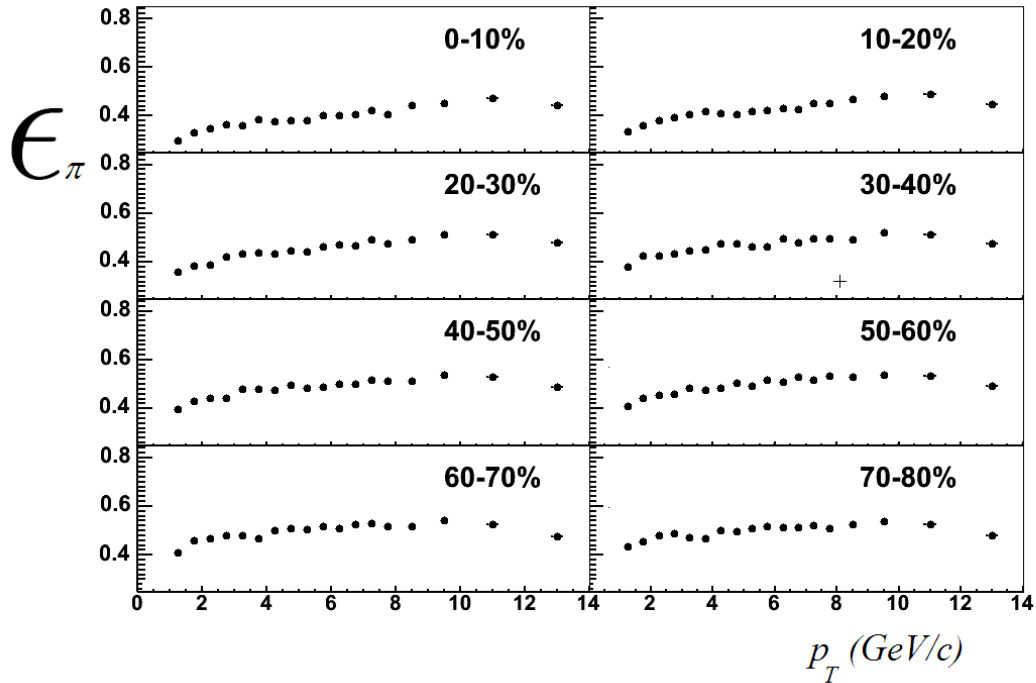


Figure 6.40: Final efficiency calculation for  $\pi^0$  vs.  $p_T$  and centrality. The noticeable drop in the efficiency at high  $p_T$  is due to the inability of the clustering algorithm to separate the two decay photon clusters into two distinct clusters already demonstrated in Figure 5.9. The efficiency shown is for the shower shape PID (PID2) cut, since this was the only PID cut used in the final results.

Here we are only concerned with how accurate our efficiency calculations derived with the simulation really are and in this section we mean to exclude the additional complications of the embedding reproduction of occupancy effects due to the high multiplicities of central events, rather focusing on the base PISA simulation itself. Also here we are only concerned with the simulation's response to photons, as this is all that is relevant for both the photon efficiency and the  $\pi^0$  efficiency calculations: because of the way we have separated our corrections, the hadronic shower response of the simulation we only matter significantly for the calculation of the charged hadron contamination which we will discuss in section 6.7. Therefore, for the photon response how can we derive or otherwise determine the level of uncertainty associated with the base simulation? This question is intimately tied to the more specific

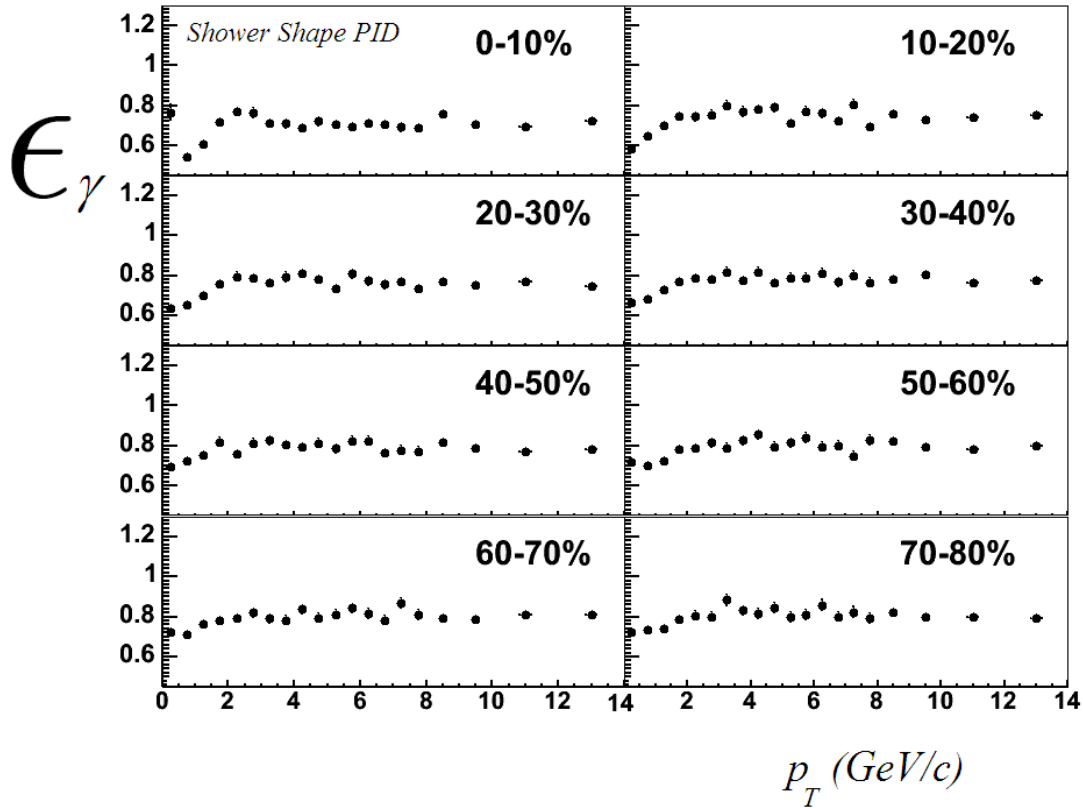


Figure 6.41: Final efficiency calculation for single photons vs.  $p_T$  and centrality. The efficiency shown is for the shower shape PID (PID2) cut, since this was the only PID cut used in the final results.

uncertainty we can place on the simulations ability to reproduce efficiencies of the various cuts, especially the PID cuts introduced in section 6.3.4.

The base simulation was tuned to match the test beam results for the properties of EM showers of testbeam electrons. For example the threshold for GEANT to follow the exponentially large quantity of the very last low energy electrons and photons in a given EM showering process and other parameters are adjusted until the shower shape produced by the simulation as well as the fluctuations associated with the shape (as parameterized in formulas 5.2 and 6.1) and are well reproduced. The reproduction of such distributions is therefore perfect in the simulation, since this is its starting point. The timing distributions are also tuned in a similar manner,

to match the timing distribution of the test beam results. This *is* in fact the best verification we can make that the simulation is correct for single particles. Under ideal test beam situations, we would simply be forced to assign a negligible amount of uncertainty to the quality of the base simulation.

Of course we are not interested in using the simulation in test beam situations, but under the real conditions that the data was taken under. The following items may reasonably be expected to change the behavior of the EMCal's photon response compared to the test beam:

- Different energy resolution due to a non-uniform calibration. See below.
- non-uniformity of response due to differences in the construction of the new sectors not included in the test beam runs (the majority of the detector) and the introduction of material from the rest of the PHENIX detector, especially the introduction of PC3 so close to the calorimeter.
- dead towers (same as hot, since hot towers are removed) inclusion in the clustering algorithm—the test beam shape parameterizations are derived from the situation where all towers will be included in the cluster energy fit and sum. Hot and dead towers will alter the behavior of the fitting procedure and the calorimeter acceptance.

Of these concerns, the first item, the change in effective energy resolution is the most important: as mentioned above, the steeply falling nature of the spectra we are trying to measure makes the shifting of particles to higher  $p_T$  bins the dominant effect in the efficiency calculation at high  $p_T$ . We will discuss this effect and derive an uncertainty for it below. This  $p_T$  shifting effect is not the only effect that the non-uniform calibration can have, however. Like the other points listed, it can also change the shower shape distribution in the calorimeter. Such a change will result in a different overall base efficiency of the cluster algorithm and fitting procedure. This will also change the photon/electron position resolution of the calorimeter, since these values are obtained from a fit. Such a change will even change the

acceptance calculation for  $\pi^0$  slightly when the asymmetry cut is applied. In other PHENIX EMCAL analyses of low multiplicity  $p+p$  [161] and  $d+Au$  [14] environments, consideration of these effects were enough to forego the full simulation completely and resort to fast MC efficiencies where the effects of such symptoms such as position resolution modification could be studied directly to evaluate systematic errors. We shall resort to such studies in this analysis, however because of the importance of accounting for occupancy effects properly as only a full simulation can do, in this  $Au + Au$  analysis, it was necessary to use the full simulation.

The best way then to derive an uncertainty in the base simulation then is to identify a clean photon or electron sample and study the distribution of clustering and shower shape parameters, *e.g.* most directly the shape distribution itself, can be measured and compared to real data or less directly the cluster  $\chi^2$  can be studied. When a differences are found, a tuning parameter that causes the distribution to change in the simulation can be modified until the simulation reproduces the real data, or until the propagated uncertainty due to the difference is understood. This is how systematic uncertainties can be reduced. Such work is very time consuming because of the large computation time involved in the full showering reconstructions in GEANT. For this reason, and others, including lack of good statistics on the various distributions (*e.g.* shower shape) at the high  $p_T$ 's we are interested in for this analysis,<sup>5</sup> an expedited method for evaluating the uncertainty in the efficiency from the simulation for all effects *other than* the energy resolution bin shifting effect was employed.

An important consideration to this method is that the shower shape  $\chi^2$  PID distribution and cut already explained in section 6.3 is directly dependent on the shower shape distribution in the calorimeter. By varying this cut, we can compare how the simulation reproduces the real data. This gives us a first level *measurement* of how large the uncertainty in the simulation is as explained in Figure 6.42. In the figure, an strong pair asymmetry cut ( $\alpha < 0.2$ ) ensures that for the  $\pi^0$ 's in the

---

<sup>5</sup>the testbeam results had excellent statistics all the way out to  $E=80\text{GeV}/c$ !—the statistics for most photon distributions become non-constrainable by about 4 GeV/c in the current data set.

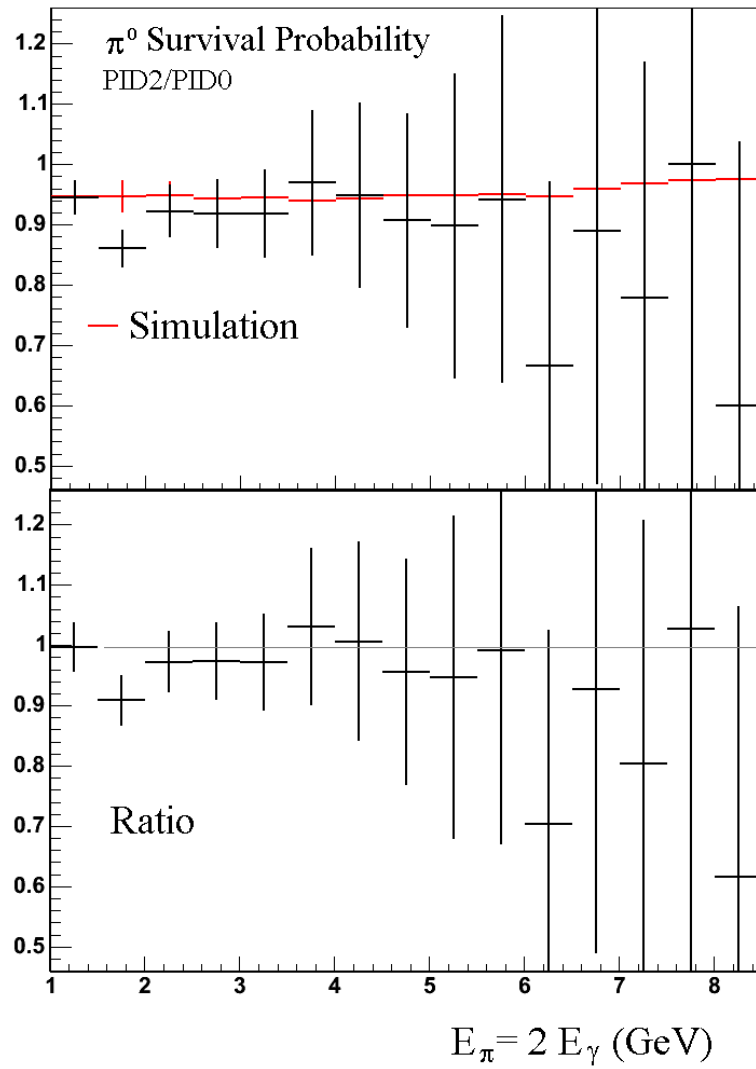


Figure 6.42: Survival probability of  $\pi^0$  with tight asymmetry cut compared between simulation and real data.

sample, both decay photons have approximately equal energy. Since for the *survival probability*  $p_{\pi^0}$ , the probability to survive the cut, is just the product of the survival probabilities of the photons, for this sample

$$p_{\gamma}(E_{\pi^0}/2) = \sqrt{p_{\pi^0}(E_{\pi^0})}$$

Therefore this is a direct measure of the real survival probability for photons, uncomplicated by contamination effects, since only real photon pairs can contribute to the  $\pi^0$  yield. This is more or less a direct comparison of the simulation's performance. Its uncertainty is only the statistical uncertainty on the  $\pi^0$  yields and the systematic error on the yield extraction, which we have already evaluated via other means (see section 6.3). It will contain conversion electrons but as discussed in 6.7.1 this should be a negligible effect since the conversion rate is small ( $\sim 7\%$ ) and the electron showers should be nearly identical to photon showers. Multiplicity effects should be considered small, as this is for the most peripheral bin where the occupancy is low and the probability of overlap is negligible. We shall consider the effects of multiplicity in the next section.

Next we verify that the efficiencies obtained with the simulation satisfy the most basic sanity checks. First we compare the distributions of the cut variable with the real data. As shown in Figure 6.43, at a qualitative level, the distribution agrees with the simulation. With no PID cuts at low energy, there is a sizable contribution from hadron showers. The effect is a distorting one, and as we apply the TOF PID cut, removing a large portion of the contamination, we see that the distribution matches even better.

This efficiencies and their uncertainties can also be studied in fast MC in order to verify that the results of the simulation are believable. In these studies we approach the problem two ways. First as the most basic sanity check, we simply assume a  $\pi^0$  survival probability measured in the data, and folding this together with acceptance, hot tower, and smearing effects, verify that indeed the efficiency we get for both  $\gamma$  and  $\pi^0$  agree with the results of the full simulation. The results of such a study yield

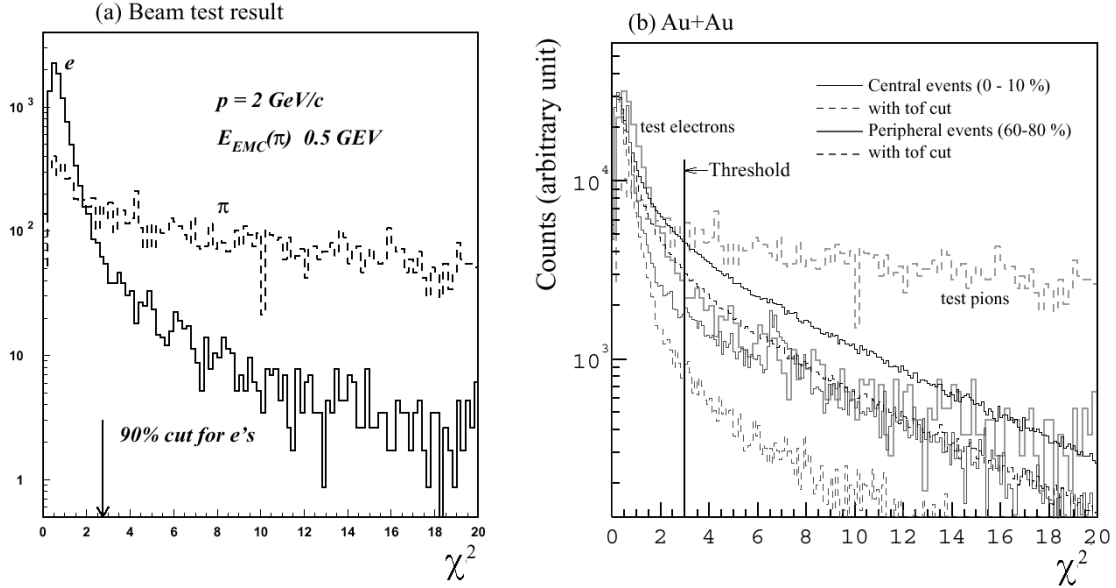


Figure 6.43: Comparison of  $\chi^2$  distributions between real data and test beam/simulation. figure from [141].

agreement with the full simulation at the better than 3% level. Then in the second approach, we estimate uncertainties on the fast MC in order to bound the possible differences with the full simulation, we can abstract the possible problems with the simulation as being reflected in, *e.g.* a modified position resolution. Such a result is shown in Figure 6.44 and is small. Indeed separating out the energy smearing effects, the rough level of uncertainty in all the fast MC estimates are on the order of  $\sim 5\%$  [161], [38].

From the considerations of the level of uncertainty between the photon survival probability in the real data, (which translates directly to the efficiency) and the agreement between the fast MC estimates within their uncertainties, we make a conservative estimate of the error in the single photon of 6.5% and 8.5% for  $\pi^0$ .

That this error estimate is reasonable can be cross checked by comparing the final fully corrected photon spectra produced with the different PID cuts. This is shown in Figure 6.45. That the timing cut results also agree well and within the same level of uncertainties serves as a cross check on the level of uncertainty we have

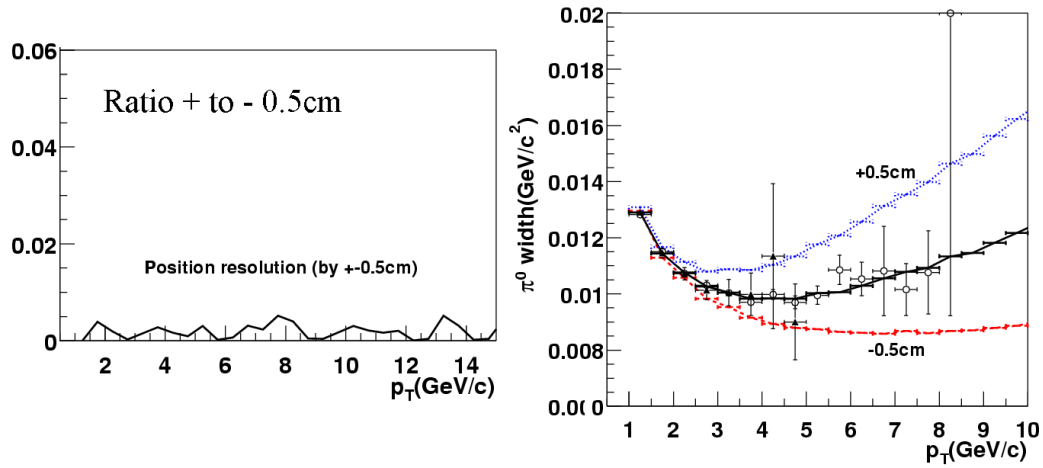


Figure 6.44: Fastmc study of position resolution effects. Relatively large modifications in the position resolution shifted  $\pi^0$  widths can correspond to very tiny differences in the overall efficiency. This must be taken into account for determining the matching between simulation and real data  $\pi^0$  resolution.

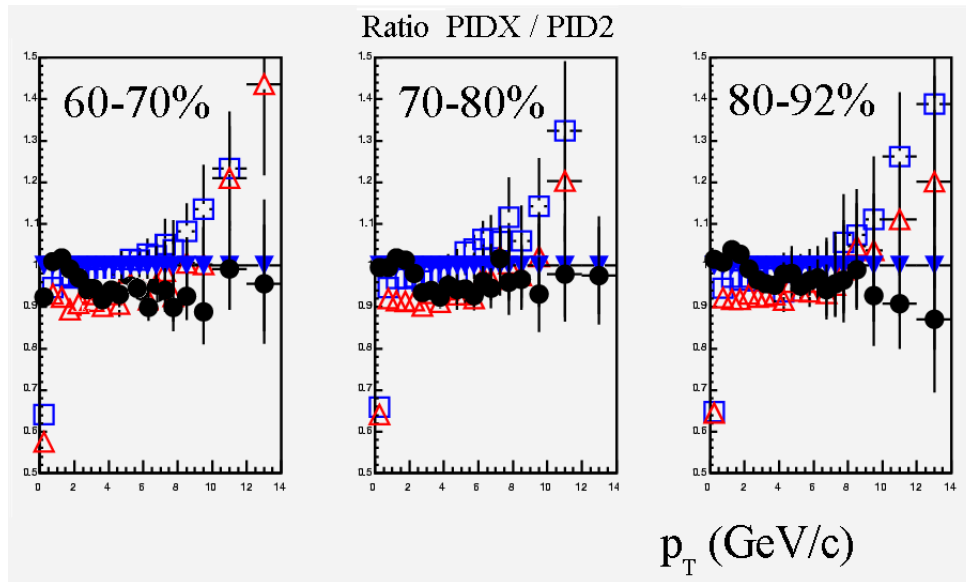


Figure 6.45: Ratios of fully corrected spectra for different PID selection for cross-check of  $\gamma$  efficiency errors. The dark black circles correspond to PID0.

assigned.

### 6.6.7 Systematic Uncertainties: Embedding

In addition to the uncertainty on the base simulation, we must also evaluate the uncertainty due to our embedding method of reproducing cluster multiplicity effects. For this we proceed in the same manner as in the evaluation of simulation, by comparing the  $\pi^0$  survival probability for the shower shape cut, and verifying that fastMC results yield the same answers within all uncertainties. In order to reproduce multiplicity effects in the fast MC, the probability of overlap is calculated for each centrality bin, and the photon cluster energy in the fast MC is modified according to this probability by sampling from the total cluster distribution. Again the  $\pi^0$  survival probabilities calculated from this method are found to agree with the full simulation results within the uncertainties of the fastMC.

The results of the comparisons across all centralities are summarized in Figure 6.46.

Based on these considerations, the already 8% conservative error on the base simulation is seen to sufficiently account for the possible uncertainties for most centralities. However going to the most central events a slight increase (2%) in the uncertainty of the efficiency calculations is justified there. Correspondingly an extra uncertainty of maximum 5% for the most central events and a minimum of 0% for central events is added in quadrature.

### 6.6.8 Systematic Uncertainties: Calibration

#### 6.6.8.1 Calibration Errors

The absolute calibration is determined by the peak locations of  $\pi^0$  at high energy in section 6.2.3. In fast MC studies the energy scale is modified by a constant value of X%. It is found that deviations within 1.5% are still consistent with the  $\pi^0$  mass peak locations from the real data. From this value a systematic error is generated by observing the differences in the yields in the fast MC for these values. This comparison is shown in Figure 6.47 This error is found to be  $p_T$  dependent as one would expect, and a simple linear parameterization is used for the final errors.

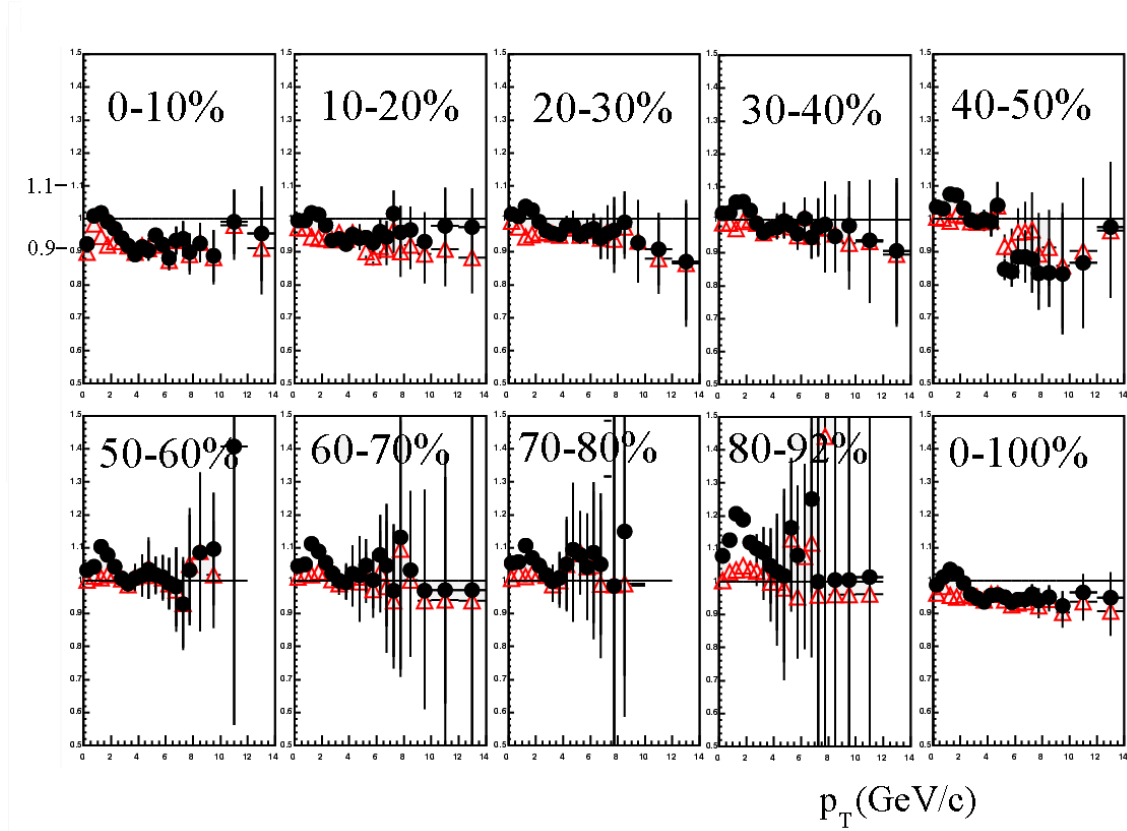


Figure 6.46: Ratio of simulated and real  $\pi^0$  survival probabilities for all centralities.

As discussed in the calibrations section (6.2) the absolute calibration can only be independently verified by looking separately at an independent check like the electron  $E/p$  location. One such cross check is shown in Figure 6.48 for PbSc only. Below 2 GeV/c this ratio is known to deviate below 1 from GEANT simulations, due to a different response for very low energy electrons. Between 2-4 GeV/c, where we have good statistics we excellent on the level of 1% of the scale, ranging from 12% at low  $p_T$  to 20% at high  $p_T$ . Furthermore a study was done to determine the maximal effect from a larger non-linearity at low  $p_T$  where the electron information is unreliable shown in the inset.

In addition to the electron check, the non-linearity of the scale was checked by the yields the cross section as a function of different asymmetry cuts, which tests the non-linearity. Unfortunately this could not constrain the non-linearity more accu-

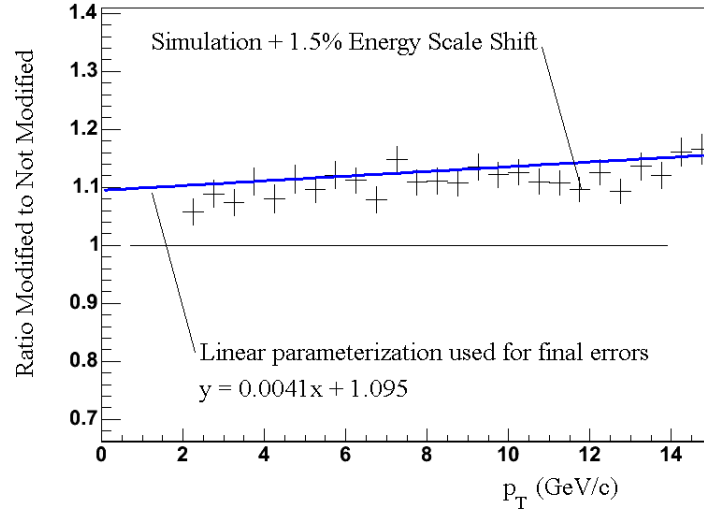


Figure 6.47: The energy scale in fast MC is modified by 1.5%, the full uncertainty of the real energy scale, in order to determine the uncertainty in the yields due to the calibration.

rately than the electron  $E/p$  because at low  $p_T$  the yield extraction error of  $\sim 10\%$  is much larger than the percent level errors that would be due to non-linearity/scale deviations, while at high  $p_T$ , where 10% would provide useful constraints on the scale, the statistical errors become too large.

### 6.6.9 Systematic Uncertainties: Smearing

For the systematic uncertainty due to the tuning of the simulation the opposite process was performed: the smearing function of the simulation was modified by adjusting the amount of additional constant-term ( $B$ ) smearing discussed above, and the results were compared to the real data points corrected with the optimal calibration. Shifts in  $B$  up to 2% were found to yield  $\pi^0$  mass plots still consistent with that of the real data across all centralities. The resulting propagated uncertainty in the efficiency due to this effect was taken to be a constant 6%. The results of this study are shown in Figure 6.49.

Thus the uncertainties due to the smearing in the simulation and the calibration

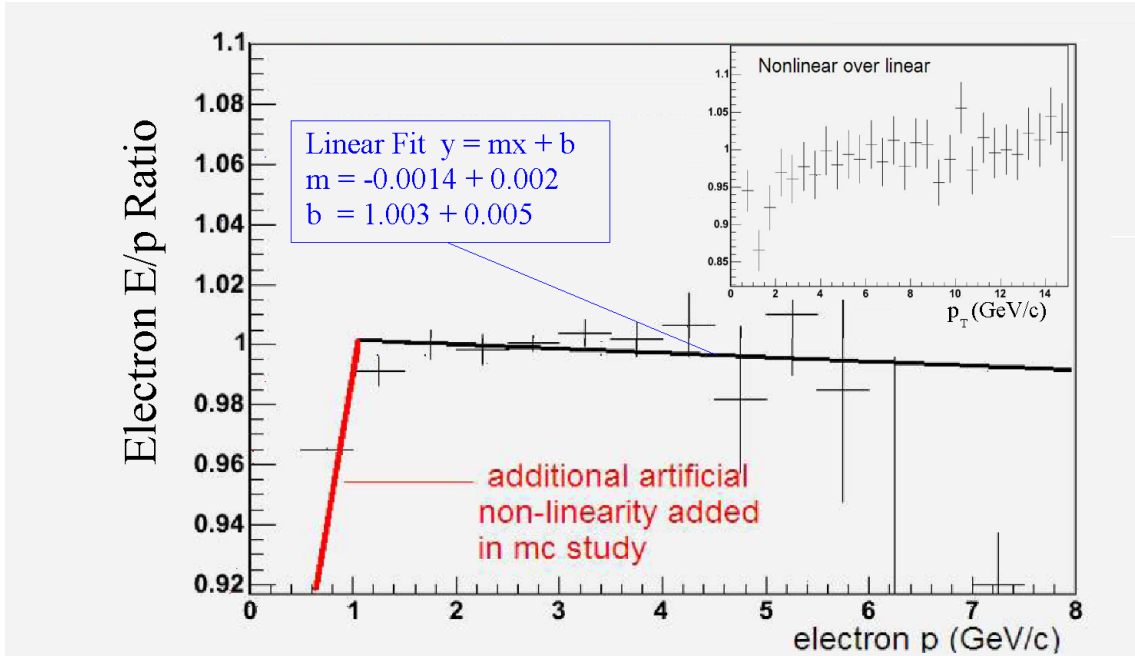


Figure 6.48: Cross check of the energy scale: electron  $E/p$ . At low momentum ( $< 2$  GeV/c) other effects (*e.g.* differences in photon-electron response, greater hadron contamination) are known to distort the ratio from one. Above this value the fit is consistent with linearity within 0.3%. The red curve was used for a fast MC systematic error study of possible non-linearity effects from this EMCal energy region. The result of the study is shown in the inset.

were determined independently. It is apparent however that since there could be small correlations between these two uncertainties: therefore this was also checked as discussed in the next section, and found not to significantly add to the uncertainties of these two error estimations.

### 6.6.10 Calibration and Smearing Correlations

As discussed in the calibration section 6.2 and above, the final calibration was determined by adjusting the  $\pi^0$  mass peak positions to the correct position as determined by the simulation based on the resolution apparent in the  $\pi^0$  mass widths, whereas the simulation itself was de-tuned back based on the resolution from the same real data. This was an iterative process belabored by the fact that it was difficult to re-pass the full data set with a new set of calibration parameters and re-pass the full

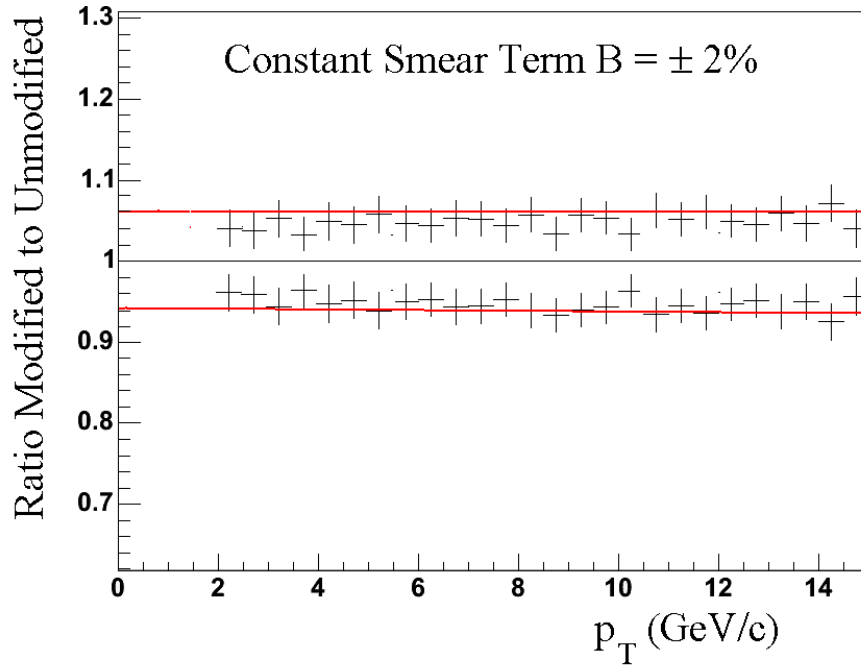


Figure 6.49: The efficiency calculation for  $\pm 2\%$  shifts in the constant term  $B$  (see above section) resolution smearing is compared to that of no modification in order to determine the error from this uncertainty.

simulation files with a new set of smearing parameters each time. Therefore, after several iterations, the best level of agreement across all centrality bins was found and *assumed* to be acceptable. Then faster MC methods were used to determine the determined the systematic bias and uncertainties that were possible from the final choice of smearing and calibration parameters and the process used to determine it. In addition, fast MC method estimations must be employed because, although the  $\pi^0$  peak *width* information is to first order independent of the the peak *position* and therefore the method can be expected to work correctly, the small amount of feedback between the two could result in larger systematic biases than would be present from the simulation or calibration separately.

In order to perform the fast MC bias estimations, the full set of simulated  $\pi^0$  photon clusters and truth information and a subset of real data clusters corresponding

to a single centrality bin were chosen at random from across the entire Run2 data set were gathered. This set of minimal information was small enough that it was able to be stored in memory and a MINUIT minimization [117] routine was performed by minimizing the  $\chi^2$  between the actual invariant mass distributions between simulation and data. Finding the optimal set of calibration and smearing parameters for this individual centrality bin, then the amount of systematic uncertainty present in the previously determined set of global calibration and smearing parameters could be evaluated by comparing to the optimal set. Results from the study are shown in 6.50. In this way the level of systematic error on each parameter was estimated but most importantly correlations between the parameters were found to be minimal, and agreed with uncertainty estimations derived independently for each parameter discussed in the previous section.

### 6.6.11 Other Sources of Uncertainty and Error Summary

One remaining uncertainty in the efficiency calculation is the uncertainty in the iteration process and the input (weighting) spectrum: the uncertainty was taken conservatively to be the systematic difference 2% between the first iteration and the second iteration, since this is the maximal change between iterations.

The systematic error from the various sources discussed in this section are summarized fully with the rest of the error sources for the entire analysis in section 6.9

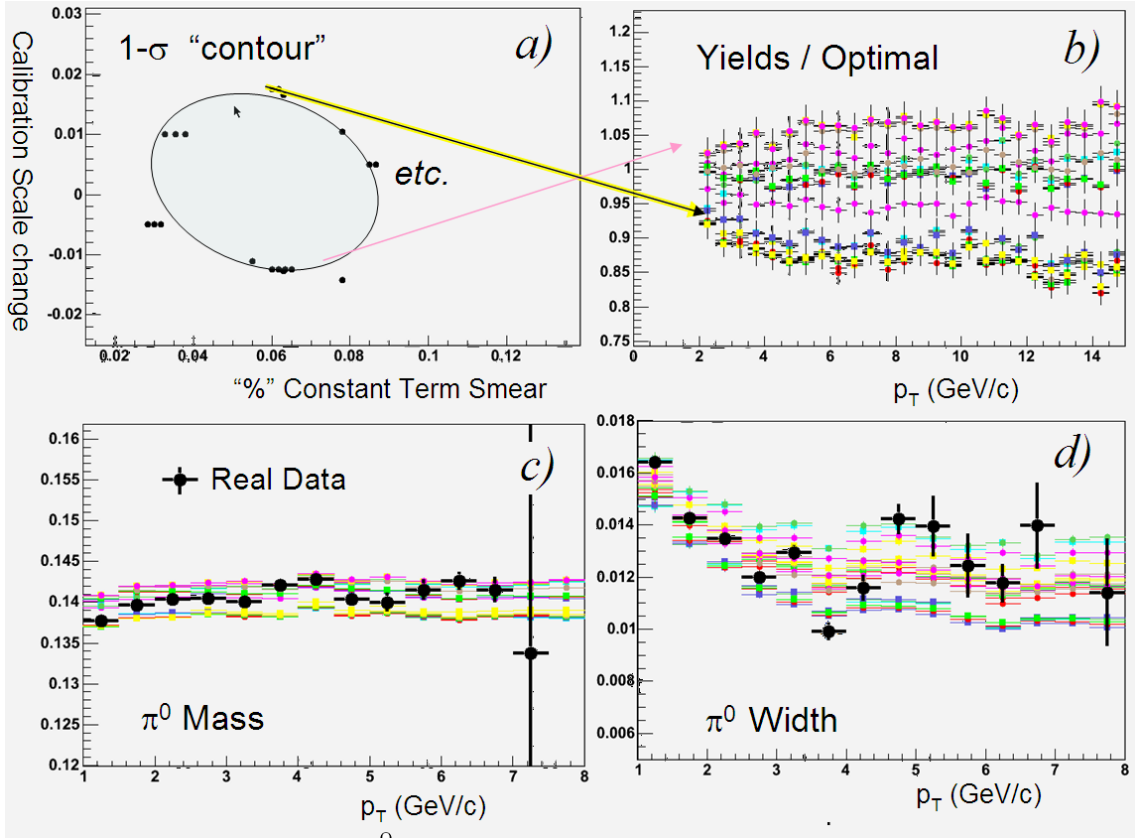


Figure 6.50: Study of error correlations between calibration scale and simulation tuning. The constant smearing parameter  $B$  as discussed in the text, was varied simultaneously with the overall calibration scale correction in a MINUIT minimization program. After the a minimum was located, trial points from along a "1-sigma" contour (a) determined by observing acceptable consistency between the  $\pi^0$  mass plots (c) and d), were used to generate fully corrected  $\pi^0$  and photon yields (b). The latter is an estimate of the systematic uncertainties due to these two quantities experimental parameters together, and thus any correlations present did not appear to dramatically increase the uncertainties from estimates based on independently varying either parameter separately, which is how the final uncertainty assignments were determined.

Material Budget In Front of the West PbSc in % of $X_0$ (East Arm)	
Beam-pipe+MVD+air/He(2m)+DC	1.3%
PC1	1.2%
$X_0$ in Magnetic Field	2.5%
RICH (CO <sub>2</sub> )	2.1%
PC2+Air	2.7%(0%)
TEC	0%(0.8%)
PC3	2.4%
Total	9.7%(7.8%)
$P_{conv}$	7.3%(5.9%)

Table 6.4: Material budget in front of the PbSc Calorimeter

## 6.7 $\gamma$ Conversions and Hadron Contamination

### 6.7.1 Photon Conversions

The amount of material in the detector is input in the full GEANT simulation and conversion probabilities for photons are determined. For the  $\pi^0$  analysis, the effects of photon conversions are small. The majority of conversions result in one or both of the electrons hitting the calorimeter, and since they are electrons, still have shower properties that pass the photon shower shape and timing PID cuts. Still there is some intrinsic loss due mostly due to the sweeping away of lower energy electrons by the magnetic field and multiple scattering in the detector. From the embedding studies, a nearly constant 10% loss is found for  $\pi^0$ . However, since the full (embedding) simulation includes all the effects of conversions, this correction is already included in the final calculation of  $\epsilon$  discussed in section 6.6.

As discussed in the next section, photon conversions are removed in the single photon analysis by our statistical method for removing all clusters associated with charged tracks. This removes virtually all conversions, since the final subtraction is done with the PC3 veto which sits just before the front face of the EMCal. The conversion rates in table 6.4 gives a first order determination of the conversion loss.

The final conversion rate however is determined from the full simulation. Care must be taken to check whether that  $\pi^0$  decay photons should be treated differently, since it is found as shown in Figure 6.51 that due to the increasing proximity of the

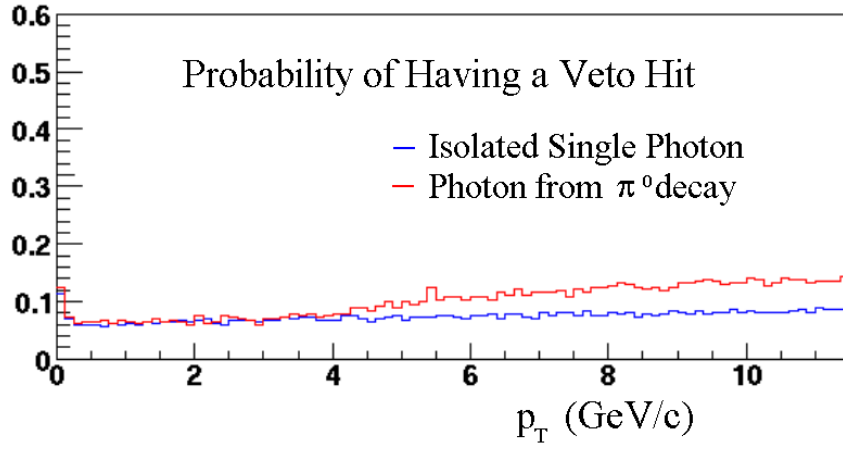


Figure 6.51: The conversion photons lost due the charged particle veto tagging. The blue curve is for uncorrelated single (*e.g.* direct) photons, while the red is for photons coming from  $\pi^0$  which have an increasing (with  $p_T$  chance of being tagged by their decay sister. The loss is incurred in a statistical subtraction of the charge particle contamination, not from true cluster vetoing.

two decay photons in  $\pi^0 \rightarrow \gamma\gamma$  as the momentum of the  $\pi^0$  increases, and therefore the conversion loss rate due to the CPV tagging also increases. However this effect is found to be negligible when the full statistical subtraction is employed, since such “false tags” also appear in the background matching region and therefore cause the net subtraction to be approximately the same as in the case when no  $\pi^0$  correlation is considered. It is known that the cross section for photon conversion based on the world data set [51] appears to rise slightly by a approximately a couple percent. Despite both of these considerations, we choose to make a constant conversion loss correction of 7.5% for single photons, and include the differences as systematic uncertainties. This results in a total uncertainty in the conversion correction of 3% which covers the possible rising trends, since the uncertainty in this trend for both effects is not significant to better than this level.

### 6.7.2 Charged Contamination

Charge particles (including electrons from photon conversions, discussed above) were removed from the photon sample through statistical subtraction. Both the full PHENIX tracking system and the Pad Chamber (PC3) which sits 5 cm before the front face of the PbSc portion EMCal are acceptable for making a charge particle veto (CPV) on clusters with a nearby track or Pad Chamber hit however, both systems suffer from dead areas which can be accounted for most accurately using the statistical method. The statistical method relies on the inherent correlations between tracks or PC hits (we shall hence refer to either of these together as CPV's) and EMCal clusters formed by the charged particles through MIP passage or showering in the calorimeter.

In each event, the distribution of minimum distances for each emcal cluster, between the cluster and the nearest CPV 's are made, in different  $p_T$  and centrality bins. Each such distribution has a natural correlation peaked around zero distance (modified by the  $1/r$  area factor) due to the EMCal clusters that are actually caused by charged tracks. The random combinatoric contribution to this distribution can be calculated separately using a mixed events procedure identical to that used for generating the  $\pi^0$  combinatoric background. This mixed event distribution is scaled such that the normalization of the foreground and background match in the large distance region where the combinatoric contribution dominates. It can then be subtracted from the real distribution resulting in a peak which can be integrated to find the number of EMC-CPV pairs. An example of this is shown in Figure 6.52.

The matching region chosen is the region  $r > 25cm$ , which was determined by looking at the combined distribution for all  $p_T$  bins and centrality. Results using the PC3 are shown in Figure 6.53. PC3 was used for the final correction. This fraction is significant at lower  $p_T$  values and can reach as high as 40% for central events. At high  $p_T$ , the difference between CGL Track and PC3 contaminations are consistent with the extra photon conversions from material between the Drift Chamber (DC) and the PC3. This is as expected since CGL tracks start with the

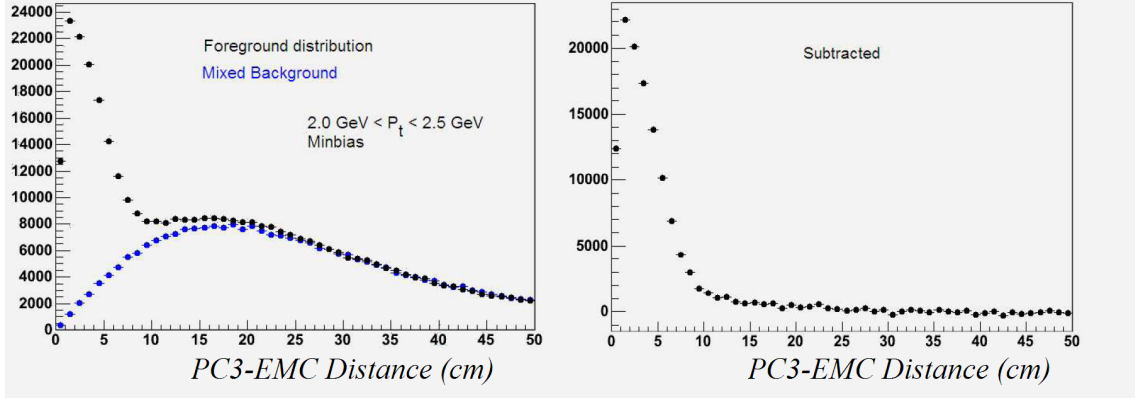


Figure 6.52: Extraction of the portion of clusters coming from charged tracks. The correlation in the hit distance between charged tracks and EMCal hits is measured in order to determine the fraction of clusters coming from charge tracks. This is used to generate the correction  $X_{ch}$ . Details are discussed in the text.

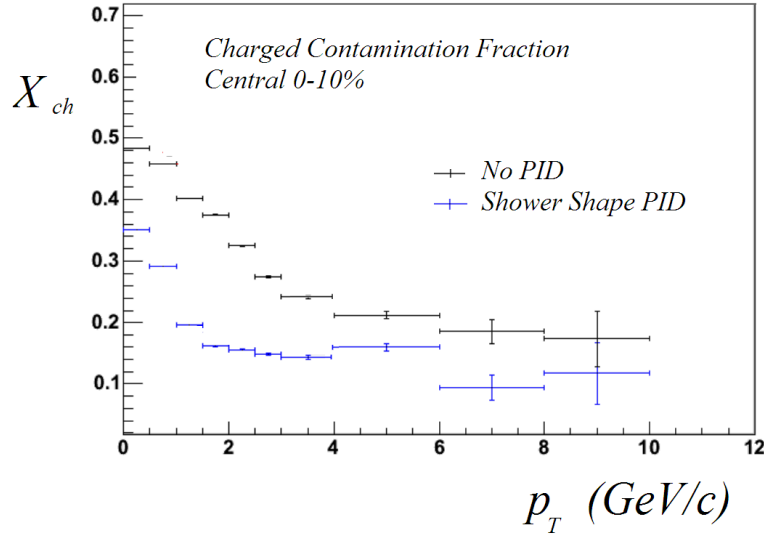


Figure 6.53: Charged contamination measured as a function of transverse momentum for central events.

DC, so conversions happening outside the DC, cannot be tracked.

### 6.7.3 Jet and Other Correlations Present in $X_{ch}$

In section 6.7.1 we noted that since photons that convert are generally included in the charge contamination fraction,  $X_{ch}$  and therefore the loss of real photons due

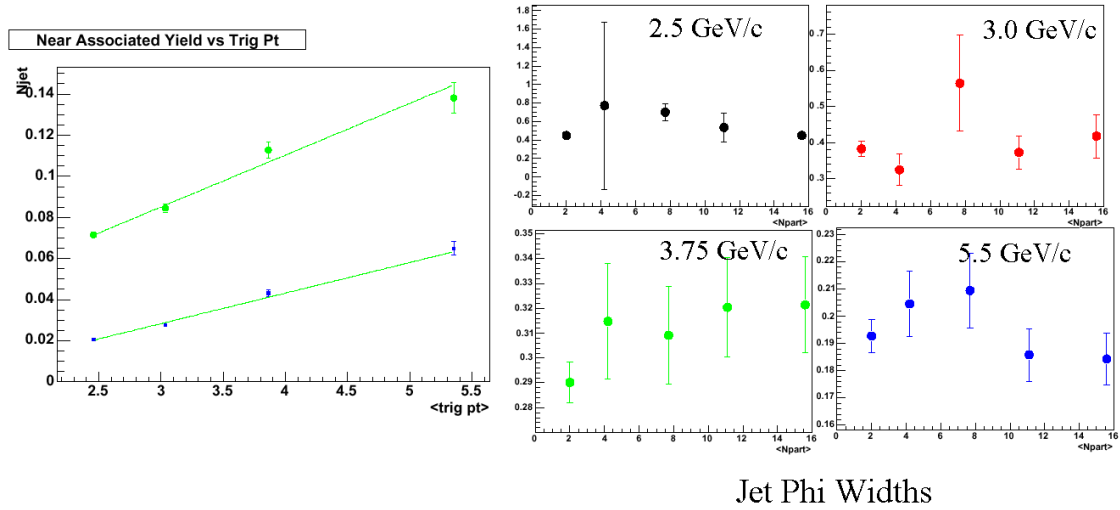


Figure 6.54: Angular widths and yields of jet correlation as a function of leading particle momentum taken from [63] for d+Au events measured by PHENIX.

to conversion increases slightly with  $p_T$  due to  $\pi^0$  decays where the two sister decay photons have a small enough opening angle that the conversion of one sister can veto the other. Another source of correlations between *real* photons and charge tracks which potentially could contribute to  $X_{ch}$  are jets. In other recent phenix measurements, [63], [121], the jet correlation between clusters from decays of jet  $\pi^0$  and the other charged hadrons in the jet cone were measured. Such a measurement is shown in Figure 6.54. The jet associated yield per leading particle or photon from leading  $\pi^0$  is found to be at a small level,  $\sim < 10\%$  and decreasing with  $p_T$ . This combined with the small solid angle fraction ( $\approx \mathcal{O}(0.05)$ ) makes this contribution negligible. The jet correlation does contract to smaller values as the leading particle (photon) momentum increases, but never small enough that it can contribute significantly in the  $p_T$  range of our measurement ( $< 14\text{GeV}/c$ )— since the gaussian-like jet correlation is spread wide enough, it is essentially subtracted away in an unexpected benefit of the mixed background removal procedure.

#### 6.7.4 Systematic Errors: $X_{ch}$

Systematic error arises in the charge contamination from both the yield extraction of the correlation peak and from the quantification of dead areas effects. The former is estimated conservatively to be the same as the yield extraction error on the  $\pi^0$ : 10%. The latter effect of dead areas for PC3 is straight forward to first order: it is just the ratio of the dead areas in the PC3 to its total coverage, the acceptance of the full central arm. 11% of the pads are known to be dead, and thus the scaling factor which must be applied to the contamination fraction measured (already applied in Figure 6.53) is  $1.0/0.89$ . However, the areas of dead EMCAL clusters can cause this to change either way. As an upper bound for the uncertainty in this first order approximation we assume all the EMCAL dead areas are not overlapping with any of the dead pad areas. Therefore the percentage of live pads must be divided only by the active EMCAL acceptance percentage (92% for pbsc) bringing the scale factor up to 1.217. There we take 21.7% as the error on the scale factor combined in quadrature with the yield extraction error yields 24.2%.

Dead area effects are present also in the CGL charge particle veto correlation subtractions, but are much more difficult to estimate than PC3 correlation because low  $p_T$  particles which contribute are bent by the magnetic field. It is also guesstimated to be on the order of 90%. It is for this reason that the the PC3 correlation subtraction was used for the final subtraction.

Since the contamination correction  $X_{ch}$  itself is small at mid to high  $p_T$ , the total contribution to the error on the single photon spectra is at the  $\sim 3\%$  percent level (see the systematic error summary 6.9) Below 3 GeV/c however, where the charge contamination gets larger it can become as high as 10% when no PID correction is applied.

#### 6.7.5 Neutral Hadron Contamination

No method of identifying neutral hadrons like the method described above for charge hadrons exists. Therefore we start from proton/antiproton measurements from other

analyses, and depend completely on our simulation to translate these into estimates of the neutral baryon contamination through the simulated neutron/antineutron response. The method employed to estimate and statistically remove expected neutral hadron contaminations, assumed to be completely neutron and anti-neutrons <sup>6</sup> is based on a combination of the GEANT/embedding simulated EMCal response to  $n/\bar{n}$  and the PHENIX measurement of  $p/\bar{p}$  [13]. From the measurement we make a calculation of the total inclusive  $n/\bar{n}$  production per  $AuAu$  event as a function of centrality, to which we then apply the detector response/efficiency as determined from the simulation.

Since the proton/antiproton measurement has been corrected for feed-downs from heavy baryon decays, the measurement needs to be back corrected to the total inclusive  $p/\bar{p}$ . In addition, the difference of this correction for neutrals as compared to charged nucleons must be taken into account, which is done by using the  $\Lambda$  decay branching ratio according to formula 6.18:

$$dN_{feeddown\ n/\bar{n}}^2/dydp_T = \frac{BR(\lambda \rightarrow n/\bar{n}\pi^0)}{BR(\lambda \rightarrow p/\bar{p}\pi^\pm)} dN_{feeddown\ p/\bar{p}}^2/dydp_T \quad (6.18)$$

For antineutrons, this formula is used directly as the input spectra into the GEANT/embedding simulation. For neutrons, even though the net baryon number is known to be very small at RHIC [48], an additional contribution from the isospin ratio of the initial  $Au$  ions is added to the measured inclusive distribution,  $Y_{extra}$ , calculated from the difference between the  $p$  and  $\bar{p}$  yields as shown in formula 6.19.

$$Y_{extra} = \frac{A - Z}{Z} (dN_p^2/dydp_T - dN_{\bar{p}}^2/dydp_T) \quad (6.19)$$

Once these initial production distributions are established, we then calculate the expected EMCal response to neutrons and anti-neutrons in an identical manner to that of the efficiency calculations for single photons and single  $\pi^0$  described in section 6.6. One additional complication for neutrons and antineutrons in using GEANT simulations, is that since there are no MIP peaks, the vast majority of  $n/\bar{n}$  do not

---

<sup>6</sup>The  $K_{long}$  contribution, expected to be  $< 1\%$  is neglected.

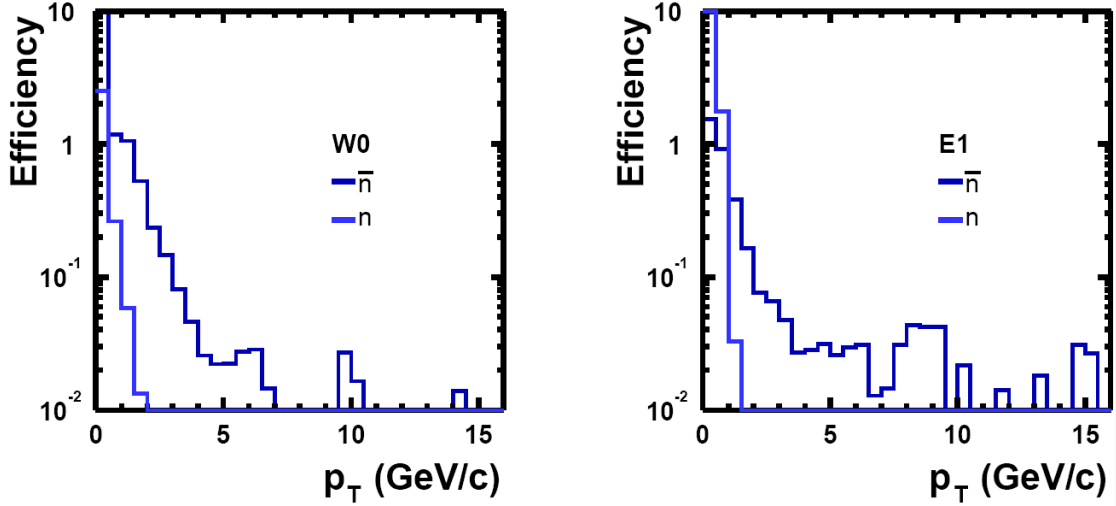


Figure 6.55: Efficiency for detecting neutrons and antineutrons in the PbSc (W0) and PbGl (E1) EMCal.

generate any interaction data whatsoever and hence by default are not kept in our PISA simulation output. Therefore, using our method of efficiency correction, one must be careful to take into account these “lost” (anti)neutrons in the final efficiency calculation, for this contains the dominant effect (non-interaction). The  $n/\bar{n}$  which do interact have such a diminished response that by  $\sim 4 - 5 - 5.5 \text{ GeV}/c$  they are a completely negligible contribution to the cluster spectrum, and with PID cuts, this value is pushed to even lower  $p_T$  in PbGl. PbGl has lower compensation than PbSc, thus lower response to  $n/\bar{n}$ . Efficiency values are shown in 6.55.

Once the response/efficiency  $\epsilon$  and single particle acceptance (same as  $\alpha_\gamma$  from section 6.6 is known, these factors are multiplied with the calculated input spectra, and normalized to the total number of EMCal clusters per event which gives the final  $X_{n/\bar{n}}$ . An example of the calculation is shown in Figure 6.56.

### 6.7.6 Systematic Uncertainty: $X_{n/\bar{n}}$

Because we are so reliant on the simulation, for the systematic error on  $X_{n/\bar{n}}$  we assume a conservative error of 50%. However since this  $X_{n/\bar{n}}$  correction is so small, this amounts to a negligible uncertainty at high  $p_T$  and at most a  $\sim 2\%$  at  $p_T \simeq 3$

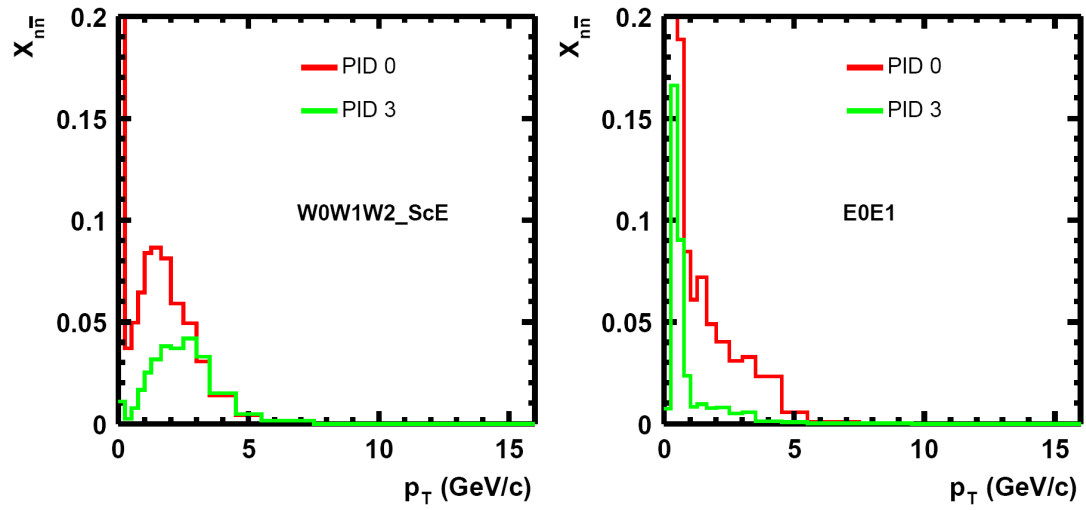


Figure 6.56: Fraction of neutron/antineutron contamination in the extracted raw photon sample for PbGl, PbSc. This fraction is the correction  $X_{n/\bar{n}}$  applied to the final data.

GeV/c. Please see section 6.9 for a summary of this and other error sources.

## 6.8 Background Decay Photon Calculation

The measurement of  $R_{\gamma_{direct}}$  is probably the single most important derived quantity in the  $\gamma_{direct}$  measurement since this determines whether the signal is significant or not. It also determines the final spectral measurement when combined with the inclusive photons  $\gamma_{all}$ . We write the formula for this quantity here again as a reminder (see section 6.5):

$$R_{\gamma_{direct}} = R_{measured}^{\gamma/\pi^0} / R_{decaysim.}^{\gamma/\pi^0} \quad (6.20)$$

where  $R_{measured}^{\gamma/\pi^0}$  is the ratio of two fully corrected invariant yields, the  $\pi^0$  yield and the yield all photons including those from meson decay, what we are calling  $\gamma_{all}$ . Since we've "structured" the corrections this way, we only need to perform a fairly simple fast MC, decay-kinematics, calculation in order to generate the expected uninteresting decay photon background. To first order this is just the photons from  $\pi^0$  and therefore depends on the shape of the  $\pi^0$  measurement itself. In fact, through  $m_T$ -scaling, we base the spectral shapes of all the parent meson species which contribute to the background, which include the  $\eta, \eta'$ , and  $\omega$ .  $K_{short}^0 \rightarrow \pi^0 \pi^0$  pions are already contained in the inclusive  $\pi^0$  measurement, since no "feed-down" correction is applied, and therefore decay photons from these are already included in the  $\pi^0$  portion. Results of the calculation are shown in Figure 6.57.

Under the  $m_T$  scaling assumption [58], the spectral shapes are all assumed to be the same when plotted as a function of  $m_T$  but with different absolute normalizations at high  $p_T$  with respect to  $\pi^0$ . For the  $\eta'$  and  $\omega$  mesons, the normalization is based on world averages [23], a conservative value of 0.8 is employed. Both of these meson contribute decay photons at the less-than-several percent level. For the  $\eta$ , which makes the second largest contribution to the decay photon background at about 20%, the "well-known" normalization of  $\eta/\pi$  at high  $p_T$ , 0.55, was adjusted to a lower value of 0.45. This change was based on on two sources: 1) an updated survey of the world data at higher energy [70] especially considering more recent measurements, [30], [34], and 2) More importantly preliminary (soon to be published) PHENIX

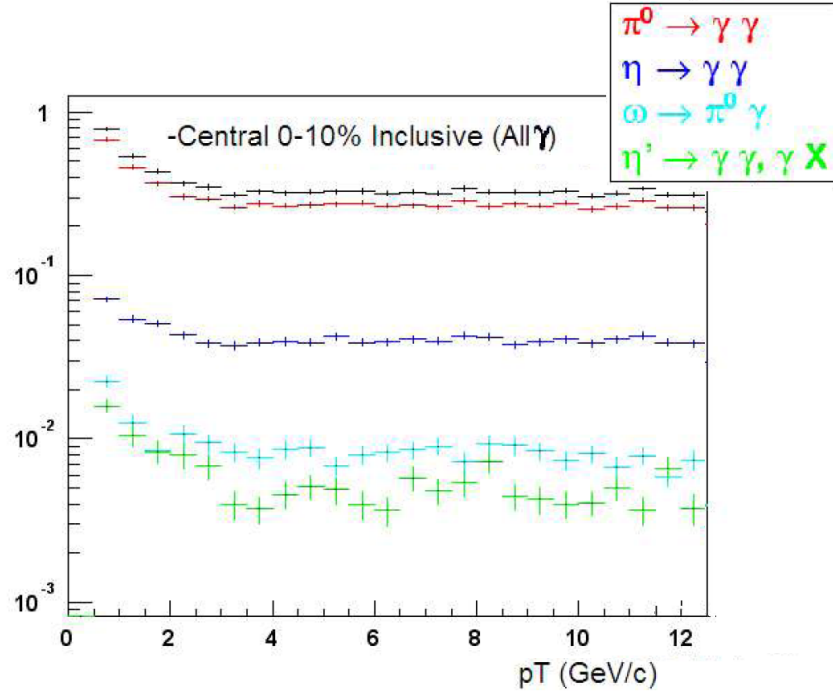


Figure 6.57: Results of the decay photon background simulation for minimum bias events.

measurements of the  $\eta$  yield from other analyses both in the same  $Au + Au$  dataset and in the 200 GeV/c  $p + p$  and  $d + Au$  datasets shown in Figure 6.58.

The ratios in 6.58 of  $\eta/\pi$  span between 0.35-0.48 at high  $p_T$ . Combining these measurements with the previous world averages, and considering that  $AuAu$  ratio has large systematic uncertainties, we used the value 0.45 as our final normalization and used 0.35 and 0.55 as the estimate of the one sigma systematic error from this source.

Since the photon decay simulation was based solely on a fit to the measured  $\pi^0$  shape, not on its normalization, the final calculations therefore depend on the uncertainties of the  $\pi^0$  measurement which are  $p_T$  dependent. However the photon to  $\pi^0$  ratio is actually quite insensitive to many potential changes in the  $\pi^0$  spectra within the uncertainties. Still, the input  $\pi^0$  spectral shape was modified within the systematic errors through a number of methods, such as modulating the fit parameters within their uncertainties from the MINUIT fit but also by taking worse

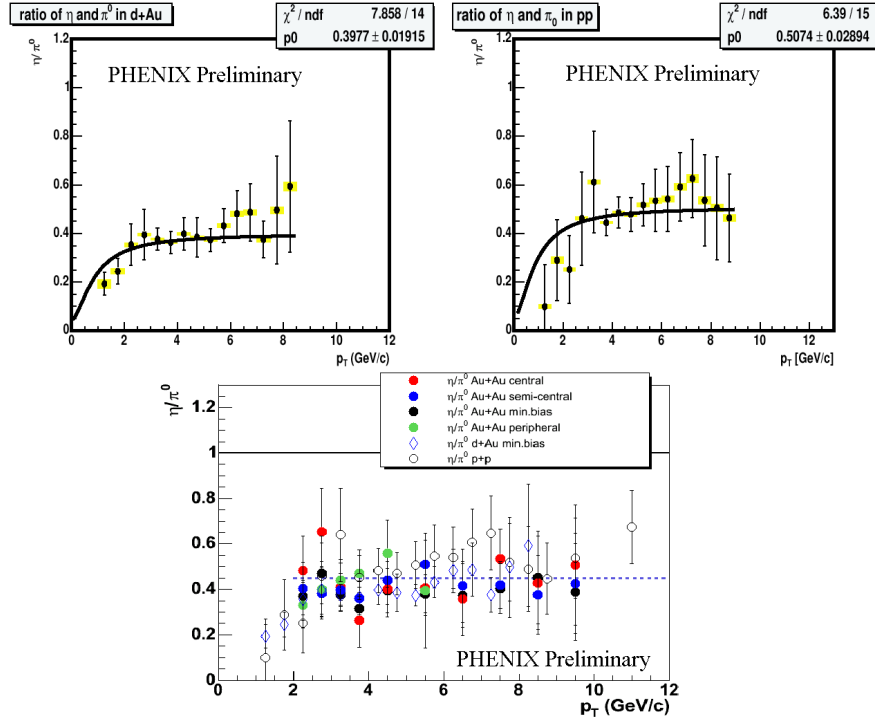


Figure 6.58: PHENIX Preliminary Measurements of  $\eta$  to  $\pi^0$  ratios, in p+p, d+Au, and Au+Au. The PHENIX results are consistently in the 0.45 range, which agrees with the current world data set for high  $p_T$  meson production at all high energies. [70]

case scenarios with some of the  $p_T$  correlated systematic errors and recalculating the decay photon  $\gamma/\pi^0$  ratio. The results of an error study is shown in Figure 6.59. Combining this with the uncertainty in the  $\eta$  normalizations, a  $p_T$  independent systematic  $1-\sigma$  error of 4% was taken in the final result for the  $\gamma_{sim}/\pi^0$  ratio.

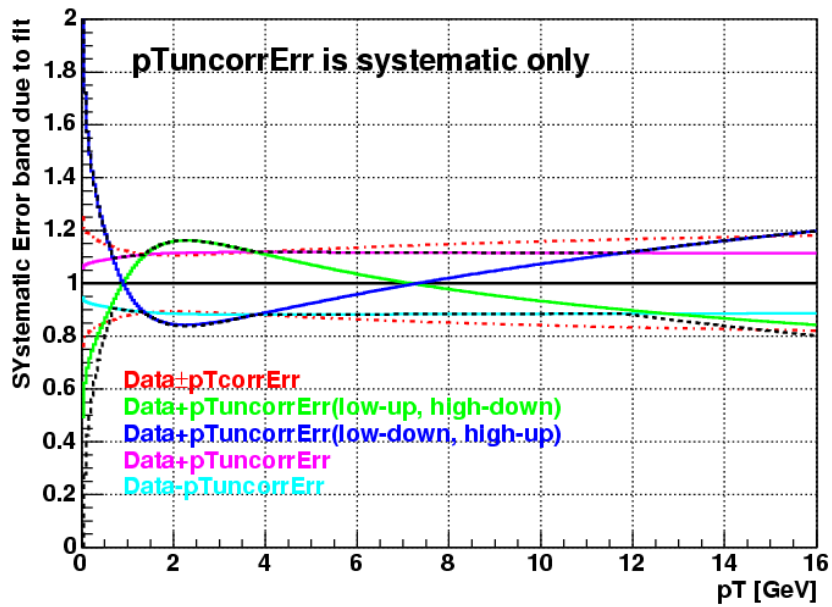


Figure 6.59: Studies of errors in the  $\gamma/\pi^0$  ratio due to the systematics of the  $\pi^0$  fit. In the figure is shown the propagated error in the  $\gamma_{sim}$  alone which can be quite large. The  $\pi^0$  fit is shifted according to the different error bands, so when the simulated photon spectra is divided by  $\pi^0$  the error is reduced to  $\sim < 4\%$ . This is another reason it is preferable to use the double ratio  $R_{\gamma_{direct}}$ .

## 6.9 Summary of Systematic Errors

In table 6.5 we present a summary of the various systematic errors for both our analysis and the PbGl analysis with which ours was combined to yield the final results. The two results, consistent within their systematic errors, were averaged according to the Particle Data Group (PDG) method for combining independent measurements [75]—this method uses a weighted (plain) average with weights equal to the inverse square of error on each measurement for each common data point. The combined error is also a weighted average of the errors, with the same weight factors  $w_i$ , but in this case the average is a quadrature sum reduced by the statistical factor  $1/N_{measurements}$  [75] according to the formula  $sigma_{combined}^2 = (w_i^2 \sigma_i^2 \dots) / N_{meas}$ .

The largest uncertainties in both the  $\pi^0$  and inclusive single  $\gamma$  measurements come from the energy scale and the efficiency calculations. These were both discussed in section 6.6. We summarize the efficiency errors from the various sources in the following tables 6.9 and 6.7:

Finally, since the final data presented in this thesis is a combination of the Klein-Boesing’s PbGl calorimeter analysis [127] and our PbSc analysis, we present the ratio of the PbGl final  $\pi^0$  and inclusive single  $\gamma$  spectra to the corresponding spectra in PbSc in Figure 6.60. The two measurements are consistent within systematic errors. The systematic difference can be attributed to residual uncertainties in the energy scales between the spectra and in the case of the  $\pi^0$  spectra to the yield extraction procedures.

Table 6.5: Summary of the dominant sources of systematic errors on the  $\pi^0$  and inclusive  $\gamma$  yields extracted independently with the PbGl and PbSc electromagnetic calorimeters. The error estimates are quoted at two  $p_T$  values in central events for the PbGl and PbSc. For the combined  $\pi^0$  and inclusive  $\gamma$  spectra and  $\gamma/\pi^0$  ratios, the approximate statistical and systematic errors are quoted for the most peripheral and most central reactions.

$\pi^0$ error source	PbGl		PbSc	
	3.25 GeV/ $c$	8.5 GeV/ $c$	3.25 GeV/ $c$	8.5 GeV/ $c$
Yield extraction	8.7%	7%	10.0%	10.0%
Yield correction	12%	12%	12%	13.3%
Energy scale	13.8%	14.1%	10.5%	11.4%
Total systematic	20.3%	19.5%	18.8%	19%
Statistical	10.6%	32.5%	3%	13.1%
$\gamma$ error source				
Non- $\gamma$ correction	2.4%	2.4%	3.2%	3.2%
Yield correction	10.2%	12.0%	12.5%	11.9%
Energy scale	15.7%	13.7%	12.4%	10.8%
Total systematic	18.9%	18.4%	16.5%	16.7%
Statistical	1.2%	14.1%	0.7%	7.9%
$\gamma/\pi^0$ syst.	10.4%	10.4%	11.3%	11.1%
$\gamma/\pi^0$ stat.	10.7%	37.7%	3%	16.5%
Total errors PbGl and PbSc combined				
Error	Peripheral		Central	
	3.25 GeV/ $c$	8.5 GeV/ $c$	3.25 GeV/ $c$	8.5 GeV/ $c$
$\pi^0$ syst.	12.9%	19.0%	13.9%	16.0%
$\pi^0$ stat.	2.2%	31.6%	1.8%	9.6%
$\gamma$ syst.	11.5%	22.6%	11.4%	13.3%
$\gamma$ stat.	2.3%	15.8%	0.6%	4%
$\gamma/\pi^0$ syst.	10.9%	15.3%	10.7%	15.2%
$\gamma/\pi^0$ stat.	3.1%	35.3%	2.1%	10.4%
$\gamma/\pi^0$ sim.	4%		3%	

$\pi^0$ Yield Correction Errors				
Correction Error Source	Central		Peripheral	
	3.0 GeV/c	9.0 GeV/c	3.0 GeV/c	9.0 GeV/c
Efficiency (Total)	13%	13%	11%	11%
Simulation/PID	8%	8%	8%	8%
Multiplicity	6%	6%	—	—
Energy Smearing	6%	6%	6%	6%
Other	4%	4%	4%	4%
Conversions	1.5%	1.5%	1.5%	1.5%
Trigger (thresh > 4 GeV)	—	3%		3%

Table 6.6: Summary of sources of systematic uncertainty for the corrections applied to the final  $\pi^0$  spectra in percent of yield.

$\gamma$ Yield Correction Errors				
Correction Error Source	Central		Peripheral	
	3.0 GeV/c	9.0 GeV/c	3.0 GeV/c	9.0 GeV/c
Efficiency (Total)	13%	13%	11%	11%
Simulation/PID	7%	7%	7%	7%
Multiplicity	6%	6%	—	—
Energy Smearing	6%	6%	6%	6%
Other	4%	4%	4%	4%
Conversions	1%	1%	1%	1%
Trigger (thresh > 4 GeV)	—	1%		1%
$X_{ch}$	5%	3%	4%	3%
$X_{n/\bar{n}}$ d	2%	—	1%	—

Table 6.7: Summary of sources of systematic uncertainty for the corrections applied to the final inclusive ( $\gamma_{all}$ ) spectra in percent of yield.

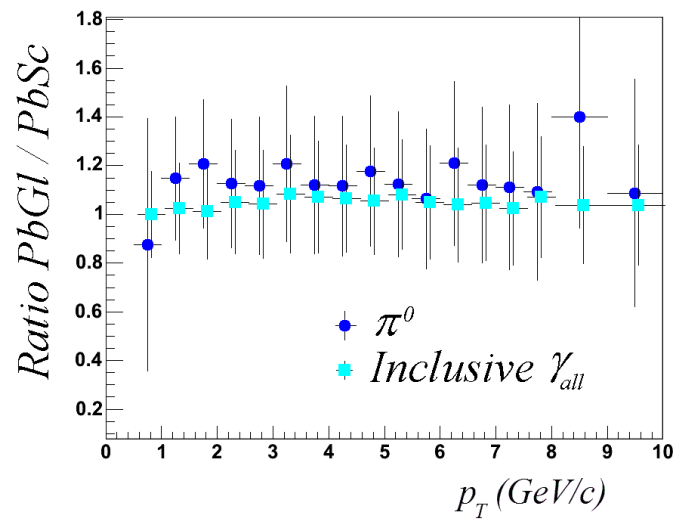


Figure 6.60: Ratio of fully corrected  $\pi^0$  and inclusive single photon spectra measured in the PbGl calorimeter to those of the PbSc calorimeter for minimum bias events.

# Chapter 7

## Results

### 7.1 $\pi^0$ Spectra

The inclusion of the level2 triggered data sample has lead to a sizable statistical improvement of the  $\pi^0$  data, making it currently the highest  $p_T$  meson measurement at RHIC for  $Au + Au$  at  $\sqrt{s}= 200$  GeV/c. Here we present the  $\pi^0$  spectra results. Significance of these measurements will be discussed in subsequent sections (starting with 8.2).

The figure includes full systematic and statistical errors combined for each point, for 10% centrality bins as labeled including the full inclusive (all centrality) Minimum Bias result. Centrality was calculated according to the calculations explained in the analysis chapter, section 6.1. The final invariant yields shown were calculated according to the formulas in section 6.5. As shown, the spectra are steeply falling, less steeply at high  $p_T$  due to the transition to the pQCD power law behavior. Power law fits ( $\propto 1/p_T^m$ ) these spectra for  $p_T > 4$  GeV/c yield power law exponents  $m$  of approximately 8.4. The pseudo-rapidity region covered is the standard PHENIX single particle  $-0.35 < \eta < 0.35$ . This corresponds to an equivalent sample of 85M total minimum bias events.

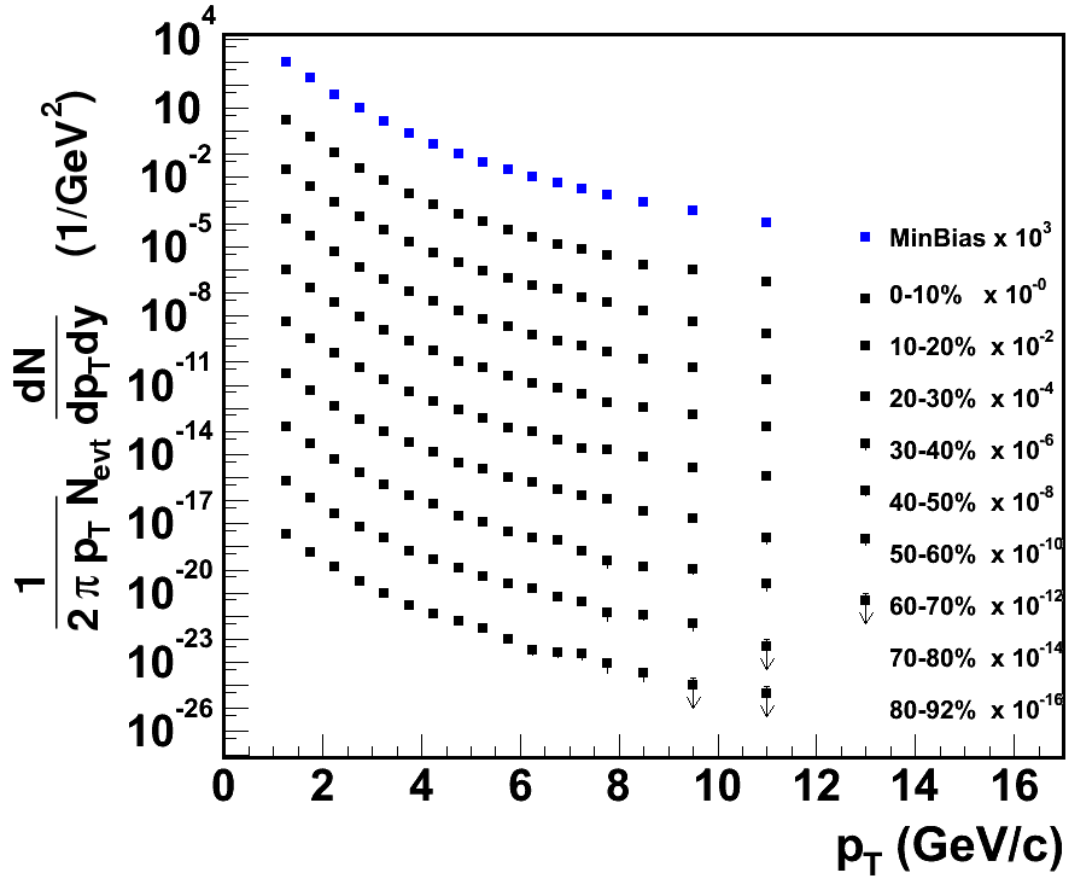


Figure 7.1: 200 GeV  $Au + Au$   $\pi^0$  Production with Level2 Trigger Sample Included.

## 7.2 $\pi^0$ $R_{AA}$ Values

As with the spectra, the  $\pi^0$   $R_{AA}$  now extends to higher  $p_T$  with inclusion of the level2 statistics. These plots represent the highest  $p_T$  measurement of  $Au + Au$  suppression yet at RHIC. Observing the suppression behavior at the highest  $p_T$  can help distinguish between different quenching models as discussed below in section 8.4.

The final  $R_{AA}$  ratios shown were calculated according to the following formula discussed in more detail in section 6.5:

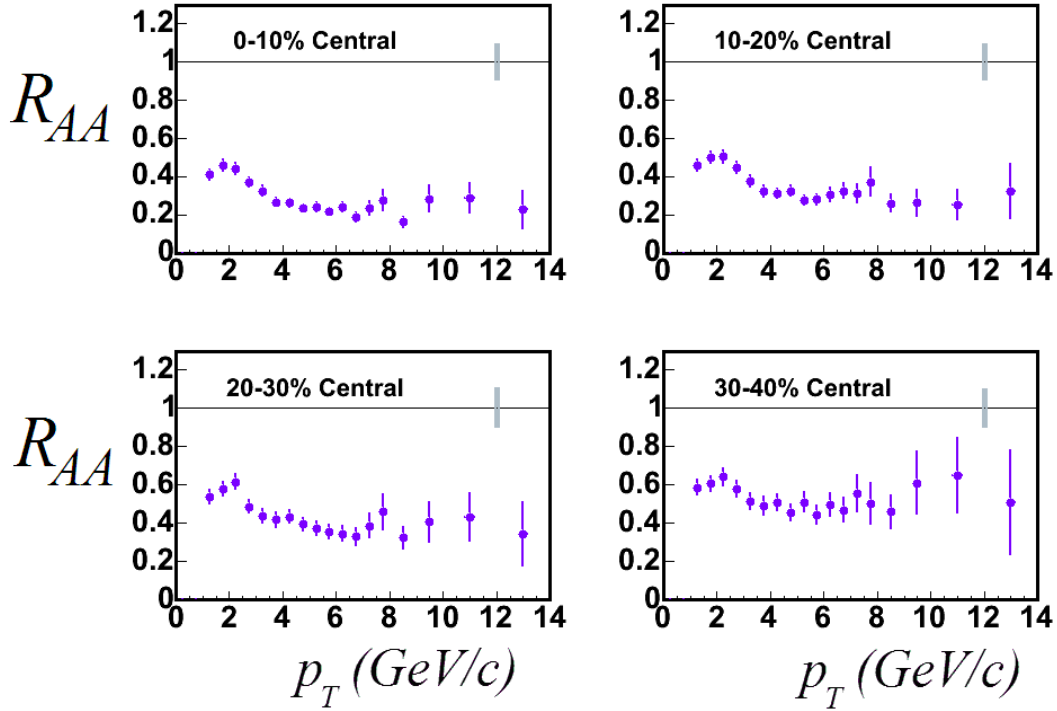


Figure 7.2:  $\pi^0$   $R_{AA}$  in 200 GeV Au + Au collisions for the four most central bins. The grey box at  $R_{AA} = 1$  represents the systematic error band for the thickness scaling, (*i.e.* from Table 6.1) not included in the data points themselves.

$$R_{AA} = \frac{EdN_f^{A+A}/d^3p}{\langle T_{AA} \rangle_f Ed\sigma^{p+p}/d^3p} = \frac{(1/N_f^{events}) (EdN_\pi^{A+A,f}/d^3p)}{(\langle N_{coll} \rangle_f / \sigma_{inel}^{p+p}) (Ed\sigma_{\pi+X}^{p+p}/d^3p)} \quad (7.1)$$

The previously published PHENIX  $p + p \rightarrow \pi^0 + X$  result [17] was used as the reference spectra in the denominator (also see Figure 8.12). The corresponding  $\langle N_{collision} \rangle / T_{AA}$  scale factors used were as calculated in Table 6.1. where Centrality was calculated according to the calculations explained in the analysis chapter, section 6.1. As indicated, results are presented in 10% centrality bins including the full inclusive (all centrality) Minimum Bias result. The results shown include the full statistical error and additionally, point by point systematic errors which are not expected to cancel in the  $R_{AA}$  ratio.

It is apparent that  $R_{AA}$  is significantly below 1 in the Central 0-10% bin and slowly rises becoming consistent with 1 in the most peripheral bins.

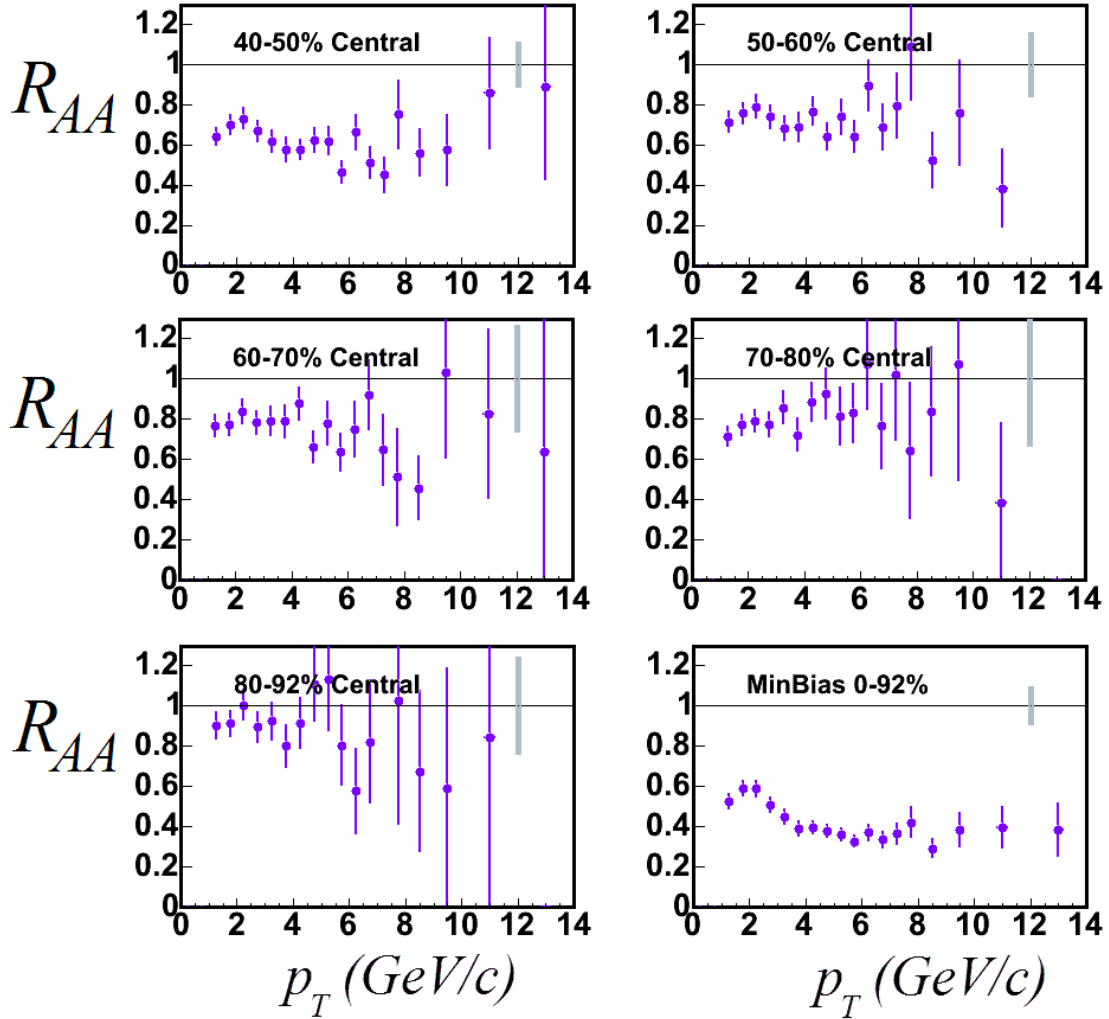


Figure 7.3:  $\pi^0$   $R_{AA}$  in 200 GeV  $Au + Au$  collisions for the remaining centrality bins, including Minimum Bias. The grey box at  $R_{AA} = 1$  represents the systematic error band for the thickness scaling, (*i.e.* from Table 6.1) not included in the data points themselves.

### 7.2.1 $\pi^0 R_{AA}$ vs. Centrality ( $N_{part}$ )

In Figure 7.4 we show integrated  $R_{AA}$  for  $\pi^0$  for three different lower  $p_T$  bounds vs the number of participants. This is a common way to summarize the suppression vs. centrality, since the number of participant nucleons are a good indicator of the geometrical volume of the overlap. Integrating is one way of taking the average across several bins because  $R_{AA}$  is relatively constant with  $p_T$ , although it is weighted most heavily by the lowest  $p_T$  in the integration.

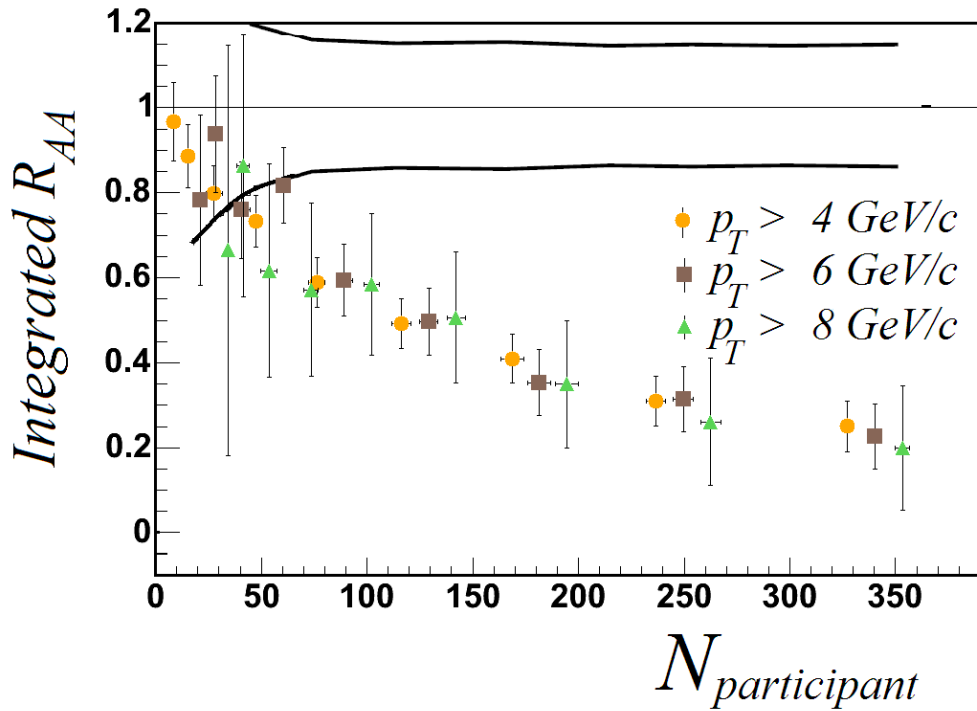


Figure 7.4: Integrated  $\pi^0 R_{AA}$  vs.  $N_{participant}$  for  $p_T \geq 4, 6,$  and  $8$  GeV/c. The 6 (8) GeV/c bin is shifted in the horizontal by 5 (10).

When integrated above 4 GeV/c, it is apparent that the suppression in  $R_{AA}$  develops very smoothly starting immediately with the second centrality bin, the point at  $N_{part} \approx 15$ . Although the statistical uncertainties when integrating above 6 GeV/c and 8 GeV/c are large, these also seem consistent with the 4 GeV/c trend. However it should be remembered that the suppression in the low  $N_{part}$  (peripheral)

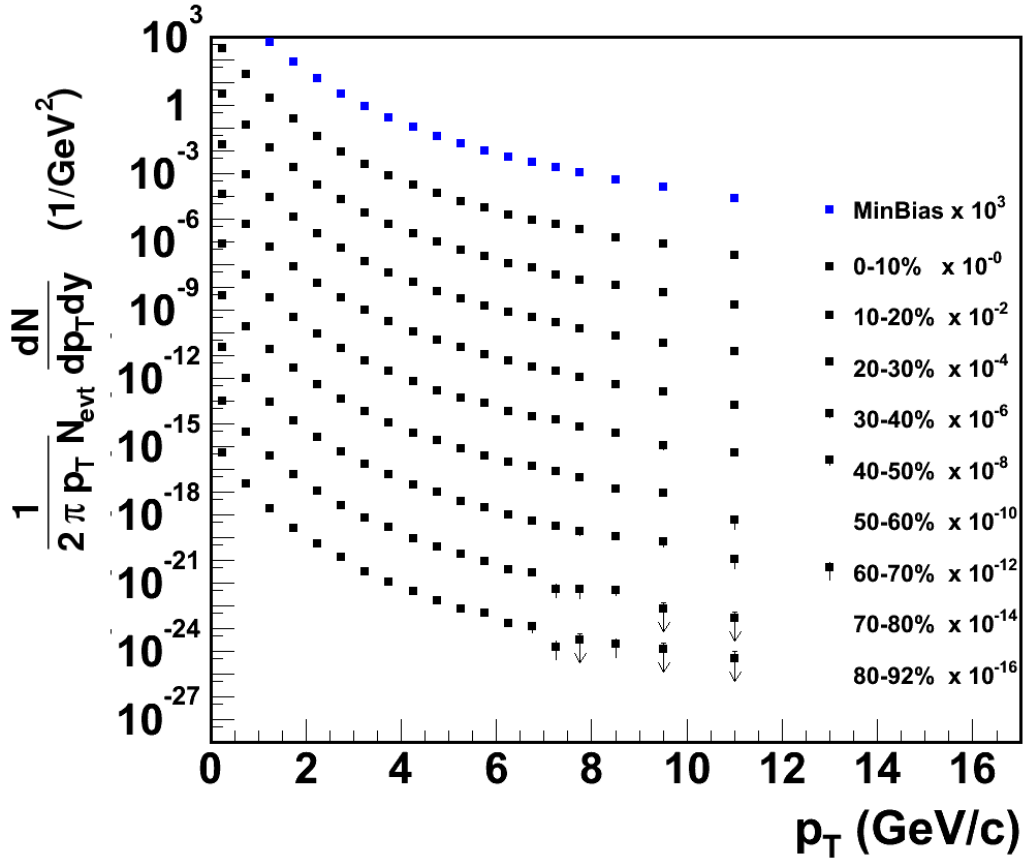


Figure 7.5: PHENIX measurement of inclusive single photons ( $\gamma_{all}$ ) which includes *all* sources including “background” photons from particles which immediately decay photonically.

bins is quite small relative to the more central bins. We shall discuss this point more below in section 8.2.

### 7.3 $\gamma_{all}$ Spectra

For completeness, we present the  $\gamma_{all}$  invariant spectra which represents the total production of photons produced in  $Au + Au$  reactions at  $\sqrt{s_{NN}} = 200$  GeV including “feed down” from particles which decay immediately into photons.

The figure includes full systematic and statistical errors combined for each point, for 10% centrality bins as labeled including the full inclusive (all centrality) Mini-

imum Bias result. Centrality was calculated according to the calculations explained in the analysis chapter, section 6.1. The final invariant yields shown were calculated according to the formulas in section 6.5. As shown, the spectra are steeply falling, less steeply at high  $p_T$  due to the transition to the pQCD power law behavior. Power law fits ( $\propto 1/p_T^m$ ) these spectra for  $p_T > 4$  GeV/c yield power law exponents  $m \approx 8.4$ . The pseudo-rapidity region covered is the standard PHENIX single particle corrected to  $-0.35 < \eta < 0.35$ . This data corresponds to an equivalent sample of 85M total minimum bias events.

## 7.4 Establishment of the Direct Photon Signal:

$$R_{\gamma_{direct}}$$

The direct photon measurement has also benefitted greatly from the addition of the level2 statistics. First the extension of the  $\pi^0$  measurement itself was crucial since knowledge of the  $\pi^0$  spectral shape must be known to calculate the photon background from decay mesons discussed in section 6.8. But more importantly, since a first “pre-preliminary” result was presented in 2001 by PHENIX this new factor of three in statistics combined with the previously unused PbSc photon data has lead to nearly a factor of 10 more statistics and has allowed the measurement to be extended to match the  $p_T$  reach of the  $\pi^0$ , which is over twice the  $p_T$  reach of the previous photon result.

In Figure 7.6, we present the  $R_{\gamma_{direct}}$  ratios as a function of transverse momentum, for each centrality bin. This is a direct measurement of (signal+background) / background. Discussed in section 6.5.2, we calculate  $R_{\gamma_{direct}}$  with the following formula:

$$R_{\gamma_{direct}}(p_T) = \frac{dN_{\gamma_{all}}/dp_T}{dN_{\gamma_{bkg}}/dp_T} = \frac{1}{F_{bkg}^{\gamma/\pi^0}(p_T)} \frac{dN_{\gamma_{all}}/dp_T}{dN_{\pi^0}/dp_T} \quad (7.2)$$

where  $F_{bkg}^{\gamma/\pi^0}(p_T)$  is our calculation of the background  $\gamma_{decay}/\pi^0$  ratio. Many systematics cancel when making the double ratio with  $\pi^0$ . The error bars shown include

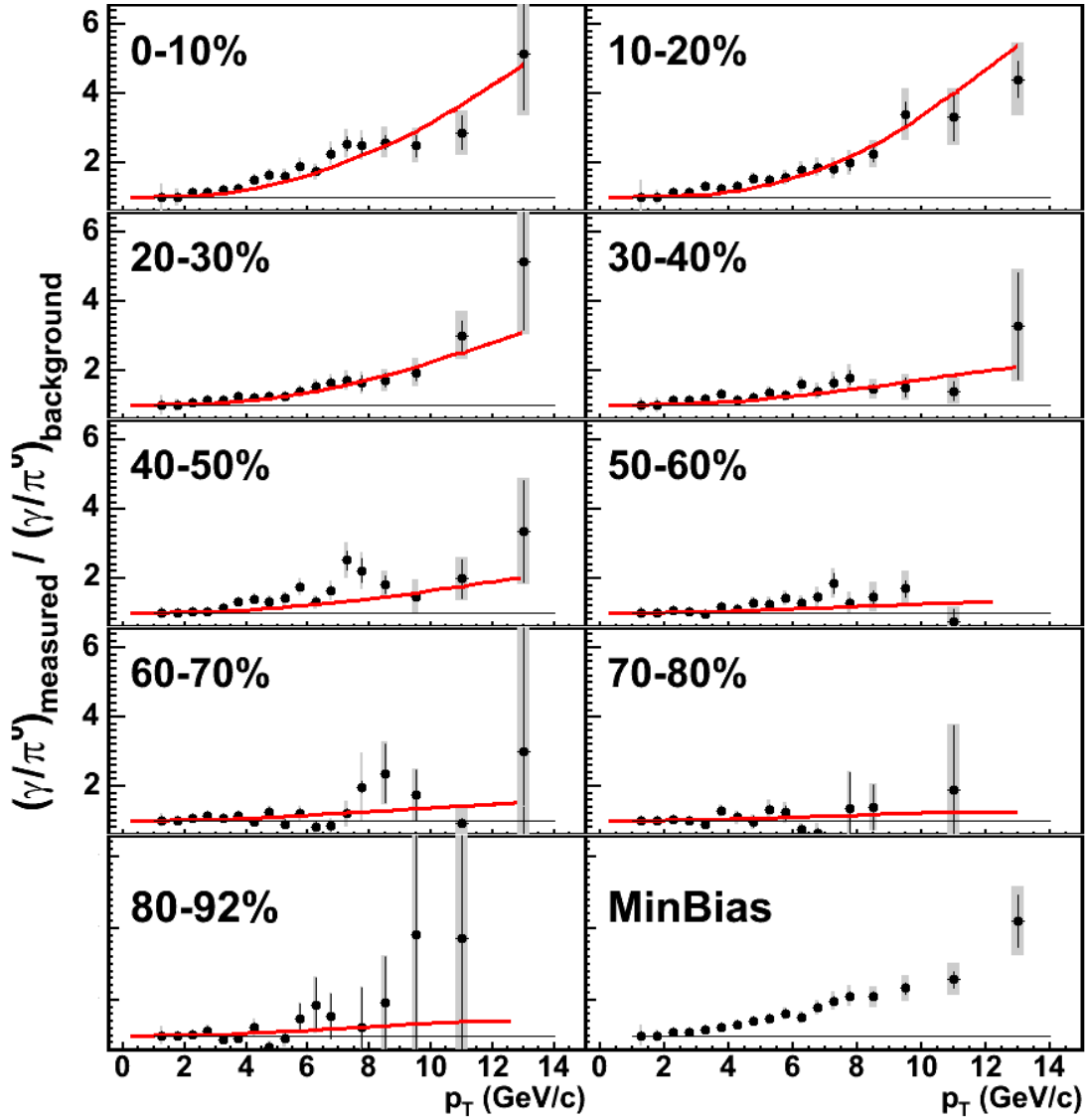


Figure 7.6: Direct photon double ratio  $R_{\gamma_{\text{direct}}}$  vs.  $p_T$  as in [85], which represents signal over background ratio (plus 1). A large signal relative to background is observed in central events, consistent with observed high  $p_T$  meson suppression. In the solid (red) curves the binary scaled pQCD  $\gamma_{\text{direct}}$  prediction is combined with our decay background calculation.

the remaining irreducible systematic uncertainty and the full statistical errors added in quadrature. Statistical errors dominate for  $p_T > \sim 7$  GeV/c

In more central events, the  $R_{\gamma_{\text{direct}}}$  signal is enhanced dramatically relative to the background while for more peripheral bins the signal level becomes small, eventually

undetectable within the level of the current systematic uncertainties. This small signal level above background, ranging from a few percent at low  $p_T$  to 15-20% at the highest  $p_T$  in the PHENIX reach, is consistent pQCD predictions [16] for  $p + p$ . Both these small signal levels in peripheral collisions and the enhanced level in the central bins are consistent with a binary scaled (and therefore plain pQCD) direct photon signal level sitting on top of the meson decay photon background, shown in the red curves, as previously published in [85]: these represent the final updated version of those results. The red curves, which we shall call  $R_{\gamma_{direct}}^{QCD}$ , are produced from a combination of our decay photon background calculation  $\gamma_{bkg}$  for each centrality bin, and the pQCD prediction for  $\gamma_{direct}$  according to the formula:

$$R_{\gamma_{direct}}^{QCD} = 1 + \gamma_{direct}^{QCD}/\gamma_{bkd}$$

which is equivalent to  $R_{\gamma_{direct}}$ . As described in those proceedings, in the case of the central events the suppressed level of meson production can account for the S/B enhancement. We will discuss this conclusion in great detail in the following chapter.

## 7.5 Direct Photon Spectra

From  $R_{\gamma_{direct}}$ , we then compute the direct photon invariant yields, (as usual normalized to the total cross section) as  $\gamma_{direct} = \gamma_{all} (1 - R_{\gamma_{direct}}^{-1})$ . These are shown below in Figure 7.7. The red curves are the plain nuclear thickness scaled pQCD  $\gamma_{direct}$  calculations from [16]. Agreement with pQCD will be discussed in detail in the next chapter, section 8.3.

The error bars, as in the other section include both statistical and systematic uncertainties added in quadrature. Upper limits represent the 90% confidence level.

## 7.6 Direct Photon $R_{CP}$

Please see section 8.2 of the next chapter (specifically 8.5 and 8.6).

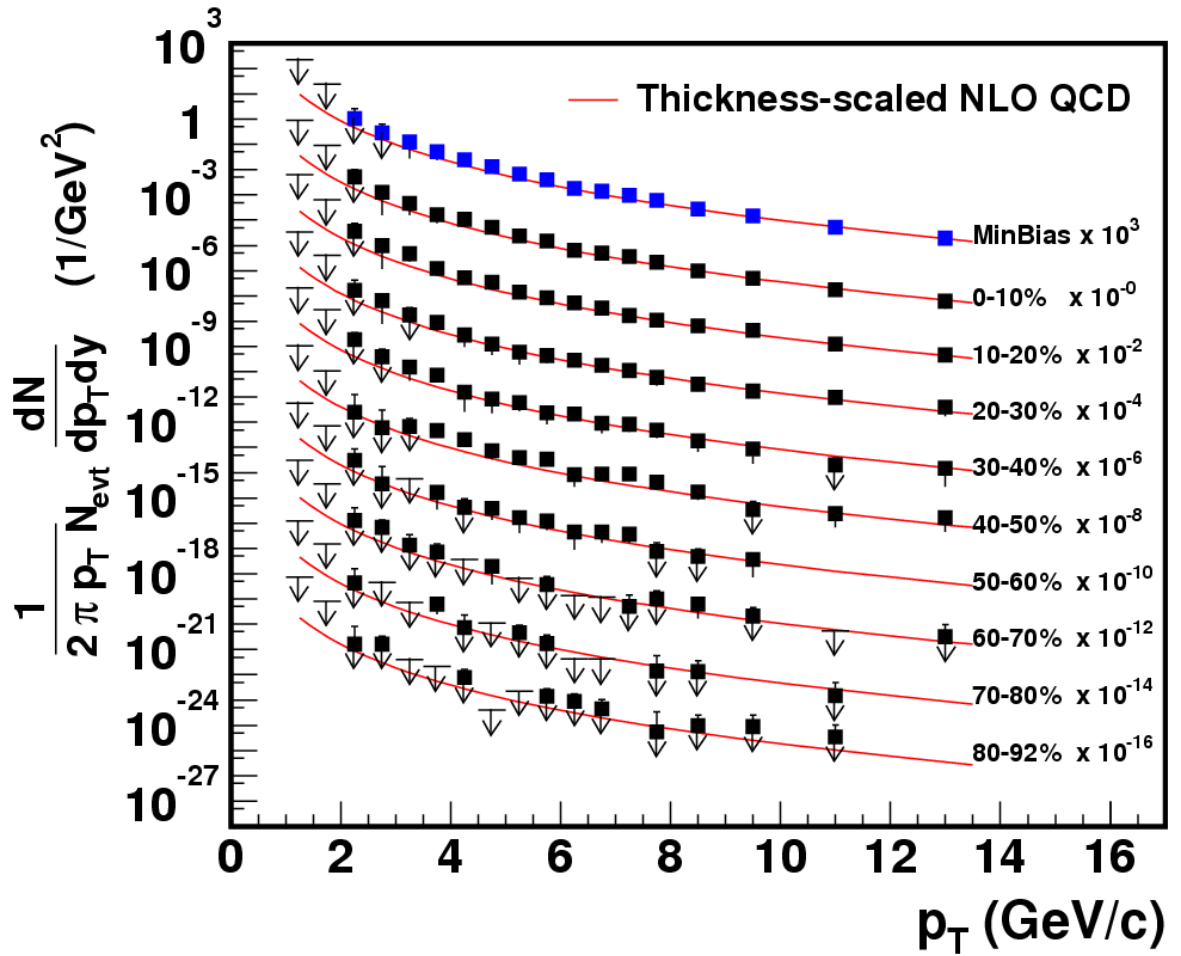


Figure 7.7: Invariant Yields of direct photons for various centrality selections.

## Chapter 8

# Discussion of Results

In the following chapter, our goal is to convey the physical interpretations of our results as well as explain their importance. This will be emphasized most in our main conclusion, that the suppression present in the  $\pi^0$  production (in our data now made visible in more detail and at higher  $p_T$ ) is not present in the direct photons, and furthermore that the photons specifically *do* appear to be following the nuclear thickness scaling expected of hard processes.

These two conclusions taken together are of fundamental importance to the study of Relativistic Heavy Ion collisions and the search for deconfined QGP matter. The suppression of high  $p_T$   $\pi^0$  mesons indicates a mechanism of jet modification never before observed in basic particle physics. The absence of this suppression in the direct photons, shown in these results for the very first time, and observed under the exact same conditions in the very same events as the  $\pi^0$  meson suppression, makes the strongest statement available that the meson behavior is indeed anomalous and equally important, *how* it is anomalous. Taken in the context of other recent results, specifically a similar absence of suppression in  $d+Au$  collisions [14], it represents the best<sup>1</sup> and final confirmation necessary that the jet quenching cause of the meson suppression is due to modifications which must occur in the final state medium, rather than by nuclear effects in the initial state of the jet-producing partons. Herein lies the specific and sizable importance of the addition of the  $\gamma_{direct}$  data to the story.

---

<sup>1</sup>certainly the best so far, and likely even the best possible within the RHIC experiments

After relaying this message, we shall then discuss in more detail the agreement of both our  $\pi^0$  and  $\gamma_{direct}$  data with pQCD. This is important because with a lack of  $N + N$  reference for the direct photons (to be used *e.g.* in making the ratio  $R_{AA}$ ), we shall rely on predictions of pQCD to discuss the potentially even more interesting purpose for observing direct photons at RHIC, possible thermal or other enhancement directly due to QGP formation. In this regard we are limited, but nonetheless we are able to make important first steps in addressing such predictions.

Finally we will discuss in more detail any new constraints on the highest  $p_T$  suppression behavior made available by the 3-4 extra GeV/ $c$  of  $p_T$  reach and the reduced uncertainties in our new  $\pi^0$  result. In this section we will further expound the details of why the suppression result is important and the subtleties involved.

## 8.1 The Setting

We start by reminding the reader of our discussions in the introductory section 4.3. Since the nucleus is composed of plain nucleons ( $N$ 's: protons and neutrons), high  $p_T$  particles, known to be produced by hard-scattering processes in high energy  $N + N$  collisions, are expected to scale according to the geometric nuclear overlap or thickness of the nucleons superimposed in the heavy ions of  $A + A$  collisions.

The suppression of high  $p_T$  mesons with respect to this nuclear thickness-scaled expectation that is made newly apparent in the updated results of  $\pi^0 R_{AA}$  shown in the plots of section 7.2, was one of the first results to come out of RHIC data [11],[7]. In the data coming out of the 130 GeV RHIC commissioning run, it was already apparent, and PHENIX and STAR both published high- $p_T$  results which indicated a suppression of about a factor of 3-5 below what was to be expected from the so-called “binary scaling”<sup>2</sup>, using  $x_T$  scaling extrapolations from other data nearby in energy as the reference. With the first Run2 data, a measured  $pp$

---

<sup>2</sup>“binary scaling” is a shortened term for “binary-collision” scaling that, as discussed in section 4.3, is in common use in the HI field and which we shall also employ generously. The reader is asked to remember that it has a precise and well-defined meaning. Nuclear thickness scaling,  $T_{AB}$ -scaling or  $N_{collision}$  scaling are also synonyms

(*i.e.*  $NN$ ) reference was provided which agreed well also with previous 200 GeV data taken at CERN and the result was even more convincing. However, suggestive though it was, comparison to this reference alone was not all that was needed to prove that the suppression was indeed an abnormal effect consistent with new states of matter being formed. This is because other “initial state” effects, inherent to the nuclear superposition were already observed in other situations or demonstrated to be possible at RHIC. Specifics about these effects are given below in one of the many re-statements of this point.

Therefore in 2003, just over a year after the completion of our Run2 data taking, a  $d + Au$  run (Run3) was performed specifically to address the question of whether the suppression was an initial or final state effect. It was thought [9] that if the observed  $Au + Au$  suppression was indeed a modification caused by the *final state* of the hot dense medium, then it should not be observed in “cold” nuclear matter  $d + Au$  collisions. In  $d + Au$  collisions, similar impact parameter configurations can be probed, *e.g.* where the deuteron goes right through the center of the larger  $Au$  nucleus<sup>3</sup>. In such collisions any nuclear modifications to the initial state parton densities (PDFs) should already be present, and if these modifications are small we can reliably expect to observe nuclear thickness scaling in hard-scattering production. In other words, the  $d + Au$  high  $p_T$  result should be a *null* effect (no suppression), if the final state quenching explanation in  $Au + Au$  is correct. On the other hand, an initial state modification to the  $Au$  PDF’s, like the well-known phenomenon of nuclear shadowing or the younger, sexier modification called the Color Glass Condensate (CGC) [126], [80] which at the time already had success describing overall soft particle production in  $Au + Au$  [8], could have provided an alternative, initial state causes of the  $Au + Au$  high  $p_T$  suppression, within theoretical uncertainties at the time of Run3. In this model gluon saturation (a limiting of the number of low momentum gluons) in the initial state limits, among other things, the multiplicative effects assumed in  $T_{AA}$  scaling.

---

<sup>3</sup>however, there are caveats, which we shall discuss below.

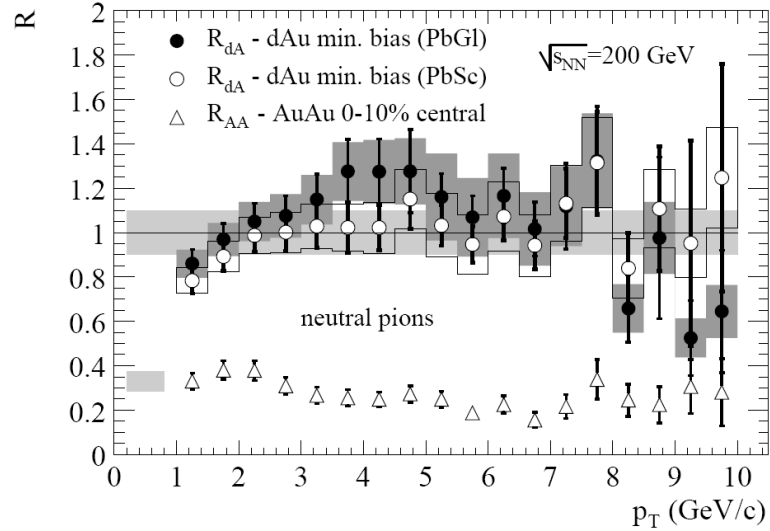


Figure 8.1:  $d + Au$   $\pi^0$  result for Central events.  $Au + Au$  suppression is also shown. figure from [14].

In Figure 8.1 we show the results of the  $d + Au$  high  $p_T$  analysis [14]. As is evident from the plot, the suppression of  $\pi^0$  in the  $Au + Au$  case was not found to be present. On the other hand, the expected Cronin enhancement was observed, and thus we had our first “proof” that binary scaling (modulo small cold nuclear modifications) was indeed the proper scaling for the high  $p_T$   $\pi^0$ .

Once again, we have convincing evidence that final state jet quenching was the cause of our high  $p_T$  hadron suppression phenomenon in  $Au + Au$  collisions. However, there is a possible deficiency of the conclusions drawn from the  $d + Au$  results. This is that, while similar impact parameters are probed *e.g.*, where the deuteron goes straight through the center of the  $Au$  nuclei,  $d + Au$  is just simply not the same as  $Au + Au$ -effects stemming from the fact that *both* reactants are large nuclei. Admittedly is hard to imagine what kind of effects these could be. Under the Glauber assumptions, all that should matter is the behavior (the collisions) of each nucleon as it passes through the target nucleus: essentially  $N_{coll}$  per  $N_{part}$ . Even though  $d + Au$  collisions can reach the the same value of  $N_{coll}/N_{part}$  (indeed even higher values than in  $Au + Au$ ) we don’t know *a priori* that there couldn’t be as yet unknown mechanisms of initial state modifications only visible in  $A + A$ .

Since we are indeed probing never before seen phenomena, this still needs checked experimentally, the limited SPS Drell-Yan results notwithstanding. RHIC is after all still only the third facility where heavy ion collisions have been studied, and the very first anywhere near the  $\sqrt{s_{NN}} = 200$  GeV energy range!

What we really need then is a control reference to compare the  $\pi^0$  production to, in actual  $Au + Au$  events themselves: A reference process that is on the hard scale *just like* the meson forming jets, and that depends on the initial state PDF's *just like* the meson forming jets. Then we can be sure that we've excluded initial state  $\mathbf{A} + \mathbf{A}$  (not just  $p + A$ ) modifications in our comparisons. And as we shall show, this is exactly what we've found with the direct photons.

## 8.2 $N_{collision}$ Scaling and High $p_T$ Suppression

That binary collision scaling is being obeyed in the Run2  $Au + Au$  dataset for direct photon hard scattering can be established with the direct photon data alone, that is, by itself. However, in what follows we feel that it is useful to compare the perceived scaling behavior to that of the  $\pi^0$ , since the differences are stark. Historically at RHIC, “not scaling” was defined before “scaling”. When we say that something does scale, what level of precision should that imply? Certainly in the hopes of locating a thermal signal (see below), we wouldn't expect scaling in the photon production at lower values of transverse momentum. And we've mentioned already, there should be some suppression even in the inclusive prompt photon spectrum [116]. Exactly how well must the scaling be observed in order for us to agree that scaling is being obeyed high  $p_T$ ? Here the  $\pi^0$ 's will give us some direction: at a very minimum, we certainly should expect the  $\gamma$ 's to scale *better* than the  $\pi^0$ . This they do with flying colors, and hence the motivation for comparing the two measurements side by side. Of course once this most basic qualitative level of scaling is established, we can move onto more quantitative measures of the scaling. In the next sections we shall start with the most qualitative comparisons possible: simple visual shape comparisons. From this point we will progress to the more quantitative comparisons.

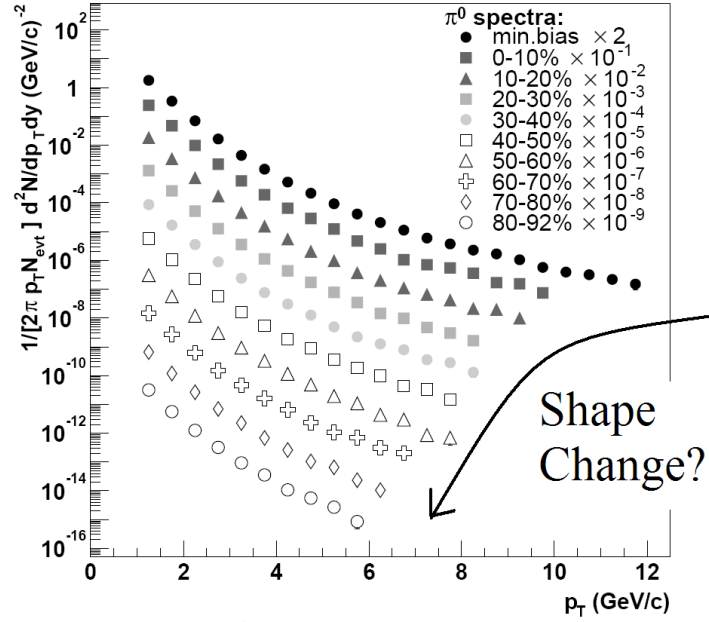


Figure 8.2: Because the more peripheral bins lacked statistics to make a positive measurement in the highest  $p_T$  bins, the eye would make it appear that the spectral shapes of these bins is changing dramatically (getting steeper). There is in fact a change, but not as large it might appear.

### 8.2.1 Spectral Shapes

In figure (8.2) we show the plot of the original PHENIX 200 GeV  $Au + Au$   $\pi^0$  result. Observing the many centralities together this way, it appears that there is marked difference in spectral shape going from central to peripheral. This is just an optical illusion however, caused by the removal of the lower statistics high  $p_T$  points in the more peripheral bins—at lower  $p_T$  the spectrum is steeper, so mentally the eye extends these spectra with a steeper slope. Looking back at Figure 7.1 we see can see what a difference adding back the high  $p_T$  points makes. Still, however, if one looks very carefully, small differences of shape can be observed in the various  $\pi^0$  spectra, differences that within the larger direct photon error do not seem to be present.

In Figure 8.3, we are able to demonstrate the qualitative difference a little better. For  $\pi^0$  we see a dramatic difference between the pQCD prediction shape (which

matches our  $p+p$  data well on this scale—see Figure 8.12) while for direct  $\gamma$ , although there is an overall difference here too, it is not nearly as noticeable. We will discuss how well pQCD describes these spectra in much more detail below in section 8.3. In the plot, the solid prediction curve is scaled arbitrarily in order to get the best “by eye” agreement (keeping in mind that this is a qualitative comparison) in mid- $p_T$  region between 3-5 GeV/ $c$ .

We can also see a slight difference in the behavior of the shape differences between the 40-50% peripheral bin and the most central 0-10%, although because the systematic uncertainties on the  $\gamma_{direct}$  are larger nothing definite can be said. We compare with the 40-50% only because this is the last bin which has definite significance for all points.

Since this is inconclusive, we also try looking at the development of shape trends in spectral ratios as a function of centrality. This is shown in Figure 8.4. Here too we see an indication of a slightly different behavior between the  $\pi^0$  and direct photon. The  $\pi^0$  ratio changes concavity in the mid to low  $p_T$  range within the first three to four centrality bins, while for the direct photon ratio, such a flip in the second derivative is not there. However due to large uncertainties in the ratio for the direct photon it cannot be ascertained with nearly the same precision as the with the  $\pi^0$  whether the shape of this ratio in fact remains constant in the four centrality bins.

If  $Au + Au$  particle production follows the Glauber estimate of binary-collision scaling, then the spectra from all centralities should have the same shape, which will then also be the same as the shape of the  $p + p$  spectrum as predicted by pQCD. For the  $\pi^0$ , this is obviously not the case, and indeed we shall see this is due to the fact that the pions are suppressed. For prompt photons, within the point to point uncertainties, the overall spectral shape matches better the pQCD prediction. Hence we have our first, if not strongest, indication that that binary scaling is working better for the direct photons than for  $\pi^0$  and, by comparing the shapes of different centralities amongst themselves within the  $Au + Au$  dataset, that shape development of the direct photons with centrality is different than that of the

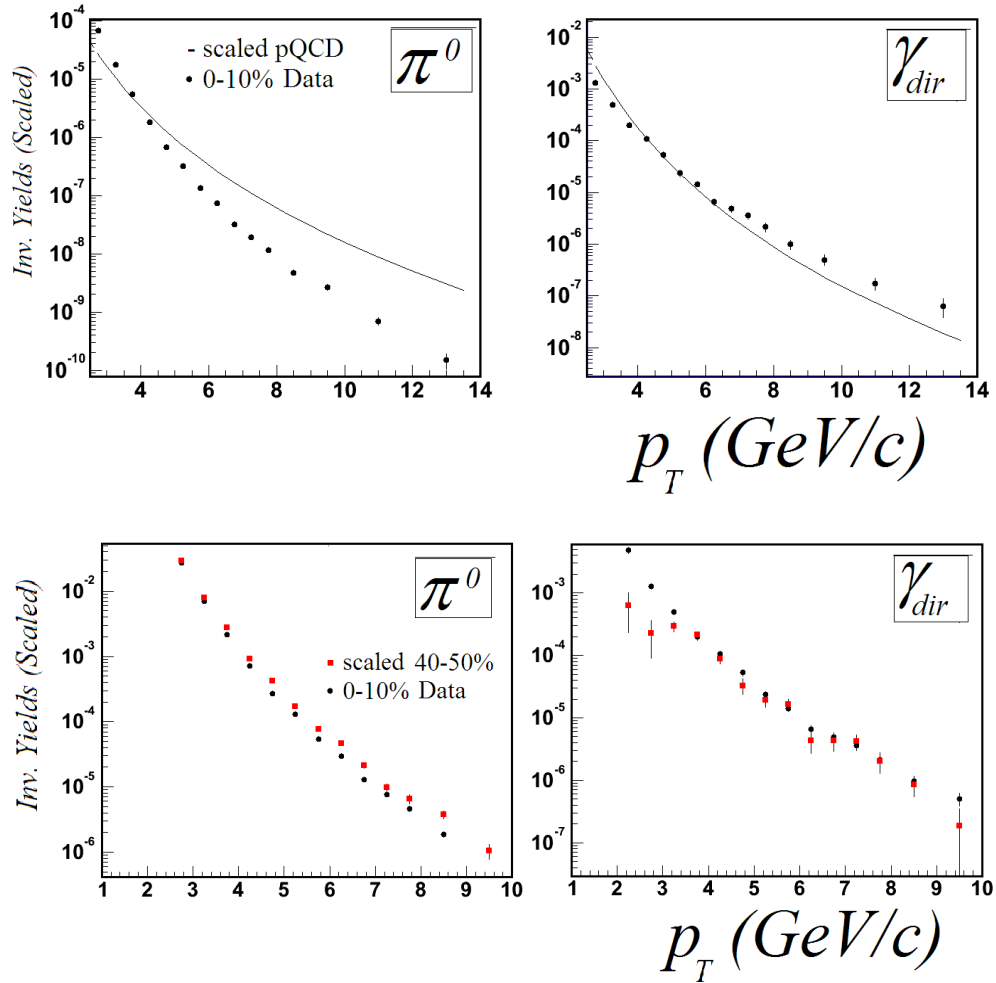


Figure 8.3: Spectral shape comparisons. A dramatic difference is observed between the shapes of the  $\pi^0$  invariant yields in Central events and the NLO pQCD prediction, but for  $\gamma_{direct}$  the shape matches much better. The spectra are scaled arbitrarily. The comparison of the same centrality bins between the  $\pi^0$  and  $\gamma_{direct}$  are inconclusive due to uncertainties, but may indicate the same difference. Therefore spectral ratios are employed in the next figure.

suppressed  $\pi^0$ .

## 8.2.2 Systematic Error Cancellations in Spectral Ratios

A word about the systematic error in spectral ratios. The great thing about taking ratios of spectra is that quite often many systematic uncertainties will cancel. In

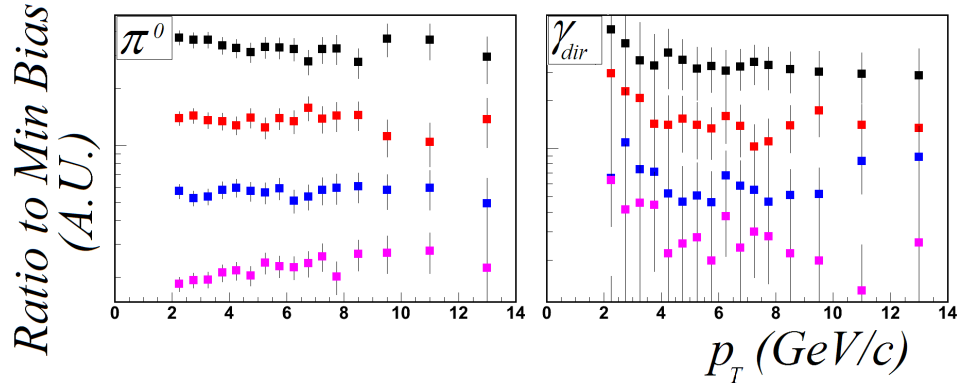


Figure 8.4: Shape comparisons of ratio of spectra for the most central bins. There does appear to be a difference—the  $\pi^0$  ratio changes concavity while the  $\gamma$  does not.

our case the biggest single source of systematic error for both the  $\pi^0$  and inclusive  $\gamma_{\text{all}}$ , and one of the largest for  $\gamma_{\text{direct}}$  is the energy scale of the EMCal. This cancels in spectral ratios not only among different spectra themselves, but also as already discussed, in ratios between the  $\gamma$  and  $\pi^0$ , such as in our ratio  $R_{\gamma_{\text{direct}}}$ . Several other There are two kinds of errors that will not cancel however. Obviously statistical errors will not cancel. Also there are several point by point systematic errors which also do not. For the  $\pi^0$ , this is mainly the yield extraction error. For the direct photons, this most of the systematic error on  $R_{\gamma_{\text{direct}}}$ , which when propagated in forming the spectra of direct photons ( $\gamma_{\text{direct}} = (1 - R_{\text{gamma}_{\text{direct}}}^{-1}) \gamma_{\text{all}}$ ) is even magnified further.

There are several reasons why we don't expect the error on  $R_{\gamma_{\text{direct}}}$  to cancel. First since  $R_{\gamma_{\text{direct}}}$  contains the  $\pi^0$  data points, we will at the minimum have its irreducible yield extraction error which is at the level of 10% but smaller at higher  $p_T$ . More importantly, secondly, since the we have already cancelled some systematics by taking  $\gamma/\pi$  in  $R_{\gamma_{\text{direct}}}$  itself, we can not be sure that the ‘‘cancellations of cancellations’’ will occur especially at the lower  $p_T$  values where  $1 - R_{\text{gamma}_{\text{direct}}}^{-1}$  becomes extremely *small*, that is to say, a very *large* multiplicative factor in the final result as discussed in section 6.9. Finally, in using the real  $\gamma$  and  $\pi^0$  data points in making  $R_{\gamma_{\text{direct}}}$ , we have chosen to incur the statistical errors from both spectra in place

of other systematic uncertainties and hence the statistical error of these individual spectra *become* irreducible point by point systematic error on  $\gamma_{direct}$ . Luckily this should only be an issue where we start to run out of statistics in the very highest  $p_T$  bins and increasing with peripherality.

However the good thing about such point by point systematics is that they are expected to still be random from point to point, and thus they should not change the overall behavior of spectral ratios across several  $p_T$  points. Their effect can be minimized by combining several bins and averaging which we shall do in several cases. In any case when observing ratios like in Figure 8.3, or subsequently in "  $R_{CP}$  " type plots of the next section, we should expect the *average* ( $p_T$  correlated) systematic behavior among all data points to be the same for each spectral ratio.

### 8.2.3 The Ratio $R_{CP}$

With the lack of a 200 GeV  $p + p$  measurement of direct photons we are in a similar situation to when the 130GeV  $Au + Au$   $\pi^0$  data was released. At that time, lacking a  $p + p$  reference measurement, the violation of binary scaling inherent in the high  $p_T$  suppression was studied using  $R_{CP}$ , the ratio of central spectra to peripheral, where each centrality bin is scaled by its glauber  $N_{collision}$  value, already defined in 6.5.2:

$$R_{CP} = \frac{\langle N_{coll} \rangle_{central} dN_{central} / N_{events}^{central}}{\langle N_{coll} \rangle_{periph} dN_{periph} / N_{events}^{periph}} \quad (8.1)$$

Making the ratio against the most peripheral bin that we are able to is desirable because we assume that nuclear and medium effects will be small in the most peripheral events, since events there become more like peripheral  $N + N$  collisions. In this way,  $Au + Au$  events provide their own  $N + N$  reference in peripheral. To the extent that the peripheral bin has no nuclear/medium effects in it,  $R_{CP}$  can tell us quantitative information about enhancement or suppression relative to  $N + N$  collisions. More generally, we can also try looking at the ratio of any two centrality bins (e.g.  $R_{PC}$ ,  $RC_1C_2$ ) just to see whether the scaling itself is obeyed between the

two centrality bins in the ratio.

Unfortunately the enlarged systematic and statistical uncertainties in the most peripheral bins limits us to making spectral comparisons with the 50-60% bin. This should still be useful since the 50-60% bin is already very peripheral. Taking 6.45 as the radius of the  $Au$  nuclei with a skin of 0.5 fm (see section 3.3.1), an upper estimate of the effective total radius as 7 fm yielding the “maximum” impact parameter is then  $\approx 14$  fm. Looking at table 6.1 we see that the *average* impact parameter for the 50-60% centrality bin is 11 fm, so the overlap region is proportionally quite small. That this bin is relatively free of nuclear/medium effects can be verified by looking at the behavior of the  $\pi^0 R_{AA}$ , figures 7.4 and 7.2 from the previous section. While it is true that for the 50-60% bin,  $R_{AA}$  is already 20% below unity, this is only slightly lower than in the remaining more peripheral bins, even the most peripheral. Considering that the systematic errors from the glauber calculations are large enough to account for this difference which is in the 10-20% range. This is small compared to the 80% (factor of 5) suppression in the most central  $\pi^0$  data. Therefore for reference we always include the  $\pi^0 R_{CP}$  made with the same 50-60% reference bin.

In Figure 8.5 then, we show the  $R_{CP}$  constructed with this centrality bin. The first thing that is immediately apparent is that it is hard to draw any definite conclusions about the  $\gamma$ 's (mauve points) in any specific  $p_T$  region due to their large error bars when looking at  $R_{CP}$  as a function of  $p_T$ . Secondly, it will be noted that points appear to be missing below 3-4 GeV. These points have been excluded simply because they fall out of the the y-axis range chosen. As is evident by the points which are visible and the systematic errors bands continued for the points that aren't (point by point systematic uncertainties which don't cancel here) on this region make the values of these points completely insignificant. Generally they lie quite high, between 2 and 3, but are still consistent with one as the error bars indicate. We have chosen to focus on this y-range because we wish to use this plot mostly to accentuate the differences between the  $\pi^0 R_{CP}$  (which again is also

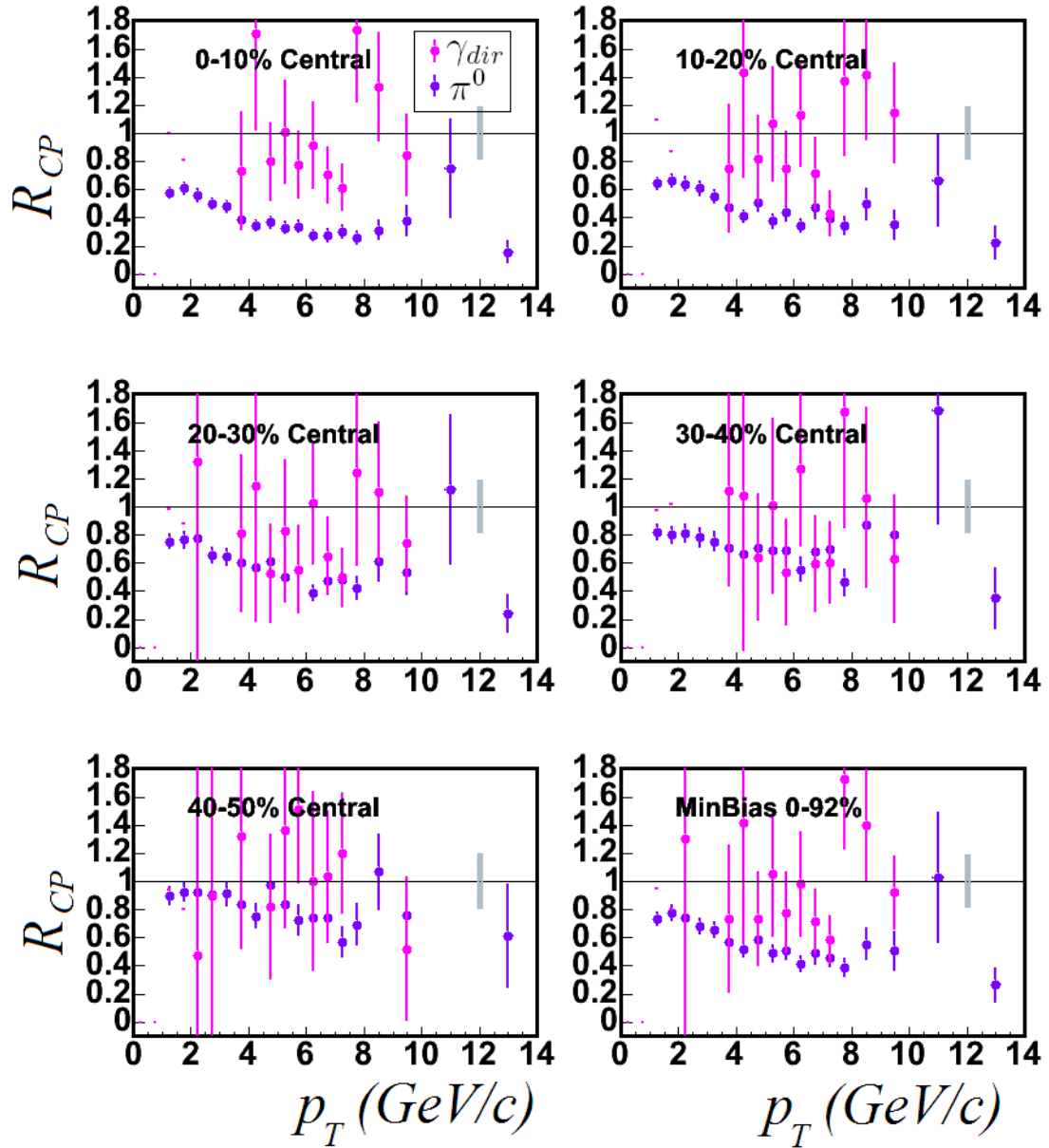


Figure 8.5:  $R_{CP}$  for  $\pi^0$  (dark points) and  $\gamma_{direct}$  (light points) using the 50-60% centrality bin. The grey box at  $R_{AA} = 1$  represents the systematic error band for the thickness scaling, (*i.e.* from Table 6.1) not included in the data points themselves. Even though many errors cancel in the spectral ratios, the point by point irreducible errors, on the direct photon spectra make it hard to draw any conclusions.

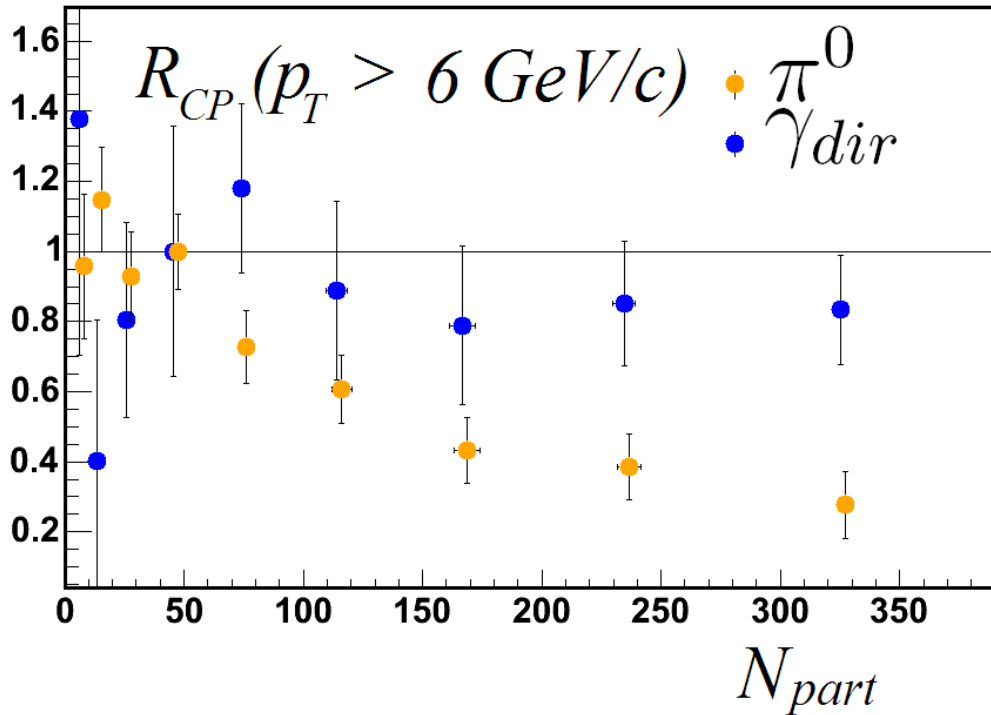


Figure 8.6: Integrated  $R_{CP}$  for  $p_T > 6$  GeV/c vs.  $N_{participants}$  for  $\pi^0$  and  $\gamma_{direct}$  using the 50-60% centrality bin. (Centrality increases with  $N_{part}$ ). This figure represents the integrated average of each bin in the previous figure, and therefore has reduced systematics. As opposed to the previous figure, it also includes the large uncertainty-laden (and therefore fairly statistically and systematically insignificant) peripheral bins for direct photons. On the other hand, are significant. Note that the  $\pi^0$  points in these peripheral bins (starting with the  $N_{part} = 50$  bin which corresponds to 50-60% centrality), with better statistics in a lower  $p_T$  bin, show a falling trend even though the behavior in this bin appears to be consistent with flat.

calculated with the 50-60% peripheral reference.) and which is most evident between  $R_{CP}$  values of zero and one. Any possible interpretation of these higher points will be discussed below.

Despite the large uncertainties in the individual  $R_{CP}$  points, we can make some general observations. Observing Figure 8.6 since it represents a summary of  $R_{CP}(p_T)$  plots, once again we see a dramatic difference between the photons and the pions. The suppression compared to the 50-60% centrality bin for the  $\pi^0$  reaches a max-

imum of about 0.25 in the most central bin and gradually lessens. On the other hand in the most central bins, the direct photon  $R_{CP}$  seems to remain flat. This is the most important point that can be made from observing this  $R_{CP}$ : namely the constancy of the more central points, which is an indication that binary scaling is being obeyed, albeit only above  $N_{part} = 50$ .

### 8.2.4 Absolute Value of $R_{CP}$

Can we make any interpretations about the absolute value of  $R_{CP}$  for the direct photons? For these most central bins, it appears to be approximately 0.85, but is also consistent with 1. Thus we cannot assign much if any significance to this value of 0.85. The reason for this is that the centrality bin we are dividing by has the largest uncertainties of any of the more central bins. Therefore, a small, statistically or systematically random fluctuation in this point within its one sigma error band. For this reason, the error on the  $N_{part} = 50$  point can be taken as a systematic on the absolute value of the number, which would also be added in quadrature to the systematic errors on the  $N_{coll}$  scaling factors. It's best not to try to interpret absolute values on this plot: it is better at showing the behavior as a function of centrality or  $N_{part}$ .

The susceptibility of  $R_{CP}$  to the larger uncertainties of the peripheral reference bin can be circumvented by using one of the stronger (higher) centrality bins as the reference bin thereby making an " $R_{PC}$ ". Then interpretation of absolute values opposite, but with smaller experimental in the central bins. An excess in this ratio above unity would then be a sign of suppression and a deficiency an enhancement. However any such deviations are hard to interpret for the physics effects we are looking for, since within the higher centrality bins where it is beneficial to look at the ratio, we already expect nuclear and medium effects to be present as we see in the  $\pi^0$ .

In Figure 8.7 we show " $R_{MBC}$ " where we've divided by the  $N_{coll}$ -scaled minimum bias direct photon spectra by the the  $N_{coll}$ -scaled most central 0-10% bin. Once

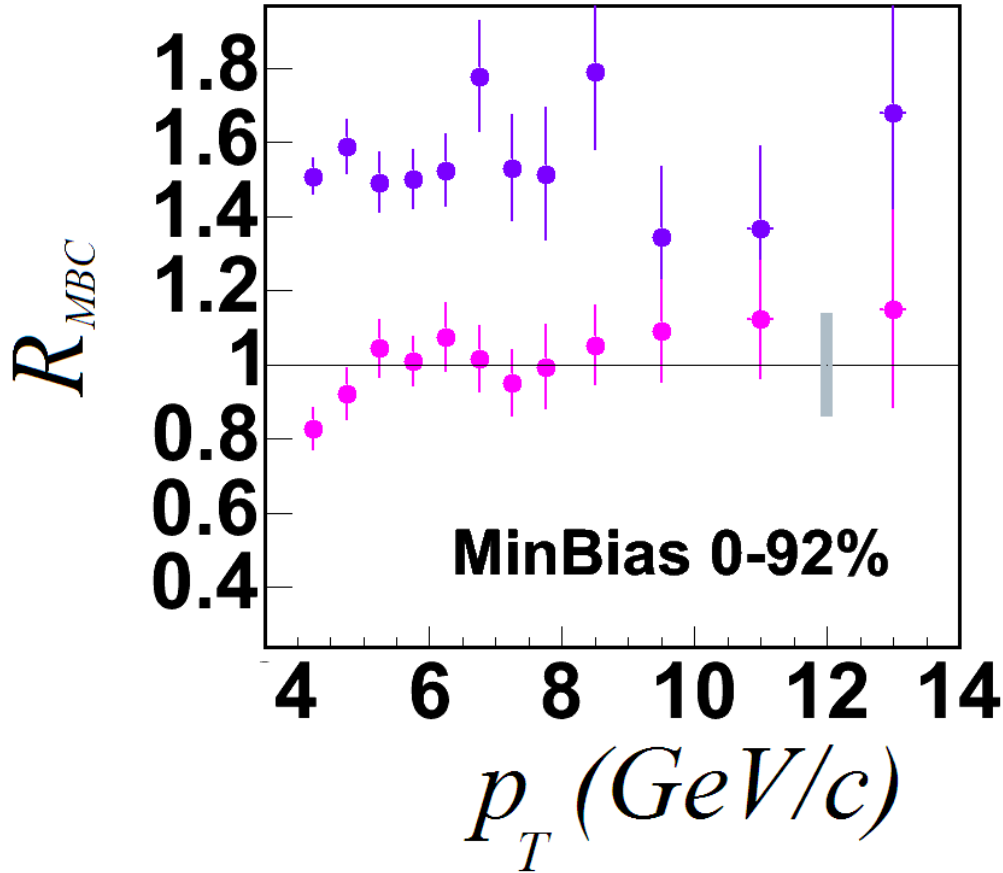


Figure 8.7:  $R_{MBC}$  vs. transverse momentum for  $\pi^0$  and  $\gamma_{direct}$  where the  $N_{coll}$ -scaled Minimum Bias spectra is divided by the  $N_{coll}$  scaled most central 10% bin. Above 5 GeV, the closeness of the ratio to unity (within 5-10%) strongly suggests that binary scaling is working obeyed between the data samples. The dramatic increase in the error bars is by construction, explained the text.

again, as with all the other results shown, a striking difference is observed between the pions and the photons. Note the smoothness of the direct photon points above 5 GeV/c. From this ratio, due to its reduced uncertainties, we assign more significance to the absolute value of the data points. Between the two centrality bins binary collision scaling is obeyed to within 5-10%, since all the points lie within a band between 1.0 to 1.05-1.1. Below 5 GeV, there appears to be the start of a trend going below 1, which would indicate an enhancement of photons in the central bin compared to minimum bias. However this is where our systematic uncertainties get

large, and may not cancel in the spectral ratio. With the full systematic errors, these points are easily consistent with 1.

### 8.2.5 $T_{AA}$ Scaling

We end our demonstration of the binary collision scaling of  $\gamma_{direct}$ , and lack thereof for the  $\pi^0$  in 200 GeV Au+Au with the strongest piece of evidence yet. For this we look in new way at  $T_{AA}$  scaling directly.

In Figure 8.8 we consider the integrated invariant cross section for each centrality bin times the integrated luminosity—the total collected yield  $Y$  defined by

$$Y(p_T > 5\text{GeV}/c) = \int dp_T d^2 N_X / dy dp_T \quad (8.2)$$

where  $X$  is either  $\pi^0$  or  $\gamma$ . It should be noted that this yield is not normalized by the number of events in each centrality bin so it is *not* the production per event. This is like the  $p_T$ -integrated invariant yield except that we do not event normalize to the full  $Au + Au$  cross section and thereby are looking at all direct photons or pions collected by PHENIX, corrected such that the luminosity for each centrality bin is the same. Therefore we can study how the actual sum of the yields of photons or pions behave as a function of the integrated overlap integral  $T_{AA}$  over the same luminosity. For minimum bias events, the value of this overlap, following our AB scaling arguments of section 4.3, will simply be  $AA = 197^2$ . Actually for us this number is only approximate, given experimental effects: *e.g.* we only see the central 92% of the full  $Au + Au$  cross section, but more importantly, in our Glauber calculations of 6.1 we did not fix the normalization to be  $AA$  but rather inferred a probabilistic normalization generated by our Glauber Monte Carlo. Inclusion of the integrated MB yield is actually the advantage of studying the scaling as function of  $T_{AA}$  as opposed to  $N_{collision}$  since the latter is only defined as an average over a centrality bin.

For this figure we chose to integrate the photon and  $\pi^0$  yields above  $p_T > 5.5$  GeV/c because, referring back to Figure 7.7, this is the highest  $p_T$  bin with good

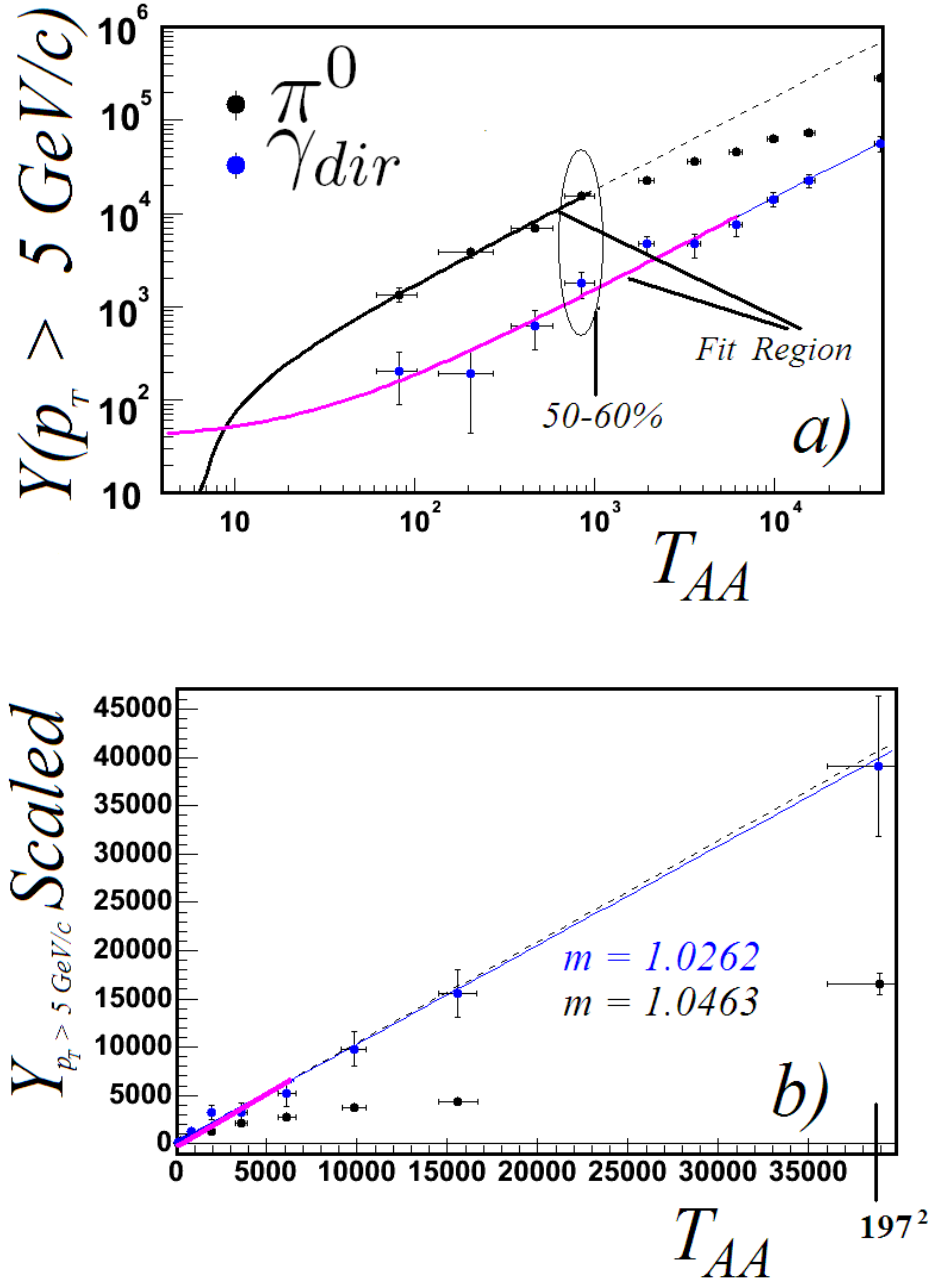


Figure 8.8: Invariant Cross Section ( $\propto$  Inv. Yields are integrated above 5.5 GeV for each centrality and plotted against the amount of nuclear overlap factor corresponding to the fraction of the total  $Au + Au$  cross section each represents. Minimum bias represents the full AB scaling at  $AA = 197^2$ . The direct photons appear to follow linear scaling rather well as expected for all centrality ranges. The same scaling appears to be present for the  $\pi^0$  in its most peripheral bins, and then high  $p_T$  suppression sets in and causes the deviation of the black points from the line. Several details regarding both subjects are discussed in the text.

statistics for which a positive direct photon signal was found in *all* centrality bins. Taking the most peripheral bins (which correspond to the lowest values of  $T_{AA}$ ) we fit a simple line in order to test whether indeed the yields scale linearly with  $T_{AA}$ . This fit is shown in the solid curves on the plot. The thick curves demonstrate visually the fitting region for each particle species, while the thin curves are just the same linear curve extended across the whole  $T_{AA}$  region. The size of the fitting region was chosen to extend to points that had small uncertainties, but are not very sensitive to whether the very highest  $T_{AA}$  point in the fit was included or not, which is visually apparent. This matters most for the  $\pi^0$ , since we know that the suppression does violate the linear scaling. In *a)* it the 50-60% points are marked. Notice that excluding this point for the  $\pi^0$  might alter the linear fit, but in a way that would violate the trend of the points, since then the 50-60% point would be in slightly in *excess* of the scaling line, not suppressed as the other points increasingly are. Thus we would likely interpret the point as still being consistent with linear scaling. In other words, as from our observations of integrated  $R_{CP}$  for the pions, this point appears to still be obeying binary scaling. We shall have more to say about this in a second. For  $\gamma_{direct}$ , obviously the uncertainties are larger, so we extend the fit to higher values of  $T_{AA}$ . For the photons, it does appear that restricting the fit range to very small values, e.g. the same values as for the  $\pi^0$  fit, may result in a fairly different answer, and thus it may seem that extending the choice to higher  $p_T$  is biasing the point we desire to make with the plot. But this is not the case: extending the points to the higher points is actually exactly the test we wish to perform since we trying to demonstrate that *all* points are consistent with the linear binary scaling, *including* the higher  $p_T$  points.

As is evident, indeed it is the case that we see binary scaling working remarkable well (!) for the entire  $T_{AB}$  range. The inclusion of the Minimum Bias point at the very highest  $p_T$ , makes the point even stronger, because of the “lever” arm it represents. This is the first conclusion from this plot. Direct photons are following linear scaling with  $T_{AA}$ . Is it the right linear scaling? What we mean here is,

if  $d\sigma = mT_{AB} + b$  are  $k$  and  $b$  what we would expect, namely  $b = 0$  and  $k = d\sigma p + p$ ? That  $b \simeq "0"$  is quite evident from the plot. From the log plot a), we can see that the  $y$ -intercept of our fit to the direct photons must be nearly an order of magnitude smaller than the yield of the lowest bin. With no  $p + p$  reference for the invariant cross section we can test the slope value by exploiting the fact that  $b \approx 0$  and scale  $d\sigma$  (all  $y$  values) such that the slope should be 1 and then test how close the slope of the fit matches. Therefore in the plot we've scaled all points such that the most central bin follows binary scaling exactly, and scaled all points by  $T_{AA}(0 - 10\%)/d\sigma(0 - 10\%)$ . As indicated on the plot, the resulting slope ( $m$ ) values are indeed very nearly one (within 2% for  $\gamma_{direct}$ ).

Of course, this numerical "quantification" is not too much to be excited by: it is mostly just a test of how close this point is to the fit line and how small  $b$  is. If there were a dramatic reduction in the  $\gamma_{direct}$  yield already in the most peripheral bin and then scaling was obeyed in all bins after, this way of looking at the data would not be sensitive to this, though granted this scenario would be completely unexpected theoretically. But scaling it this way does illustrate another feature of the plot—the close similarity of slope of the  $\pi^0$  fit.

### 8.2.5.1 The $\pi^0$ Scaling and Suppression

So far we have been trying to demonstrate that the direct photons are scaling as expected with "little" nuclear or medium effects. Insofar as this message is concerned we have only used the  $\pi^0$  as an indicator of what "not scaling" looks like together with the  $\gamma$  data, but mainly focused on evidence in the  $\gamma$  data or  $\pi^0$  data separately by forming spectral ratios, for the  $\pi^0$  noting  $R_{AA}$  behavior, and observing the level to which scaling is occurring or being violated in each data set individually. The statement we have painted so far with Figure 8.8 becomes even more significant if we start realizing the anticipated potential use of high  $p_T$  direct photons at RHIC as a control reference and consider both results together. The simplest explanation of Figure 8.8 is that the reason the slope of both lines is the same within 2% or so is that both are obeying the same scaling in the regions where they are fit. Not

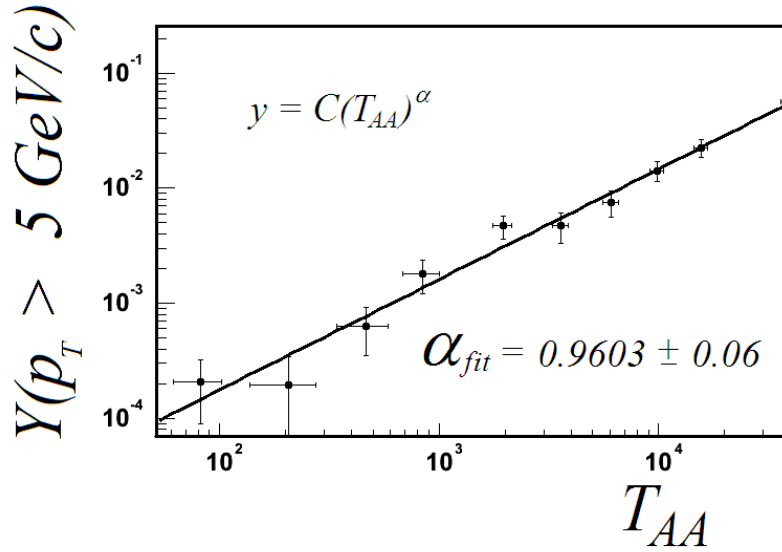
only is this the simplest explanation, it's the one we expect given the predicted suppression mechanisms: for the  $\pi^0$  production in the most peripheral collisions, the low liberated gluon density should not yet cause quenching effects that would result in a large suppression, and, in the case of the  $\gamma_{direct}$  production, the photons should be relatively insensitive to the same liberated gluon density at any centrality. Taken together this way, we have our most convincing demonstration yet that the  $\gamma$ 's are following thickness scaling and the  $\pi^0$  suppression level is small all the out into the 50-60% bin.

As for point 2), we already noted this behavior in the  $\pi^0$  from looking at Figure 8.6. Thus it has now been confirmed in a different fashion, with different systematics. At what centrality  $\pi^0$  suppression onsets is actually an interesting physics question which we hope to probe at RHIC. [71], [76]. A percolation effect suggested by [71], by which modifications to hard-scattering products (in [71] to  $J/Psi$  production) occur only after a sufficient liberated parton density is reached, might cause suppression to "turn-on" abruptly. The smooth trend apparent in our best statistics  $p_T > 4\text{GeV}/c$  data points in 7.4 and elsewhere [8] appear to rule out such an effect, at least for  $N_{part} > \sim 9$ . And it is possible that at 4 GeV/c or 4.5GeV/c, production is still in a regime where other modifications to hard scattering such as the Cronin effect, discussed again in the next section, could cause the suppression onset to be obscured somewhat. Therefore it will be interesting to verify the behavior at higher  $p_T$  values such as will be made available in the recently collected, much larger  $\pi^0$  data set obtained in PHENIX Run4.

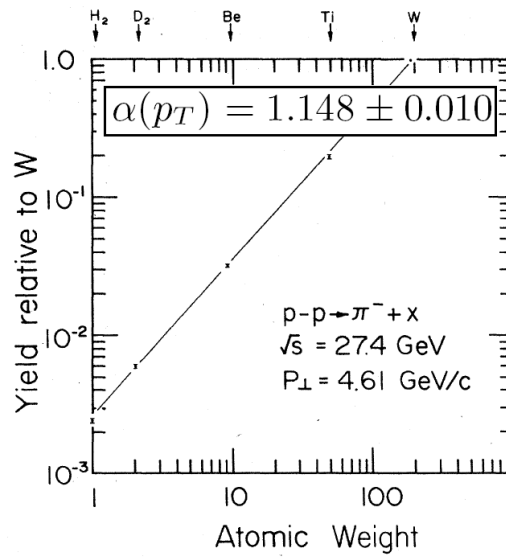
### 8.2.5.2 Cronin Inspiration?

If Figure 8.8 seems strangely reminiscent of the Cronin effect [67], [31], that's because this *is* the generalization of the original Cronin result now being studied  $A + A$ , as opposed to  $p + A$ . In Figure 8.9 b) we show a plot from this seminal paper.

As is apparent from the figure, the main observation was that the approximate linear scaling of p+A  $\pi^-$  production with  $A$  ( $d\sigma \propto A^{1.0}$ ) was altered by some sort of nuclear effect such that it was made proportional to  $A$  to some power  $\alpha$  ( $d\sigma \propto A^\alpha$ ).



(a)



(b)

Figure 8.9: A fit function  $\propto T_{AA}^\alpha$  in a) which is the generalization of the original  $A^\alpha$  Cronin fit shown in b) (figure from [31]), sees no Cronin effect at least at the order of the size in b), since the result of the fit to our data yields  $\alpha = 0.96 \pm 0.06$ .

The generalization of this idea in  $A + A$  would obviously be to test the  $T_{AA}$  scaling this way to determine whether the production is proportional to  $T_{AA}^\alpha$  with  $\alpha \neq 1$ . So far we have been assuming  $\alpha \equiv 1$  and fitting a approximate  $mx + b$  form under that assumption, but there is no reason we cannot also repeat the same Cronin scaling test. The result is shown in Figure 8.9.

As the figure shows, we observe no Cronin-like effect above 5.5 GeV/c. Would we expect to? As discussed in the next section, Cronin was observed in  $d + A$  ( $\sim p + A$ ) collisions at the same energy however for  $\pi^0$  only below  $\sim 5$  GeV/c if at all. This was already shown in Figure 4.5 in the introductory section 4.4.2, where it also appears that the Cronin enhancement is present at higher  $p_T$  for charged particles. This behavior is experimentally expected: baryons are generally observed to have a larger Cronin effect. One would naturally expect smaller Cronin effect for  $\gamma_{direct}$  in pictures where it is explained as  $k_T$  broadening due to multiple scattering, since again this should be absent for photons in the final state.

### 8.2.6 Other Evidence

So far we've presented evidence of various sorts for binary scaling in the direct photons. The ultimate purpose for making such a statement is to legitimize the claim that the  $\pi^0$  and other meson suppression is indeed an abnormality, that is, in the absence of suppression we should expect binary scaling to hold— and we submit that this is exactly the situation for  $\gamma_{direct}$ . Although this evidence is very suggestive, if not conclusive on its own, there may be doubt left in the readers' mind since there is still room within this data set for alternative albeit less believable explanations of the observed phenomena, as we shall discuss in a moment. However, we can quickly remove most remaining doubts by referring to another major result of the RHIC experiments especially PHENIX: the high  $p_T$  results of the  $d + Au$  run in 2003, which were originally released slightly before those of our work (Summer 2003), but essentially in parallel with this result. In addition, other  $Au + Au$  data for charm production also tells a similar story to our  $\gamma_{direct}$  results, though less authoritatively.

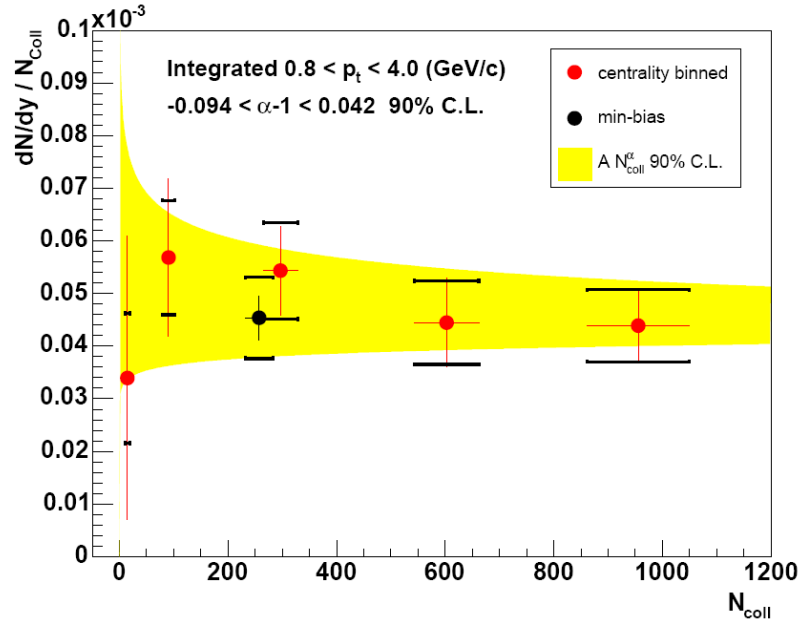


Figure 8.10: The 90% confidence level for Binary Scaling is shown. Between  $0.8 < p_T < 4.0$  (GeV/c), the single electron spectra are expected to be dominated by charmed meson decays. Therefore the total integrated yield even at these  $p_T$  values should be due to hard scattering.

We also note that evidence for binary scaling has been also observed in another  $Au + Au$  probe where it was expected to be. PHENIX has measured open charm ( $D$  mesons) production indirectly in a measurement of non-photonic single electron production  $Au + Au$  and found that within large uncertainties, this production also follows binary ( $N_{\text{coll}}$ ) scaling. Heavy quark production requires hard scattering momentum transfers to even occur due to the heavy mass threshold, and it is expected that the same gluon radiative quenching mechanisms which suppress the  $\pi^0$  and other light mesons by inducing energy loss in their parent partons, will not have as large of an effect on the heavier charm and bottom quarks as they traverse the hot dense colored matter [179], [73], [72].

The charm results in Figure 8.10 have similar systematics but larger statistical errors and less centrality bins than our direct photon data. However it may not be considered quite as strong of a statement as our  $\gamma_{\text{direct}}$  result for two reasons. First,

due to the indirect measurement method, contributions from *bquarks* and possibly other unknown sources are less pinned down, even though the distinctions between bottom and charm would not matter in the case that binary scaling is obeyed for both. Second, the influence of hydrodynamical flow on heavy quarks are expected to be more complicated than in the case of direct photons, for which there is by definition no hydro, since the photon does not have a rest frame. Nonetheless the result, taken together with that of our  $\gamma_{direct}$  and the  $d + Au$  result, gives an even “warmer feeling”.

### 8.3 Direct Photon $R_{AA}$ and NLO pQCD Performance at RHIC

In the previous section we were able to demonstrate scaling for the direct photons by considering data by itself without a  $p + p$  reference. Except for some very loose statements we may be able to make from results like our “ $R_{MBC}$ ” Figure 8.7, with no measured  $p + p$  reference, we cannot make precise statements about some of the more interesting physic questions which we hope can be addressed with the direct photons, such as possible thermal or other enhancement in lower  $p_T$  regions. Even though we consider our  $\gamma_{direct}$  result to be mostly relevant at high  $p_T$  since that is where our uncertainties allow us to make stronger statements, it would still be nice to see how our measurements compare to absolute estimates and predictions, and whether these are consistent or inconsistent within uncertainties in any range.

We are again faced with a lack of  $p + p$  reference. This time our options are two-fold: First, we could try to extrapolate a reference from other world data taken at the same or other  $\sqrt{s}$  energies as was also done for the pions both in the original 130 GeV/c high  $p_T$  suppression results. [11] and more recently for 62.4 GeV/c data taken at RHIC in the 2004 run (this analysis is under progress). However in both of these cases it was found that these extrapolations or estimates simply could not be trusted enough to draw any definite conclusions. For the 130 GeV data this was just due to the lack of faith and large systematics in the extrapolation procedure, and in

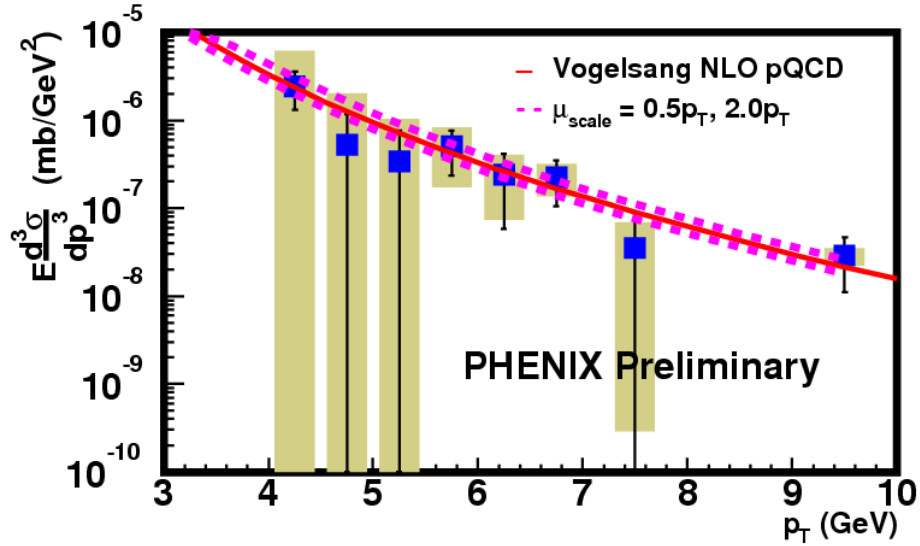


Figure 8.11: A very preliminary  $p + p$  measurement of  $\gamma_{direct}$  was presented at the Quark Matter 2004 conference [85]. The result suffered from large systematic uncertainties such that a precise statement about the level of agreement of pQCD cannot be made.

the case of 62.4 GeV, where several other experiments had measured pion production at exactly the same energy, contradiction between the many datasets rendered the answer even more uncertain than extrapolations. Direct photon measurements are considered rather more difficult than pion measurements and contradictions are already known to exist in several experimental results as discussed in section 4.7. Also there is a much larger disparity in the  $\sqrt{s}$  values where  $\gamma_{direct}$  measurements have been made. Therefore we consider this exercise rather fruitless.

Instead we shall find it more instructive to turn to pQCD in order to make absolute comparisons of our direct photon data with other theoretical predictions of enhancement. We have already noted discrepancies in the level of agreement between pQCD *inclusive* predictions and the world data set, despite the spectacular successes of pQCD in other areas. (see section 4.7). Therefore the question is to what level shall we trust the pQCD predictions of inclusive production of direct photons?

To address this question we have three avenues. First, we actually do have our

own PHENIX measurement of direct photons for 200 GeV  $p + p$ . This is shown in Figure 8.11. The uncertainties of this measurement are too large to make it useful to use as a reference but we can at least use it as a set of upper and lower limits in order to very loosely check the QCD prediction of production at this energy. As the figure shows, pQCD is consistent with the measurement, but systematic errors are so large, so would variations of 200 to 300%.

As described in section 4.4.3 of the introduction, discrepancies of this magnitude from pQCD are entirely possible. For example, see figures 4.6, 4.6. As shown there, the discrepancies with the data can be as large as 500% but at higher collider energies can be smaller. Falling right in between the two regimes, without looking at any RHIC data, we must consider the possibility that such discrepancies will exist. Of course, quality  $p + p$  RHIC data does exist, if not for direct photons, so this is the first place we can look for guidance as to whether we expect pQCD to work.

Most relevantly, exactly how well does pQCD agree with our  $p + p$   $\pi^0$  result? In [18] the message was that pQCD described our data well. However, this statement is at best qualitative. In Figure 8.12 we address the question slightly more quantitatively. As is evident, the erstwhile good agreement of pQCD is dependent on a single choice of  $p_T$  scales and fragmentation function. The choice of these yielding the “best” agreement demonstrated so far, still disagrees by nearly 50% at high  $p_T$ : and high  $p_T$  is where the theory should work better. Therefore we should really look at the  $p_T$  scales/FF combinations that work best at high  $p_T$  and based on the figure, these will yield sizable discrepancies at low  $p_T$ . It is dubious at this point whether the good agreement attributed to the PHENIX  $p+p$   $\pi^0$  data is actually so at one might call a quantitative level. But the main message is even if one were able to find even better agreement with some PDF, FF, and  $p_T$  scale combination: given the uncertainty in the theory due these degrees of freedom for the  $\pi^0$ , before we can claim whether or not QCD works or not at RHIC, we must see the  $p + p$  measurement of  $\gamma_{direct}$ . Then, if a single PDF choice and set of scales can describe *both* well (the FF for the  $\pi^0$  can still be freely chosen to yield the best agreement)

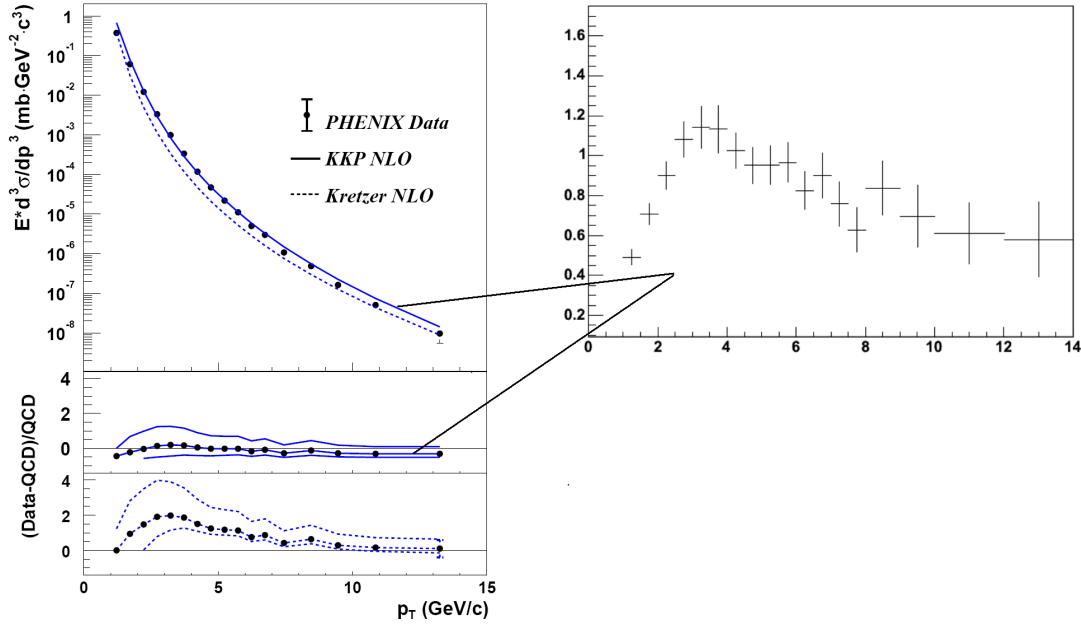


Figure 8.12: Agreement of NLO pQCD calculations with the PHENIX 200 GeV  $p+p$   $\pi^0$  result. The level of agreement is fairly sensitive to the fragmentation choice and  $p_T$  scales chosen. Even the best agreement of the chosen values has disagreements of 40% at high  $p_T$ . Only with a corresponding direct photon measurement will one be able to fully address whether pQCD, with current PDF sets and fragmentation can really describe the data at our energy well, or, for example whether further refinements, such as the phenomenological “ $k_T$  smearing” models will need to be invoked.

then we will have substantiated the claim that pQCD is working well, but not until then. Until this point we must consider the possibility that deviations already exist in the  $\pi^0$ , but are just being compensated for by FF, PDF, and scale choices in the not-so-golden “best agreement” shown so far.

To get an idea of what kind of discrepancies we might be talking about, we shall use the “ $k_T$  smearing” phenomenological model whose main proponent is the E706 experiment of Fermilab *e.g.* described in [32] or [33]). Several different methods for calculating such effects with the use of  $k_T$  based on equation 4.14 have been developed and studied by that experimental group as discussed in that section (4.4.3).

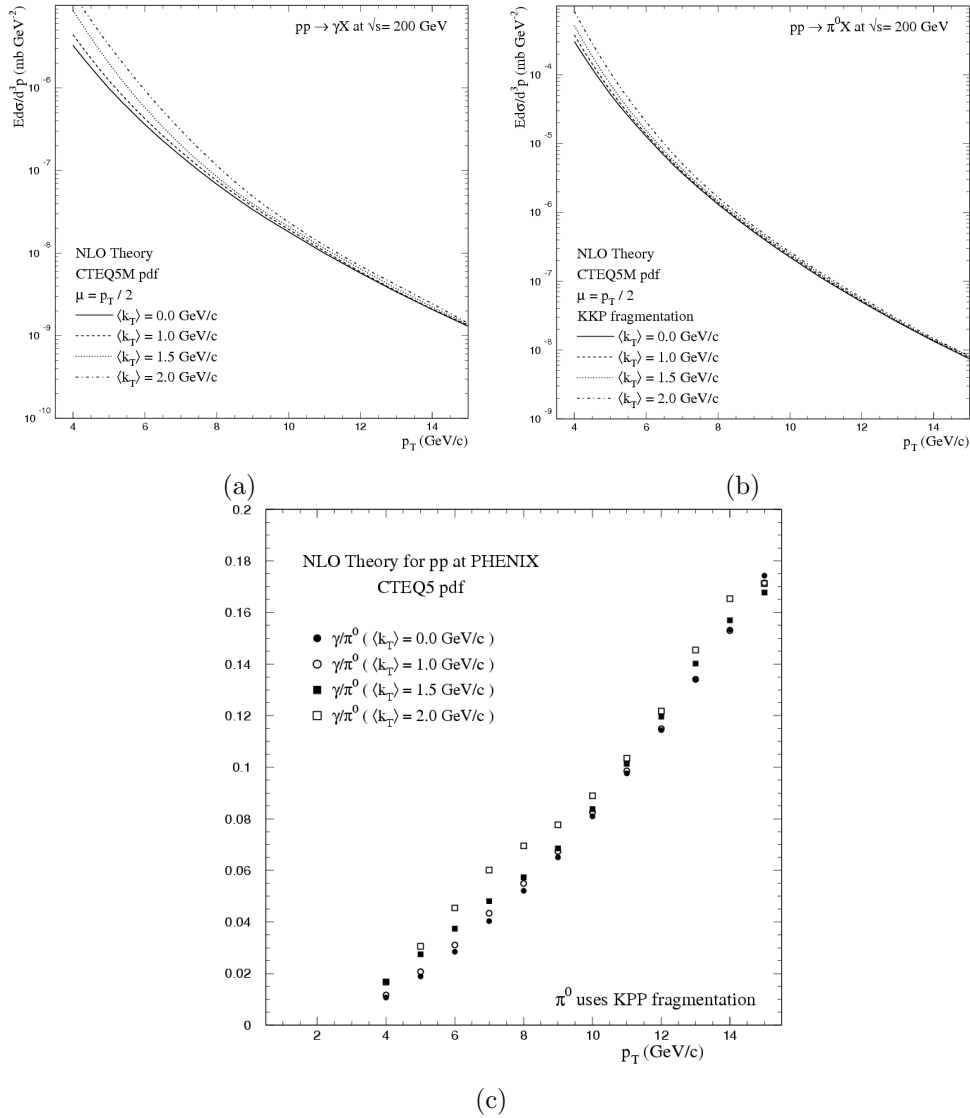


Figure 8.13: Possible sizes of “ $k_T$  smearing” deviations of pQCD

Their “preferred calculation” as of late is a method developed by Owens and Qiu [1] (two prominent pQCD theorists—Owens could easily be considered one of the “founding fathers” of direct photon and jet pQCD calculations) where the convoluting formula 4.14 is incorporated into actual NLO calculations themselves. In the following figures (8.13) we show calculations obtained from members of experiment e706 ([35],[1]) for how much pQCD might over or under predict our data.

As the calculations show, discrepancies consistent with the situation at other

energies can range from factors of 2 at values of  $k_T$  necessary to describe the lower energy data, while for higher values of  $k_T$  discrepancies could be even much higher. Higher values of  $k_T$  of 2-4 GeV are cited to describe higher (1800 and 630 GeV) energy data [131], as discussed in the introduction (4.4.3) putting the “expected value” of  $k_T$  at our energy most likely somewhere between 1.5-2.0 shown in the above calculations, so substantial deviations from pQCD should definitely be considered possible in the soon to measured  $p + p \gamma_{direct}$  reference.

Without anymore todo, Figure 8.14 shows how the binary scaled pQCD comparison of binary scaled NLO pQCD results compare with our current  $Au + Au$  measurements, again for the centrality bins where the results are most significant. As with our  $R_{CP}$  plots, the uncertainties are large. Below 4 GeV/c they are too large for any behavior of the data there to be taken very seriously.

Note that it is also useful to discuss  $k_T$  smearing since the exact same type of smearing calculations are also used to describe potential nuclear effects, such as the Cronin effect. In fact some of the disagreement found by the proponents of  $k_T$  smearing has been attributed to *nuclear*  $k_T$  effects, since e.g. e706 strongest measurements are p+A, where A is relatively small, e.g. A = Be in there most recent results. However such nuclear  $k_T$  effects.

Comparing our  $R_{AA}$  values, we do see a discrepancy from the binary scaled pQCD. Summarizing what we’ve said so far, we cannot answer whether this implies poor performance of the pQCD calculation itself or just a medium or nuclear modification in  $Au + Au$ . However, observing that this discrepancy appears to be present in all the centrality bins, we would have to conclude that our data slightly favors the former explanation. Fortunately we will be able address this question when a better  $p + p$  reference is available. This is expected soon.

### 8.3.1 Modifications or Enhancements of Direct $\gamma$ ?

The most interesting potential of the direct photon measurements in  $Au + Au$  is to look for production modifications due to the final state medium effects. Several

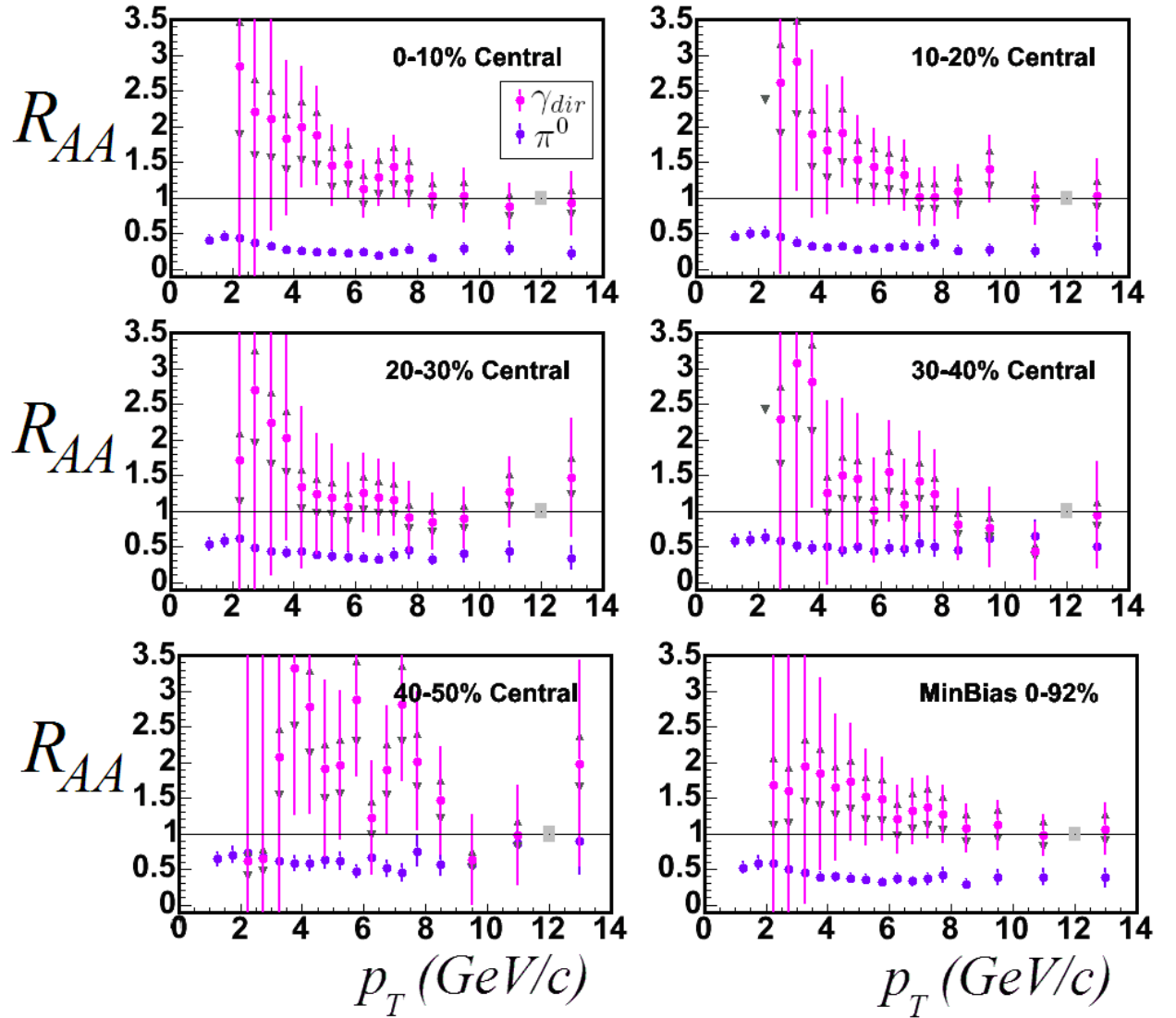


Figure 8.14:  $\gamma_{direct}$   $R_{AA}$  values, using the  $\mu_{scale} = 1.0p_T$  NLO prediction for  $\gamma_{direct}$  [16] as the "p + p" reference. The grey box at  $R_{AA} = 1$  represents the systematic error band for the thickness scaling, (*i.e.* from Table 6.1) not included in the data points themselves. For the  $\gamma$  (light circles) the systematic difference from using the  $\mu_{scale} = 0.5, 2.0 p_T$  NLO predictions are included as the triangular points.

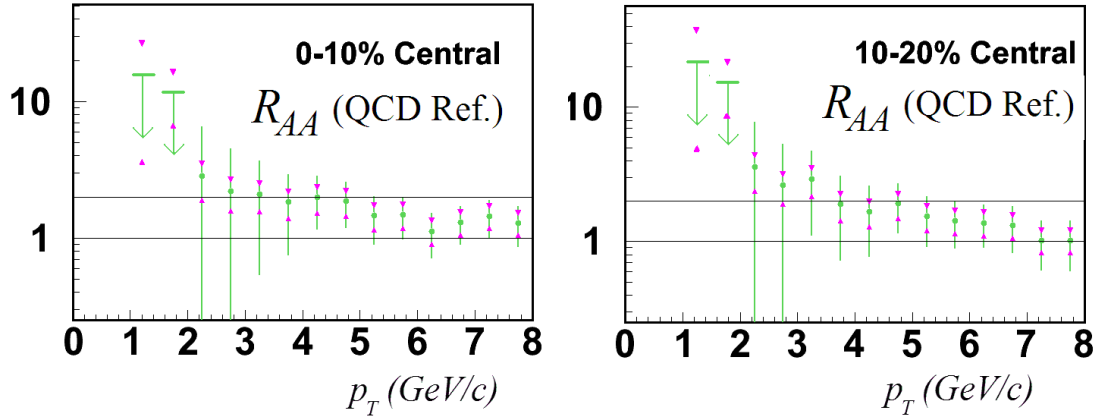


Figure 8.15: Close-up of  $\gamma_{direct} R_{AA}$  showing the full extent of the upper limits for the two most central bins.

predictions of enhancement above normal pQCD rates exist. We shall address two types of such enhancement. Thermal and Jet-Plasma radiation. Then we shall conclude by discussing the possibility of modifications to only Bremsstrahlung or fragmentation contributions to the  $\gamma_{direct}$  spectrum.

### 8.3.1.1 Thermal Enhancement

The first order of business shall be thermal enhancement. With the large number density of charged particles interacting at very high temperature, whether they be hadrons, partons, or some other intermediate as yet unidentified QCD state, the matter produced in HI collisions will radiate thermally. However since this radiation is energetically on order of the temperature. Current estimates from other sources [8] place the average temperature of the HI matter created  $\lesssim 500$  MeV, so naturally we would only expect such radiation to be significant at very low values of energy and correspondingly transverse momentum compared to those of hard scattering regimes. In Figure 8.15 we show an enlarged version of our  $R_{AA}$  for the most central bin in the lowest  $p_T$  bins. Unfortunately as is apparent, our systematic uncertainties in this region are quite large. Nonetheless it is interesting to note how the various predictions may be constrained even by these large uncertainties.

Unfortunately, there several issues about the state of theoretical calculations

that makes it hard to compare things quantitatively. This is because most of the work thus far has concentrated on simply determining the bounds of the  $p_T$  region where thermal enhancement may be visible and quantitative estimates as to the actual magnitude of such radiation are hard to take very seriously. Therefore, and also keeping in mind our large uncertainties at low  $p_T$ , the strongest statements we can make about constraints that our data may impose are best kept to similar identifications of  $p_T$  regions where our signal may be consistent with thermal enhancement.

As regards the situation with the theoretical calculations, there are three important points to keep in mind when discussing thermal enhancement. First, there are two potential sources of the thermal radiation which will add together to form the observed thermal signal, that of the potential QGP but also of hot hadrons which form later but still before the medium stops interacting thermally [144]. These two phases will exist predominantly at different times and locations within the collision 4-volume but will also occur together in regions of mixed phase. Second, as discussed in the introduction (please refer to section 4.7.2 for references), the rate calculations of the fundamental processes for both a QGP and a hot hadron gas (HHG) have not been proven to work with a large degree of confidence, because there are many approximations which must be made and it remains to be seen whether those approximations can correctly account for observed rates. Third, the details of how the thermodynamic evolution occur can be modified by periods of non-equilibrium and by hydrodynamic behavior.

The currently considered best known rate calculations are those done with the HTL 2-loop calculations. A set of basic calculations done “purely” with these rates with no additional modifications due to other types of effects such as non-equilibrium effects by Srivastava [154] is shown in Figure 8.16 a). This calculation focused on the QGP rates, and the HM matter was taken from a non-state of the art basic parameterization where only most basic photon producing hadronic processes were included. Here we see that the plasma radiation only outshines that of the HHG

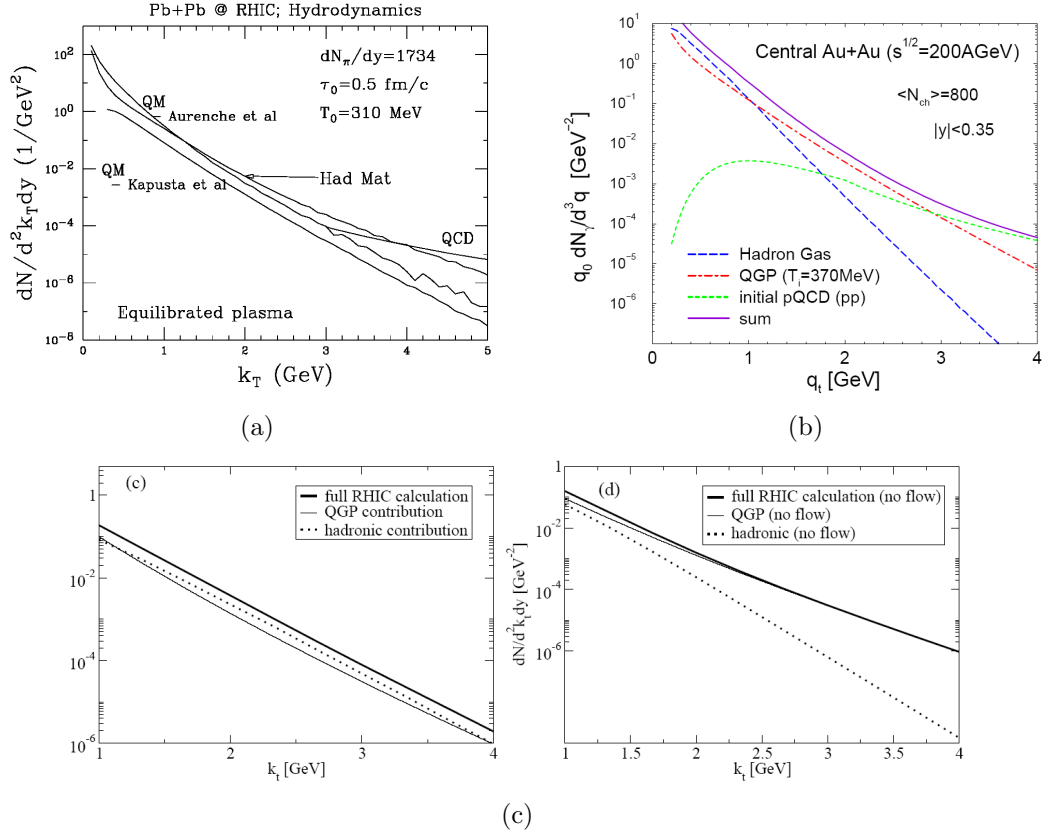


Figure 8.16: Three predictions of HI Thermal Radiation. Please see the discussion in the text. figures from a) [154], b) [162], and c) [149]

below 1 GeV, but that the HHG radiation does appear to rise above the plain perturbative QCD production below about 3-4 GeV.

In 8.16 b) is shown second prediction with perhaps the most state of the art hadron gas approximations, along with a similar HTL calculation for the plasma contribution [162]. Here the opposite behavior for which phase outshines which is apparent, but again the total thermal radiation is found to be above the pQCD rate starting below 4 GeV.

Finally in 8.16 c) is shown perhaps the most sophisticated total calculation of thermal radiation yet. Fairly state of the art rate calculations are used for both the HHG And QGP phase but these are then folded with a full hydrodynamic fireball evolution which includes phase boundaries (but not actual mixed phase regions) and simultaneously takes position information obtained with the *HBT* method of

boson correlations in other RHIC analyses as input [149]. The surprising result of this study was that the HHG radiation is enhanced relative to the that of *e.g.* the basic calculation in a) by the inclusion of hydrodynamic flow in the evolving medium. This makes hadronic radiation the dominant source over the entire  $p_T$  range below 4 GeV. Although the plot does not include or show the level at which pQCD contributes, the QGP component is approximately the same as the QGP calculation in b), so comparing to that figure we would essentially slightly more than double the excess above pQCD.

Taken such predictions, what can we then say about how they compare to our data? First of all, as we already discussed below 4 GeV/c our systematic errors become extremely large. So it is hard to say much. We shall restrict our discussions then to qualitative ones. Secondly, the predictions differ by quite a bit, so it is hard to have a warm fuzzy feeling about them, but on the bright side, with good data, they should be distinguishable. One thing they all agree upon with though is that there should be some thermal production, whether it be from quarks or hadrons, visible starting below 4 GeV/c. Referring to our data in Figure 8.15, we thus can make a few very rough statements: Namely the upper limit of the excess above scaled pQCD  $R_{AA}$  does allow for thermal excesses below 4 GeV. As discussed above, the centrality independence of these results would indicate that they are more likely present in all centralities and therefore not a final state medium effect, but rather quite possibly will even be present in forthcoming  $p + p \gamma_{direct}$  data itself. Nonetheless with no further information our must say our data between  $\sim 3 - 4 \text{ GeV}$  allows for it. However if we look lower, say around 2 GeV/c, there *e.g.* the [162] prediction would be an order of magnitude above pQCD. This is would be disfavored at the half sigma level considering our  $R_{AA}$  values in both of the two most central bins. However, also taking into account the uncertainty of the pQCD reference in our  $R_{AA}$ 's, this statement cannot be taken too seriously.

### 8.3.1.2 Jet-Plasma Enhancement

As discussed in section 4.7.3, several authors starting with the authors of [89], and including Gale and Bass, have made theoretical predictions of a previously not considered form of radiation which can be induced by jets as they transverse a Quark Gluon Plasma. See Figure 4.14. This process is assumed to be distinct from the Bremsstrahlung and higher order radiative processes that are analogous to the gluon radiation responsible for high  $p_T$  suppression. Instead these photons are produced by (predominantly) second scatterings of the quark partons themselves as they traverse the QGP matter. Obviously such calculations assume the presence of the QGP so they represent a potentially new signature available from direct photons. It should be noted that although a “QGP” is assumed, this signature suffers from many of the same ambiguities in trying to interpret the high  $p_T$  suppression is as a conclusive signature of QGP formation: just as in the case of high  $p_T$  suppression, the production of these photons are only sensitive to the parton (mostly gluon) density, irregardless of whether those partons are confined within a hadron, hadron-like object, or other confined state. Nonetheless, since this signature comes from a distinct source, we should expect it to probe different systematics in the physical picture than the quenching, and so combined with suppression studies could yield a much more powerful statement than the suppression alone. Furthermore, since the source of this radiation comes from parton products of high  $Q^2$  hard collisions, the expected  $p_T$  window of observation naturally extends higher, making it easier to detect, depending on the relative size of the signal.

In Figure 8.17 we show how the prediction compares with our central 0-10% data set. The prediction for the sum of  $\gamma_{direct}$  from pQCD and this new source of high  $p_T$  photons agrees with the data points themselves remarkably well. However there are several caveats. First it should be noted that the pQCD calculation used by the authors in [89] is not the “authoritative” NLO pQCD prediction of [16] for the same  $p_T$  scale choice. This is not surprising since they used a LO calculation with a  $K$  factor of 2.5 to compensate for higher order effects and they used a different PDF

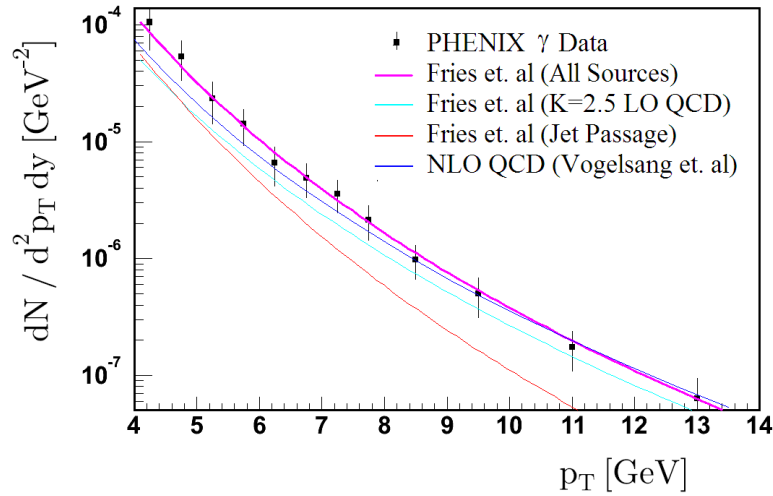


Figure 8.17: Comparison of PHENIX (this thesis) data, and prediction of hard photon enhancement from [89]. The NLO pQCD prediction [16] is also shown for comparison, and disagrees with the LO calculation used in [89].

set (CTEQ5L as opposed to the CTEQ6 set used by Vogelsang et.al. [16]). With the addition of the "Bremsstrahlung" component, the two calculations are similar but not identical. If we were to add the extra "Jet Passage" yield instead to the [16] predictions, it would no doubt throw the prediction above the data, but probably not by much, and considering our full systematic errors, it would certainly still be consistent, but the match would no longer be quite as spectacular. However, in any case, considering the uncertainties on the level of the pQCD predictions already discussed, we cannot really take this consistency too seriously.

On the other hand, since in [89], the same LO calculation was used as input to the Jet Passage calculation, upon input of the full NLO calculation, this contribution may change as well, so the total effect of doing so is not clear. Also, considering that the quark parents of this new type of hard photon are dominantly LO objects, we would expect the change to be small. Nonetheless in any case it would likely have the effect of moving the total sum prediction up at least by some small amount, and this would indeed worsen the current level of agreement.

Considering all these points, it is clear that in order to interpret whether we have

indeed discovered a new signature of the the QGP or lack thereof in this new source of photons with our current  $Au + Au$  dataset, at least two things are necessary. First just as with most of our other conclusions beyond demonstrating binary scaling, good  $p + p$  reference data is necessary. It is hoped that from a maturing current analysis of the 2003 Run3  $p + p$  dataset, this reference will be forthcoming soon. Secondly, if the  $p + p$  reference turns out to disagree with the QCD calculations in [89], these calculations should be re-run using the  $p_T$  scales, PDF sets, and the full NLO calculations that match the reference data the best. This could no doubt be done in conjunction with several other improvements to the calculations which the authors stated would be released in the future.

We should discuss one more thing: Namely, since this new source of photons is only expected to be present in central events where QGP formation is expected to be present, we should not expect the [89] calculations to agree as well in more peripheral bins. As Figure 8.18 shows, the “good” agreement of this calculation at a rough level seems to persist when compared to peripheral bins (albeit, with less constraint from the data) and also Minimum Bias. To put it another way, if the QGP only exists in central events, as is expected, we should see this relatively large enhancement appear as an increase going from peripheral to central events. Looking at our  $R_{CP}$  plots in section 8.2 (Figure 8.5) this does not appear to be case on the whole certainly above 5 GeV/c, albeit the contribution from this the new source should be smaller as we go higher in transverse momentum. This might weakly hint that either the enhancement from this source is not as large either absolutely or even relative to the pQCD baseline—which comparing it to the full NLO calculation would also seem to hint,—or the signal simply isn’t there.

On the other hand, the most central bin data is in excess of the prediction between 4-5 GeV/c by  $\sim 50\%$ . This same excess is not present in the peripheral bin or even Minimum Bias. Accounting for the possible increase in the total sum due to NLO effects we’ve already discussed, since the Jet-Passage photons are largest relative to the pQCD baselines here, this actually could be an indication that the

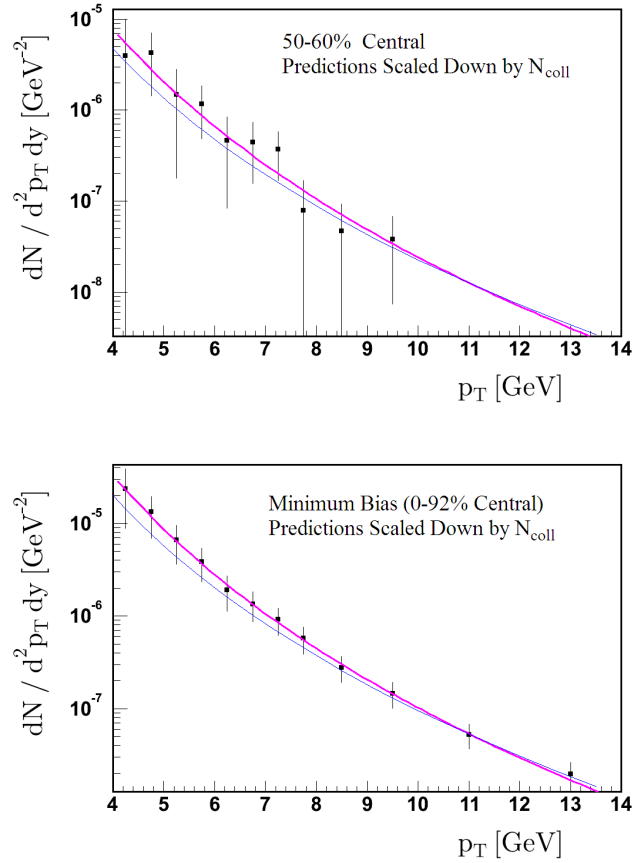


Figure 8.18: Again the prediction in [89] is compared to our data, but this time for other centrality bins. A similar level of matching is observed. The theoretical prediction should only work well in the most central events if a QGP is present. Therefore the excellent agreement between the prediction and the data in the central bin is probably an accident.

signal is present. Note that all thermal enhancement predictions do fall off quickly such that by 4 GeV there shouldn't be a contribution from them above 4 GeV/c. One potential source of enhancement above binary scaled pQCD in this  $p_T$  region is Cronin enhancement or some type of anti-shadowing. But in our discussions of scaling above, we pointed out that there may be evidence for a lack of a Cronin enhancement in our  $\gamma_{direct}$  looking across *all* centrality bins. Therefore we would have to conclude that our data favors some type of enhancement beyond that of either standard Cronin or commonly regarded thermal radiation in this region with

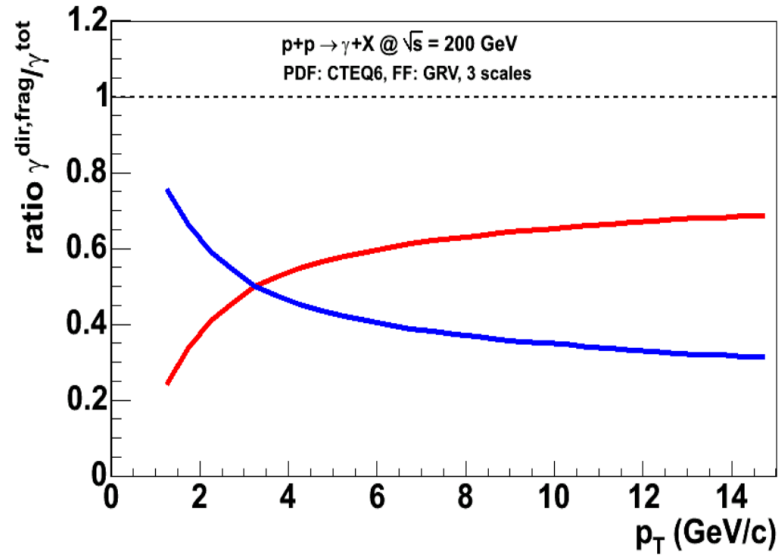


Figure 8.19: Fractions of direct (red) and Bremsstrahlung/fragmentation (photons) photons from the same NLO pQCD prediction [16].

very low significance and with albeit somewhat shaky arguments. Since this is one of the few remaining proposed sources of photons above the pQCD level which have been put forth so far for this  $p_T$  region, (although see our discussion of the Zakharov prediction for Bremsstrahlung below) the consequences of this statement could be exciting.

Whether the lack of centrality dependence above 5 GeV/ $c$  could be one of the few RHIC results that indicates a lack of the QGP formation, or whether this apparent insignificant excess amounts to one more signature in favor of QGP formation, would deserve both much more scrutiny of the calculations and all the assumptions used to derive it, and as always, improved smaller systematic uncertainties on our data set. Most likely the latter will need to wait until the new much larger most recent Run4 data set is available. The first step however, will be to get the  $p + p$  reference under control.

### 8.3.2 Suppression of Bremsstrahlung/Fragmentation Photons?

One question that must be addressed when interpreting the  $\gamma_{direct}$  data in  $Au + Au$  is the potential role of normal (NLO) Bremsstrahlung or Fragmentation photons. As discussed in the introduction, it turns out that such direct photons contribute to the total production cross section at nearly the same order as LO Compton and annihilation diagrams. Specifically, in Figure 8.19 we show the ratio of the different such contributions to the total spectra from the same NLO calculations we have been referring to in the previous section.

These fragmentation photons are important because it has been argued [116] *should* be suppressed since they come from the radiation of the same partons which presumably are parenting the suppressed mesons. Unfortunately such a suppression would not be significantly visible in our current dataset given its uncertainties. Even if the 20% were suppressed by a factor of 5, this would only be a drop of 15%, like the other uncertainties, this level of uncertainty doesn't change our conclusions. However factoring in this reduction, we may conclude that the enhancements hinted at in the data discussed in the previous section are actually slightly larger.

Given the uncertainties about using the pQCD calculations as a comparison reference, we can turn again to  $R_{CP}$  and  $R_{MB}$ . As demonstrated in section 8.2.4 above, these ratios are consistent with a small amount of suppression in the central data as compared to the more peripheral bins. Even though as already discussed there, the  $\sim 0.8$  value of  $R_{CP}$  above  $p_T$  of 6 GeV/c could very well be caused only by a fluctuation in the reference 50-60% centrality bin, looking at  $R_{MBC}$  in Figure 8.7, we again see a 5-10% excess above one which corresponds to a deficiency in the central compared to the binary scaled min bias data set. This systematic trend, though still consistent with no effect within the uncertainties may be interpreted as room for suppression of Bremsstrahlung photons to exist.

That there should be suppression in the fragmentation photons has generally been the accepted viewpoint for some time [116]. However recently Zakharov has

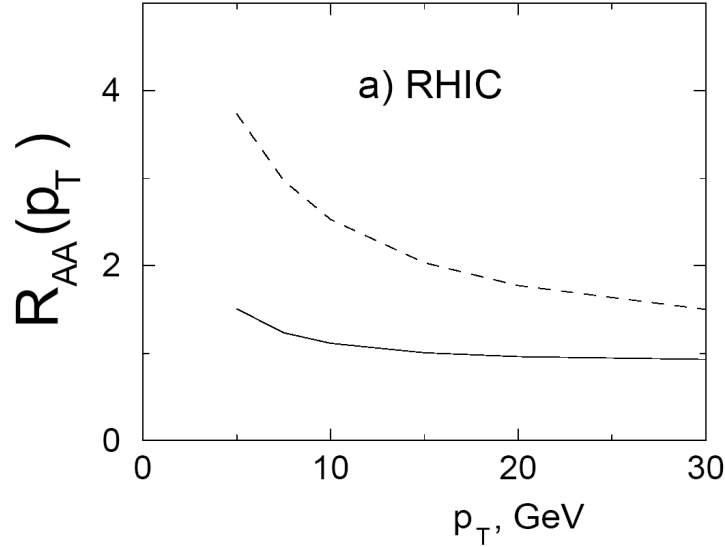


Figure 8.20: Prediction of medium-induced enhancement of Bremsstrahlung/fragmentation photons in the form of  $R_{AA}$  from [178].

called into question whether this should really be the case [178]. Using a light cone formulism he contends two points. First, he stresses the importance of the interplay between the photon and gluon formation lengths in the determination of when parton quenching occurs in relation to when EM bremsstrahlung does. He argues that since these two formation lengths are similar, a large portion of photon radiation will occur before gluon radiations, and hence before energy loss can have an effect. Therefore previous levels of suppression of Bremsstrahlung have been overestimated. Secondly, in a light cone wave-function formulism he adds an in medium fragmentation term to the normal fragmentation function which takes into account the same types of complicated quantum effects (*e.g.* LPM) in a manner similar to the BDPMS derivations of gluon radiation effects. This leads to a dramatic enhancement of the photonic Bremsstrahlung radiation demonstrated in a prediction for  $R_{AA}$  shown in Figure 8.20.

Note the qualitative similarities between this type of enhancement and the Jet-Passage enhancement of [89] discussed in the previous section. From a naive point of view the two sources of radiation seem quite similar. In fact the language used by Zakharov and the [89] authors is almost identical. As we've already stated, the

Jet Passage radiation should be considered distinct from normal NLO Bremsstrahlung because it involves scattering of real not virtual quark partons. However, because Zakharov uses a Beite-Heitler type approximation for his “Bremsstrahlung” it is not clear whether what Zakharov is in fact calling Bremsstrahlung includes or is even the same as the Jet-Passage radiation of [89]. In the Zakharov’s derivation, the same type of parton jet-photon conversion as in the Jet-Passage case is derived but by means of a fragmentation function which is strongly peaked at 1, whereas in [89] the conversion is argued on the basis of a commonly cited approximate behavior of the  $\propto \frac{u}{s} + \frac{s}{u}$  Compton and  $\propto \frac{u}{t} + \frac{t}{u}$  annihilation LO cross sections (which as we’ve seen in section 2.3.1, equation 2.9, also extends to NLO treatments as well). There are many other similarities in the two calculations, including the use of the same LO input distribution for the initial parton distribution.

Whether the two calculations do in fact amount to the same or overlapping effects we shall leave as an open question that should be resolved amongst the theorists. From our standpoint, the semi-classical nature of the [89] derivation would certainly make it seem possible. We should concern ourselves with how this prediction is compatible with the current data set. But in this regard, the similarities of the two prediction levels would lead us to the same conclusions as above in our discussion of the Jet-Passage contribution: the prediction is consistent with the actual absolute level of our measured central data points (compare central bins of Figure 8.14 with Figure 8.20), but is plagued by the same questions about the pQCD baseline and the lack of a substantial difference in the effect going from peripheral to more central events. On this latter point however, the Zakharov prediction may have an advantage in that as there is no explicit requirement in his derivation of a QGP *per se*, (by the same logic which renders high  $p_T$  suppression inconclusive as to QGP existence) we may expect these effects to persist in the higher centralities and therefore we might be less able to confirm or deny an effect like this by only looking at the top four or five 10% centrality bins where our uncertainties are relatively small. If the two calculations are completely distinct we would then add them

together. The lack of any apparent centrality dependence argument would then make the existence of both together slightly less favored given the current data set.

## 8.4 High(*er?*) $p_T$ $\pi^0$ Suppression

High- $p_T$  suppression was predicted in the early 1990's [168] and there are many models which provide quantitative predictions of the amount of suppression. These included basic absorption models which focused on the geometry of the collision the evolution of the matter created, more complicated treatments of the LPM effect e.g. [170]) as discussed in the introduction, and specific modifications (e.g. [45]) of the QCD fragmentation processes and nuclear parton distributions. Each of these models have certain distinctive signatures of how the energy loss will exhibit itself as a function of  $p_T$ . For example, it is expected in most models that as one approaches higher values of  $p_T$  the partons which would otherwise be quenched will have sufficient "escape" energy that they will no longer be quite as suppressed. In these models, energy loss  $dE/dx$  is taken to be proportional to a constant value. This implies a strong  $p_T$  dependence of the suppression as mesons from parent partons of higher and higher energy will be suppressed less and less proportionately. Even in some of the more complicated treatments [169], [104], the energy dependence of  $dE/dx$  is often found to be proportional to  $\log E$  such that a similar  $p_T$  dependence would be expected.

One of the major experimental results of the original high  $p_T$  suppression results was that the suppression appeared to be constant with  $p_T$  implying an overall energy dependence for  $dE/dx$  that is proportional to  $E$  itself. Such a behavior was predicted by the GLV model and can also be accounted for in the calculations of Wang [104]. However in the case of the latter, the  $p_T$  independence is only predicted if a complicated *detailed balance* of stimulated emission and absorption is invoked in their LPM coherence calculation approximation. Whether or not this effect is important determines whether or not the calculations of  $R_{AA}$  suppression will be  $p_T$  independent. Since the RHIC suppression appears to be relatively constant with

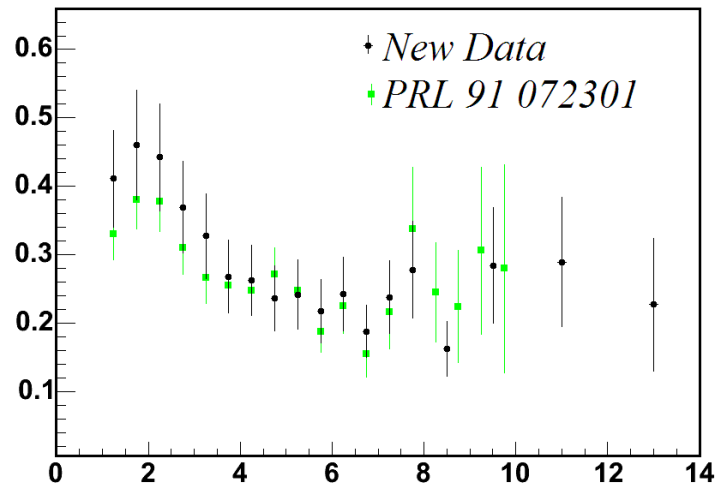


Figure 8.21: Comparison of new data points for  $R_{AA}$  (from this thesis) with that of the previously published PHENIX result [69].

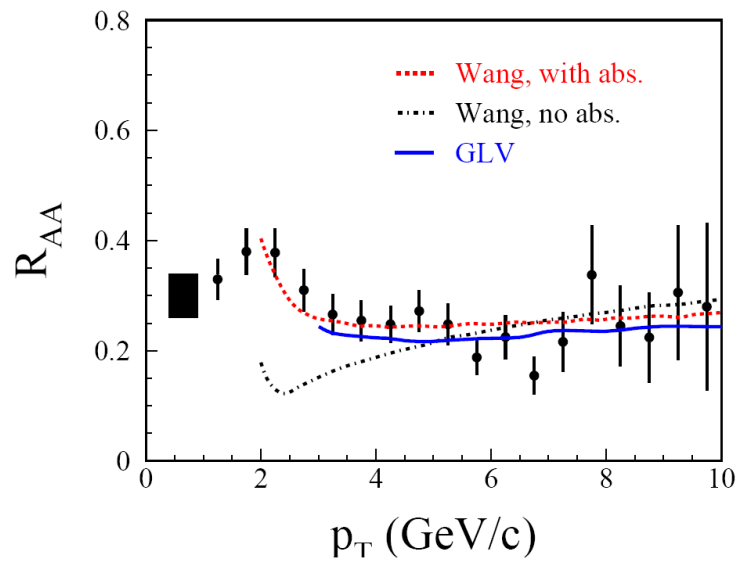


Figure 8.22: Comparison plot of  $R_{AA}$  predictions from suppression models [104] and [105] against the same PHENIX result [69].

$p_T$ , the detailed balance contribution was deemed to be important and both the GLV and Wang with absorption included are generally believed to provide accurate descriptions of the suppression pattern.

What can our new  $\pi^0$  data contribute to this situation? The answer is not too much, but there are some small questions that can be addressed. These fall into two main areas. First in the old PHENIX  $\pi^0$  dataset as shown in 8.21, there was a slight hint that  $R_{AA}$  might be starting to rise. Such a rise might cause a rethinking of the success of the  $p_T$  independent calculations. Specifically in the case of the Wang prediction, the detailed balance effect goes away for higher and higher energies, so measuring this higher  $p_T$  suppression area could put more constraints on the level at which the effect contributes. The second place where the new data can help is by constraining the GLV model's estimates of the gluon density,  $dN_g/dy$ , as this calculation is sensitive to this as an input parameter. Reduced uncertainties due to the inclusion of the new statistics in our data can further constrain these values.

As the figure shows, the new data denies the previous hints of a rise and continues to show an  $R_{AA}$  that is  $p_T$  independent (at a value of approximately 1/5). Therefore the previous conclusions about the success of the GLV model, which as shown in the figure has already made definite predictions all the way out to  $p_T = 20\text{GeV}/c$  are strengthened. The implications with regard to the Wang inclusion of detailed balance, also seem to be strengthened, and constraints on the importance of the detailed balance energy absorption become slightly more improved. For example, while one may have argued previously that *both* Wang predictions, with and without the absorption were still consistent with the data above  $\sim 6\text{GeV}/c$ , the new data points now favor the absorption model even more strongly. Also, clearly models with energy independent or nearly independent  $dE/dx$  are more strongly disfavored considering the newer high  $p_T$  points.

## 8.5 Au+Au: An Ideal $\gamma_{direct}$ Laboratory?

The suppression of the  $\pi^0$  and other meson decay photons ( $\eta$  has been more or less verified as well with other PHENIX preliminary data) leads to a new phenomena which is interesting on its own right. This is the intrinsic enhancement of the signal to background level. In Figure 8.23 we demonstrate the  $\gamma_{direct}$  over  $\pi^0$  ratios *measured* in 200 GeV  $Au + Au$ . Comparing to Figure 8.24 one can see that at for the same  $x_T$  value this ratio is greatly enhanced in  $Au + Au$  central events, by the same factor of the suppression  $\sim 5$ .

There are two interesting things about this ratio. First as a signature of the suppression/medium effects, there is no need to refer to  $p + p$  references.

Looking towards the future, this phenomena may have very interesting implications for physics at the LHC. This is because photon decay of the Higgs meson is expected to be a detection channel. It very well may turn out that in the future, the suppression of the jet meson decay background can be reduced substantially by looking for the Higgs in Heavy Ion collisions.

The phenomena of direct photon enhancement relative to meson suppression, may also have interesting implication for verification of the Color Glass Condensate at forward rapidity. Right now, suppression of forward rapidity mesons in  $d + Au$  collisions is being touted as potential evidence of CGC existence. Since the direct photon production is sensitive to the gluon distribution in a slightly different way, measurement of  $\gamma_{direct}$  there could provide strong constraints, and possibly a way to unambiguously distinguish CGC physics from other shadowing calculations.

## 8.6 Summary and Restatement of Conclusions

Using our results, which were aided by the inclusion of new statistics from a trigger data sample, and include the first positive direct photon ( $\gamma_{direct}$ ) measurement in  $Au + Au$  at  $\sqrt{s_{NN}} = 200$  GeV over 10 centrality bins, and reduced statistical uncertainties and greater  $p_T$  reach of a new  $\pi^0$  result, we have been able demonstrate

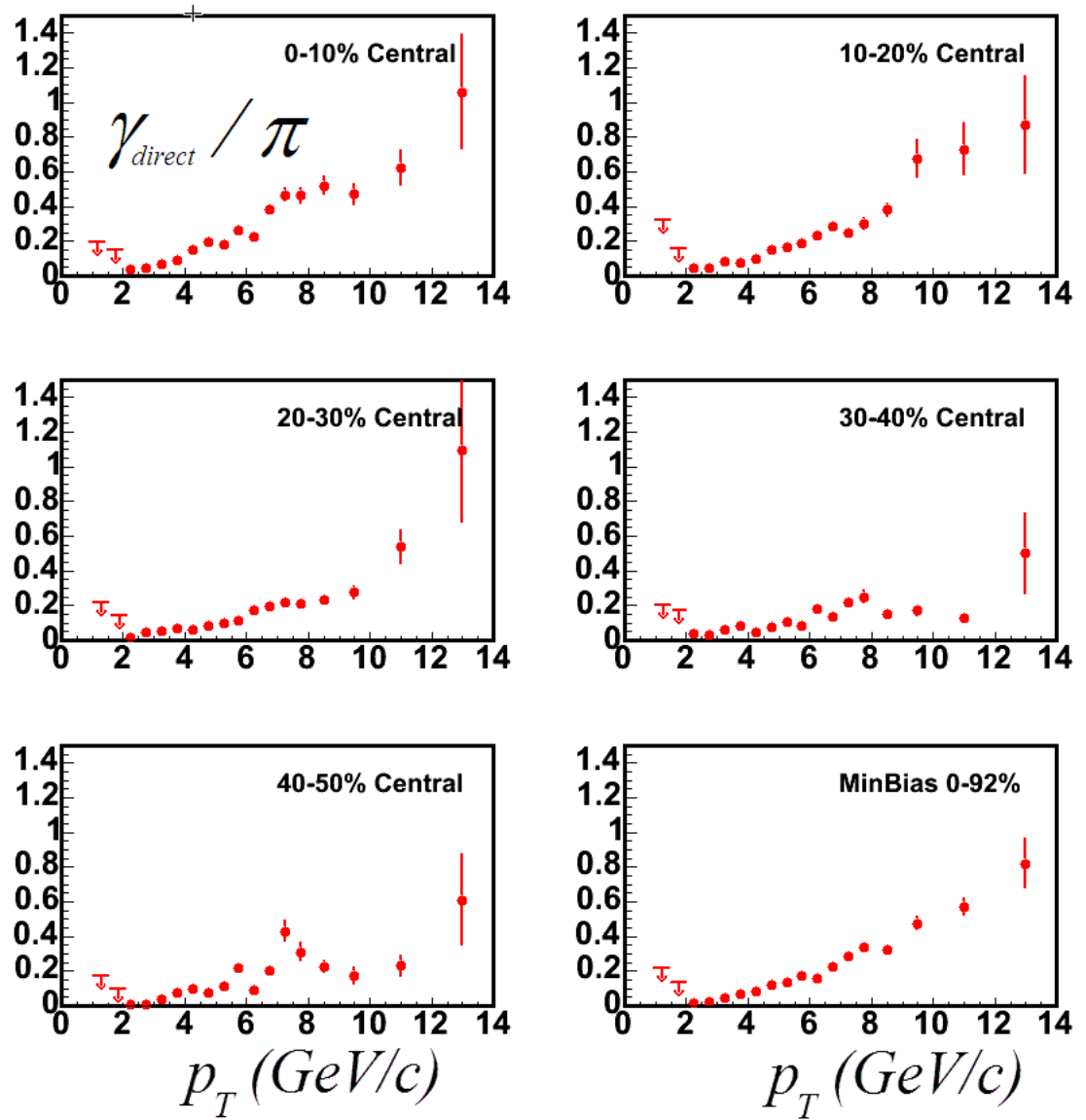


Figure 8.23:  $\gamma/\pi^0$  Ratio in our data. Significant enhancement is seen in this ratio. Hence the title of this thesis.

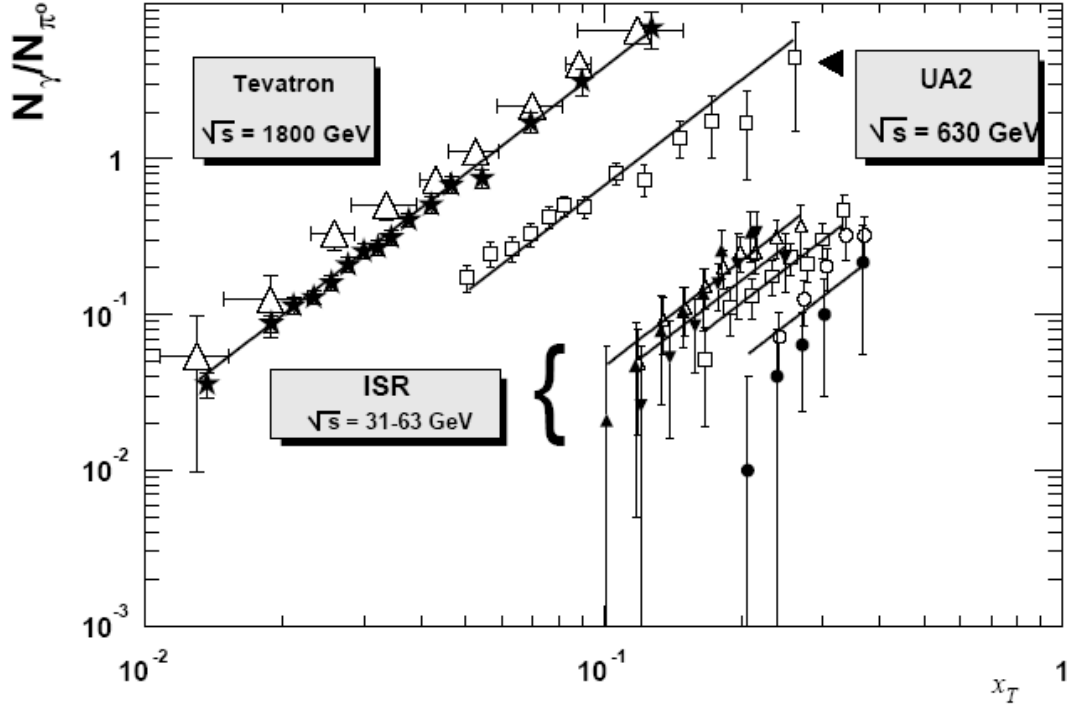


Figure 8.24:  $\gamma$  to  $\pi^0$  ratios at various energies. Such a large value of this ratio at this value of  $x_T$  would normally only be seen at higher  $\sqrt{s}$ . Figure taken from [36].

several important assertions:

- Foremost we've been able to contrast the behavior of high  $p_T$  meson production suppression with that of direct photons in the same transverse momentum regime which do not show the same suppression behavior. At the most basic qualitative level, this contrast is visible in comparing the spectral shapes between peripheral and central: for  $\pi^0$  there is a noticeable difference, for  $\gamma_{direct}$ , within larger systematics, does not appear to be pronounced if present at all.
- More quantitatively,  $\gamma_{direct}$  and  $\pi^0$  yields as a function of  $p_T$  are scaled in different centrality bins by the appropriate nuclear thickness and compared amongst themselves in ratios, such as  $R_{CP}$  and our new invention, " $R_{MBC}$ ". In all cases, the direct photon production scaling ratio is consistent with the

thickness scaling assumption—that is, the various  $R$ 's are consistent with 1. The ratio data points are consistent with 1 within  $\sim 15\%$  and within  $\sim 30\%$  at the 90% confidence level considering all uncertainties. On the other hand, the  $\pi^0$  production strongly deviates from the scaling with unambiguous significance. For the most central events this deviation is as large  $\sim 75\%$ , a factor of  $\sim 4$  suppression, at the  $> 7$  sigma level.

- Also quantitatively, in an observation of the total collected yields as a function of nuclear overlap  $T_{AA}$  the same message is demonstrated clearly and convincingly. The direct photons show a nearly perfect linear scaling with  $T_{AA}$  having a measured Cronin  $\propto T_{AA}^\alpha$   $\alpha$  parameter of  $0.96 \pm 0.06$ . In addition, the direct side by side observation of the thickness scaling between the  $\gamma_{direct}$  and  $\pi^0$  shows the same scaling for  $\pi^0$  in the most peripheral bins before suppression sets in substantially.

In the context of previous  $d + Au$  results also showing a lack of suppression in hard meson production, these direct photon measurements represent the final necessary and possibly the best available confirmation of the conclusion that the aforementioned effect is not due to differences in initial state hard-scattering, but rather, is due to a final state medium which quenches hard quarks and gluons, but not hard direct photons. Direct photons obey binary collision scaling while mesons are suppressed. This conclusion is consistent with predicted final state modifications [171] to jet formation due to a new phenomena, and possibly a QGP.

In addition, other types of interesting information about direct photon and high  $p_T$   $\pi^0$  production Heavy Ion was explored with the data set.

For  $\gamma_{direct}$ , a  $p + p$  reference was not measured. However using NLO pQCD predictions in place of  $p + p$  reference data, the nuclear modification ratio  $R_{AA}$  was constructed. Its value is consistent with 1 within  $\sim 10\%$  on average and within  $\sim 30\%$  at the 90% confidence level for  $p_T > 6$  GeV/c ( $x_T > 0.06$ ). Comparing to the  $\pi^0$  suppression ( $R_{AA}$ ) value of  $\sim 0.2$  this also confirms our previous statements about thickness scaling in  $\gamma_{direct}$  production and lack thereof for the  $\pi^0$ . Furthermore it

shows that NLO pQCD can describe our data well in this  $p_T$  region without resorting to  $k_T$  phenomenological smearing methods. For  $p_T < 6 \text{ GeV}/c$  however, a trend, though barely significant within the larger uncertainties, shows a disagreement with the NLO pQCD prediction as large as  $\sim 300\%$ . If this trend is real, it is likely not to be due primarily to final-state medium (*e.g.* QGP) effects, since it is observed across all centrality bins where the signal is resolvable including peripheral collisions where the  $\pi^0$  final state suppression is already small. Therefore for  $p_T < 6 \text{ GeV}/c$  ( $x_T < 0.06$ ), these deviations could indicate the need for  $k_T$ -like modifications to the QCD calculations in order to account for soft gluon radiation.

Due to reduced statistical uncertainties and the increased  $p_T$  reach (+ 4 GeV/c) in the most central 0-10% fraction of events, the possible model-generated mechanisms for this suppression are constrained further by our updated  $\pi^0 R_{AA}$  results. These  $R_{AA}$  results exhibit more strongly than before the strong energy dependence of the suppression ( $\Delta E \propto E$ ) with a  $p_T$ -independence that extends to 14 GeV/c with smaller uncertainties than the previous measurements.

Finally, the direct photon invariant yields mainly in the low ( $p_T < 3 \text{ GeV}/c$ ) region are compared to predictions of enhancement and suppression due to QGP medium effects. While large uncertainties in both experimental systematics and the inclusive QCD  $\gamma_{direct}$  prediction do not allow any definite conclusions, we compare models in two different low  $p_T$  regions:

- At high  $p_T$  ( $> 6 \text{ GeV}/c$ ) the ratios of thickness scaled production in different centrality bins  $R_{CP}$  and  $R_{MBC}$  show a trend consistent with a small amount of suppression ( $< 20\%$ ) as in the original predictions (*e.g.* [116]) for suppression for fragmentation/Bremstrahlung photons, but within the systematic errors the data points are also consistent with no such suppression. Also arguments of binary collision scaling concluded above also disfavor this possibility but do not rule it out.
- In the mid-  $p_T$  ( $3 < p_T < 6 \text{ GeV}/c$ ) region we compare with two models of new mechanisms of hard photon enhancement that assume the existence of a QGP

[89],[178]. The [89] prediction is found to fit the measured direct photon production rates in the most central events very well. However, large systematic errors in the data, in the pQCD predictions used in the model calculation, and a similar level of agreement between the data and model in peripheral events, imply that this potential signature of the QGP cannot be confirmed or denied. The same is true of the [178] medium-induced Bremsstrahlung prediction since it is quite similar in magnitude.

- In the low  $p_T$  region ( $p_T < 3$  GeV/c) various calculations of thermal quark and hot-hadron gas radiation are compared to the data. The systematic uncertainties of the data much larger in this region cannot exclude any of these predictions, which themselves do not seem to be in a stable theoretical state.

In both cases, the improvements necessary to make more definite conclusions about thermal or other direct photon enhancement are made apparent and noted.

In summary, the ability to compare high  $p_T$  meson production in the  $\pi^0$  with the direct photon rates in the same hard regime is found to be a fruitful endeavor. Direct photons themselves represent an interesting probe of Heavy Ion collisions over all  $p_T$  ranges measured.

# Bibliography

- [1] Connecting quarks with the cosmos: Eleven science questions for the new century. Washington, USA: Nat. Acad. Pr. (2003) 206 p.
- [2] 2003. A comprehensive overview of RHIC and its detectors is available in a dedicated issue of *Nucl. Instr. and Meth.* **A499**, Issues 2-3, Pages 235-880 (1 March 2003) The Relativistic Heavy Ion Collider Project: RHIC and its Detectors, M. Harrison, T. Ludlam and S. Ozaki, ed.
- [3] M. C. Abreu et al. J / psi and drell-yan cross-sections in pb pb interactions at 158 gev/c per nucleon. *Phys. Lett.*, B410:327–336, 1997.
- [4] Alberto Accardi. Cronin effect in proton nucleus collisions: A survey of theoretical models. 2002.
- [5] D. Adams et al. Measurement of the spin dependent structure function  $g_1(x)$  of the proton. *Phys. Lett.*, B329:399–406, 1994.
- [6] J. Adams et al. Transverse momentum and collision energy dependence of high  $p(t)$  hadron suppression in au + au collisions at ultrarelativistic energies. *Phys. Rev. Lett.*, 91:172302, 2003.
- [7] J. Adams et al. Multi-strange baryon production in au au collisions at  $\sqrt{s_{nn}} = 130$ -gev. *Phys. Rev. Lett.*, 92:182301, 2004.
- [8] K. Adcox. Formation of dense partonic matter in relativistic nucleus nucleus collisions at rhic: Experimental evaluation by the phenix collaboration. 2004.

- [9] K. Adcox et al. <http://www.phenix.bnl.gov/WWW/publish/zajc/sp/presentations/RBUPAug02/>.
- [10] K. Adcox et al. Centrality dependence of charged particle multiplicity in au au collisions at  $s(n n)^{1/2} = 130$ -gev. *Phys. Rev. Lett.*, 86:3500–3505, 2001.
- [11] K. Adcox et al. Suppression of hadrons with large transverse momentum in central au + au collisions at  $s^{1/2}(n n) = 130$ -gev. *Phys. Rev. Lett.*, 88:022301, 2002.
- [12] K. Adcox et al. Phenix central arm tracking detectors. *Nucl. Instrum. Meth.*, A499:489–507, 2003.
- [13] K. Adcox et al. Single identified hadron spectra from  $s(nn)^{1/2} = 130$ -gev au + au collisions. *Phys. Rev.*, C69:024904, 2004.
- [14] S. S. Adler, , et al. Absence of suppression in particle production at large transverse momentum in  $\sqrt{s}[\text{sub nn}] = 200$  gev d + au collisions. *Physical Review Letters*, 91(7):072303, 2003.
- [15] S. S. Adler. High-p(t) charged hadron suppression in au + au collisions at  $s(nn)^{1/2} = 200$ -gev. *Phys. Rev.*, C69:034910, 2004.
- [16] S. S. Adler et al. Private communication.
- [17] S. S. Adler et al. Mid-rapidity neutral pion production in proton proton collisions at  $s^{1/2} = 200$ -gev. *Phys. Rev. Lett.*, 91:241803, 2003.
- [18] S. S. Adler et al. Mid-rapidity neutral pion production in proton proton collisions at  $s^{1/2} = 200$ -gev. *Phys. Rev. Lett.*, 91:241803, 2003.
- [19] S. S. Adler et al. Phenix on-line systems. *Nucl. Instrum. Meth.*, A499:560–592, 2003.
- [20] S. S. Adler et al. Jet structure of baryon excess in au + au collisions at  $s(nn)^{1/2} = 200$ -gev. 2004.

- [21] S. S. Adler et al. Jet structure of baryon excess in au + au collisions at  $s(\text{nn})^{1/2} = 200\text{-gev}$ . 2004.
- [22] T. L. Ainsworth, E. Baron, G. E. Brown, J. Cooperstein, and M. Prakash. Equation of state of dense nuclear matter. *Nucl. Phys.*, A464:740–768, 1987.
- [23] R. Albrecht et al. Production of eta mesons in 200-a/gev s + s and s + au reactions. *Phys. Lett.*, B361:14–20, 1995.
- [24] R. Albrecht et al. Transverse momentum distributions of neutral pions from nuclear collisions at 200-a-gev. *Eur. Phys. J.*, C5:255–267, 1998.
- [25] J. Alitti et al. A measurement of the direct photon production cross-section at the cern anti-p p collider. *Phys. Lett.*, B263:544–550, 1991.
- [26] B. Alper et al. Production of high transverse momentum particles in p p collisions in the central region at the cern isr. *Phys. Lett.*, B44:521–526, 1973.
- [27] G. Alverson et al. Production of direct photons and neutral mesons at large transverse momenta by pi- and p beams at 500-gev/c. *Phys. Rev.*, D48:5–28, 1993.
- [28] Bo Andersson, G. Gustafson, G. Ingelman, and T. Sjostrand. Parton fragmentation and string dynamics. *Phys. Rept.*, 97:31, 1983.
- [29] A. L. S. Angelis et al. Large transverse momentum pi0 production in alpha alpha d d and p p collisions at the cern isr. *Phys. Lett.*, B185:213, 1987.
- [30] J. Antille et al. A measurement of the inclusive pi0 and eta production cross-sections at high p(t) in p anti-p and p p collisions at  $s^{1/2} = 24.3\text{-gev}$ . *Phys. Lett.*, B194:568, 1987.
- [31] D. Antreasyan et al. Production of hadrons at large transverse momentum in 200- gev, 300-gev and 400-gev p p and p n collisions. *Phys. Rev.*, D19:764, 1979.

- [32] L. Apanasevich et al. Examination of direct photon and pion production in proton nucleon collisions. *Phys. Rev.*, D63:014009, 2001.
- [33] L. Apanasevich et al. Measurement of direct photon production at tevatron fixed target energies. 2004.
- [34] L. Apanasevich et al. Production of pi0 and eta mesons at large transverse momenta in pi- p and pi- be interactions at 515-gev/c. *Phys. Rev.*, D69:032003, 2004.
- [35] Private Communication Apanasevich, Begel. calculations of kt smearing at 200 gev from the code of owens and qiu.
- [36] Enterria Martinez et.al. Aphecetche, Delgrange. Alice internal analysis note alice-int-2002-02: Predictions for high pt and pi0 production at alice/lhc.
- [37] L. Aphecetche et al. Phenix calorimeter. *Nucl. Instrum. Meth.*, A499:521–536, 2003.
- [38] L. et. al. Aphecetche. Phenix internal analysis note 203.
- [39] M. Arneodo et al. The a dependence of the nuclear structure function ratios. *Nucl. Phys.*, B481:3–22, 1996.
- [40] Michele Arneodo. Nuclear effects in structure functions. *Phys. Rept.*, 240:301–393, 1994.
- [41] P. Aurenche, F. W. Bopp, and J. Ranft. Particle production in hadron hadron collisions at collider energies in an exclusive multistring fragmentation model. *Z. Phys.*, C23:67–76, 1984.
- [42] P. Aurenche, M. Fontannaz, J. P. Guillet, Bernd A. Kniehl, and M. Werlen. Large p(t) inclusive pi0 cross-sections and next-to- leading-order qcd predictions. *Eur. Phys. J.*, C13:347–355, 2000.

- [43] P. Aurenche, F. Gelis, R. Kobes, and H. Zaraket. Bremsstrahlung and photon production in thermal QCD. *Phys. Rev.*, D58:085003, 1998.
- [44] T. C. Awes et al. Search for direct photon production in 200-a-gev s + au reactions: A status report. *Nucl. Phys.*, A590:81c–91c, 1995.
- [45] R. Baier, Yuri L. Dokshitzer, Alfred H. Mueller, and D. Schiff. Quenching of hadron spectra in media. *JHEP*, 09:033, 2001.
- [46] R. Baier, Yuri L. Dokshitzer, S. Peigne, and D. Schiff. Induced gluon radiation in a qcd medium. *Phys. Lett.*, B345:277–286, 1995.
- [47] G. G. Barnafoldi, G. Papp, P. Levai, and George I. Fai. Nuclear reaction mechanisms and the cronin effect. 2003.
- [48] Steffen A. Bass, Berndt Muller, and Dinesh K. Srivastava. Transverse momentum distribution of net baryon number at rhic. *J. Phys.*, G29:L51–L58, 2003.
- [49] Francesco Becattini. A thermodynamical approach to hadron production in e+ e- collisions. *Z. Phys.*, C69:485–492, 1996.
- [50] M. Begel. Photons and diphotons from e706. *Nucl. Phys. Proc. Suppl.*, 79:244–246, 1999.
- [51] M. Berger et al. Xcom photon cross section database. *www.physics.nist.gov*.
- [52] S. M. Berman, J. D. Bjorken, and John B. Kogut. Inclusive processes at high transverse momentum. *Phys. Rev.*, D4:3388, 1971.
- [53] J. D. Bjorken. Can we measure parton parton cross-sections? *Phys. Rev.*, D8:4098, 1973.
- [54] J. D. Bjorken. Highly relativistic nucleus-nucleus collisions: The central rapidity region. *Phys. Rev.*, D27:140–151, 1983.

- [55] R. E. Blair. Tevatron photon measurements. Prepared for 8th International Workshop on Deep Inelastic Scattering and QCD (DIS 2000), Liverpool, England, 25-30 Apr 2000.
- [56] Richard Blankenbecler, Stanley J. Brodsky, and J. F. Gunion. Inclusive processes at high transverse momentum. *Phys. Lett.*, B42:461, 1972.
- [57] D. Boyanovsky and H. J. de Vega. Are direct photons a clean signal of a thermalized quark gluon plasma? *Phys. Rev.*, D68:065018, 2003.
- [58] E. L. Bratkovskaya, W. Cassing, and U. Mosel. Meson  $m(t)$ -scaling in heavy-ion collisions at sis energies. *Phys. Lett.*, B424:244–252, 1998.
- [59] Raymond Brock et al. Handbook of perturbative qcd: Version 1.0. *Rev. Mod. Phys.*, 67:157–248, 1995.
- [60] R. Brun, R. Hagelberg, M. Hansroul, and J. C. Lassalle. Geant: Simulation program for particle physics experiments. user guide and reference manual. CERN-DD-78-2-REV.
- [61] R. Brun, F. Rademakers, and S. Panacek. Root, an object oriented data analysis framework. Prepared for CERN School of Computing (CSC 2000), Marathon, Greece, 17-30 Sep 2000.
- [62] G. J. H. Burgers, C. Fuglesang, R. Hagedorn, and V. Kuvshinov. Multiplicity distributions in hadron interactions derived from the statistical bootstrap model. *Z. Phys.*, C46:465–480, 1990.
- [63] M. Chiu. A comparison of jet properties between p+p,d+au,and au+au collisions at rhic using photon-hadron angular correlation measurements. *Columbia University Doctoral Dissertation*.
- [64] Mickey et. al. Chiu. Phenix internal analysis note 014.

- [65] N. H. Christ, R. Friedberg, and T. D. Lee. Random lattice field theory: General formulation. *Nucl. Phys.*, B202:89, 1982.
- [66] Harry Contopanagos and Edmond L. Berger. Perturbative resummation of gluon radiation for top quark production. Presented at Top Quark Workshop, Ames, IA, 25-26 May 1995.
- [67] J. W. Cronin et al. Production of hadrons with large transverse momentum at 200-gev, 300-gev, and 400-gev. *Phys. Rev.*, D11:3105, 1975.
- [68] Lucy de Barbaro et al. Parton distributions working group. 2000.
- [69] David d'Enterria. High-p(t) pi0 suppression in au + au collisions at  $s(\text{nn})^{1/2} = 200\text{-gev}$ . *Nucl. Phys.*, A715:749–752, 2003.
- [70] David et. al. d'Enterria. Phenix internal analysis note 337.
- [71] S. Digal, S. Fortunato, P. Petreczky, and H. Satz. Parton percolation and j/psi suppression. *Phys. Lett.*, B549:101–108, 2002.
- [72] Magdalena Djordjevic and Miklos Gyulassy. Heavy quark radiative energy loss: Applications to rhic. *J. Phys.*, G30:S1183–S1188, 2004.
- [73] Yuri L. Dokshitzer and D. E. Kharzeev. Heavy quark colorimetry of qcd matter. *Phys. Lett.*, B519:199–206, 2001.
- [74] A. Dumitru, L. Frankfurt, L. Gerland, H. Stoecker, and M. Strikman. Nuclear broadening effects on hard prompt photons at cern- sps and bnl-rhic energies. *Phys. Rev.*, C64:054909, 2001.
- [75] S. Eidelman et al. Review of particle physics. *Phys. Lett.*, B592:1, 2004.
- [76] David et.al. Enterria. Phenix internal analysis note 200.
- [77] K. J. Eskola, H. Honkanen, V. J. Kolhinen, P. V. Ruuskanen, and C. A. Salgado. Nuclear parton distributions in the dglap approach. 2001.

- [78] K. J. Eskola, K. Kajantie, and K. Tuominen. Centrality dependence of multiplicities in ultrarelativistic nuclear collisions. *Phys. Lett.*, B497:39–43, 2001.
- [79] K. J. Eskola and J. Lindfors. Rescattering production of dileptons in nucleus-nucleus collisions. *Z. Phys.*, C46:141, 1990.
- [80] K. J. Eskola, P. V. Ruuskanen, S. S. Rasanen, and K. Tuominen. Multiplicities and transverse energies in central a a collisions at rhic and lhc from pqed, saturation and hydrodynamics. *Nucl. Phys.*, A696:715–728, 2001.
- [81] S. Bazilevsky et. al. Preliminary results from  $\pi^0$  measurements in p-p collisions at 200 gev from run-3. *PHENIX Analysis Note 224*.
- [82] Glennys R. Farrar and Steven C. Frautschi. Copious direct photon production as a possible resolution of the prompt lepton puzzle. *Phys. Rev. Lett.*, 36:1017, 1976.
- [83] A. Fasso et al. The physics models of fluka: Status and recent development. *ECONF*, C0303241:MOMT005, 2003.
- [84] Z. Fodor and S. D. Katz. A new method to study lattice qcd at finite temperature and chemical potential. *Phys. Lett.*, B534:87–92, 2002.
- [85] Justin Frantz. Phenix direct photons in 200-gev p + p and au + au collisions. *J. Phys.*, G30:S1003–S1006, 2004.
- [86] J. H. Friedman. Data analysis techniques for high energy particle physics proceedings of the 1974 cern school of computing. *CERN Report*, 74-23.
- [87] Jerome I. Friedman and Henry W. Kendall. Deep inelastic electron scattering. *Ann. Rev. Nucl. Part. Sci.*, 22:203–254, 1972.
- [88] R. J. Fries. Recombination models. *J. Phys.*, G30:S853–S860, 2004.

- [89] Rainer J. Fries, Berndt Muller, and Dinesh K. Srivastava. High energy photons from passage of jets through quark gluon plasma. *Phys. Rev. Lett.*, 90:132301, 2003.
- [90] H. Fritzsche and P. Minkowski. Measuring qcd compton effects. *Phys. Lett.*, B69:316, 1977.
- [91] T. A. Gabriel. Calor89: The code system for calorimeter analysis and design. Presented at Workshop on Calorimetry for the Superconducting Super Collider, Tuscaloosa, AL, Mar 13-17, 1989.
- [92] C. Gale and Joseph I. Kapusta. Dilepton radiation from high temperature nuclear matter. *Phys. Rev.*, C35:2107–2116, 1987.
- [93] Klaus Geiger and Berndt Muller. How dense does parton matter get in pb + pb collisions at the cern sps? *Heavy Ion Phys.*, 7:207–214, 1998.
- [94] Murray Gell-Mann. A schematic model of baryons and mesons. *Phys. Lett.*, 8:214–215, 1964.
- [95] Walter T. Giele, Stephane A. Keller, and David A. Kosower. Parton distribution function uncertainties. 2001.
- [96] R. J. Glauber. Cross-sections in deuterium at high-energies. *Phys. Rev.*, 100:242–248, 1955.
- [97] W. Greiner and A. Schafer. Theoretical physics. vol. 10: Quantum chromodynamics. (in german). THUN, SWITZERLAND: DEUTSCH (1989) 445 P. (THEORETICAL PHYSICS, 10).
- [98] D. J. Griffiths. Introduction to elementary particles. NEW YORK, USA: WILEY (1987) 392p.

- [99] K. Guettler et al. Inclusive production of low momentum charged pions, kaons, and protons at  $x = 0$  at the cern intersecting storage rings. *Nucl. Phys.*, B116:77, 1976.
- [100] Joao Pedro Barreiro Guimaraes da Costa. Search for a fourth generation quark more massive than the  $z_0$  boson in proton anti-proton collisions at  $s^{*(1/2)} = 1.8\text{-tev}$ . FERMILAB-THESIS-2000-31.
- [101] Xiao-feng Guo and Xin-Nian Wang. Multiple scattering, parton energy loss and modified fragmentation functions in deeply inelastic e a scattering. *Phys. Rev. Lett.*, 85:3591–3594, 2000.
- [102] M. Gyulassy. What have we learned at rhic? *J. Phys.*, G30:S911–S918, 2004.
- [103] Miklos Gyulassy, Peter Levai, and Ivan Vitev. Jet quenching in thin plasmas. *Nucl. Phys.*, A661:637–640, 1999.
- [104] Miklos Gyulassy, Ivan Vitev, Xin-Nian Wang, and Ben-Wei Zhang. Jet quenching and radiative energy loss in dense nuclear matter. 2003.
- [105] Miklos Gyulassy, Ivan Vitev, Xin-Nian Wang, and Ben-Wei Zhang. Jet quenching and radiative energy loss in dense nuclear matter. 2003.
- [106] R. Hagedorn. Ultimate temperature and the structure of elementary particles. *Progr.Sci.Culture* 1 (1976) 395-411.
- [107] K. Haglin, S. Das Gupta, and C. Gale. A case study in intermittency: The thermodynamic model for intermediate-energy heavy ion collisions. *Nucl. Phys.*, A538:129C–138C, 1992.
- [108] Kevin Lee Haglin. Rate of photon production from hot hadronic matter. *J. Phys.*, G30:L27–L33, 2004.
- [109] Peter Hasenfratz and Julius Kuti. The quark bag model. *Phys. Rept.*, 40:75–179, 1978.

- [110] R. W. Hasse and W. D. Myers. Geometrical relationships of macroscopic nuclear physics. BERLIN, GERMANY: SPRINGER (1988) 141 P. (SPRINGER SERIES IN NUCLEAR AND PARTICLE PHYSICS).
- [111] E. Hoffmann and E. Reya. Quantum chromodynamic higher order contributions to deep inelastic scaling violations. *Phys. Rev.*, D27:2630, 1983.
- [112] D. Holmgren, A. Singh, P. Mackenzie, J. Simone, and Steven A. Gottlieb. Lattice qcd production on commodity clusters at fermilab. *ECONF*, C0303241:TUIT004, 2003.
- [113] Rudolph C. Hwa and C. B. Yang. Recombination of shower partons in fragmentation processes. *Phys. Rev.*, C70:024904, 2004.
- [114] J. D. Jackson. Criticism of 'necessity of simultaneous co-existence of instantaneous and retarded interactions in classical electrodynamics'. *Int. J. Mod. Phys.*, A17:3975–3979, 2002.
- [115] Robert L. Jaffe and Frank Wilczek. Diquarks and exotic spectroscopy. *Phys. Rev. Lett.*, 91:232003, 2003.
- [116] J. Jalilian-Marian, K. Orginos, and I. Sarcevic. Prompt photons at rhic. *Phys. Rev.*, C63:041901, 2001.
- [117] F. James and M. Roos. 'minuit' a system for function minimization and analysis of the parameter errors and correlations. *Comput. Phys. Commun.*, 10:343–367, 1975.
- [118] Jiangyong Jia. High-pt charged hadron suppression in auau collisions. *Ph.D Thesis*, 89, 2003.
- [119] K. Johnson. The m.i.t. bag model. *Acta Phys. Polon.*, B6:865, 1975.
- [120] P. G. Jones et al. Hadron yields and hadron spectra from the na49 experiment. *Nucl. Phys.*, A610:188c–199c, 1996.

- [121] Masashi Kaneta. Event anisotropy of identified  $\pi^0$ , photon and electron compared to charged  $\pi$ ,  $k$ ,  $p$  and deuteron in  $s(\text{nn})^{1/2} = 200\text{-gev}$  au + au at phenix. *J. Phys.*, G30:S1217–S1220, 2004.
- [122] Frithjof Karsch. Lattice qcd at finite temperature and density. *Nucl. Phys. Proc. Suppl.*, 83:14–23, 2000.
- [123] Frithjof Karsch. Lattice qcd at high temperature and density. *Lect. Notes Phys.*, 583:209–249, 2002.
- [124] Frithjof Karsch et al. Hadron correlators, spectral functions and thermal dilepton rates from lattice qcd. *Nucl. Phys.*, A715:701–704, 2003.
- [125] Frithjof Karsch et al. Hadron correlators, spectral functions and thermal dilepton rates from lattice qcd. *Nucl. Phys.*, A715:701–704, 2003.
- [126] D. Kharzeev and K. Tuchin. Open charm production in heavy ion collisions and the color glass condensate. *Nucl. Phys.*, A735:248–266, 2004.
- [127] et. al. Klein-Boseing, Christian. Phenix internal analysis note 3xx: Final run2 auau direct photon and  $\pi^0$  analysis.
- [128] Peter F. Kolb and Ralf Rapp. Transverse flow and hadro-chemistry in au + au collisions at  $s(\text{nn})^{1/2} = 200\text{-gev}$ . *Phys. Rev.*, C67:044903, 2003.
- [129] B. Z. Kopeliovich, J. Raufeisen, and A. V. Tarasov. The color dipole approach to the drell-yan process in p a collisions. 2001.
- [130] Maria Krawczyk and Wolfgang Ochs. Direct and indirect production of photon, lepton and hadron pairs in hadron - hadron collisions. *Phys. Lett.*, B79:119, 1978.
- [131] Ashish Kumar et al. Study of parton kt smearing effects in direct photon production at the fermilab tevatron. *Phys. Rev.*, D68:014017, 2003.

- [132] D. Lincoln. Qcd results using the  $k(t)$  jet-finding algorithm in  $p$  anti-  $p$  collisions at  $s^{**}(1/2) = 1800$ -gev. Presented at 32nd Rencontres de Moriond: QCD and High- Energy Hadronic Interactions, Les Arcs, France, 22-29 Mar 1997.
- [133] A. Maghakian. Direct photon cross-section measurement in anti- $p$   $p$  collisions at  $s^{**}(1/2) = 630$ -gev. Prepared for 31st Rencontres de Moriond: QCD and High- Energy Hadronic Interactions, Les Arcs, France, 23-30 Mar 1996.
- [134] Mario Martinez. Jet physics at 2-tev. 2004.
- [135] M. L. Miller and D. H. Hardtke. Charged particle jet studies in  $s(nn)^{**}(1/2) = 200$ -gev  $p + p$ ,  $d + au$ , and  $au + au$  collisions at rhic. *AIP Conf. Proc.*, 698:729–731, 2004.
- [136] James Nagle. Antiproton production and search for antideuterons and negatively charged strange quark matter in relativistic heavy ion collisions. *Ph.D Dissertation, Yale University*, 1, 1997.
- [137] T. Nakano. Evidence for penta-quark states. *Nucl. Phys.*, A738:182–187, 2004.
- [138] H. B. O’Connell, B. C. Pearce, Anthony W. Thomas, and Anthony G. Williams. Rho - omega mixing, vector meson dominance and the pion form-factor. *Prog. Part. Nucl. Phys.*, 39:201–252, 1997.
- [139] S. Ostapchenko, T. Thouw, and K. Werner. The new venus model of hadronic interactions at ultrarelativistic energies. *Nucl. Phys. Proc. Suppl.*, 52B:3–7, 1997.
- [140] J. F. Owens. Large momentum transfer production of direct photons, jets, and particles. *Rev. Mod. Phys.*, 59:465, 1987.
- [141] K. Oyama.  $\text{Pi}0$  production in  $auau$  collisions at  $\text{sqrt}(s) 130$  gev. *Doctoral Dissertation, University of Tokyo, Japan*, 2002.

- [142] W. K. H. Panofsky, J. N. Steinberger, and J. Steller. Further results on the production of neutral mesons by photons. *Phys. Rev.*, 86:180, 1952.
- [143] T. Peitzmann. Direct photon production in 158-a-gev pb-208 + pb-208 collisions. *Nucl. Phys.*, A685:399–406, 2001.
- [144] Thomas Peitzmann and Markus H. Thoma. Direct photons from relativistic heavy-ion collisions. *Phys. Rept.*, 364:175–246, 2002.
- [145] Michael E. Peskin and D. V. Schroeder. An introduction to quantum field theory. Reading, USA: Addison-Wesley (1995) 842 p.
- [146] PHENIX, 1993. PHENIX Conceptual Design Report 1993 (PX20, BNL48922, internal report).
- [147] B. Povh, K. Rith, C. Scholz, and F. Zersche. Particles and nuclei: An introduction to the physical concepts. Berlin, Germany: Springer (1995) 340 p.
- [148] P. Reiter, T. L. Khoo, C. J. Lister, D. Seweryniak, I. Ahmad, M. Alcorta, M. P. Carpenter, J. A. Cizewski, C. N. Davids, G. Gervais, J. P. Greene, W. F. Henning, R. V. F. Janssens, T. Lauritsen, S. Siem, A. A. Sonzogni, D. Sullivan, J. Uusitalo, I. Wiedenhover, N. Amzal, P. A. Butler, A. J. Chewter, K. Y. Ding, N. Fotiades, J. D. Fox, P. T. Greenlees, R.-D. Herzberg, G. D. Jones, W. Korten, M. Leino, and K. Vetter. Ground-state band and deformation of the  $z = 102$  isotope no. *Physical Review Letters*, 82(3):509–512, 1999.
- [149] Thorsten Renk. Thermal photon spectra and hbt correlations at full rhic energy. 2004.
- [150] Dirk H. Rischke. The quark-gluon plasma in equilibrium. *Prog. Part. Nucl. Phys.*, 52:197–296, 2004.
- [151] E. Shuryak. A strongly coupled quark-gluon plasma. *J. Phys.*, G30:S1221–S1224, 2004.

- [152] Edward V. Shuryak. Quantum chromodynamics and the theory of superdense matter. *Phys. Rept.*, 61:71–158, 1980.
- [153] Dinesh K. Srivastava, Charles Gale, and Rainer J. Fries. Large mass dileptons from the passage of jets through quark gluon plasma. *Phys. Rev.*, C67:034903, 2003.
- [154] Dinesh Kumar Srivastava and Bikash Chandra Sinha. A second look at single photon production in s + au collisions at 200-a-gev and implications for quark hadron phase transition. 2001.
- [155] Frank D. Steffen and Markus H. Thoma. Hard thermal photon production in relativistic heavy ion collisions. *Phys. Lett.*, B510:98–106, 2001.
- [156] W. James Stirling. Photons in high-energy physics: A theoretical overview. *J. Phys.*, G14:163–171, 1988.
- [157] T. Suzuki et al. Neutron skin of na isotopes studied via the interaction cross-sections. *Phys. Rev. Lett.*, 75:3241–3244, 1995.
- [158] Markus H. Thoma. Photon photon interaction in a photon gas. *Europhys. Lett.*, 52:498, 2000.
- [159] Anthony W. Thomas and Wolfram Weise. The structure of the nucleon. Berlin, Germany: Wiley-VCH (2001) 389 p.
- [160] H. et.al. Torii. Phenix internal analysis note 156.
- [161] Hisayuki Torii. Midrapidity neutral pion production in proton-proton collisions at sqrt(s) 200 gev. *Doctoral Dissertation, Kyoto University, Japan*, 2002.
- [162] Simon Turbide, Ralf Rapp, and Charles Gale. Photon production in relativistic nuclear collisions at sps and rhic energies. 2004.
- [163] S. E. Vance, M. Gyulassy, and X. N. Wang. Baryon junction stopping at the sps and rhic via hijing/b. *Nucl. Phys.*, A638:395c–398c, 1998.

- [164] R. Vogt. Relation of hard and total cross sections to centrality. *Heavy Ion Phys.*, 9:339–348, 1999.
- [165] Enke Wang and Xin-Nian Wang. Jet tomography of dense and nuclear matter. *Phys. Rev. Lett.*, 89:162301, 2002.
- [166] Xin-Nian Wang and Miklos Gyulassy. Hijing: A monte carlo model for multiple jet production in p p, p a and a a collisions. *Phys. Rev.*, D44:3501–3516, 1991.
- [167] Xin-Nian Wang and Miklos Gyulassy. A systematic study of particle production in p + p (anti-p) collisions via the hijing model. *Phys. Rev.*, D45:844–856, 1992.
- [168] Xin-Nian Wang, Miklos Gyulassy, and Michael Plumer. The lpm effect in qcd and radiative energy loss in a quark gluon plasma. *Phys. Rev.*, D51:3436–3446, 1995.
- [169] Xin-Nian Wang, Miklos Gyulassy, and Michael Plumer. The lpm effect in qcd and radiative energy loss in a quark gluon plasma. *Phys. Rev.*, D51:3436–3446, 1995.
- [170] Xin-Nian Wang, Miklos Gyulassy, and Michael Plumer. The lpm effect in qcd and radiative energy loss in a quark gluon plasma. *Phys. Rev.*, D51:3436–3446, 1995.
- [171] Xin-Nian Wang and Zheng Huang. Medium-induced parton energy loss in gamma + jet events of high-energy heavy-ion collisions. *Phys. Rev.*, C55:3047–3061, 1997.
- [172] Sebastian White. Direct production of electrons in very high energy proton-proton collisions. *Ph.D. Dissertation, Columbia University (Nevis Labs)*, 1976.
- [173] J. W. Wilson. Multiple scattering of heavy ions, glauber theory, and optical model. *Phys. Lett.*, B52:149–152, 1974.

- [174] Kenneth G. Wilson. Quarks and strings on a lattice. New Phenomena In Subnuclear Physics. Part A. Proceedings of the First Half of the 1975 International School of Subnuclear Physics, Erice, Sicily, July 11 - August 1, 1975, ed. A. Zichichi, Plenum Press, New York, 1977, p. 69, CLNS-321.
- [175] C. Y. Wong. Boundary effects as signals for the quark-gluon plasma. Prepared for 3rd Rio de Janeiro Workshop on Relativistic Aspects of Nuclear Physics, Rio de Janeiro, Brazil, 25-27 Aug 1993.
- [176] C. Y. Wong. Introduction to high-energy heavy ion collisions. Singapore, Singapore: World Scientific (1994) 516 p.
- [177] Cheuk-Yin Wong and Hui Wang. Effects of parton intrinsic transverse momentum on photon production in hard-scattering processes. *Phys. Rev.*, C58:376–388, 1998.
- [178] B. G. Zakharov. Induced photon emission from quark jets in ultrarelativistic heavy-ion collisions. *JETP Lett.*, 80:1–6, 2004.
- [179] Ben-Wei Zhang, Enke Wang, and Xin-Nian Wang. Heavy quark energy loss in nuclear medium. *Phys. Rev. Lett.*, 93:072301, 2004.
- [180] M. Zielinski. Jet and photon physics at d0. Prepared for 31st International Conference on High Energy Physics (ICHEP 2002), Amsterdam, The Netherlands, 24-31 Jul 2002.
- [181] M. Zielinski. Parton  $k(t)$  and large- $p(t)$  production of direct photons and  $\pi^0$  mesons. *Nucl. Phys. Proc. Suppl.*, 64:84–89, 1998.

# Appendix A

## Run Info

The following runs from the 2001  $Au + Au$  RHIC Run Period were used in this thesis analysis.

28163 28170 28199 28209 28212 28282 28284 28286 28302 28367 28371 28375  
28377 28379 28381 28414 28415 28418 28444 28447 28450 28479 28483 28485 28488  
28490 28570 28573 28577 28579 28623 28625 28627 28632 28717 28718 28749 28750  
28751 28761 28765 28768 28775 28777 28781 28791 28794 28795 28797 28798 28805  
28902 28903 28949 28951 28956 28958 28961 28962 28966 28968 28971 28972 28973  
28986 28987 29014 29015 29016 29017 29035 29036 29114 29116 29122 29146 29171  
29173 29178 29179 29183 29184 29185 29186 29190 29197 29212 29213 29218 29255  
29256 29267 29268 29362 29368 29372 29380 29386 29392 29393 29401 29404 29444  
29445 29446 29451 29454 29459 29461 29510 29512 29514 29515 29528 29529 29531  
29534 29536 29537 29561 29562 29563 29566 29987 29988 29989 29991 29999 30000  
30001 30002 30003 30007 30009 30010 30014 30015 30019 30022 30024 30026 30060  
30062 30069 30074 30087 30088 30089 30112 30113 30114 30116 30117 30119 30123  
30126 30128 30145 30146 30148 30149 30153 30157 30158 30159 30193 30195 30196  
30197 30226 30292 30306 30321 30326 30328 30329 30344 30346 30350 30356 30358  
30388 30631 30633 30637 30642 30650 30807 30812 30813 30814 30816 30820 30910  
30911 30913 30916 30917 30920 30921 31009 31013 31014 31020 31021 31024 31025  
31058 31060 31067 31072 31073 31075 31076 31079 31080 31140 31142 31143 31145  
31147 31148 31152 31230 31232 31233 31239 31240 31243 31244 31249 31252 31254

31256 31343 31459 31460 31463 31464 31497 31500 31501 31503 31515 31517 31520  
31521 31628 31631 31633 31637 31639 31641 31807 31810 31811 31814 31815 31824  
31831 31836 31837 31868 31870 32010 32011 32017 32028 32043 32123 32125 32127  
32128 32217 32218 32221 32222 32239 32241 32242 32271 32272 32275 32279 32280  
32382 32387 32435 32437 32438 32440 32441 32523 32524 32525 32526 32543 32546  
32548 32549 32709 32711 32713 32716 32717 32719 32720 32721 32722 32747 32748  
32757 32761 32762 32763 32765 32766 32770 32771 32774 32776 32777 32779 32780  
32781 32782 32906 32908 32911 32912 32913 32914 32925 32927 32928 32929 32932  
32933 32934 32947 32948 32949 33049 33050 33051 33055 33056 33064 33065 33067  
33068 33069 33077 33078 33082 33083 33085 33086 33095 33098 33113 33116 33117  
33118 33119 33121 33122 33123 33124 33125 33149 33150 33153 33157 33158 33161  
33163 33164 33166 33168 33169 33295 33298 33299 33303 33308 33309 33311 33314  
33318 33321 33323 33327 33334 33336 33337 33341 33343 33345 33347 33388 33392  
33393 33455 33458 33460 33463 33467 33468 33521 33522 33523 33526 33527 33535  
33536 33539 33541 33542 33545 33547 33550 33552 33557 33558 33560 33567 33573  
33574 33575 33577 33608 33609 33610 33611 33612 33614 33616 33693 33694

# Appendix B

## $\pi^0$ Invariant Yields

Data tables for  $\pi^0$  invariant yields as explained and plotted in results section 7.

$p_T$	Yield	Stat. Error	%	Sys. Error	%
1.25	3.314E+00	2.518E-02	0.76	4.026E-01	12.15
1.75	5.981E-01	4.946E-03	0.83	6.784E-02	11.34
2.25	1.208E-01	1.253E-03	1.04	1.447E-02	11.98
2.75	2.718E-02	3.744E-04	1.38	3.521E-03	12.96
3.25	6.970E-03	1.270E-04	1.82	9.751E-04	13.99
3.75	2.158E-03	4.713E-05	2.18	2.686E-04	12.44
4.25	7.185E-04	2.133E-05	2.97	9.349E-05	13.01
4.75	2.715E-04	1.063E-05	3.92	3.575E-05	13.17
5.25	1.288E-04	5.931E-06	4.61	1.702E-05	13.21
5.75	5.417E-05	2.606E-06	4.81	7.731E-06	14.27
6.25	2.940E-05	1.560E-06	5.31	4.106E-06	13.97
6.75	1.280E-05	9.501E-07	7.43	1.922E-06	15.02
7.25	7.641E-06	6.459E-07	8.45	1.241E-06	16.24
7.75	4.630E-06	4.668E-07	10.08	7.508E-07	16.22
8.50	1.883E-06	1.809E-07	9.61	3.033E-07	16.11
9.50	1.057E-06	1.276E-07	12.07	1.952E-07	18.47
11.00	2.777E-07	4.274E-08	15.39	5.664E-08	20.39
13.00	5.941E-08	—	—	—	—

Table B.1:  $\pi^0$  invariant yield vs.  $p_T$  for centrality fraction 0-10%. For points with no errors given, data value represents 90% confidence level upper limit.

$p_T$	Yield	Stat. Error	%	Sys. Error	%
1.25	2.054E+00	1.461E-02	0.71	2.655E-01	12.93
1.75	4.137E-01	2.933E-03	0.71	4.616E-02	11.16
2.25	8.576E-02	7.654E-04	0.89	1.039E-02	12.11
2.75	2.028E-02	2.305E-04	1.14	2.612E-03	12.88
3.25	5.057E-03	7.980E-05	1.58	6.778E-04	13.40
3.75	1.665E-03	3.170E-05	1.90	1.995E-04	11.98
4.25	5.859E-04	1.511E-05	2.58	7.301E-05	12.46
4.75	2.253E-04	7.948E-06	3.53	3.003E-05	13.33
5.25	9.486E-05	4.369E-06	4.61	1.246E-05	13.14
5.75	4.651E-05	2.087E-06	4.49	6.696E-06	14.40
6.25	2.224E-05	1.249E-06	5.62	3.252E-06	14.62
6.75	1.109E-05	8.621E-07	7.78	1.899E-06	17.13
7.25	6.455E-06	5.485E-07	8.50	1.091E-06	16.90
7.75	3.568E-06	3.999E-07	11.21	7.173E-07	20.10
8.50	1.724E-06	1.718E-07	9.96	3.279E-07	19.01
9.50	6.318E-07	9.789E-08	15.49	1.144E-07	18.11
11.00	1.701E-07	3.347E-08	19.68	3.147E-08	18.51
13.00	5.093E-08	—	—	—	—

Table B.2:  $\pi^0$  invariant yield vs.  $p_T$  for centrality fraction 10-20%. For points with no errors given, data value represents 90% confidence level upper limit.

$p_T$	Yield	Stat. Error	%	Sys. Error	%
1.25	1.601E+00	9.668E-03	0.60	1.852E-01	11.57
1.75	2.879E-01	1.911E-03	0.66	3.260E-02	11.32
2.25	6.045E-02	5.117E-04	0.85	7.416E-03	12.27
2.75	1.429E-02	1.537E-04	1.08	1.761E-03	12.32
3.25	3.983E-03	5.534E-05	1.39	5.192E-04	13.04
3.75	1.233E-03	2.340E-05	1.90	1.546E-04	12.53
4.25	4.749E-04	1.158E-05	2.44	6.115E-05	12.88
4.75	1.732E-04	5.898E-06	3.41	2.258E-05	13.04
5.25	7.761E-05	3.503E-06	4.51	1.074E-05	13.84
5.75	3.573E-05	1.627E-06	4.55	4.870E-06	13.63
6.25	1.714E-05	9.568E-07	5.58	2.389E-06	13.94
6.75	9.015E-06	6.625E-07	7.35	1.384E-06	15.36
7.25	5.146E-06	4.423E-07	8.59	8.214E-07	15.96
7.75	2.878E-06	3.267E-07	11.35	5.465E-07	18.99
8.50	1.363E-06	1.452E-07	10.65	2.517E-07	18.46
9.50	6.216E-07	8.347E-08	13.43	1.088E-07	17.50
11.00	1.825E-07	2.972E-08	16.28	3.299E-08	18.08
13.00	3.552E-08	—	—	—	—

Table B.3:  $\pi^0$  invariant yield vs.  $p_T$  for centrality fraction 20-30%. For points with no errors given, data value represents 90% confidence level upper limit.

$p_T$	Yield	Stat. Error	%	Sys. Error	%
1.25	1.040E+00	5.648E-03	0.54	1.244E-01	11.96
1.75	1.754E-01	1.100E-03	0.63	2.001E-02	11.41
2.25	3.833E-02	3.102E-04	0.81	4.567E-03	11.91
2.75	9.610E-03	9.930E-05	1.03	1.175E-03	12.23
3.25	2.670E-03	3.764E-05	1.41	3.512E-04	13.15
3.75	8.612E-04	1.667E-05	1.94	1.097E-04	12.74
4.25	3.270E-04	8.158E-06	2.49	4.185E-05	12.80
4.75	1.252E-04	4.421E-06	3.53	1.619E-05	12.94
5.25	5.266E-05	2.822E-06	5.36	7.394E-06	14.04
5.75	2.761E-05	1.348E-06	4.88	3.839E-06	13.90
6.25	1.189E-05	8.138E-07	6.85	1.949E-06	16.39
6.75	7.115E-06	5.804E-07	8.16	1.198E-06	16.84
7.25	3.705E-06	3.972E-07	10.72	6.264E-07	16.91
7.75	1.898E-06	2.549E-07	13.42	3.307E-07	17.42
8.50	1.168E-06	1.301E-07	11.13	1.967E-07	16.83
9.50	5.043E-07	8.312E-08	16.48	9.634E-08	19.10
11.00	1.541E-07	2.748E-08	17.83	2.910E-08	18.89
13.00	2.941E-08	—	—	—	—

Table B.4:  $\pi^0$  invariant yield vs.  $p_T$  for centrality fraction 30-40%. For points with no errors given, data value represents 90% confidence level upper limit.

$p_T$	Yield	Stat. Error	%	Sys. Error	%
1.25	6.389E-01	3.367E-03	0.53	7.216E-02	11.29
1.75	1.156E-01	6.789E-04	0.59	1.315E-02	11.37
2.25	2.442E-02	1.926E-04	0.79	2.911E-03	11.92
2.75	6.172E-03	6.521E-05	1.06	7.890E-04	12.78
3.25	1.682E-03	2.455E-05	1.46	2.194E-04	13.04
3.75	5.822E-04	1.161E-05	1.99	7.179E-05	12.33
4.25	1.927E-04	6.113E-06	3.17	2.480E-05	12.87
4.75	8.818E-05	3.476E-06	3.94	1.169E-05	13.26
5.25	3.627E-05	2.166E-06	5.97	4.995E-06	13.77
5.75	1.611E-05	9.656E-07	5.99	2.261E-06	14.04
6.25	9.635E-06	6.880E-07	7.14	1.490E-06	15.47
6.75	4.467E-06	4.278E-07	9.58	7.232E-07	16.19
7.25	2.044E-06	2.585E-07	12.65	3.197E-07	15.64
7.75	1.363E-06	2.198E-07	16.13	2.882E-07	21.15
8.50	7.878E-07	1.056E-07	13.41	1.409E-07	17.88
9.50	2.197E-07	5.630E-08	25.62	4.969E-08	22.61
11.00	1.053E-07	2.280E-08	21.66	2.116E-08	20.10
13.00	2.792E-08	—	—	—	—

Table B.5:  $\pi^0$  invariant yield vs.  $p_T$  for centrality fraction 40-50%. For points with no errors given, data value represents 90% confidence level upper limit.

$p_T$	Yield	Stat. Error	%	Sys. Error	%
1.25	3.593E-01	1.941E-03	0.54	4.022E-02	11.19
1.75	6.197E-02	4.018E-04	0.65	7.069E-03	11.41
2.25	1.309E-02	1.175E-04	0.90	1.553E-03	11.87
2.75	3.479E-03	4.211E-05	1.21	4.205E-04	12.09
3.25	1.019E-03	1.695E-05	1.66	1.291E-04	12.67
3.75	3.480E-04	8.518E-06	2.45	4.380E-05	12.59
4.25	1.329E-04	4.558E-06	3.43	1.763E-05	13.26
4.75	4.959E-05	2.434E-06	4.91	6.310E-06	12.73
5.25	2.125E-05	1.585E-06	7.46	3.032E-06	14.27
5.75	9.917E-06	7.569E-07	7.63	1.540E-06	15.52
6.25	6.127E-06	5.471E-07	8.93	9.978E-07	16.29
6.75	3.246E-06	3.392E-07	10.45	4.965E-07	15.30
7.25	1.664E-06	2.449E-07	14.72	3.102E-07	18.65
7.75	1.129E-06	1.886E-07	16.70	2.114E-07	18.72
8.50	3.362E-07	7.419E-08	22.07	6.694E-08	19.91
9.50	1.817E-07	4.619E-08	25.42	3.329E-08	18.32
11.00	2.858E-08	1.112E-08	38.89	4.803E-09	16.81
13.00	2.311E-08	—	—	—	—

Table B.6:  $\pi^0$  invariant yield vs.  $p_T$  for centrality fraction 50-60%. For points with no errors given, data value represents 90% confidence level upper limit.

$p_T$	Yield	Stat. Error	%	Sys. Error	%
1.25	1.731E-01	1.121E-03	0.65	1.985E-02	11.47
1.75	3.022E-02	2.288E-04	0.76	3.425E-03	11.33
2.25	6.567E-03	7.011E-05	1.07	7.773E-04	11.84
2.75	1.644E-03	2.565E-05	1.56	2.057E-04	12.51
3.25	5.255E-04	1.158E-05	2.20	6.682E-05	12.72
3.75	1.801E-04	6.044E-06	3.36	2.259E-05	12.54
4.25	6.986E-05	3.184E-06	4.56	9.254E-06	13.25
4.75	2.312E-05	1.631E-06	7.06	3.101E-06	13.41
5.25	1.156E-05	1.145E-06	9.90	1.720E-06	14.87
5.75	4.884E-06	5.045E-07	10.33	7.560E-07	15.48
6.25	2.690E-06	3.650E-07	13.57	4.303E-07	16.00
6.75	1.822E-06	2.658E-07	14.58	3.369E-07	18.48
7.25	6.281E-07	1.480E-07	23.57	1.178E-07	18.76
7.75	2.446E-07	1.082E-07	44.22	4.632E-08	18.94
8.50	1.417E-07	4.482E-08	31.62	2.707E-08	19.10
9.50	1.094E-07	3.843E-08	35.14	2.106E-08	19.26
11.00	2.492E-08	1.114E-08	44.72	4.816E-09	19.33
13.00	4.728E-09	—	—	—	—

Table B.7:  $\pi^0$  invariant yield vs.  $p_T$  for centrality fraction 60-70%. For points with no errors given, data value represents 90% confidence level upper limit.

$p_T$	Yield	Stat. Error	%	Sys. Error	%
1.25	7.416E-02	5.166E-04	0.70	8.842E-03	11.92
1.75	1.282E-02	1.189E-04	0.93	1.496E-03	11.67
2.25	2.721E-03	3.774E-05	1.39	3.245E-04	11.92
2.75	7.455E-04	1.514E-05	2.03	9.131E-05	12.25
3.25	2.461E-04	7.508E-06	3.05	3.248E-05	13.20
3.75	7.200E-05	3.689E-06	5.12	9.687E-06	13.46
4.25	2.609E-05	2.071E-06	7.94	4.034E-06	15.46
4.75	1.288E-05	1.308E-06	10.15	2.161E-06	16.78
5.25	4.650E-06	7.727E-07	16.62	9.050E-07	19.46
5.75	2.416E-06	3.897E-07	16.13	4.736E-07	19.60
6.25	1.763E-06	2.713E-07	15.39	2.795E-07	15.85
6.75	5.945E-07	1.651E-07	27.77	1.221E-07	20.53
7.25	4.817E-07	1.245E-07	25.84	8.088E-08	16.79
7.75	1.344E-07	6.718E-08	50.00	2.545E-08	18.94
8.50	1.135E-07	4.012E-08	35.36	2.167E-08	19.10
9.50	4.968E-08	2.484E-08	50.00	9.568E-09	19.26
11.00	5.060E-09	5.060E-09	100.00	9.778E-10	19.33

Table B.8:  $\pi^0$  invariant yield vs.  $p_T$  for centrality fraction 70-80%. For points with no errors given, data value represents 90% confidence level upper limit.

$p_T$	Yield	Stat. Error	%	Sys. Error	%
1.25	3.494E-02	6.093E-04	1.74	4.504E-03	12.89
1.75	6.037E-03	1.291E-04	2.14	7.607E-04	12.60
2.25	1.319E-03	3.628E-05	2.75	1.701E-04	12.89
2.75	3.321E-04	1.243E-05	3.74	4.570E-05	13.76
3.25	1.059E-04	5.281E-06	4.99	1.483E-05	14.01
3.75	3.625E-05	2.408E-06	6.64	4.455E-06	12.29
4.25	1.233E-05	1.293E-06	10.48	1.730E-06	14.03
4.75	6.501E-06	7.988E-07	12.29	9.044E-07	13.91
5.25	3.018E-06	5.360E-07	17.76	4.224E-07	13.99
5.75	1.072E-06	2.315E-07	21.60	1.815E-07	16.94
6.25	3.265E-07	1.154E-07	35.36	5.945E-08	18.21
6.75	2.805E-07	9.918E-08	35.36	5.185E-08	18.48
7.25	2.231E-07	8.434E-08	37.80	4.187E-08	18.76
7.75	8.467E-08	4.888E-08	57.74	1.604E-08	18.94
8.50	3.602E-08	2.080E-08	57.74	6.880E-09	19.10
9.50	1.077E-08	1.077E-08	100.00	2.074E-09	19.26
11.00	4.375E-09	4.375E-09	100.00	8.455E-10	19.32

Table B.9:  $\pi^0$  invariant yield vs.  $p_T$  for centrality fraction 80-92%. For points with no errors given, data value represents 90% confidence level upper limit.

$p_T$	Yield	Stat. Error	%	Sys. Error	%
1.25	1.078E+00	3.333E-03	0.31	1.205E-01	11.17
1.75	1.928E-01	6.847E-04	0.36	2.171E-02	11.26
2.25	4.038E-02	1.742E-04	0.43	4.822E-03	11.94
2.75	9.578E-03	5.293E-05	0.55	1.202E-03	12.55
3.25	2.564E-03	1.858E-05	0.72	3.375E-04	13.17
3.75	8.115E-04	7.353E-06	0.91	1.013E-04	12.48
4.25	2.906E-04	3.475E-06	1.20	3.729E-05	12.84
4.75	1.121E-04	1.806E-06	1.61	1.466E-05	13.08
5.25	4.924E-05	1.031E-06	2.09	6.494E-06	13.19
5.75	2.240E-05	4.723E-07	2.11	3.012E-06	13.45
6.25	1.190E-05	2.909E-07	2.44	1.647E-06	13.83
6.75	5.970E-06	1.943E-07	3.25	8.494E-07	14.23
7.25	3.246E-06	1.273E-07	3.92	4.758E-07	14.65
7.75	1.715E-06	9.049E-08	5.28	2.658E-07	15.49
8.50	8.583E-07	3.892E-08	4.53	1.285E-07	14.98
9.50	3.078E-07	2.351E-08	7.64	5.041E-08	16.38
11.00	9.178E-08	7.770E-09	8.47	1.417E-08	15.44
13.00	2.380E-08	—	—	—	—

Table B.10:  $\pi^0$  invariant yield vs.  $p_T$  for centrality fraction 0-100%. For points with no errors given, data value represents 90% confidence level upper limit.

# Appendix C

## Direct Photon Invariant Yields

Data tables for direct photon invariant yields as explained and plotted in results section 7.

$p_T$	Yield	Stat. Error	%	Sys. Error	%
1.25	6.225E-01	–	–	–	–
1.75	5.316E-02	–	–	–	–
2.25	4.824E-03	5.003E-04	10.37	6.216E-03	128.85
2.75	1.288E-03	1.434E-04	11.13	1.341E-03	104.15
3.25	4.960E-04	5.289E-05	10.66	3.663E-04	73.86
3.75	1.964E-04	2.292E-05	11.67	1.145E-04	58.33
4.25	1.065E-04	1.155E-05	10.85	4.401E-05	41.33
4.75	5.332E-05	6.758E-06	12.67	1.873E-05	35.13
5.25	2.346E-05	3.184E-06	13.57	8.609E-06	36.69
5.75	1.412E-05	1.611E-06	11.41	4.543E-06	32.18
6.25	6.602E-06	9.623E-07	14.58	2.223E-06	33.67
6.75	4.887E-06	7.337E-07	15.01	1.365E-06	27.94
7.25	3.574E-06	5.843E-07	16.35	9.352E-07	26.17
7.75	2.137E-06	4.183E-07	19.57	5.639E-07	26.38
8.50	9.803E-07	1.866E-07	19.04	2.528E-07	25.79
9.50	4.980E-07	1.159E-07	23.26	1.452E-07	29.15
11.00	1.731E-07	4.489E-08	25.92	4.677E-08	27.01
13.00	6.289E-08	2.556E-08	40.64	1.717E-08	27.30

Table C.1: Direct photon invariant yield vs.  $p_T$  for centrality fraction 0-10%. For points with no errors given, data value represents 90% confidence level upper limit.

$p_T$	Yield	Stat. Error	%	Sys. Error	%
1.25	4.624E-01	—	—	—	—
1.75	3.653E-02	—	—	—	—
2.25	3.850E-03	3.299E-04	8.57	4.384E-03	113.86
2.75	9.663E-04	9.079E-05	9.40	9.860E-04	102.03
3.25	4.335E-04	3.343E-05	7.71	2.684E-04	61.93
3.75	1.275E-04	1.416E-05	11.11	7.813E-05	61.27
4.25	5.636E-05	8.010E-06	14.21	2.968E-05	52.67
4.75	3.440E-05	4.746E-06	13.80	1.314E-05	38.19
5.25	1.565E-05	2.502E-06	15.99	5.882E-06	37.60
5.75	8.641E-06	1.305E-06	15.10	3.069E-06	35.52
6.25	5.141E-06	7.702E-07	14.98	1.640E-06	31.89
6.75	3.130E-06	5.456E-07	17.43	1.068E-06	34.13
7.25	1.589E-06	3.601E-07	22.66	5.296E-07	33.33
7.75	1.069E-06	2.766E-07	25.88	3.428E-07	32.08
8.50	6.572E-07	1.363E-07	20.74	1.904E-07	28.97
9.50	4.269E-07	1.040E-07	24.37	1.013E-07	23.74
11.00	1.242E-07	3.678E-08	29.62	2.850E-08	22.95
13.00	4.423E-08	1.862E-08	42.10	1.189E-08	26.88

Table C.2: Direct photon invariant yield vs.  $p_T$  for centrality fraction 10-20%. For points with no errors given, data value represents 90% confidence level upper limit.

$p_T$	Yield	Stat. Error	%	Sys. Error	%
1.25	2.128E-01	—	—	—	—
1.75	1.884E-02	—	—	—	—
2.25	1.135E-03	2.001E-04	17.64	3.101E-03	273.34
2.75	6.163E-04	6.276E-05	10.18	7.182E-04	116.54
3.25	2.065E-04	2.425E-05	11.74	1.959E-04	94.87
3.75	8.500E-05	1.051E-05	12.37	5.952E-05	70.02
4.25	2.789E-05	5.869E-06	21.04	2.307E-05	82.71
4.75	1.378E-05	3.336E-06	24.21	8.884E-06	64.48
5.25	7.539E-06	1.880E-06	24.94	4.336E-06	57.51
5.75	3.963E-06	7.886E-07	19.90	2.191E-06	55.28
6.25	2.905E-06	5.622E-07	19.35	1.175E-06	40.46
6.75	1.764E-06	4.160E-07	23.59	6.799E-07	38.55
7.25	1.130E-06	2.938E-07	25.99	4.089E-07	36.17
7.75	5.983E-07	2.142E-07	35.79	2.498E-07	41.76
8.50	3.192E-07	9.622E-08	30.15	1.176E-07	36.83
9.50	1.707E-07	5.801E-08	33.98	5.829E-08	34.15
11.00	9.792E-08	2.798E-08	28.57	2.742E-08	28.00
13.00	3.897E-08	1.938E-08	49.74	1.083E-08	27.79

Table C.3: Direct photon invariant yield vs.  $p_T$  for centrality fraction 20-30%. For points with no errors given, data value represents 90% confidence level upper limit.

$p_T$	Yield	Stat. Error	%	Sys. Error	%
1.25	1.104E-01	—	—	—	—
1.75	1.389E-02	—	—	—	—
2.25	1.434E-03	1.316E-04	9.18	2.095E-03	146.13
2.75	3.069E-04	4.086E-05	13.31	4.726E-04	154.00
3.25	1.670E-04	1.787E-05	10.70	1.343E-04	80.42
3.75	6.905E-05	8.118E-06	11.76	4.271E-05	61.85
4.25	1.538E-05	4.318E-06	28.07	1.537E-05	99.94
4.75	9.860E-06	2.798E-06	28.38	6.485E-06	65.77
5.25	5.378E-06	1.230E-06	22.87	3.220E-06	59.87
5.75	2.238E-06	6.564E-07	29.33	1.483E-06	66.29
6.25	2.116E-06	4.774E-07	22.56	8.470E-07	40.03
6.75	9.440E-07	3.311E-07	35.08	4.591E-07	48.63
7.25	8.098E-07	2.467E-07	30.46	3.229E-07	39.88
7.75	4.749E-07	1.811E-07	38.15	1.640E-07	34.54
8.50	1.803E-07	7.942E-08	44.04	7.915E-08	43.89
9.50	8.571E-08	4.811E-08	56.13	4.138E-08	48.28
11.00	1.982E-08	1.530E-08	77.17	1.100E-08	55.51
13.00	1.474E-08	1.050E-08	71.26	5.552E-09	37.67

Table C.4: Direct photon invariant yield vs.  $p_T$  for centrality fraction 30-40%. For points with no errors given, data value represents 90% confidence level upper limit.

$p_T$	Yield	Stat. Error	%	Sys. Error	%
1.25	5.157E-02	—	—	—	—
1.75	2.850E-03	—	—	—	—
2.25	1.312E-04	8.299E-05	63.27	1.245E-03	949.34
2.75	4.731E-05	2.857E-05	60.40	2.953E-04	624.20
3.25	6.152E-05	1.148E-05	18.67	8.373E-05	136.10
3.75	4.474E-05	5.923E-06	13.24	2.719E-05	60.77
4.25	1.870E-05	3.174E-06	16.97	9.590E-06	51.28
4.75	6.874E-06	1.909E-06	27.78	4.041E-06	58.80
5.25	3.997E-06	8.915E-07	22.30	1.937E-06	48.47
5.75	3.475E-06	6.224E-07	17.91	1.140E-06	32.80
6.25	9.097E-07	3.491E-07	38.37	4.821E-07	53.00
6.75	9.032E-07	2.936E-07	32.50	3.133E-07	34.69
7.25	8.812E-07	2.337E-07	26.52	2.456E-07	27.87
7.75	4.244E-07	1.501E-07	35.37	1.393E-07	32.84
8.50	1.771E-07	6.382E-08	36.04	6.599E-08	37.26
9.50	3.852E-08	3.498E-08	90.81	1.661E-08	43.13
11.00	2.429E-08	1.477E-08	60.80	9.396E-09	38.68
13.00	1.699E-08	1.087E-08	63.96	6.147E-09	36.17

Table C.5: Direct photon invariant yield vs.  $p_T$  for centrality fraction 40-50%. For points with no errors given, data value represents 90% confidence level upper limit.

$p_T$	Yield	Stat. Error	%	Sys. Error	%
1.25	2.627E-02	–	–	–	–
1.75	2.711E-03	–	–	–	–
2.25	1.401E-04	5.183E-05	37.00	6.894E-04	492.12
2.75	2.666E-05	1.929E-05	72.35	1.657E-04	621.57
3.25	2.013E-06	8.752E-06	434.83	4.674E-05	2322.46
3.75	1.720E-05	4.374E-06	25.43	1.554E-05	90.32
4.25	3.976E-06	2.193E-06	55.17	5.406E-06	135.95
4.75	4.271E-06	1.482E-06	34.69	2.409E-06	56.39
5.25	1.486E-06	6.422E-07	43.22	1.137E-06	76.52
5.75	1.167E-06	3.638E-07	31.17	5.809E-07	49.77
6.25	4.622E-07	2.198E-07	47.55	3.077E-07	66.57
6.75	4.439E-07	1.967E-07	44.32	2.085E-07	46.98
7.25	3.722E-07	1.495E-07	40.18	1.380E-07	37.09
7.75	7.880E-08	7.296E-08	92.58	5.222E-08	66.27
8.50	4.715E-08	4.011E-08	85.07	2.290E-08	48.56
9.50	3.778E-08	2.522E-08	66.75	1.685E-08	44.60
11.00	2.238E-09	–	–	–	–

Table C.6: Direct photon invariant yield vs.  $p_T$  for centrality fraction 50-60%. For points with no errors given, data value represents 90% confidence level upper limit.

$p_T$	Yield	Stat. Error	%	Sys. Error	%
1.25	1.510E-02	–	–	–	–
1.75	1.452E-03	–	–	–	–
2.25	3.477E-05	3.227E-05	92.80	3.390E-04	974.93
2.75	5.576E-05	1.267E-05	22.73	8.405E-05	150.72
3.25	1.510E-05	5.907E-06	39.12	2.395E-05	158.62
3.75	6.059E-06	3.056E-06	50.44	7.996E-06	131.96
4.25	1.416E-06	–	–	–	–
4.75	2.160E-06	1.171E-06	54.21	1.289E-06	59.67
5.25	3.158E-07	–	–	–	–
5.75	3.772E-07	2.521E-07	66.84	2.883E-07	76.43
6.25	1.391E-07	–	–	–	–
6.75	8.401E-08	–	–	–	–
7.25	5.423E-08	8.638E-08	159.30	4.051E-08	74.71
7.75	1.002E-07	1.022E-07	101.99	3.005E-08	29.98
8.50	6.434E-08	4.106E-08	63.82	2.285E-08	35.52
9.50	2.148E-08	2.230E-08	103.82	1.004E-08	46.74
11.00	5.319E-09	–	–	–	–
13.00	3.134E-09	6.176E-09	197.09	8.593E-10	27.42

Table C.7: Direct photon invariant yield vs.  $p_T$  for centrality fraction 60-70%. For points with no errors given, data value represents 90% confidence level upper limit.

$p_T$	Yield	Stat. Error	%	Sys. Error	%
1.25	5.597E-03	–	–	–	–
1.75	6.115E-04	–	–	–	–
2.25	2.560E-05	1.921E-05	75.02	1.399E-04	546.53
2.75	6.225E-06	–	–	–	–

Table C.8: Direct photon invariant yield vs.  $p_T$  for centrality fraction 70-80%. For points with no errors given, data value represents 90% confidence level upper limit.

$p_T$	Yield	Stat. Error	%	Sys. Error	%
1.25	4.405E-03	–	–	–	–
1.75	4.292E-04	–	–	–	–
2.25	5.964E-06	1.513E-05	253.76	6.932E-05	1162.32
2.75	1.673E-05	6.419E-06	38.37	1.814E-05	108.40
3.25	1.645E-07	–	–	–	–
3.75	2.032E-06	–	–	–	–
4.25	7.552E-07	6.880E-07	91.11	5.951E-07	78.80
4.75	3.533E-08	–	–	–	–
5.25	1.893E-07	–	–	–	–
5.75	1.408E-07	1.123E-07	79.78	7.139E-08	50.70
6.25	8.799E-08	7.622E-08	86.62	3.626E-08	41.21
6.75	4.468E-08	5.138E-08	114.99	2.716E-08	60.79

Table C.9: Direct photon invariant yield vs.  $p_T$  for centrality fraction 80-92%. For points with no errors given, data value represents 90% confidence level upper limit.

$p_T$	Yield	Stat. Error	%	Sys. Error	%
1.25	1.414E-01	–	–	–	–
1.75	1.071E-02	–	–	–	–
2.25	7.713E-04	6.691E-05	8.68	1.986E-03	257.51
2.75	2.515E-04	1.966E-05	7.82	4.443E-04	176.68
3.25	1.242E-04	7.470E-06	6.02	1.231E-04	99.13
3.75	5.308E-05	3.228E-06	6.08	3.879E-05	73.08
4.25	2.376E-05	1.702E-06	7.16	1.477E-05	62.15
4.75	1.325E-05	1.030E-06	7.78	6.289E-06	47.48
5.25	6.607E-06	4.995E-07	7.56	2.919E-06	44.18
5.75	3.842E-06	2.591E-07	6.74	1.491E-06	38.80
6.25	1.912E-06	1.676E-07	8.77	7.638E-07	39.94
6.75	1.341E-06	1.199E-07	8.94	4.593E-07	34.25
7.25	9.169E-07	8.874E-08	9.68	2.854E-07	31.12
7.75	5.736E-07	6.589E-08	11.49	1.714E-07	29.88
8.50	2.784E-07	2.898E-08	10.41	8.240E-08	29.60
9.50	1.465E-07	1.894E-08	12.93	4.192E-08	28.61
11.00	5.240E-08	7.458E-09	14.23	1.371E-08	26.16
13.00	1.953E-08	4.554E-09	23.32	4.898E-09	25.08

Table C.10: Direct photon invariant yield vs.  $p_T$  for centrality fraction 0-100%. For points with no errors given, data value represents 90% confidence level upper limit.

# Appendix D

## $\pi^0 R_{AA}$ Values

Data tables for  $\pi^0 R_{AA}$  as explained and plotted in results section 7.

$p_T$	Yield	Stat. Error	%	Sys. Error	%
1.25	4.113E-01	1.030E-02	2.50	6.991E-02	17.00
1.75	4.603E-01	1.600E-02	3.48	7.824E-02	17.00
2.25	4.427E-01	2.229E-02	5.04	7.511E-02	16.97
2.75	3.696E-01	2.952E-02	7.99	6.043E-02	16.35
3.25	3.273E-01	3.347E-02	10.23	5.254E-02	16.05
3.75	2.683E-01	9.259E-03	3.45	5.285E-02	19.70
4.25	2.628E-01	1.560E-02	5.94	4.864E-02	18.51
4.75	2.363E-01	1.656E-02	7.01	4.494E-02	19.01
5.25	2.417E-01	1.533E-02	6.34	4.828E-02	19.98
5.75	2.181E-01	1.952E-02	8.95	4.205E-02	19.28
6.25	2.422E-01	2.621E-02	10.82	4.725E-02	19.51
6.75	1.878E-01	2.849E-02	15.18	2.546E-02	13.56
7.25	2.379E-01	2.960E-02	12.44	4.394E-02	18.47
7.75	2.781E-01	5.742E-02	20.65	4.132E-02	14.86
8.50	1.627E-01	3.460E-02	21.26	1.971E-02	12.11
9.50	2.845E-01	4.820E-02	16.94	6.919E-02	24.32
11.00	2.894E-01	7.860E-02	27.17	5.305E-02	18.33
13.00	2.272E-01	7.135E-02	31.40	6.526E-02	28.72

Table D.1: Nuclear modification factor  $R_{AA}$  vs.  $p_T$  for centrality fraction 0-10%. Additional (overall) systematic uncertainty from thickness scaling factor listed in table 6.1 and not included here.

$p_T$	Yield	Stat. Error	%	Sys. Error	%
1.25	4.605E-01	1.153E-02	2.50	7.825E-02	16.99
1.75	5.015E-01	1.744E-02	3.48	8.520E-02	16.99
2.25	5.070E-01	2.553E-02	5.04	8.596E-02	16.96
2.75	4.497E-01	3.592E-02	7.99	7.342E-02	16.33
3.25	3.749E-01	3.835E-02	10.23	6.009E-02	16.03
3.75	3.250E-01	1.122E-02	3.45	6.391E-02	19.67
4.25	3.132E-01	1.859E-02	5.94	5.786E-02	18.48
4.75	3.259E-01	2.284E-02	7.01	6.153E-02	18.88
5.25	2.772E-01	1.758E-02	6.34	5.545E-02	20.00
5.75	2.812E-01	2.516E-02	8.95	5.414E-02	19.25
6.25	3.063E-01	3.314E-02	10.82	5.978E-02	19.52
6.75	3.267E-01	4.957E-02	15.18	4.199E-02	12.85
7.25	3.124E-01	3.887E-02	12.44	5.789E-02	18.53
7.75	3.741E-01	7.723E-02	20.65	5.516E-02	14.75
8.50	2.607E-01	5.544E-02	21.26	2.976E-02	11.42
9.50	2.644E-01	4.480E-02	16.94	7.018E-02	26.54
11.00	2.549E-01	6.926E-02	27.17	5.956E-02	23.36
13.00	3.247E-01	1.019E-01	31.40	9.824E-02	30.26

Table D.2: Nuclear modification factor  $R_{AA}$  vs.  $p_T$  for centrality fraction 10-20%. Additional (overall) systematic uncertainty from thickness scaling factor listed in table 6.1 and not included here.

$p_T$	Yield	Stat. Error	%	Sys. Error	%
1.25	5.368E-01	1.344E-02	2.50	9.120E-02	16.99
1.75	5.785E-01	2.011E-02	3.48	9.827E-02	16.99
2.25	6.160E-01	3.102E-02	5.04	1.044E-01	16.95
2.75	4.854E-01	3.877E-02	7.99	7.924E-02	16.33
3.25	4.376E-01	4.476E-02	10.23	7.012E-02	16.02
3.75	4.170E-01	1.439E-02	3.45	8.194E-02	19.65
4.25	4.332E-01	2.571E-02	5.94	7.983E-02	18.43
4.75	3.934E-01	2.757E-02	7.01	7.426E-02	18.87
5.25	3.711E-01	2.354E-02	6.34	7.405E-02	19.95
5.75	3.553E-01	3.179E-02	8.95	6.839E-02	19.25
6.25	3.440E-01	3.723E-02	10.82	6.776E-02	19.70
6.75	3.274E-01	4.969E-02	15.18	4.459E-02	13.62
7.25	3.863E-01	4.807E-02	12.44	7.249E-02	18.76
7.75	4.594E-01	9.486E-02	20.65	7.031E-02	15.30
8.50	3.226E-01	6.861E-02	21.26	3.973E-02	12.32
9.50	4.053E-01	6.867E-02	16.94	1.034E-01	25.52
11.00	4.308E-01	1.170E-01	27.17	8.898E-02	20.65
13.00	3.446E-01	1.082E-01	31.40	1.263E-01	36.66

Table D.3: Nuclear modification factor  $R_{AA}$  vs.  $p_T$  for centrality fraction 20-30%. Additional (overall) systematic uncertainty from thickness scaling factor listed in table 6.1 and not included here.

$p_T$	Yield	Stat. Error	%	Sys. Error	%
1.25	5.857E-01	1.466E-02	2.50	9.949E-02	16.99
1.75	6.053E-01	2.105E-02	3.48	1.028E-01	16.99
2.25	6.407E-01	3.226E-02	5.04	1.086E-01	16.95
2.75	5.774E-01	4.612E-02	7.99	9.424E-02	16.32
3.25	5.133E-01	5.250E-02	10.23	8.224E-02	16.02
3.75	4.901E-01	1.691E-02	3.45	9.633E-02	19.66
4.25	5.088E-01	3.020E-02	5.94	9.380E-02	18.44
4.75	4.529E-01	3.174E-02	7.01	8.585E-02	18.96
5.25	5.087E-01	3.226E-02	6.34	1.016E-01	19.97
5.75	4.433E-01	3.966E-02	8.95	8.605E-02	19.41
6.25	4.937E-01	5.341E-02	10.82	9.737E-02	19.72
6.75	4.685E-01	7.109E-02	15.18	6.462E-02	13.79
7.25	5.549E-01	6.905E-02	12.44	1.064E-01	19.18
7.75	5.025E-01	1.037E-01	20.65	8.715E-02	17.35
8.50	4.574E-01	9.727E-02	21.26	6.043E-02	13.21
9.50	6.103E-01	1.034E-01	16.94	1.625E-01	26.63
11.00	6.462E-01	1.755E-01	27.17	1.381E-01	21.36
13.00	5.066E-01	1.591E-01	31.40	2.185E-01	43.13

Table D.4: Nuclear modification factor  $R_{AA}$  vs.  $p_T$  for centrality fraction 30-40%. Additional (overall) systematic uncertainty from thickness scaling factor listed in table 6.1 and not included here.

$p_T$	Yield	Stat. Error	%	Sys. Error	%
1.25	6.420E-01	1.607E-02	2.50	1.091E-01	16.99
1.75	7.009E-01	2.437E-02	3.48	1.190E-01	16.99
2.25	7.322E-01	3.687E-02	5.04	1.241E-01	16.95
2.75	6.704E-01	5.355E-02	7.99	1.094E-01	16.32
3.25	6.209E-01	6.351E-02	10.23	9.946E-02	16.02
3.75	5.779E-01	1.994E-02	3.45	1.137E-01	19.67
4.25	5.785E-01	3.434E-02	5.94	1.072E-01	18.53
4.75	6.259E-01	4.386E-02	7.01	1.189E-01	19.00
5.25	6.214E-01	3.941E-02	6.34	1.255E-01	20.19
5.75	4.663E-01	4.172E-02	8.95	9.249E-02	19.84
6.25	6.641E-01	7.185E-02	10.82	1.333E-01	20.07
6.75	5.110E-01	7.755E-02	15.18	7.686E-02	15.04
7.25	4.514E-01	5.617E-02	12.44	9.813E-02	21.74
7.75	7.530E-01	1.555E-01	20.65	1.336E-01	17.74
8.50	5.611E-01	1.193E-01	21.26	8.606E-02	15.34
9.50	5.751E-01	9.744E-02	16.94	1.734E-01	30.15
11.00	8.584E-01	2.332E-01	27.17	2.027E-01	23.61
13.00	8.916E-01	2.800E-01	31.40	3.547E-01	39.78

Table D.5: Nuclear modification factor  $R_{AA}$  vs.  $p_T$  for centrality fraction 40-50%. Additional (overall) systematic uncertainty from thickness scaling factor listed in table 6.1 and not included here.

$p_T$	Yield	Stat. Error	%	Sys. Error	%
1.25	7.163E-01	1.793E-02	2.50	1.217E-01	16.99
1.75	7.581E-01	2.636E-02	3.48	1.288E-01	16.99
2.25	7.931E-01	3.993E-02	5.04	1.345E-01	16.95
2.75	7.408E-01	5.917E-02	7.99	1.210E-01	16.33
3.25	6.824E-01	6.980E-02	10.23	1.096E-01	16.05
3.75	6.904E-01	2.383E-02	3.45	1.362E-01	19.73
4.25	7.681E-01	4.559E-02	5.94	1.428E-01	18.59
4.75	6.444E-01	4.516E-02	7.01	1.250E-01	19.39
5.25	7.411E-01	4.700E-02	6.34	1.527E-01	20.61
5.75	6.451E-01	5.772E-02	8.95	1.300E-01	20.15
6.25	8.947E-01	9.680E-02	10.82	1.843E-01	20.60
6.75	6.879E-01	1.044E-01	15.18	1.115E-01	16.22
7.25	7.970E-01	9.918E-02	12.44	1.759E-01	22.07
7.75	1.089E+00	2.248E-01	20.65	2.155E-01	19.79
8.50	5.258E-01	1.118E-01	21.26	1.150E-01	21.87
9.50	7.598E-01	1.287E-01	16.94	2.574E-01	33.87
11.00	3.843E-01	1.044E-01	27.17	1.771E-01	46.08
13.00	1.456E+00	4.571E-01	31.40	7.005E-01	48.12

Table D.6: Nuclear modification factor  $R_{AA}$  vs.  $p_T$  for centrality fraction 50-60%. Additional (overall) systematic uncertainty from thickness scaling factor listed in table 6.1 and not included here.

$p_T$	Yield	Stat. Error	%	Sys. Error	%
1.25	7.676E-01	1.922E-02	2.50	1.304E-01	16.99
1.75	7.723E-01	2.685E-02	3.48	1.312E-01	16.99
2.25	8.387E-01	4.223E-02	5.04	1.423E-01	16.96
2.75	7.819E-01	6.245E-02	7.99	1.279E-01	16.36
3.25	7.913E-01	8.093E-02	10.23	1.275E-01	16.12
3.75	7.877E-01	2.718E-02	3.45	1.565E-01	19.87
4.25	8.762E-01	5.201E-02	5.94	1.652E-01	18.85
4.75	6.580E-01	4.611E-02	7.01	1.332E-01	20.24
5.25	7.778E-01	4.933E-02	6.34	1.710E-01	21.98
5.75	6.349E-01	5.681E-02	8.95	1.377E-01	21.68
6.25	7.512E-01	8.128E-02	10.82	1.791E-01	23.85
6.75	9.181E-01	1.393E-01	15.18	1.682E-01	18.32
7.25	6.480E-01	8.064E-02	12.44	1.859E-01	28.69
7.75	5.108E-01	1.055E-01	20.65	2.319E-01	45.40
8.50	4.551E-01	9.678E-02	21.26	1.461E-01	32.10
9.50	1.029E+00	1.744E-01	16.94	4.202E-01	40.83
11.00	8.248E-01	2.241E-01	27.17	3.801E-01	46.08
13.00	6.374E-01	2.001E-01	31.40	6.347E-01	99.58

Table D.7: Nuclear modification factor  $R_{AA}$  vs.  $p_T$  for centrality fraction 60-70%. Additional (overall) systematic uncertainty from thickness scaling factor listed in table 6.1 and not included here.

$p_T$	Yield	Stat. Error	%	Sys. Error	%
1.25	7.148E-01	1.790E-02	2.50	1.215E-01	16.99
1.75	7.697E-01	2.676E-02	3.48	1.309E-01	17.00
2.25	7.902E-01	3.979E-02	5.04	1.343E-01	16.99
2.75	7.736E-01	6.179E-02	7.99	1.271E-01	16.43
3.25	8.577E-01	8.773E-02	10.23	1.395E-01	16.26
3.75	7.218E-01	2.491E-02	3.45	1.465E-01	20.30
4.25	8.846E-01	5.250E-02	5.94	1.735E-01	19.61
4.75	9.261E-01	6.490E-02	7.01	1.971E-01	21.28
5.25	8.149E-01	5.168E-02	6.34	1.996E-01	24.49
5.75	8.294E-01	7.421E-02	8.95	1.971E-01	23.76
6.25	1.070E+00	1.158E-01	10.82	2.745E-01	25.65
6.75	7.647E-01	1.161E-01	15.18	2.091E-01	27.35
7.25	1.022E+00	1.272E-01	12.44	3.392E-01	33.18
7.75	6.450E-01	1.332E-01	20.65	3.293E-01	51.05
8.50	8.374E-01	1.781E-01	21.26	2.996E-01	35.78
9.50	1.074E+00	1.820E-01	16.94	5.819E-01	54.16
11.00	3.849E-01	1.046E-01	27.17	3.873E-01	100.62

Table D.8: Nuclear modification factor  $R_{AA}$  vs.  $p_T$  for centrality fraction 70-80%. Additional (overall) systematic uncertainty from thickness scaling factor listed in table 6.1 and not included here.

$p_T$	Yield	Stat. Error	%	Sys. Error	%
1.25	9.016E-01	2.257E-02	2.50	1.539E-01	17.07
1.75	9.121E-01	3.171E-02	3.48	1.562E-01	17.12
2.25	1.003E+00	5.051E-02	5.04	1.721E-01	17.16
2.75	8.937E-01	7.138E-02	7.99	1.496E-01	16.74
3.25	9.231E-01	9.442E-02	10.23	1.551E-01	16.80
3.75	7.994E-01	2.759E-02	3.45	1.695E-01	21.20
4.25	9.130E-01	5.419E-02	5.94	1.952E-01	21.38
4.75	1.109E+00	7.775E-02	7.01	2.579E-01	23.24
5.25	1.130E+00	7.165E-02	6.34	3.162E-01	27.98
5.75	8.045E-01	7.198E-02	8.95	2.373E-01	29.49
6.25	5.761E-01	6.234E-02	10.82	2.301E-01	39.94
6.75	8.220E-01	1.247E-01	15.18	3.046E-01	37.05
7.25	1.339E+00	1.666E-01	12.44	5.515E-01	41.19
7.75	1.029E+00	2.124E-01	20.65	6.032E-01	58.65
8.50	6.728E-01	1.431E-01	21.26	3.902E-01	58.00
9.50	5.893E-01	9.985E-02	16.94	6.020E-01	102.14
11.00	8.422E-01	2.288E-01	27.17	8.474E-01	100.62

Table D.9: Nuclear modification factor  $R_{AA}$  vs.  $p_T$  for centrality fraction 80-92%. Additional (overall) systematic uncertainty from thickness scaling factor listed in table 6.1 and not included here.

$p_T$	Yield	Stat. Error	%	Sys. Error	%
1.25	5.239E-01	1.312E-02	2.50	8.896E-02	16.98
1.75	5.890E-01	2.048E-02	3.48	9.999E-02	16.98
2.25	5.879E-01	2.960E-02	5.04	9.956E-02	16.93
2.75	5.050E-01	4.033E-02	7.99	8.228E-02	16.29
3.25	4.460E-01	4.562E-02	10.23	7.122E-02	15.97
3.75	3.915E-01	1.351E-02	3.45	7.664E-02	19.57
4.25	3.965E-01	2.353E-02	5.94	7.247E-02	18.28
4.75	3.755E-01	2.631E-02	7.01	6.977E-02	18.58
5.25	3.606E-01	2.287E-02	6.34	7.007E-02	19.43
5.75	3.273E-01	2.928E-02	8.95	6.139E-02	18.76
6.25	3.692E-01	3.994E-02	10.82	6.930E-02	18.77
6.75	3.340E-01	5.068E-02	15.18	3.859E-02	11.55
7.25	3.642E-01	4.532E-02	12.44	6.137E-02	16.85
7.75	4.213E-01	8.698E-02	20.65	4.832E-02	11.47
8.50	2.913E-01	6.194E-02	21.26	2.126E-02	7.30
9.50	3.827E-01	6.483E-02	16.94	8.360E-02	21.85
11.00	3.952E-01	1.074E-01	27.17	5.328E-02	13.48
13.00	3.815E-01	1.198E-01	31.40	4.554E-02	11.93

Table D.10: Nuclear modification factor  $R_{AA}$  vs.  $p_T$  for centrality fraction 0-100%. Additional (overall) systematic uncertainty from thickness scaling factor listed in table 6.1 and not included here.